

eman ta zabal zazu



Universidad
del País Vasco

Euskal Herriko
Unibertsitatea

Design of functional hybrid coatings with anti-biofouling, self-cleaning and anti-reflecting applications



POLYMAT

Author:

Alexander Santiago Sánchez

Supervisors:

Dr. Lourdes Irusta Maritxalar

Dr. Alba González Vives

POLYMAT, Polymer Science and Technology Department, Faculty of Chemistry,
University of the Basque Country (UPV/EHU)

Donostia, February 2016

Agradecimientos/ Acknowledgements

Al finalizar un trabajo tan esclavo y lleno de trampas como el desarrollo de una tesis doctoral es inevitable que te asalte el egocentrismo que te lleva a concentrar la mayor parte del mérito en el aporte que ha hecho uno mismo. Sin embargo, cualquier análisis te muestra inmediatamente que la obtención de esta meta que comenzó años atrás, hubiera sido imposible sin la participación de personas e instituciones que han facilitado las cosas para que este trabajo llegue a un feliz término. Por ello, es para mí un verdadero placer utilizar este espacio para ser justo y consecuente con ellas, expresándoles mis más sinceros agradecimientos.

En primer lugar, debo agradecer a la Dra. Lourdes Irusta Maritxalar y a la Dra. Alba González Vives su confianza y su consejo durante estos años en los que se ha ido desarrollando el trabajo. Sin sus consejos e indicaciones cuando nos estábamos dando de frente contra muros infranqueables hubieran hecho imposible la finalización de esta tesis doctoral. Tampoco puede uno olvidarse del resto de personas que forman parte del grupo en el que se ha desarrollado este trabajo como son la Dra. María José Fernandez-Berridi o el Dr. Juan José Iruin, que siempre han aportado su granito de arena ayudando a resolver imprevistos que siempre van surgiendo como piedras en el camino.

Debo agradecer de manera especial al Dr. Geraud Dubois por aceptar que realizara una estancia predoctoral en el centro tecnológico IBM Almaden Research Center de San Jose (California). Durante los meses que pasé allí tanto él como la Dra. Krystelle Lioni y el Dr. Willi Volksen guiaron mis pasos en técnicas y procedimientos que me eran totalmente desconocidas. Fueron unos meses de mucho trabajo pero que guardo con especial cariño.

Dentro de este trabajo, hay ciertos resultados que se han dado gracias a la colaboración entre distintos grupos de investigación. Por ello debo agradecer a la Dra. María Eugenia Muñoz y al grupo de Reología su ayuda durante el desarrollo de las medidas en su laboratorio así como sus consejos.

También debo agradecer al Dr. Thomäs Schafer y a su grupo, en especial a Ana, su ayuda durante los últimos años de la tesis y su ayuda en la medición de adsorción de proteínas.

A otra de las personas a las que debo dar un especial agradecimiento es a la Dra. Loli Martin. Su ayuda con el AFM y con el UV ha sido inestimable.

Ha sido un largo camino desde que entre a formar parte al grupo de investigación y muchos de los que estuvieron guiando mis pasos en los inicios ya han emigrado de la universidad. Pero no por ello puedo olvidarme de ellos. De Joseba, Haritz, Izaskun, personas que se convirtieron en amigos y que gracias a sus consejos, bromas y compañerismo hicieron que los días fueran alegres y los obstáculos no tan elevados como parecían.

Pero unos se fueron y otros han ido entrando. Como quien no quiere la cosa, pasé de ser el novato que necesitaba consejo y ayuda para realizar cualquier experimento, por sencillo que fuera a ser el “veterano” al que pedían consejo y ayuda, incluso tener a un pupilo al cargo e intentar enseñarle todos los trucos. Lo mejor de todo es que el buen ambiente se ha ido manteniendo a pesar del cambio de personal. Y eso se debe agradecer a la alegría que han ido trayendo cada nuevo “invitado” al laboratorio como han sido June, Oihane, Ane, Ainara, Álvaro, Robert. En resumen, un gran grupo de amigos que tenemos que repetir quedada para hacer rafting o alguna otra actividad juntos (siempre y cuando no haya altura por medio).

Mención especial merece Oihane por su contribución con el Chemdraw a las figuras de la tesis.

No me puedo olvidar del resto de grupo de becarios de otros departamentos de la Facultad. A pesar de que con el tiempo ya no hagamos tantas cenas o eventos en los que desahogarnos de los problemas de la investigación, no puedo olvidar que durante bastante tiempo siempre estuvieron allí ayudando, escuchando penas y levantando la moral cuando más se necesitaba. Todos los años, la visita al Anixeta para la comida de Navidad era un acto obligatorio para cualquier becario para disfrutar de la amistad y el buen ambiente que se respiraba.

Dentro de todos esos becarios de otros grupos, mención especial merecen aquellos que formamos el Sfinter de Milan. Un equipo, por decirlo de alguna manera, de fútbol cinco indoor que pese a las derrotas continuas que sufríamos y de lo malos que éramos no desfallecíamos y seguíamos jugando y celebrando en los pintxopotes post-partido cualquier jugada memorable (tanto para lo bueno como para lo malo) que habíamos realizado. Era una válvula de escape para todos los jueves a la tarde. Por ello gracias a Jorge “Barrilete galáctico”, Fa-Ion Velezco, EP7, David “muete”, Maxi Yo, Héctor Nodoyuna y un largo etc.

Otro de los grupos a destacar, son los grupos de “Catálisis” y “Biomal”. Entre la locura de Biomal (cualquiera que entra en ese laboratorio merece ir directo al psicólogo o psiquiatra) y las ocurrencias de Catálisis era imposible aburrirse en las comidas. Además que por si fuera poco, Dartagnan y los 3 mosqueteros (Iban, Iñigo y David), una organización sin ánimo de lucro, aprovechaba cualquier ocasión para hacerla Legendaria.

Antes de empezar el doctorado, durante la carrera, se formó el Friki Taldea (María, Ion, Andrea, Jorge y Nerea). Y aunque cada uno acabamos en un departamento

diferente, la relación nunca se ha enfriado. Han sido muchos años juntos, y los que todavía nos quedan. O eso es lo que espero y cada vez aumentando más nuestra “familia” con la adhesión de Unax y el/la que viene en camino.

Antes de acabar, debo dar las gracias también a Arrigorrista Taldea. Mis amigos en Salvatierra/Agurain. Por mucho que les haya explicado, alguno todavía habrá que crea que soy médico. Son muchos como para nombrarlos a todos, pero todos han contribuido con su granito de arena a ayudarme a superar los retos que me iban surgiendo a lo largo de estos años haciéndome ver que siempre hay una solución a cualquier problema, que solo se necesita tiempo y esfuerzo para encontrarlo.

Por último, a los que más les tengo que agradecer el apoyo que me han dado, es a mi familia. A mis padres José y María Dolores, que me han soportado durante todos los años y especialmente estos difíciles meses de escritura en los que me he acordado mil y una vez de la madre del creador de Word y de la informática por todos los problemas que me he ido encontrando, que no solucionando. También a mi hermano Ion, que aunque discutamos y nunca nos pongamos de acuerdo en prácticamente nada, siempre ha estado ahí. Además de inculcarme el amor por la bici de montaña que me ha ayudado a desconectar en momentos de estrés. Y también a Luna, por siempre alegrarse de verme cuando entro en casa.

Finalmente, debo agradecer al Gobierno Vasco, por haber financiado la investigación concediéndome la beca pre doctoral así como la ayuda para movilidad, así como a la Universidad del País Vasco (UPV/EHU).

Una vez que voy cerrando esta etapa en mi vida, viendo cómo se abren nuevas delante, uno se da cuenta de que lo importante son las circunstancias que lo rodean, sin las cuales nada sería igual. Por ello reitero mis agradecimientos a todos ya que sin vosotros nada de esto hubiera sido posible.

“En cuanto a la adversidad, difícilmente la soportarías si no tuvieras un amigo que sufriese por ti más que tú mismo”.

Marco Tulio Cicerón

General Index:

1.	Chapter 1: Introduction	7
2.	Chapter 2: Synthesis and characterization of Urethane/Siloxane copolymers with anti-biofouling applications	41
3.	Chapter 3: Preparation of superhydrophobic silica surfaces by basic Sol-Gel method with self-cleaning applications	91
4.	Chapter 4: Preparation of porous silica surfaces by acid Sol-Gel method with anti-reflecting applications	135
5.	Chapter 5: General conclusions	171
6.	Annex I: Summary/Resumen	177
7.	Annex II: Experimental techniques	185
8.	Annex III: Publications	219

Chapter 1

Introduction

Chapter 1:

Introduction

1.1.	Introduction	11
1.2.	Hydrophobic surfaces	12
1.2.1.	General concepts	12
1.2.2.	Strategies to generate hydrophobic surfaces	20
1.2.3.	Hydrophobic surfaces with self-cleaning applications	21
1.2.4.	Hydrophobic surfaces with anti-biofouling applications	24
1.3.	Anti-reflecting surfaces	29
1.4.	Background and objectives	31
1.5.	Thesis structure	32
1.6.	Bibliography	33

1.1. Introduction

Coatings are mainly applied on surfaces for decorative, protective or functional purposes. Traditional coatings are designed to passively protect the substrate to which they are applied by providing a barrier between the surface and the environment. Typical expectations of coatings include durability, reproducibility, easy application, cost effectiveness, and environmental friendliness.

The term “functional coatings” describes systems which possess, besides the classical properties of a coating (i.e., decoration and protection), an additional functionality¹. This additional functionality may be diverse, and depend upon the actual application of a coated substrate. Typical characteristics of functional coatings include self-cleaning, easy-to clean (anti-graffiti), anti-fouling, soft feel and anti-bacterial properties. Usually every coating could be understood as functional as the aim of the coating application is to fulfil a certain function on the surface (e.g. corrosion protection).

The design of a functional coating implies control of the surface chemical composition and morphology. A first example, the spatial arrangement of ligands and atoms in the top surface region of a coating defining the surface wettability was demonstrated by Langmuir in 1938². Furthermore, topological roughness and chemical heterogeneity have also influence on wetting. By adjusting functional moieties in a coating material, the resulting surface shows the desired permanent wettability, adjustable in a range between hydrophilic and hydrophobic behaviour, in respect to the chemical functions used. The most explored functional coatings are provably those presenting modified surface wetting. Thus hydrophobic coatings can impart anti-biofouling and “self-cleaning” properties to the surfaces. However, anti-fogging properties are expected for hydrophilic coatings.

Besides adjustment of wettability, various functional coatings are used in different applications such as surfaces with modified optical properties (anti-reflection, selective reflection), and surfaces with modified electromagnetic properties (conductive coatings).

To achieve the desired functions the development of new or advanced coating materials is necessary. Among them hybrid organic/inorganic materials with complex morphologies are being extensively investigated. The advantages of these hybrids are their hardness combined with excellent transparency and additional functions, such as anti-fouling.

In this work, three different types of functional hybrid coatings were obtained. These coatings were selected to impart self-cleaning, anti-biofouling and anti-reflection abilities to the surfaces. Self-cleaning and anti-biofouling properties were obtained by hydrophobization of the surface via roughness generation. However, porous surfaces were used to obtain anti-reflection coatings.

1.2. Hydrophobic surfaces

1.2.1. General concepts

The generation of surfaces which present water static contact angles higher than 90° , called hydrophobic, has aroused great interest because properties such as self-cleaning and anti-biofouling are expected^{3,4}. Low surface energy materials such as fluorinated polymers and polysiloxanes⁵ are hydrophobic and therefore have high water contact angles. However, according to literature the contact angle of a surface cannot be increased beyond 120° by a purely chemical process and higher contact angles can only be obtained if the hydrophobic surface is roughened⁶. In practice,

hydrophobic surfaces can be prepared using different methods such as etching and lithography^{7,8}, Sol-Gel processing^{9,10}, electrospinning^{11,12} and by nanostructuring of block copolymers¹³.

The wettability of a surface, which can be defined as the ability of a liquid to maintain contact with a solid surface, is a very important property in many applications. The contact angle is a quantitative measure of the wettability of a surface, represented by the angle at which a drop of liquid interfaces with a horizontal solid surface.

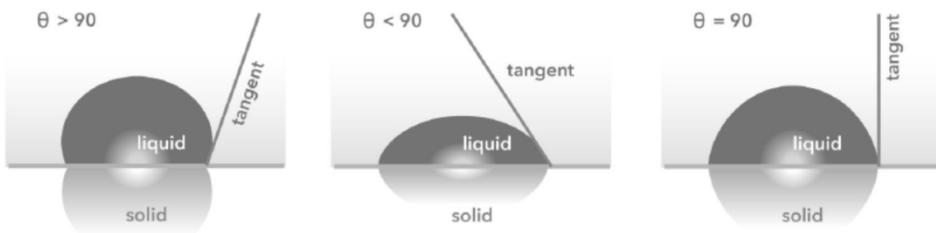


Figure 1.1. Water contact angle on different surfaces.

Figure 1.1. shows the three different states that can be observed when a drop is deposited on a surface. The surfaces in which the water drops generate contact angles higher than 90° are known as hydrophobic. High contact angles mean that the wetting of the surface is unfavorable so the fluid minimizes its contact with it and tries to form a compact liquid drop. However, the surfaces where the contact angles are smaller than 90° are called hydrophilic. In this case, the wetting is favorable and the fluid (water) spreads over the surface. The shape of the drop varies depending on the type of liquid and surface, thereby influencing the contact angle and thus the wettability.

There is another kind of surface in which the contact angle is extremely high, higher than 150° . In these surfaces, also referred to as superhydrophobic^{14,15}, there is almost no contact between the liquid drop and the surface.

In nature there are some plants or animals which exhibit the water repellent property. The most well-known and studied example is the Lotus-flower leaf¹⁶⁻¹⁹. Years ago, it was thought the water-repellent properties were only governed by the surface chemistry. However, research into the Lotus leaf surface using Electron Microscopy has shown that this surface has a special and characteristic nano-micro roughness as can be seen in Figure 1.2.

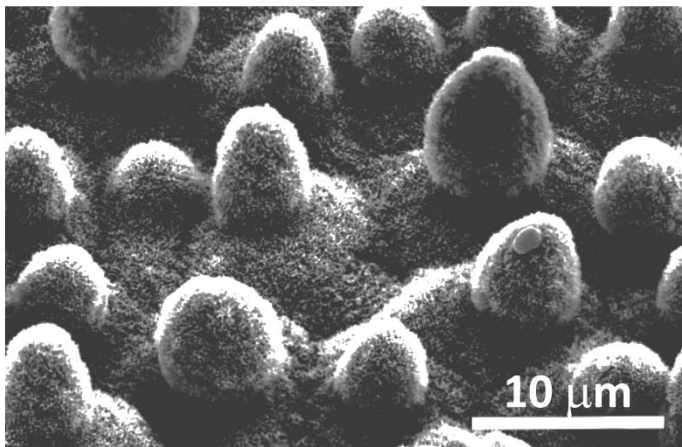


Figure 1.2. Electron Microscope image of Lotus flower leaf.

Besides the Lotus flower another plant leaves, some animals and insects have these kinds of properties in their skin, such as dolphins, butterflies and reptiles. Reptiles, as an example, show superhydrophobic properties in their skin due to the nano-micro roughness, as can be observed in Figure 1.3.

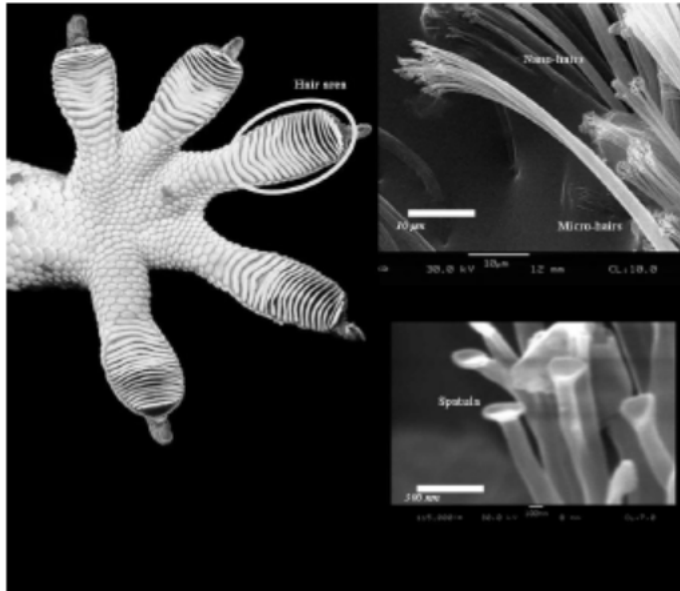


Figure 1.3. Image (left) and Electron Microscope image (right) of the reptile toe.

When a water drop is on an ideal surface: smooth, rigid and chemically homogeneous, the angle formed is a function of the interfacial energies at solid-liquid, liquid-vapour and solid-vapour boundaries as expressed in Young's equation²⁰ (equation 1.1).

$$\cos \theta = \frac{\gamma_{SV} - \gamma_{SL}}{\gamma_{LV}} \quad \text{Eq: 1.1}$$

Where γ_{LV} , γ_{SV} and γ_{SL} are the interfacial surface tensions and S, L and V indicate the state S-Solid, L-Liquid or V-Vapour respectively. Young's angle could be defined as a result of the thermodynamic balance of the free energy in the interface solid (surface)-liquid (drop)-gas (usually air). Figure 1.4. shows a water drop on an ideal surface.

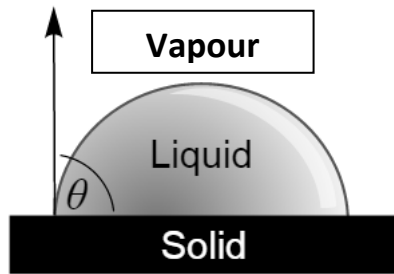


Figure 1.4. Water drop behaviour on a smooth surface.

According to the equation, water shows the highest values of the angle in materials with low surface energy such as Teflon or Silicon. However, it is well demonstrated in literature that the highest angle that can be obtained over a smooth surface²¹ is approximately 120 °. To obtain higher angles, the surface has to be rough²²⁻²⁴.

Furthermore, it can be demonstrated that the rough surfaces are more effective repelling water than the smooth surfaces even if the material is the same in both cases. Many studies have tried to seek the relation between the surface energy, roughness and contact angle. There are two theoretical models that are widely accepted, the Wenzel model and the Cassie-Baxter model.

The Wenzel model²⁵ predicts that water penetrates into the surface roughness (Figure 1.5.). The condition for it to happen is known as Wenzel state. According to this model, the contact angle that can be reached by a rough surface is determined by equation 1.2:

$$\cos \theta_w = r_s \cos \theta \quad \text{Eq: 1.2}$$

Where θ and θ_w are the contact angles of a smooth and a rough surface respectively and r_s is the superficial roughness (real area/ projected area).

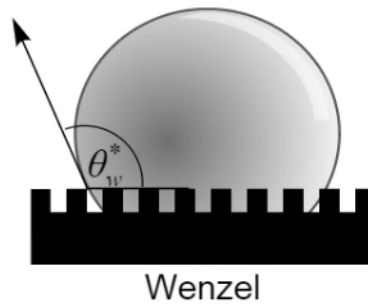


Figure 1.5. Water drop penetrating into the roughness (Wenzel state).

The Wenzel equation shows that the surface micro structure increases the natural tendency of the surface. A hydrophobic surface which has an angle higher than 90° , is more hydrophobic (the angle is higher than the original) when the surface is nanostructured. However, when the surface is hydrophilic (contact angle smaller than 90°), the rough structure makes the surface more hydrophilic.

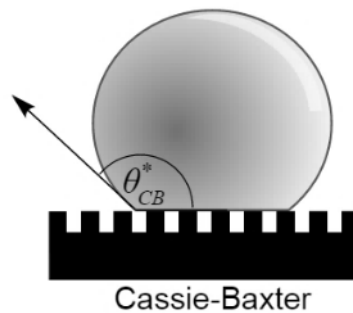


Figure 1.6. Water drop on roughness, not penetrating (Cassie-Baxter state).

In the Cassie-Baxter state²⁶, the water drop does not penetrate into the roughness but the drop remains on the rough peaks of the surface, due to the air trapped in the roughness as can be seen in Figure 1.6. In this case, the contact angle is defined by equation 1.3:

$$\cos \theta_{CB} = \varphi(\cos \theta - 1) - 1 \quad \text{Eq: 1.3}$$

Where φ is the solid fraction which is in contact with the liquid, θ_{CB} is the rough surface angle and θ is the angle of the smooth surface. The Cassie-Baxter model assumes that the water drop is not able to wet the microstructure spaces because the weight of the water drop cannot surpass the surface tension.

Generally, when a drop is on a real surface, both states described by Wenzel and Cassie-Baxter are possible. It is also possible that the drop could be in an intermediate state between both models. However, for the development of the hydrophobic surfaces with self-cleaning applications, the desirable state is that in which the drop is on top of the peaks. In this way, the adhesive force between the water and the solid surface is extremely low. On the contrary, in the Wenzel state, as mentioned previously, the water drop penetrates inside the roughness increasing the adhesion between the surface and the drop.

On account of that previously explained, it is very important to determine in which state the drop is. This can be achieved by a parameter called hysteresis of the contact angle. To improve the understanding of this parameter, it is advisable to pay attention to the behaviour of a drop on a sloping surface as can be observed in Figure 1.7.

When the drop is in contact with a sloping surface, the angle formed in the lower part of the drop and the angle formed in the upper part can be different. These angles are called advancing angle (θ_a) and receding angle (θ_r) respectively and are considered to be the maximum and the minimum experimental contact angles for the surface. The difference between both angles, advancing and receding is contact angle hysteresis parameter which is essential in order to establish if the drop is on or inside the surface roughness^{27,28}.

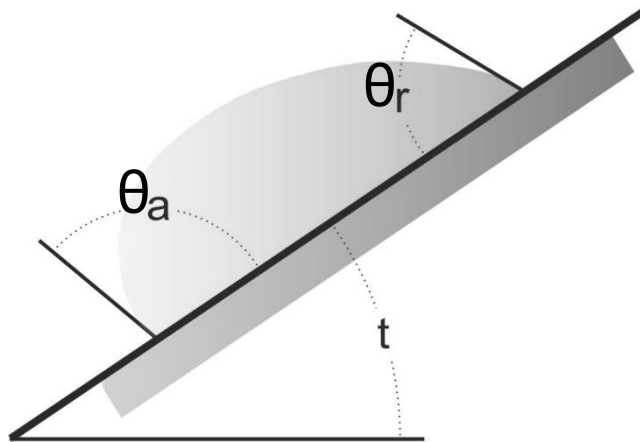


Figure 1.7. Water drop behaviour on a sloping surface.

In the Cassie-Baxter state, in which the drop is on the roughness peaks, the advancing and the receding contact angles are quite similar. That can be interpreted as low values of hysteresis. However, in the Wenzel state in which the drop is inside the superficial roughness, the advancing and receding angles are different, the advancing angle being higher meaning that the hysteresis values are high. It could be considered that the transition between the Cassie-Baxter and Wenzel state happens at values of hysteresis of 10° .

To resume, the contact angle and the hysteresis values are essential to determine the hydrophobicity of any surface. In order to obtain good results to real applications, hydrophobic surfaces with a high contact angle (higher than $\theta \geq 90^\circ$) and low values of hysteresis which minimize the adhesion of water are of great interest.

The resulting technological and industrial interest that these surfaces have generated is evident. Consequently, many researchers have studied different methods for producing artificial hydrophobic surfaces. Thus, these materials present

applications in coatings, textiles, anti-ice surfaces^{29,30}, anti-biofouling³¹ and self-cleaning surfaces^{32,33}. These applications are of great interest due to the economic impact that could be generated.

1.2.2. Strategies to generate hydrophobic surfaces

As explained in previous sections, roughness is an important parameter to obtain hydrophobic surfaces. There are many methods to make and control the surface roughness. However, according to the nomenclature used in nanoscience and nanotechnology, the different strategies can be classified as Top-Down and Bottom-Up (Figure 1.8.).

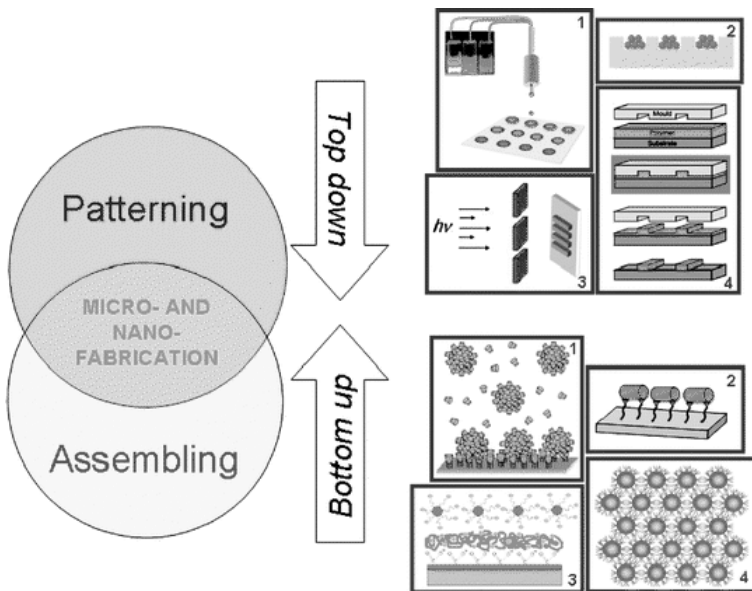


Figure 1.8. Different strategies to achieve hydrophobic surfaces.

Top-Down strategies are referred to the generation of the roughness from a smooth macroscopic surface. The surface roughness can be generated using lasers, mould, or other techniques, such as ink jet printing (1.8.1T), capillary assembly (1.8.2T), photolithography (1.8.3T) or nanoimprinting lithography (1.8.4T).

On the contrary, in Bottom-Up strategies, the roughness is generated by spontaneous or directed assembly of the molecules. Techniques such as host-guest chemistry (1.8.1B), covalent immobilization onto substrate (1.8.2B), electrostatic layer-by-layer deposition (1.8.3B) and self-assembly (1.8.4B) are used. It has been demonstrated in literature that all these strategies have the ability to generate hydrophobic surfaces.

1.2.3. Hydrophobic surfaces with self-cleaning applications

Superhydrophobic surfaces with a static contact angle above 150 ° and low contact angle hysteresis play an important role in technical applications ranging from self-cleaning window glasses, paints, and textiles and include low-friction surfaces for fluid flow and energy conservation. Lotus (*Nelumbo nucifera*) leaves have been the inspiration for the development of several commercially available self-cleaning products.

The self-cleaning property of plant surfaces was demonstrated by Barthlott and Neinhuis¹⁸. The surfaces of plants were artificially contaminated with various particles and subsequently subjected to artificial rinsing by a sprinkler or fog generator. In the case of water repellent leaves, particles were removed completely by water drops that rolled off the surfaces. If water moves over a structured hydrophobic surface, contaminating particles are picked up by the water drops or

they adhere to the surface of the drops and are then removed with the drops. Their experimental data, carried out on smooth and rough water-repellent plants, showed that the interdependence between surface roughness, degree of particle adhesion, and water repellence is the key to the self-cleaning efficiency of many plant surfaces. Figure 1.9. shows an example that illustrates the self-cleaning effect.

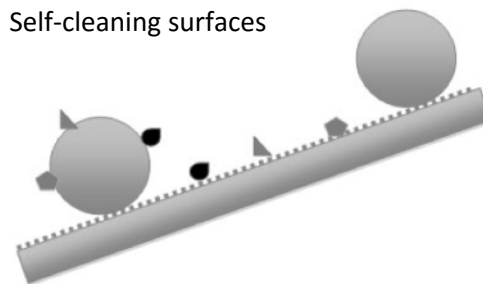


Figure 1.9. Self-cleaning effect.

In order to obtain self-cleaning property the surfaces must show high static contact angles, but low adhesion between the drop and the surface is also essential. The low adhesion is obtained if the water drop is on the hills of the roughness, in the Cassie-Baxter state, which is characterized by a low value of the contact angle hysteresis. If this condition is fulfilled, the water drop will roll-off the surface if it is slightly tilted.

A measuring method for self-cleaning surfaces is the study of the roll-off behaviour of drops on inclined surfaces. The minimum tilting angle that provokes the drop rolling is called as “sliding angle” as is also a usual parameter to determine the self-cleaning effectiveness of a surface.

Inspired by the extraordinary hydrophobic behaviour of the Lotus leaf, many researchers have studied different kind of methods for producing artificial superhydrophobic surfaces. Most of the methods chosen to obtain hydrophobic surfaces demand a complex long and expensive process. In addition, the coatings generated have low adhesion to the substrate, decreasing their application range.

The strategy most used commercially to obtain these kinds of surfaces consists of modifying the paint technology that already exists. The coatings contain particles, solvents and polymers. If the number of particles in the paint formulation is high, when the solvent is evaporated, the particles present in the formulation give the roughness to the coating surface. With a careful selection of the polymer and particles in the coating formulation, the surface morphology can be controlled. According to this, hydrophobic properties containing paints can be produced at relatively low cost³⁴.

The polymers that are most commonly used for these kinds of coatings have a low surface energy, such as polysiloxane or fluoride polymers. These compounds are hydrophobic themselves and can present surfaces with high contact angles. However, to improve the hydrophobicity, the introduction of the roughness via nanoparticles is a very important parameter³⁵ as has been previously described.

An example of these approaches is described by Yang et. al³⁶ who obtained a superhydrophobic surface adding SiO₂ and CaCO₃ into a Poly(dimethyl siloxane) matrix. Another example is described by Das et. al³⁷ in which the superhydrophobicity is obtained by means of the addition of Carbon Nanotubes in a mixture of Poly(methyl methacrylate) and Poly(vinylidene fluoride) matrix.

The SiO₂ particles are suitable for this kind of approach to obtain the superhydrophobic surfaces. These particles can be obtained easily at low

temperature by the hydrolysis and condensation of alkoxy silanes. This reaction is known as Sol-Gel process and it is thoroughly described in literature³⁸⁻⁴⁰.

One of the most well-known methods to generate the nanoparticles is the method described by Stöber et al⁴¹. In this method, an alcoholic solution of silicon alkoxides at high pH conditions is used. Some authors have explored this process^{42,43}. In most cases, the alkoxide chosen for this process is tetraethyl orthosilicate (TEOS).

By controlling the environment in which the silica nanoparticles are made, it is possible to synthesize particles with sizes ranging from 10 nm to 2 µm. The size can be tuned by adjusting the solution temperature, the catalyst concentration or using a different alcohol as solvent.

1.2.4. Hydrophobic surfaces with anti-biofouling applications

Biofouling, or biological fouling, is defined as the accumulation of microorganisms, plants, algae or animals on wetted surfaces⁴⁴. This phenomenon causes adverse effects for the environment, unwanted transport of the organisms from one ecosystem to another, or economic impact due to the increase of fuel consumption. This phenomenon causes harmful effects to the environment as well as significant economic losses, for example, it accounts for about 0.25 % of the Growth Domestic Product (GDP) in countries like Japan, UK, Germany and USA and 0.17 % in China⁴⁵.

Despite the fact that biofouling happens everywhere, the most significant economic impact of biofouling is centred in the shipping industry. Historically, the severe impact due to this fouling on the speed of the marine vessels has attracted attention. Over time, the accumulation of biofouling on ships hulls can increase both the hydrodynamic volume of a vessel and the frictional effects leading to

increased drag up to 60 %. The drag increase has been seen to decrease speeds by up to 10 %, which can require up to a 40 % increase in fuel to compensate. With fuel typically comprising up to half of marine transport costs, antifouling methods are estimated to save the shipping industry around \$60 billion per year. Increased fuel used due to biofouling contributes to adverse environmental effects and is predicted to increase emissions of Carbon Dioxide and Sulphur Dioxide between 38 and 72 % by 2020.

In addition, the biofouling phenomenon is also found in almost all circumstances where water based liquids are in contact with other materials such as membrane systems⁴⁶, cooling water systems⁴⁷ and power stations. In Figure 1.10. some effects of the biofouling in different surfaces can be seen.



Figure 1.10. Examples of biofouling.

The process of removing or preventing biofouling is defined as anti-biofouling technology. The first approaches to combat this phenomenon were based on the idea of killing the organisms responsible for the fouling process by using biocides. Biocides are chemical substances that can kill the organisms releasing toxic products into the environment, the most common of which is the tributyltin moiety (TBT).

The prevalence of TBT and other biocide based anti-fouling coatings on marine vessels is a current environmental problem due to the toxicity that TBT has shown to many marine organisms. Extremely low concentrations of TBT could be toxic for many organisms. The international maritime community has recognized this problem and there is a ban on using this kind of coating on newly built vessels. TBT compounds are banned by the Rotterdam Convention and by the International Convention on the Control of Harmful Anti-fouling Systems on Ships of the International Maritime Organization. Despite the ban, TBT will most likely be present in the water column and sediment for up to twenty years because of its long half-life time⁴⁸.

This phase out of toxic biocides in marine coatings is a severe problem for the shipping industry. Due to that, the search for new safer methods of biofouling control is active. One of the materials being considered is Copper. Copper compounds have successfully been used in paints^{49, 50} and continue to be used as metal sheeting, though there is still a debate as to its safety.

In order to solve this problem a strategy could be to avoid the adhesion of the microorganisms to the coating^{51, 52}. The new coatings, which are being developed, are non-toxic and anti-sticking to prevent attachment of microorganisms. The action mode of these coatings relies on low friction and low surface energies to try to prevent adhesion.

In Figure 1.11. a summary of the three anti-biofouling possible strategies is shown. In the first strategy, image A, the surface is not treated. In that case, the microorganisms will be on the surface producing the biofouling and the problems derived from this. In the second strategy, image B, the surface is treated with a biocide coating. In this case, the coating releases into the environment some toxic

substances that kill the organisms. Finally, the last method shown in the image represents the non-sticking coating. In this case, the microorganisms do not adhere to the surface.

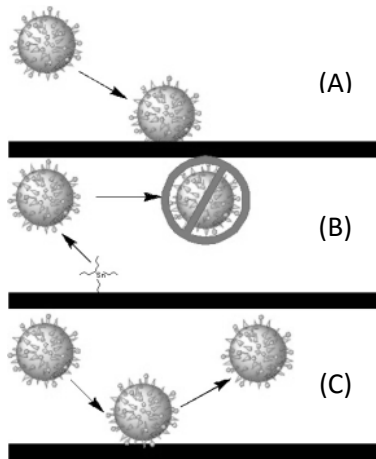


Figure 1.11. A) Untreated surface B) Biocide coating C) Non-sticking coating.

Poly(dimethyl siloxane) (PDMS) or silicone materials have been the focus of extensive research as potential anti-biofouling materials for marine applications, among other things, owing to their good fouling-release performance. However, PDMS has some obvious disadvantages, such as poor adhesion to substrates, low mechanical strength and high cost. The self-stratified Poly(siloxane-urethane) coatings try to solve some of the PDMS disadvantages such as their poor adhesion while keeping the fouling-release properties.

The introduction of the non-polar macrodiols like Poly(dimethyl siloxane) in the polyurethane chain, can give rise to nanostructured surfaces that can be used to generate hydrophobic materials^{53,54}.

Figure 1.12. shows an Atomic Force Microscopy (AFM) image of a Polyurethane/Polysiloxane (PU/PDMS) block copolymer. As can be seen, the surface

of this copolymer shows a phase separated structure the dispersed phase being composed of siloxane domains.

Furthermore, in these types of copolymers, the migration of the siloxane to the surface due to the immiscibility between components has been demonstrated⁵⁵⁻⁶⁰. The migration can generate roughness in the system that in combination with the low surface energy of the siloxane groups, improves the hydrophobic properties of the material.

These kind of surfaces are of great interest and have demonstrated their efficiency to reduce the interaction related to biofouling^{31,61}, reducing the adhesion strength of the microorganisms^{62,63}. These copolymers can be classified as non-sticky coatings and they are potential candidates to replace the toxic biocide based anti-biofouling coatings.

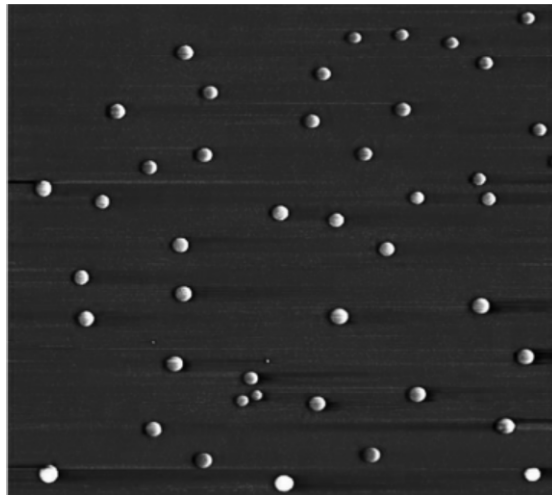


Figure 1.12. AFM image (20x20 μm) of a PU/PDMS block copolymer.

1.3. Anti-reflecting surfaces

Anti-reflecting coatings (ARC) have recently gained great interests for their possible applications in optical and display devices since the AR coatings not only remove ghost images but also enhance the transmittance of light.

For example, the total reflection loss of uncoated glass at normal incidence of light is about 8.0 % over much of the visible spectrum. This value can be decreased to below 0.2 % by coating the glass with an ARC (Figure 1.13.).

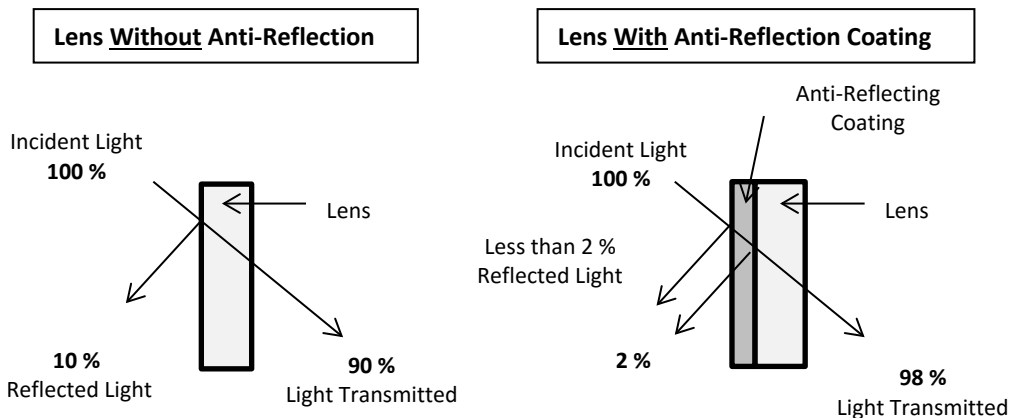


Figure 1.13. Difference of reflection with and without coating.

Basic theoretical calculations require an ideal single antireflection coating to be thin relative to the wavelength of incident light (e.g. thickness= $\lambda/4$, λ is the wavelength).

In addition, in order to obtain an anti-reflecting coating, the refractive index (RI) must be lower than that of the substrate (typically glass) and must be tuneable for broadband applications. Since the lowest refractive index for a dense material is 1.34, porous materials are an obvious choice for applications requiring even lower RI. In addition, the porosity in thin-films can be modified hence the RI can be tuneable.

Various techniques to generate porous films have been proposed including leaching of glasses⁶⁴ and Sol–Gel condensation^{65,66}. In microelectronics, the search for low dielectric constant (low-k) materials for interlayer dielectrics (ILD) has led to much work on the generation of porous thin-films. The so-called sacrificial-porogen approach uses the removal of organic polymer domains from a nano-hybrid of the organic polymer and inorganic Poly(methyl silsesquioxane) (PMSSQ) matrix to generate nanoporous structures⁶⁷.

This process utilizes phase separation of two component systems where one component (e.g., organosilicates matrix) crosslinks into a network, effectively limiting domain growth and coarsening of the porogen phase (an organic, labile polymeric component) that is ultimately expelled from the film by thermal decomposition. Figure 1.14. depicts the scheme of pore generating process.

Since the resulting pore sizes are much smaller than visible wavelengths, thus minimizing scattering, these films are potentially useful for optical applications including ARCs.

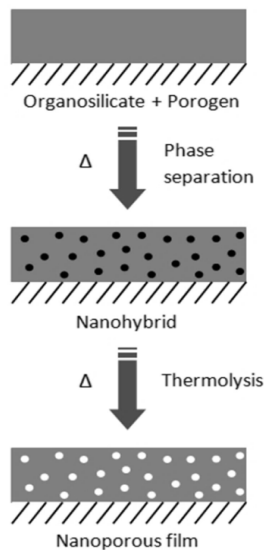


Figure 1. 14. Scheme to obtain a porous film.

1.4. Background and objectives

The origin of this thesis can be found in the project of the Polymat Institute entitled “Polymers for hydrophobic and anti-ice formation surfaces” funded by the “Diputación Foral de Gipuzkoa” during the years 2011-2012. The aim of that project was to apply the wide experience in the field of polymeric hydrophobic surfaces of the members of the different groups of the Polymat Institute to finding applications in self-cleaning and anti-ice coating technology. The supervisors of the present thesis and me were part of the research group of that project where our contribution was basically related to the development of functional coatings with self-cleaning applications.

In January 2012 the Basque Government conceded a pre-doctoral grant to a more general research project related to the design of functional coatings. Thus, in addition to continue exploring the self-cleaning effect, coatings with other functions such as anti-biofouling and anti-reflecting abilities were considered. The present document summarizes the results obtained during this scholarship period.

Thus, the main objective of the present thesis is centred on obtaining functional coatings with specific applications in self-cleaning, anti-biofouling and anti-reflecting coatings. As described in previous sections, these kinds of coatings present a great academic and commercial interest.

Our first objective was centred in obtaining an economically and technically competitive coating with anti-biofouling abilities. The employed strategy, included in the “Bottom-Up” methodology implied the synthesis of Urethane/Siloxane block copolymers, which according to some literature data could give rise to the desired surfaces.

The followed strategy in order to obtain self-cleaning coatings was based on the conventional painting application methods and consisted of introducing inorganic nanoparticles in polymeric matrixes using the methodologies described in previous paragraphs (Top-Down strategy). Our goal was to establish a relation between the obtained surface morphology (that was changed with the type, size and proportion of the employed nanoparticles as well as with the application method) and the self-cleaning abilities of the coatings.

The manuscript also contains a description of the creation of porous surfaces that have applications as anti-reflection coating. This part of the work was carried out in the IBM research centre of Almaden (EEUU) and is the result of the pre-doctoral stage funded by the Basque Government that took place during February-May 2015. These results constitute the initial steps of a new line of research and collaboration.

1.5. Thesis Structure

Taking into consideration the objectives, described in section 1.4, this manuscript has been organized in the following chapters:

- ✓ Chapter II is devoted to obtaining hydrophobic anti-biofouling surfaces by self-assembly of block copolymers. Thus, the synthesis and characterization of Urethane/Siloxane block copolymers is described. As the main application of the obtained coating is centred in the field of anti-biofouling coatings, some preliminary fouling resistance tests are also included.

- ✓ Chapter III is devoted to obtaining hydrophobic self-cleaning surfaces by introducing inorganic silica nanoparticles into polymeric matrixes. The nanoparticles were obtained by hydrolysis and condensation of alkoxy silanes, using the Sol-Gel process. Silica nanoparticles of different sizes were introduced into polymeric matrixes in order to give the surface the necessary roughness to obtain self-cleaning properties.
- ✓ Chapter IV describes the work developed in the IBM Almaden Research Center in San Jose, in the frame of the pre-doctoral stage funded by the Basque Government. In that work, porous coatings synthesised by the Sol-Gel acid process were developed in order to obtain materials with anti-reflecting properties. These materials are of great interest in the industry because of their potential applications in multiple fields.
- ✓ Chapter V summarizes the most relevant conclusions of this work.
- ✓ The manuscript also contains three annexes. The first one is a summary of the thesis that is the only part written in Spanish. The second one devoted to explain the employed experimental techniques. Finally, the papers derived from this thesis are also attached in the third annex.

1.6. Bibliography

1. Mathiazhagan, A. & Joseph, R. Nanotechnology-A New Prospective in Organic Coating. *Int. J. Chem. Eng. Appl.* **2**, 228–237 (2011).
2. Langmuir, I. Overturning and anchoring of monolayers. *Science*. **87**, 493–500 (1938).

3. Euvananont, C., *et al.* TiO₂ optical coating layers for self-cleaning applications. *Ceram. Int.* **34**, 1067–1071 (2008).
4. Feng, B. L., *et al.* Super-Hydrophobic Surfaces: From Natural to Artificial. *Adv. Mater.* **14**, 1857–1860 (2002).
5. Nishino, T., *et al.* The Lowest Surface Free Energy Based on - CF₃ Alignment. *Langmuir.* **15**, 4321–4323 (1999).
6. Verplanck, N., Galopin, E., Camart, J-C. & Thomy V. Reversible electrowetting on superhydrophobic silicon nanowires. *Nano Lett.* **7**, 813–817 (2007).
7. Sung, Y. H., *et al.* Fabrication of superhydrophobic surfaces with nano-in-micro structures using UV-nanoimprint lithography and thermal shrinkage films. *Appl. Surf. Sci.* **349**, 169–173 (2015).
8. Milionis, A., *et al.* Superhydrophobic/superoleophilic magnetic elastomers by laser ablation. *Appl. Surf. Sci.* **351**, 74–82 (2015).
9. Rezayi, T. & Entezari, M. H. Achieving to a superhydrophobic glass with high transparency by a simple sol-gel-dip-coating method. *Surf. Coat. Technol.* **276**, 557–564 (2015).
10. Liu, S., *et al.* Self-cleaning transparent superhydrophobic coatings through simple sol-gel processing of fluoroalkylsilane. *Appl. Surf. Sci.* **351**, 897–903 (2015).
11. Buruaga, L., Gonzalez, A., Irusta, L. & Iruin, J.J. Production of hydrophobic surfaces in biodegradable and biocompatible polymers using polymer solution electrospinning. *J. Appl. Polym. Sci.* **120**, 1520–1524 (2011).
12. Dong, F., *et al.* Superhydrophobic/hydrophobic nanofibrous network with tunable cell adhesion: Fabrication, characterization and cellular activities. *Colloids Surf. A.* **482**, 718–723 (2015).
13. Wen, X., *et al.* Crosslinked superhydrophobic films fabricated by simply casting (methacrylate)-b-poly(perfluorohexylethyl methacrylate) solution. *Appl. Surf. Sci.* **339**, 109–115 (2015).

14. Feng, L., *et al.* Super-Hydrophobic Surfaces: From Natural to Artificial. *Adv. Mater.* **14**, 1857–1860 (2002).
15. Wang, S. & Jiang, L. Definition of superhydrophobic states. *Adv. Mater.* **19**, 3423–3424 (2007).
16. Marmur, A. The lotus effect: Superhydrophobicity and metastability. *Langmuir.* **20**, 3517–3519 (2004).
17. Yamamoto, M., *et al.* Theoretical Explanation of the Lotus Effect: Superhydrophobic Property Changes by Removal of Nanostructures from the Surface of a Lotus Leaf. *Langmuir.* **31**, 7355–7363 (2015).
18. Barthlott, W. & Neinhuis, C. Purity of the sacred lotus, or escape from contamination in biological surfaces. *Planta.* **202**, 1–8 (1997).
19. Neinhuis, C. Characterization and Distribution of Water-repellent, Self-cleaning Plant Surfaces. *Ann. Bot.* **79**, 667–677 (1997).
20. Young, T. An Essay on the Cohesion of Fluids. *Vasa.* **95**, 65–87 (1894).
21. Erbil, H. Y., Demirel, A. L., Avci, Y. & Mert, O. Transformation of a Simple Plastic into a Superhydrophobic Surface. *Science.* **299**, 1377–1380 (2003).
22. Coulson, S. R., *et al.* Super-Repellent Composite Fluoropolymer Surfaces. *J. Phys. Chem. B.* **104**, 8836–8840 (2000).
23. Chen, W., *et al.* Ultrahydrophobic and ultralyophobic surfaces: some comments and examples. *Langmuir.* **15**, 3395–3399 (1999).
24. Paxson, A. T. & Varanasi, K. K. Self-similarity of contact line depinning from textured surfaces. *Nat. Commun.* **4**, 1492–1500 (2013).
25. Wenzel, R. N. Surface Roughness and Contact Angle. *J. Phys. Colloid Chem.* **53**, 1466–1467 (1949).
26. Liu, T. L., Chen, Z. & Kim, C. J. A dynamic Cassie–Baxter model. *Soft Matter.* **11**, 1589–1596 (2015).

27. Krumpfer, J. W., *et al.* Contact Angle Hysteresis on Superhydrophobic Surfaces : An Ionic Liquid Probe Fluid Offers Mechanistic Insight. *Langmuir*. **27**, 2166–2169 (2011).
28. Hejazi, V. & Nosonovsky, M. Contact angle hysteresis in multiphase systems. *Colloid. Polym. Sci.* **291**, 329–338 (2013).
29. Farhadi, S., Farzaneh, M. & Kulinich, S. Anti-icing performance of superhydrophobic surfaces. *Appl. Surf. Sci.* **257**, 6264–6269 (2011).
30. Kulinich, S. A. & Farzaneh, M. Ice adhesion on super-hydrophobic surfaces. *Appl. Surf. Sci.* **255**, 8153–8157 (2009).
31. Krishnan, S., *et al.* Anti-biofouling properties of comblike block copolymers with amphiphilic side chains. *Langmuir*. **22**, 5075–5086 (2006).
32. Latthe, S. S., *et al.* Development of sol–gel processed semi-transparent and self-cleaning superhydrophobic coatings. *J. Mater. Chem. A*. **2**, 5548–5553 (2014).
33. Yoon, H., *et al.* Highly Transparent Self-Cleaning Superhydrophobic Surface by Electrospayed Silica-Alumina Composite. *J. Mater. Chem. A*. **3**, 11403–11410 (2015).
34. Yüce, M. Y. & Demirel, A. L. The effect of nanoparticles on the surface hydrophobicity of polystyrene. *Eur. Phys. J. B*. **64**, 493–497 (2008).
35. Verplanck, N., Coffinier, Y., Thomy, V. & Boukherroub, R. Wettability Switching Techniques on Superhydrophobic Surfaces. *Nanoscale Res. Lett.* **2**, 577–596 (2007).
36. Yang, J., *et al.* A novel method to fabricate superhydrophobic surfaces based on well-defined mulberry-like particles and self-assembly of polydimethylsiloxane. *Appl. Surf. Sci.* **255**, 3507–3512 (2009).
37. Das, A., *et al.* Superhydrophobic and conductive carbon nanofiber/PTFE composite coatings for EMI shielding. *J. Colloid Interface Sci.* **353**, 311–315 (2011).

38. Omid, Z., Ghasemi, A. & Bakhshi, S. R. Synthesis and characterization of SiC ultrafine particles by means of Sol-Gel and carbothermal reduction methods. *Ceram. Int.* **41**, 5779–5784 (2015).
39. Sorochkina, K., Smotraiev, R. & Chepurna, I. Zirconium and aluminum oxyhydroxides particles formation during sol–gel process. *Colloids Surf. A.* **484**, 56–61 (2015).
40. Sardon, H., Irusta, L., Aguirresarobe, R. H. & Fernandez-Berridi, M. J. Polymer/silica nanohybrids by means of tetraethoxysilane Sol-Gel condensation onto waterborne polyurethane particles. *Prog. Org. Coat.* **77**, 1436–1442 (2014).
41. Stöber, W., Fink, A. & Bohn, E. Controlled growth of monodisperse silica spheres in the micron size range. *J. Colloid Interface Sci.* **26**, 62–69 (1968).
42. Li, W. & Zhao, D. Extension of the stöber method to construct mesoporous SiO₂ and TiO₂ shells for uniform multifunctional core-shell structures. *Adv. Mater.* **25**, 142–149 (2013).
43. Mily, E., *et al.* Silica nanoparticles obtained by microwave assisted Sol-Gel process: Multivariate analysis of the size and conversion dependence. *J. Sol-Gel Sci. Technol.* **53**, 667–672 (2010).
44. Shirtliff, M. & Leid, J. G. Control of Biofilm Infections by Signal Manipulation *Springer Series on Biofilms. Springer Series on Biofilms. Vol 3.* **2**, (2008).
45. Divulgación Marina by AZTI-Tecnalia. "Resolviendo el problema del biofouling". <http://itsasnet.com> (2013).
46. Chen, V., Mansouri, J. & Charlton, T. Biofouling in Membrane System. *Memb. Tec.* 25-51 (2010).
47. Nebot, E., *et al.* Marine biofouling in heat exchangers. *Biofouling: Types, Impact and Anti-Fouling.* 65-104 (2010).
48. Antizar-Ladislao, B. Environmental levels, toxicity and human exposure to tributyltin (TBT)-contaminated marine environment. A review. *Environ. Int.* **34**, 292–308 (2008).

49. Cotou, E., *et al.* Short-term exposure of the European sea bass *Dicentrarchus labrax* to copper-based antifouling treated nets: Copper bioavailability and biomarkers responses. *Chemosphere*. **89**, 1091–1097 (2012).
50. Braithwaite, R. A., Carrascosa M. C. & McEvoy L. A. Biofouling of salmon cage netting and the efficacy of a typical copper-based antifoulant. *Aquaculture*. **262**, 219–226 (2007).
51. Schultz, M. P. Effects of coating roughness and biofouling on ship resistance and powering. *Biofouling*. **23**, 331–341 (2007).
52. Magin, C. M., Cooper, S. P. & Brennan, A. B. Non-toxic antifouling strategies. *Mater. Today*. **13**, 36–44 (2010).
53. Rahman, M. M., Chun, H. & Park, H. Waterborne polysiloxane-urethane-urea for potential marine coatings. *J. Coat. Technol. Res.* **8**, 389–399 (2011).
54. Pergal, M. V., *et al.* Microstructure and properties of poly(urethane-siloxane)s based on hyperbranched polyester of the fourth pseudo generation. *Prog. Org. Coat.* **76**, 743–756 (2013).
55. Majumdar, P., Ekin, A. & Webster, D. C. Thermoset Siloxane-Urethane fouling release coatings. *Smart Coatings*. **957**, 5–61 (2007).
56. Majumdar, P. & Webster, D. C. Surface microtopography in siloxane–polyurethane thermosets: The influence of siloxane and extent of reaction. *Polymer*. **48**, 7499–7509 (2007).
57. Majumdar, P. & Webster, D. C. Influence of solvent composition and degree of reaction on the formation of surface microtopography in a thermoset siloxane–urethane system. *Polymer*. **47**, 4172–4181 (2006).
58. Majumdar, P., Stafslie, S., Daniels, J. & Webster, D. C. High throughput combinatorial characterization of thermosetting siloxane–urethane coatings having spontaneously formed microtopographical surfaces. *J. Coat. Technol. Res.* **4**, 131–138 (2007).
59. Ma, M. & Hill, R. M. Superhydrophobic surfaces. *Curr. Opin. Colloid Interface Sci.* **11**, 193–202 (2006).

60. Sommer, S., *et al.* A preliminary study on the properties and fouling-release performance of siloxane–polyurethane coatings prepared from poly(dimethylsiloxane) (PDMS) macromers. *Biofouling*. **26**, 961–972 (2010).
61. Gudipati, C. S., *et al.* Hyperbranched fluoropolymer and linear poly(ethylene glycol) based amphiphilic crosslinked networks as efficient antifouling coatings: An insight into the surface compositions, topographies, and morphologies. *J. Polym. Sci. Part A Polym. Chem.* **42**, 6193–6208 (2004).
62. Callow, M. E., *et al.* Microtopographic cues for settlement of zoospores of the green fouling alga *Enteromorpha*. *Biofouling*. **18**, 237–245 (2002).
63. Schumacher, J. F., *et al.* Engineered antifouling microtopographies-Effect of feature size, geometry, and roughness on settlement of zoospores of the green alga *Ulva*. *Biofouling*. **23**, 55–62 (2007).
64. Mukherjee, S. P. & Lowdermilk, W. H. Gel-derived single layer antireflection films. *J. Non-Cryst. Solids*. **48**, 177–184 (1982).
65. Yang, H. L., *et al.* Self-Cleaning and Antireflective Films for All-Glass Evacuated Tube Solar Collectors. *Energy Procedia*. **69**, 226–232 (2015).
66. Uhlmann, D. R., *et al.* Sol–gel derived coatings on glass. *J. Non-Cryst. Solids*. **218**, 113–122 (1997).
67. Biswas, K., Gangopadhyay, S., Kim, H. & Miller, R. Nanoporous organosilicate films as antireflection coatings. *Thin Solid Films*. **514**, 350–354 (2006).

Chapter 2

Synthesis and characterization of
Urethane/Siloxane copolymers
with anti-biofouling applications

Chapter 2:

Synthesis and characterization of Urethane/Siloxane copolymers with anti-biofouling applications

2.1.	Introduction	45
2.2.	Materials	46
2.3.	Characterization techniques	47
2.4.	Preliminary study	48
	2.4.1. Results and discussion	50
2.5.	Life-extender effect in the morphology	58
2.6.	Urethane/Siloxane copolymers with low siloxane content	62
	2.6.1. Morphology and wettability	62
	2.6.2. Anti-biofouling behaviour	74
2.7.	Conclusions	85
2.8.	Bibliography	86

2.1. Introduction

Segmented Poly(Urethane/Siloxane) copolymers present unusual properties directly related to their two-phase microstructure. This microstructure is a consequence of the thermodynamic incompatibility between the hard and soft segments.

The introduction of nonpolar Poly(dimethyl siloxane)(PDMS)¹⁻³ in the polyurethane backbone gives rise to nanostructured surfaces that can be used to generate hydrophobic materials⁴⁻⁶. Surface composition analysis of block and graft copolymers containing Poly(dimethyl siloxane) segments have shown that PDMS predominates on the surface due to its immiscibility with other polyurethane components and its low surface energy. These types of surfaces are of special interest because they have shown to be effective in reducing the interactions associated with biofouling. PDMS elastomers with well-defined microtopographical features inhibit the settlement of fouling organisms and this is important since Copper and Tributyltin (TBI) boat paints, used to prevent fouling, cause particular environmental damage.

The extent to which microphase separation occurs to form supramolecular structures in multiblock copolymers such as PDMS copolymers depends on four features. First is the chemical composition dissimilarity, which leads to a difference in solubility parameters and chain interactions. Second is the segment molar mass of the copolymer components; third, the crystallinity of one or both segments, and fourth, the molecular architecture of the copolymer⁴⁻¹⁰. Furthermore, the morphology of multiblock copolymers also depends on the way in which the materials are synthesized and the method of the film preparation¹¹.

Bearing in mind these considerations, the present chapter is devoted to the generation of hydrophobic surfaces by nanostructuring of Poly(Urethane/Siloxane) copolymers. The particular surface properties of these copolymers are obtained

through the segregation of incompatible and less polar soft siloxane domains towards the surface to minimize the interfacial tension with air. These kinds of surfaces are of special interest as antibiofouling coatings because they couple the toughness and good adhesion of polyurethanes with the hydrophobic surface properties of polysiloxanes.

2.2. Materials

Aliphatic Polyisocyanate Vestanat T 1890 E (IPDI trimer, 70 wt. % in Butyl acetate) was obtained from Evonik Industries. The isocyanate structure is represented in Figure 2.1.

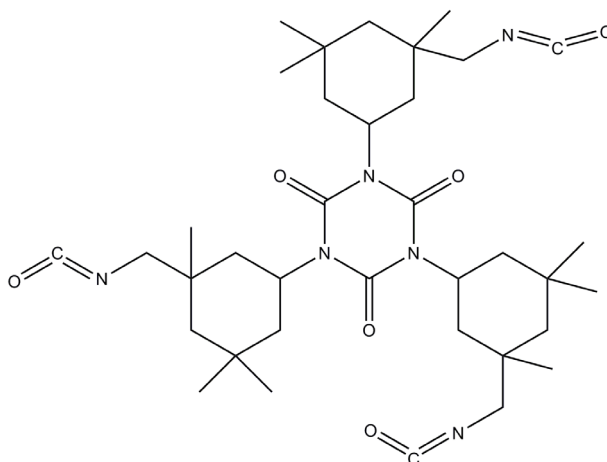


Figure 2. 1. Isophorone diisocyanate trimer structure.

Poly(dimethyl siloxane) terminated in Poly(ethylene glycol) (PDMS, M_n 1000 g/mol, 20 wt. % non-siloxane component) was supplied by Gelest Inc. The structure of the PDMS is shown in Figure 2.2.

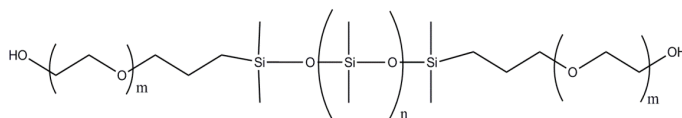


Figure 2. 2. Hydroxyl terminated Poly(dimethyl siloxane) structure.

Trifunctional polyol Polycaprolactone, (PCL, Mn 900 g/mol) was selected as a second polyol to synthesise the polyurethane. Its structure is shown in Figure 2.3.

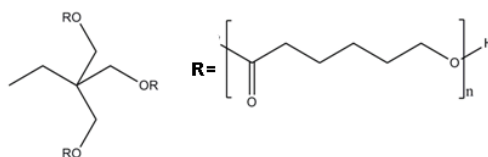


Figure 2. 3. Polycaprolactone triol structure.

Dibutyltin dilaurate (DBTDL), Butyl acetate (BA) and Acetyl Acetone (AA) were supplied by Sigma-Aldrich and were used as catalyst, solvent and life-extender respectively.

2.3. Characterization techniques

Fourier Transform Infrared Spectroscopy (FTIR) in transmission mode was used to characterize the reaction. The siloxane surface concentration was calculated by using an Attenuated Total Reflection (ATR) accessory.

The phase separation was studied by Dynamic Mechanical Thermal Analysis (DMTA), Atomic Force Microscopy (AFM) and Transmission Electron Microscopy (TEM). Contact angle values were used to determine the surface wettability.

Finally, anti-biofouling properties were studied by protein adsorption measurements. UV spectroscopy, Quartz Crystal Microbalance with dissipation (QCM-D) and Surface Plasmon Resonance (SPR) experiments were carried out.

A description of these experimental techniques as well as a description of the employed equipment and experimental conditions can be found in Annex II.

2.4. Preliminary study

The particular surface properties of Poly(Urethane/Siloxane) copolymers are obtained through the segregation of incompatible and less polar soft siloxane domains towards the surface to minimize the interfacial tension with air.

In order to get a good adhesion with the substrate, our goal was to obtain hydrophobic surfaces using the minimum PDMS amount. According to this, several syntheses were performed changing the relation of the polyols (PCL/PDMS) from 0 % to 100 % in order to determine the best composition.

The isocyanate and alcohol groups react via polyaddition reaction to give rise urethane groups. Figure 2.4. shows the scheme of polyurethane synthesis.

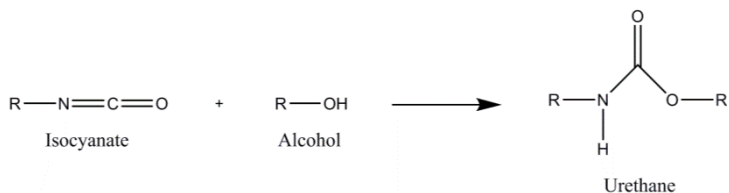


Figure 2.4. Urethane polymerization reaction scheme.

This reaction is catalysed by organometallic tin catalysts. The followed methodology is described before.

PCL and PDMS solutions in Butyl Acetate (33 wt. % of solids) were introduced in a 100 mL Erlenmeyer at room temperature and mixed for 1 minute under magnetic stirring. Then, the required amount of IPDI trimer and DBTDL (0.1 % total solids) solutions in 33 wt. % of solids in Butyl Acetate were added. The equivalent ratio between NCO:OH was kept constant for all formulations as 1.1:1.0 in excess of isocyanate. Table 2.1. summarizes the reagent amounts of all the prepared copolymers.

Formulation (PCL/PDMS)	PCL (g)	Solvent BA (mL)	PDMS (g)	Solvent BA (mL)	IPDI[70%] (g)	Solvent BA (mL)
100/0	9	20.25	0	0	10.48	11.13
90/10	8.1	18.22	1	2.25	10.13	10.76
80/20	7.2	16.20	2	4.50	9.78	10.39
70/30	6.3	14.17	3	6.75	9.43	10.02
60/40	5.4	12.15	4	9.00	9.08	9.65
50/50	4.5	10.12	5	11.25	8.73	9.28
40/60	3.6	8.10	6	13.50	8.38	8.91
30/70	2.7	6.07	7	15.75	8.03	8.54
20/80	1.8	4.05	8	18.00	7.68	8.17
10/90	0.9	2.02	9	20.25	7.34	7.79
0/100	0	0	10	22.50	6.99	7.42

Table 2. 1. Summary of reagent amounts of all the copolymers.

As the employed alcohol PCL is trifunctional, a crosslinked network is obtained. Therefore, gelification occurs at different reaction times. For each composition, the gel-time was measured as it will be shown in the next paragraphs.

The solutions were casted over aluminium pans before gelification occurs and the solvent was evapored at room temperature for 24 h followed by oven curing at 80 °C for 45 minutes.

2.4.1. Results and discussion

The polymerization reaction of the different samples was monitored by infrared spectroscopy, collecting several spectra before reaching the gel-point of the reaction mixture.

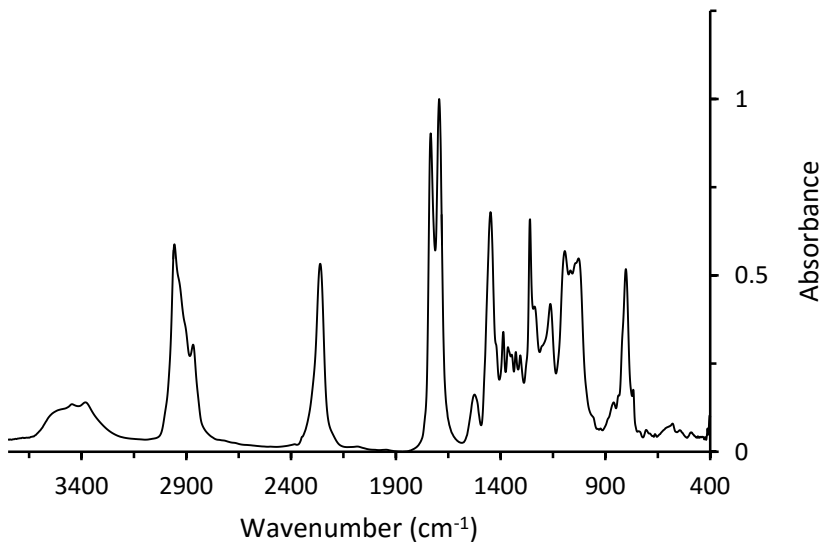


Figure 2.5. Infrared spectrum of the 70/30 sample after 30 minutes of reaction.

Figure 2.5. shows the infrared spectrum of the 70/30 sample after 30 minutes of reaction. All FTIR spectra of polyurethane have in common a band at 3300 cm^{-1} assigned to the N-H stretching vibration associated by hydrogen bonding. Moreover, a band attributed to the stretching vibration of carbonyl groups appears at 1720 cm^{-1} (Amide I). In some cases this band can present two contributions. In addition, all polyurethanes present a band at 1550 cm^{-1} (known as Amide II) attributable to a combination of C-N stretching and N-H bending vibrations. Due to the presence of Polycaprolactone, an intense band assigned to -C=O stretching vibrations can be also observed at 1740 cm^{-1} . In addition, bands assigned to siloxane moieties (1110 cm^{-1} Si-O stretching and 800 cm^{-1} CH_3 -Si stretching and CH_3 bending) are presented in the spectrum. Finally a band at 2240 cm^{-1} which is assigned to the isocyanate stretching vibration is detected. This band, whose relative intensity decreased in the polymerization process, was used to calculate the conversion of the reaction.

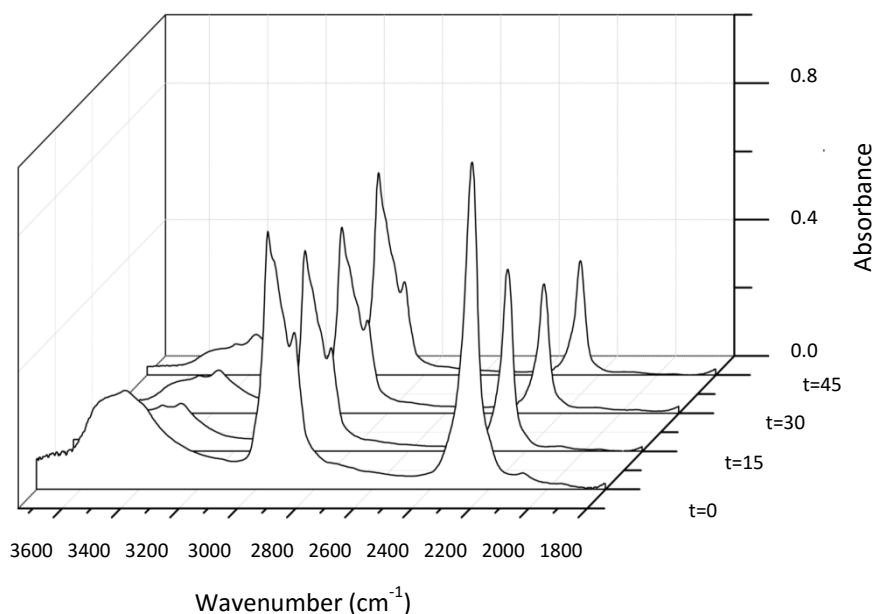


Figure 2.6. Scale expanded infrared spectra of sample 70/30 PCL/PDMS versus reaction time.

Figure 2.6. shows the scale expanded infrared spectra of sample 70/30 PCL/ PDMS, as a function of the reaction time. As can be observed, the absorbance of the band at 2240 cm^{-1} , assigned to the isocyanate stretching vibration decreased with the reaction time, which was indicative of the polymerization reaction process. Consequently, the band absorption was measured at different reaction times. In order to take into account the path length of the samples, the band at 3000 cm^{-1} , assigned to the C-H stretching was used to normalize sample thickness. Equation 2.1. was used to calculate the reaction conversion.

$$\text{Conversion} = \frac{(A_{2240}/A_{3000})_t}{(A_{2240}/A_{3000})_{t_0}} \quad \text{Eq: 2.1}$$

Conversion data were obtained until the gel-point was reached. The average deviation of the conversion measured by FTIR technique was ± 0.1 .

Figure 2.7. shows the conversion of the reaction for different copolymer composition as a function of the mixing time. As can be observed, as the content of the trifunctional polyol (PCL) in the samples increased less experimental points could be obtained because the gel-point was reached at lower conversions. This can be explained due to the addition of more reticulation points with the presence of the PCL, given that this polyol is trifunctional and the PDMS is bifunctional.

However, comparing the conversion obtained at the same reaction time for different systems, except for the sample containing only PCL (100/0 PCL/PDMS) it seems that the conversion was lower as the PDMS content increased. This result can be explained upon the basis of a lower reactivity of PDMS polyol.

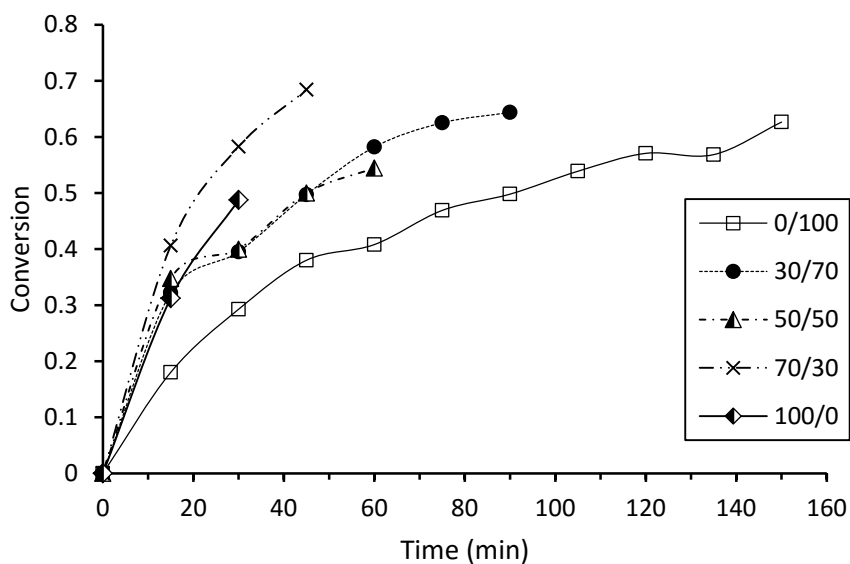


Figure 2.7. Conversion versus reaction time for different samples (PCL/PDMS).

The samples, obtained before gelification, were casted and cured in an oven. As a consequence of the thermodynamic incompatibility between the siloxane and urethane components, a phase separation happens. This separation process was analysed by Dynamic Mechanical Thermal Analysis (DMTA). In this technique, the glass transition temperature (measured as the maximum in Tangent δ value) can be measured. If the system is phase separated, each segment will present its glass transition temperature while if phase mixing happens, only one glass transition temperature will be observed. Figure 2.8. shows the Tan δ values as a function of the temperature for different systems. The average deviation for this technique measurements was ± 2 °C.

For PCL/PDMS (0/100) sample, two peaks were observed (named I and III). The lower temperature mechanical loss process (I), located at -95 °C was assigned to the

segmental motion of PDMS units¹. In addition, the strength of this relaxation reduced with the PDMS content, supporting this assignment. The higher temperature segmental loss process at 48 °C (III) was associated to the mixing of the PDMS final Poly(ethylene glycol) end groups with the IPDI trimer. These segments are not compatible with the PDMS units and therefore in (0/100) PCL/PDMS sample two transitions were observed.

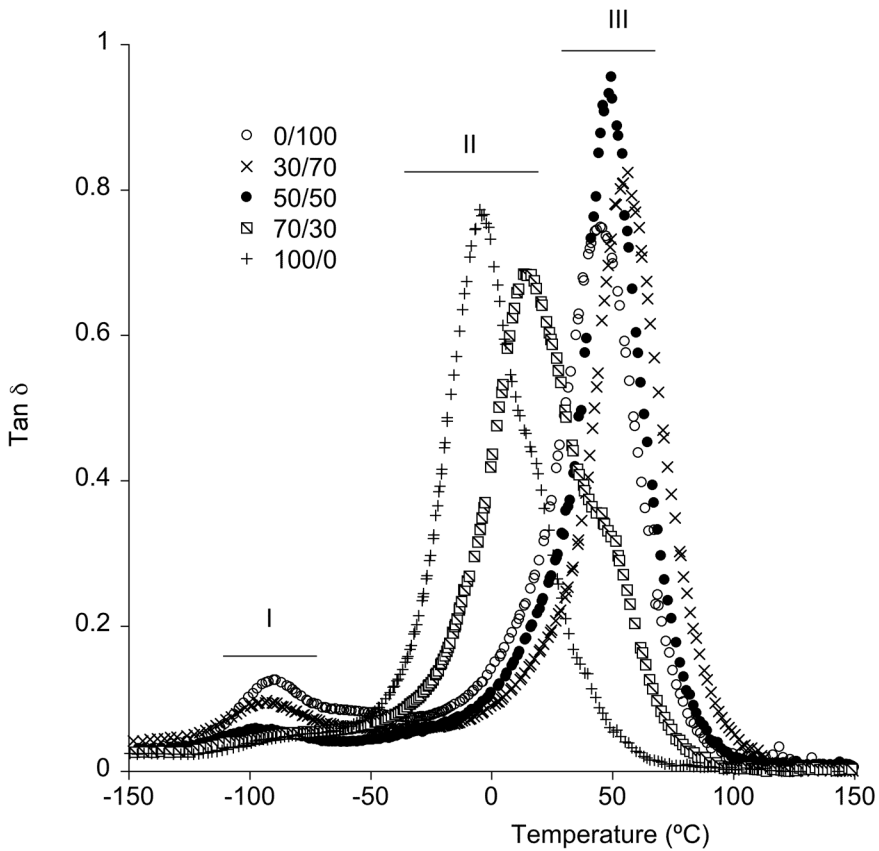


Figure 2.8. $\tan \delta$ versus temperature for different compositions PCL/PDMS.

For PCL/PDMS (100/0) sample, one main transition (II) was observed at $-1\text{ }^{\circ}\text{C}$, indicating the total compatibility between the PCL and IPDI segments. For the sample containing 30 % of PDMS (70/30), the transition assigned to the PCL/IPDI segments (II) shifted towards higher temperatures and for the samples containing higher PDMS contents the transition was not detected, probably because it was overlapped with III. The shift of the II peak can be explained taking into account that there is a partial mixing between the PCL segments and the final Poly(ethylene glycol) groups of PDMS units.

However, the position of the segmental motion of PDMS units (I) did not change with the introduction of PCL in the structure, indicating no discernible mixing between the siloxane units and PCL, and the formation of pure PDMS unit microphases¹².

The hydrophobicity of the samples was estimated by static water contact angle measurements. Different composition samples casted and cured were detached of the aluminium pan and contact angles of the surfaces generated in contact with air and aluminium were determined. Figure 2.9. shows the obtained results. The average deviation of the static water contact angle measurements was $\pm 4\text{ }^{\circ}$.

As can be seen, no PDMS containing sample showed a contact angle near 77 ° , characteristic of a hydrophilic surface. However, the incorporation of a 10 % of PDMS to the polyol mixture caused an important increase of the water contact angle, especially on the face in contact with air, where the value increased to 96 ° , making the surface hydrophobic. Additional increments of the PDMS content did not significantly affect the air contact surface hydrophobicity.

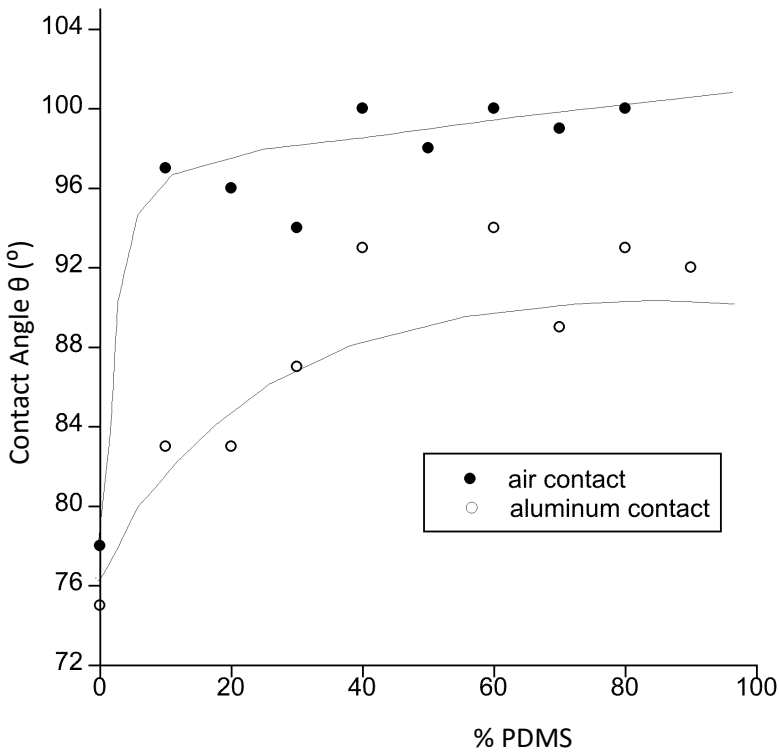


Figure 2. 9. Water contact angle versus siloxane content for both faces of different films.

Comparing the data of the contact angles obtained in both surfaces, it is clear that higher angles were obtained in the air contact generated surface what means that there was a higher concentration of less polar siloxane domains in this surface. It can be explained due to the low superficial tension of the PDMS segments that forces the migration of this component to the air surface of the sample.

Atomic Force Microscopy (AFM) images were obtained in order to compare the morphology of these surfaces. Figure 2.10. shows the AFM height image for both surfaces of the 70/30 sample. As can be observed, two-phase morphology was observed in the film obtained in contact with air while a homogeneous surface was observed on the aluminum generated surface.

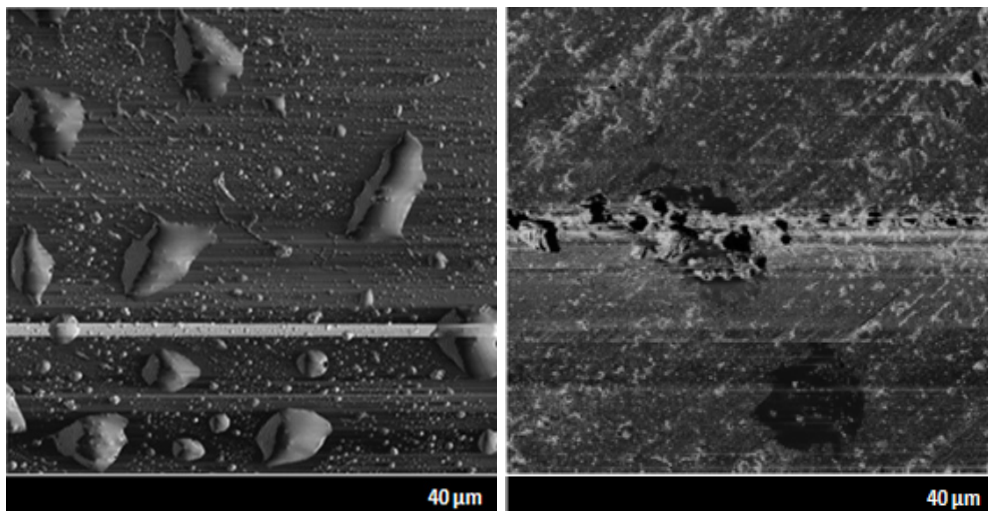


Figure 2. 10. AFM images (40 x 40 μm) of the 70/30 sample (PCL/PDMS). Air contact (left) aluminium contact (right).

From these results it could be deduced that probably the dispersed phase observed on the surface in contact with air is mainly composed of siloxane domains. This morphology is probably the reason of the higher water contact angle shown by this surface.

In order to observe the morphology of the whole film, the samples were transversely cut with an ultramicrotome and Transmission Electron Microscopy (TEM) studies were performed. Figure 2.11. shows the image of the sample 70/30 (PCL/PDMS).

As can be seen in the image, small silicon domains were observed in the surface of the sample. However, there were larger silicon domains inside the film but they presented higher size than the domains present in the surface. This result confirmed the AFM data where a non-homogeneous silicon distribution was observed.

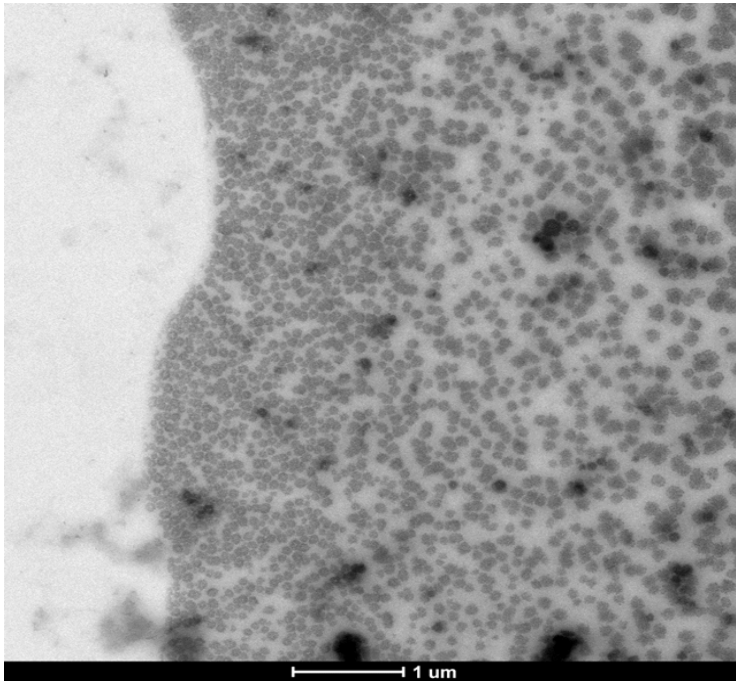


Figure 2. 11. TEM image of the transversal cut for the 70/30 (PCL/PDMS) sample film.

2.5. Life-extender effect in the morphology

The preliminary studies displayed in the previous section have shown that the sample containing only a 10 % of siloxane showed a high increase in the contact angle value. Moreover, additional increment of the PDMS content on the polymer composition did not give rise to higher water contact angle values.

Bearing in mind these results, all the following analysis were performed with the sample containing 10 % of PDMS. The analysis was centred to obtain the surface stratification of the copolymer in order to get a higher surface hydrophobicity.

As stated by Webster et al.^{6,7,13,14}, the reaction time before the casting defines the sample morphology. Thus, samples casted at different reaction times show different

morphologies and therefore different wettability. The main problem is that sample containing 90 % of PCL in its composition showed the gel-point at very low reaction time which limits the range of times that can be analysed. Following the methodology of Webster, we added Acetyl Acetone (AA) to the formulation as a life-extender in order to control the phase separation of the copolymer, increasing the mixing time of the reaction before reaching the gel-point.

The polymerization reaction resulting from a variation in AA from 0 to 10 % was monitored by infrared spectroscopy, and several spectra were collected before the gel-point of the reaction mixture was reached.

The absorbance of the infrared band at 2240 cm^{-1} assigned to the isocyanate stretching vibration, whose relative concentration decreased during the polymerization process, was used to calculate the conversion as described in a previous section (Eq 2.1). The conversion for samples containing different Acetyl Acetone (AA) concentration is shown in Figure 2.12.

As can be observed in Figure 2.12., the time when the gelification happens increased considerably with Acetyl Acetone concentration. Thus sample without AA showed a gelification at 30 minutes while samples containing 1 and 10 % of AA showed their gel-point at 400 minutes and 1500 minutes respectively. This result proves that the Acetyl Acetone reduces the reaction rate and therefore the gel-point is reached at longer reaction times. This fact can be explained upon the basis of the complexation of Acetyl Acetone with the stannous catalyst, which decreases the catalytic effect of DBTDL¹⁵. Similar conclusions were obtained in literature¹⁴.

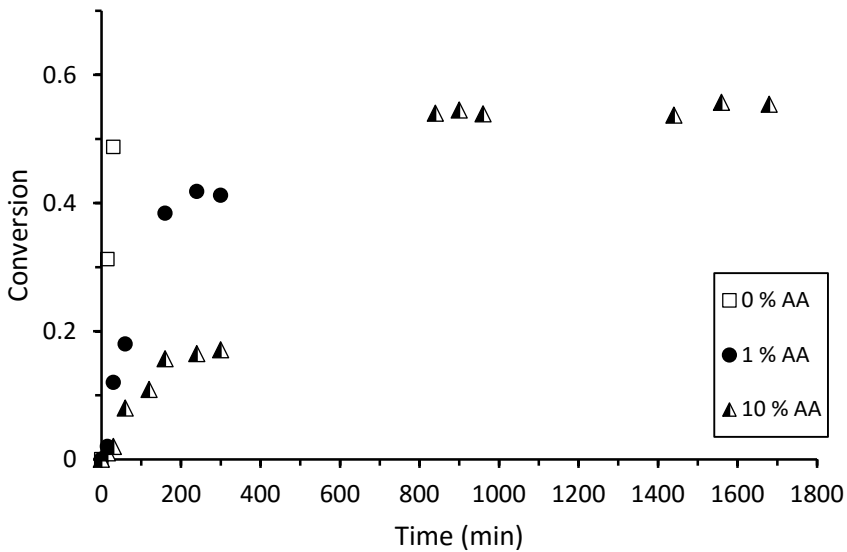


Figure 2. 12. Conversion versus reaction time for formulations with different amounts of Acetyl Acetone (AA) as life-extender.

As we are interested in preparing films at different reaction conversions, trying to obtain phase separation morphology, the subsequent experiments were performed using 10 % of Acetyl Acetone. The reason for this choice was that this percentage of AA delays the gel-point of the reaction for one day, offering the possibility of controlling the conversion of the reaction.

In order to determine if the delay of the reaction allows us generating phase-separation morphology in the system, AFM study was made to the films with 10 % of AA. In order to perform the experiments after variable reaction times, the solutions were casted under room conditions for 24 hours. This step was followed by oven curing at 80 °C for 45 minutes.

Figure 2.13. shows the AFM images of the films obtained by casting at different reaction times. As can be observed, some of the images showed a phase separated structure with microtopographical surfaces. According to literature⁷, the dispersed phase was composed of siloxane domains.

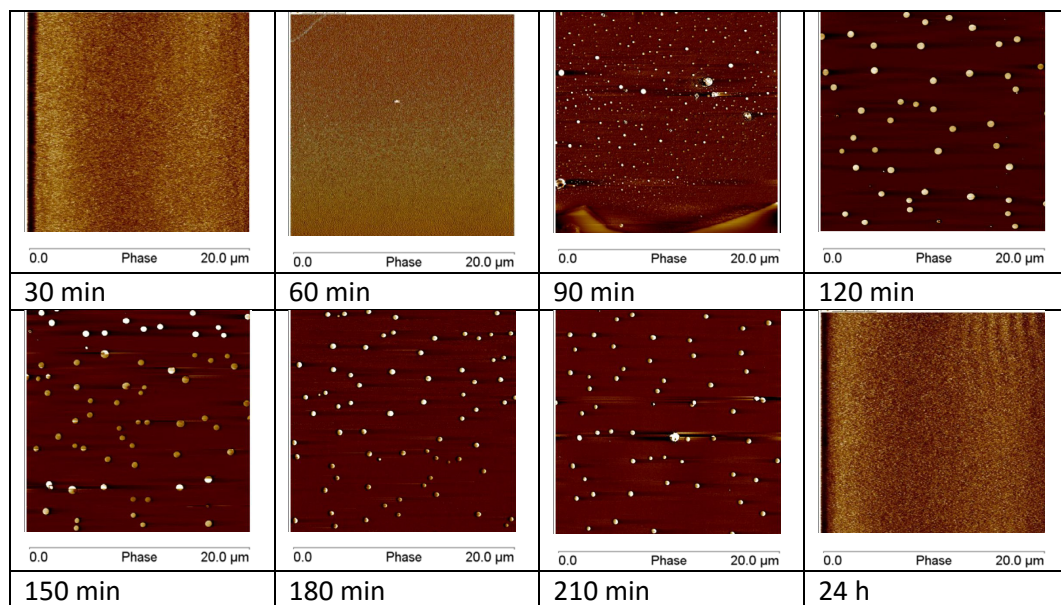


Figure 2. 13. AFM phase images (20 μm X 20 μm) for films obtained at different reaction times.

As can be seen in Figure 2.13. the images of the samples obtained after 30 and 60 minutes of reaction time showed a homogeneous surface. After 90 minutes of reaction, microdomains with uniform spherical shapes were observed. The size of these microdomains grew with the reaction time reaching a maximum at 150 minutes. Then, the size decreased and at 24 hours no microdomains were formed.

According to these results, the reaction time and therefore, the extent of the reaction prior to film formation, had a significant influence in the microdomain

formation. This behaviour has also been observed by Webster et al.¹³ According to these authors, the final mixing observed at high reaction times is related to the higher compatibility of the PDMS-IPDI/PCL-IPDI system at high conversion.

2.6. Urethane/Siloxane copolymers with low siloxane content

In previous sections, the effect of the life-extender in the sample morphology has been studied. Bearing in mind these results, the present section of the chapter is devoted to study the properties such as hydrophobicity and roughness, of the copolymers with low siloxane content. It is interesting to note that, as can be seen in the preliminary study, the addition of small quantities of Poly(dimethyl siloxane) increased substantially the water contact angle.

According to some literature results⁷, the anti-fouling ability of block copolymers is also related to the phase separated morphology. The anti-biofouling ability of these phase separated copolymers was evaluated through protein sorption measurements.

2.6.1. Morphology and wettability

Following the methodology used in previous section, Acetyl Acetone was added to the formulation in order to control the phase separation of the copolymers. Three different formulations containing 5 %, 10 % and 15 % of siloxane were synthesized using different mixing times to control sample morphology. The samples were casted following two methods. In the first one, the samples were kept under room

temperature (25 °C) for 24 hours. In the second one, the coatings were kept at 50 °C for 24 hours on a hot plate in a fume hood.

Figure 2.14. shows the AFM phase images of the samples casted at room temperature.

As can be seen, some of the images showed a phase separated structure with microtopographical surfaces, being the dispersed phase composed of siloxane domains. For each composition, no phase separated images were obtained at low and high mixing times and domain formation was observed at intermediate times. According to these results the formation of microtopographical surfaces only happened when the films were casted at intermediate conversion and if the conversion was higher, total miscibility between the urethane and siloxane components was obtained. The behaviour of the samples containing 10 and 15 % of PDMS was similar. However, in the sample containing 5 % of PDMS, the phase separated structures and the final mixing were obtained at lower mixing times.

In order to analyse the effect of the casting temperature on the sample morphology, similar samples were obtained but performing the casting process at 50 °C. The AFM phase images of these samples are shown in Figure 2.15.

The behaviour was the same as that obtained for the room temperature casted samples but the microdomain formation process took place in a shorter time interval. This result could be explained upon the basis of a faster evaporation of Acetyl Acetone at 50 °C. As described in previous section [2.5.] Acetyl Acetone slowed down the reaction rate and therefore the evaporation of this compound accelerated the phase formation process.

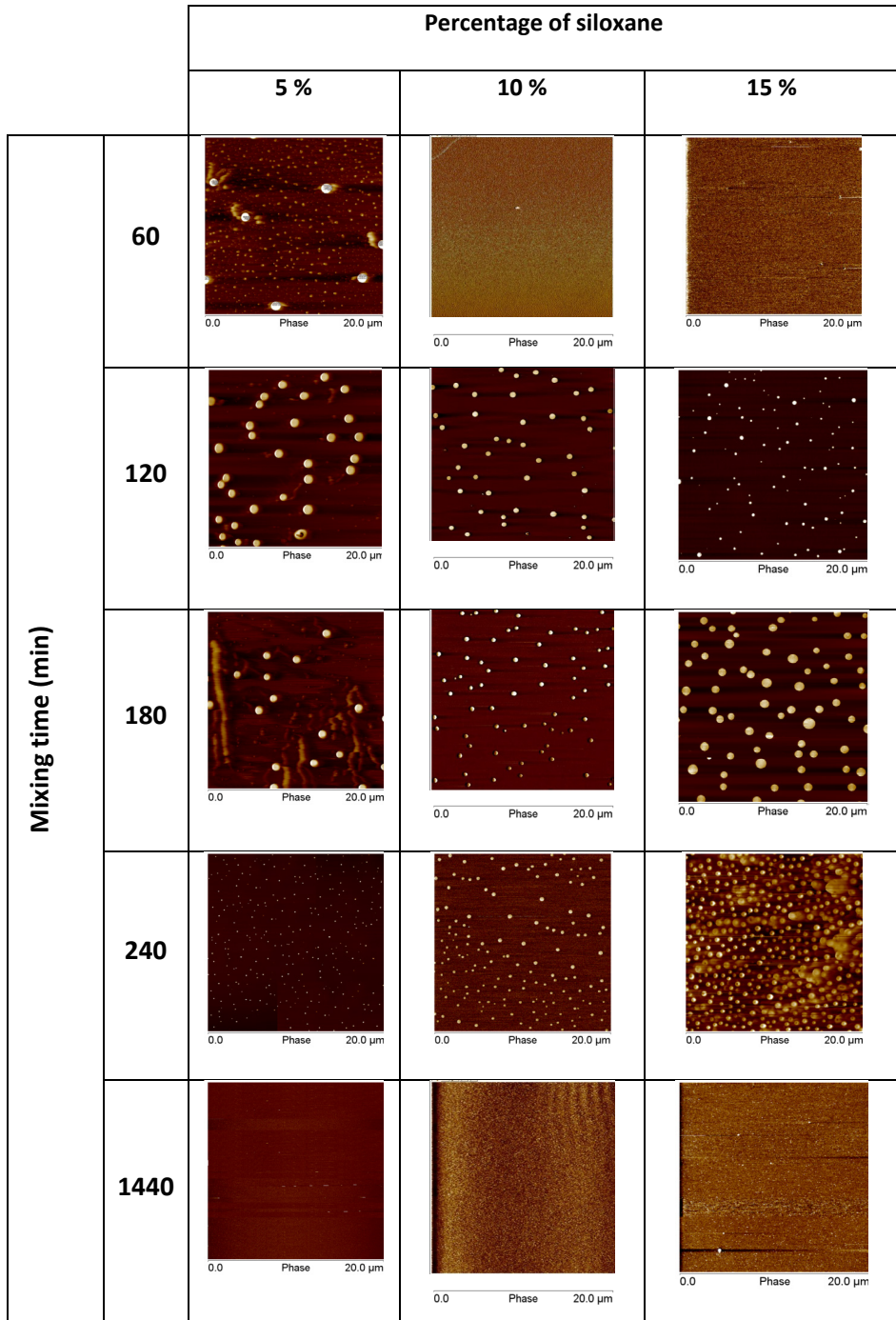


Figure 2. 14. AFM phase images (20 μm X 20 μm) for films obtained at room temperature with different amount of PDMS at different mixing times.

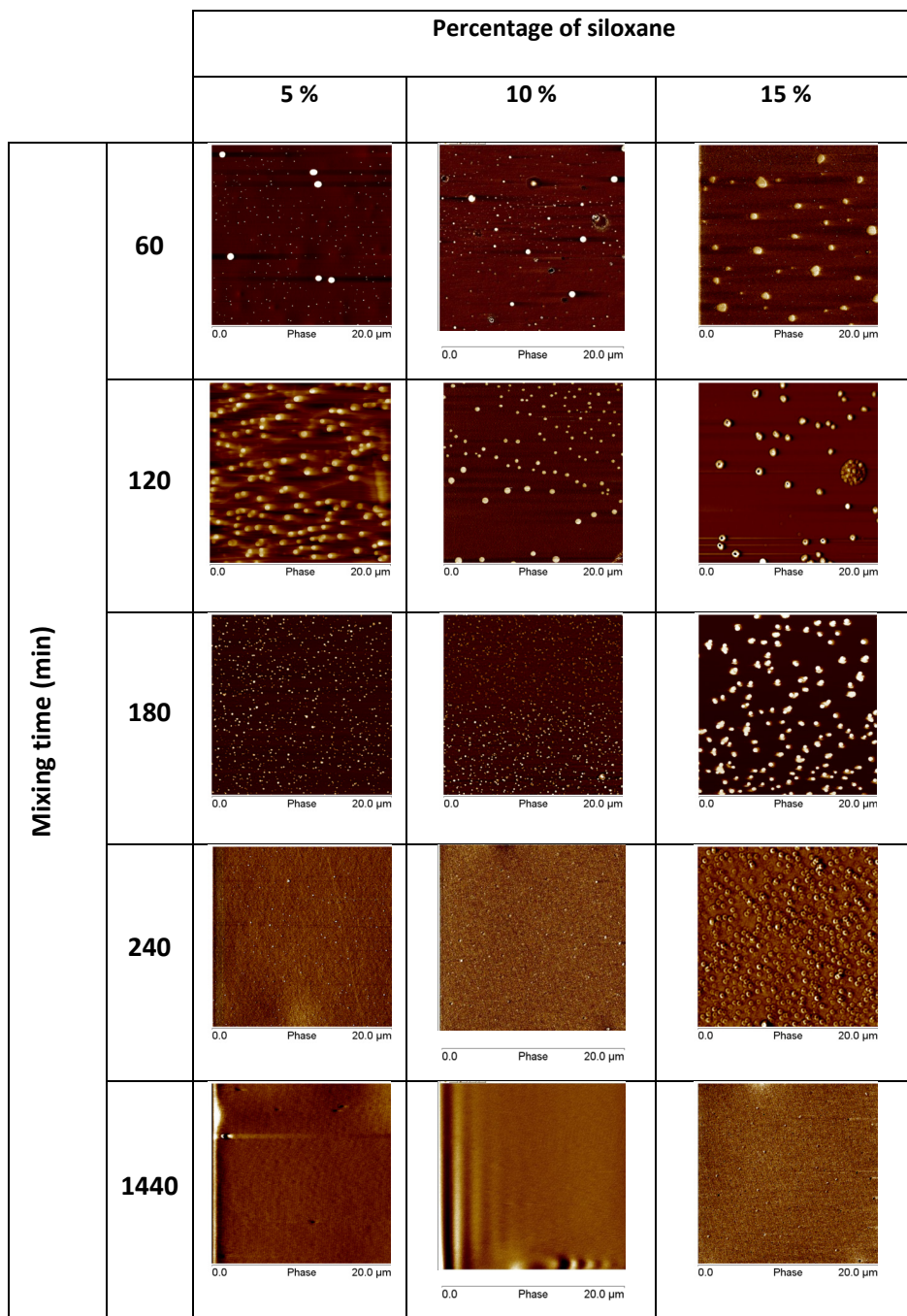


Figure 2. 15. AFM phase images (20 μm X 20 μm) for films obtained at 50 $^{\circ}\text{C}$ with different amount of PDMS at different mixing times.

The hydrophobicity of the samples was determined by means of contact angle measurements. Figure 2.16. shows the obtained results.

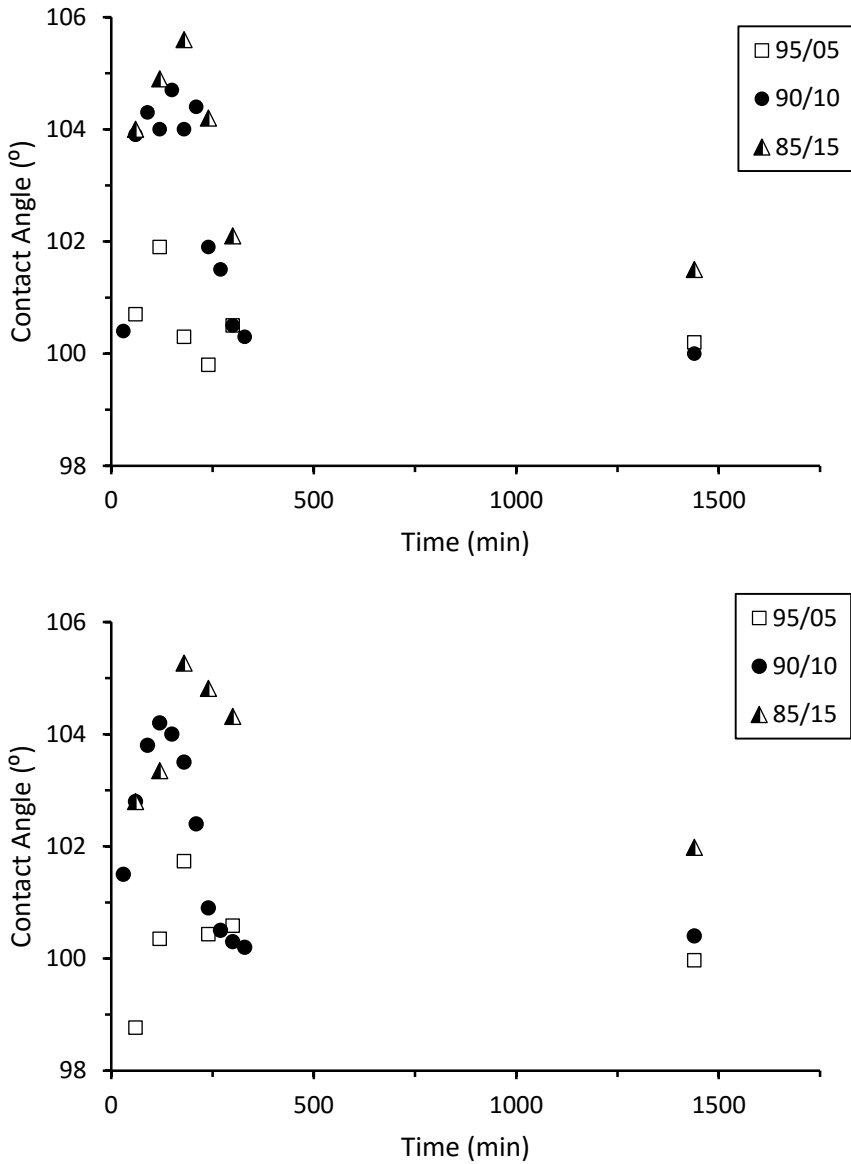


Figure 2.16. Contact angle values for the coatings generated at room temperature (up) and at 50 °C (down).

As can be observed in Figure 2.16., all the coatings showed contact angles higher than 90° , which means that all the surfaces were hydrophobic. The average deviation for the data was $\pm 1.8^\circ$. In addition, regardless sample composition and casting temperature the maximum contact angles were obtained at intermediate mixing times. In relation to the sample composition, for both temperatures, the maximum contact angles of samples containing 10 and 15 % of siloxane were in the same order, although slightly higher values were obtained for the sample containing 15 % of siloxane. Lower contact angle values were obtained for sample with a 5 % of siloxane. Finally it must be pointed out that, for samples casted at 50°C , the maximum of the contact angle was obtained at lower mixing times than in the samples casted at room temperature.

All these results clearly showed that higher contact angles were obtained for samples generated at intermediate mixing times, where the samples presented nanostructured morphologies. According to this, the surface morphology plays an important role in the wetting surface behaviour.

According to literature, the hydrophobicity of the film surfaces could be due to the segregation towards the surface of the more incompatible and less polar siloxane domains so as to minimize the interfacial tension with air^{6,13,16}. In order to calculate the concentration of siloxane at the surface, FTIR-ATR spectroscopy measurements were performed. Figure 2.17. shows as an example the spectrum of the 90/10 sample generated at room temperature after 60 minutes of reaction.

The ratio of the bands at 800 cm^{-1} , assigned to the Si-C stretching and siloxane methyl groups bending, and the band at 3000 cm^{-1} , assigned to the C-H stretching of all components was used as a relative measure of the siloxane concentration. The results obtained for the samples prepared at room temperature and at 50°C are

shown in Figure 2.18. The average deviation for the Siloxane ratio measurements was ± 0.15 for the room temperature sample and ± 0.1 for the 50 °C generated samples.

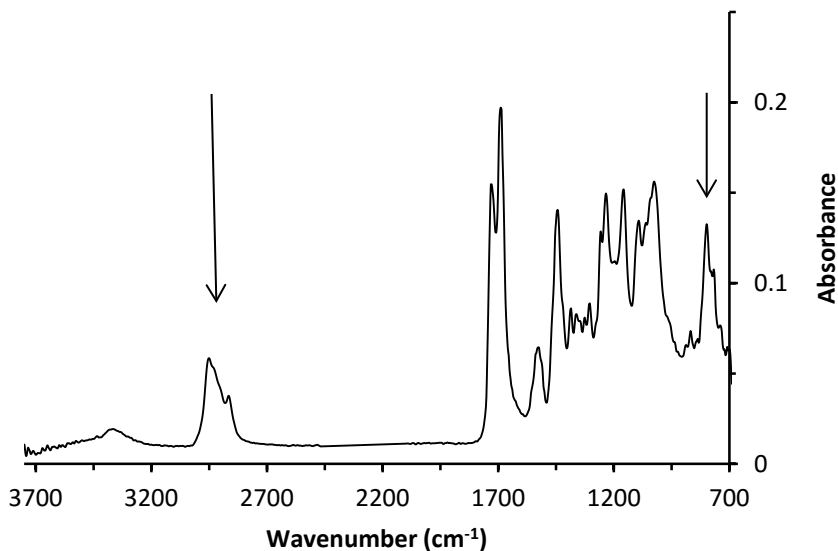


Figure 2.17. FTIR-ATR spectrum of 90/10 sample generated at room temperature after 60 minutes of reaction.

As observed in Figure 2.18, the amount of siloxane increased with the reaction progress reaching a plateau at long times. In the surfaces generated at room temperature, the behaviour of the samples containing 10 and 15 % of siloxane was similar. However, the sample containing only 5 % of siloxane showed a clearly lower siloxane ratio which means that the siloxane surface concentration of this sample was lower.

The surface siloxane concentration of the samples generated at 50 °C also increased with the reaction time. However, the maximum values were lower than those obtained in the room temperature casted samples.

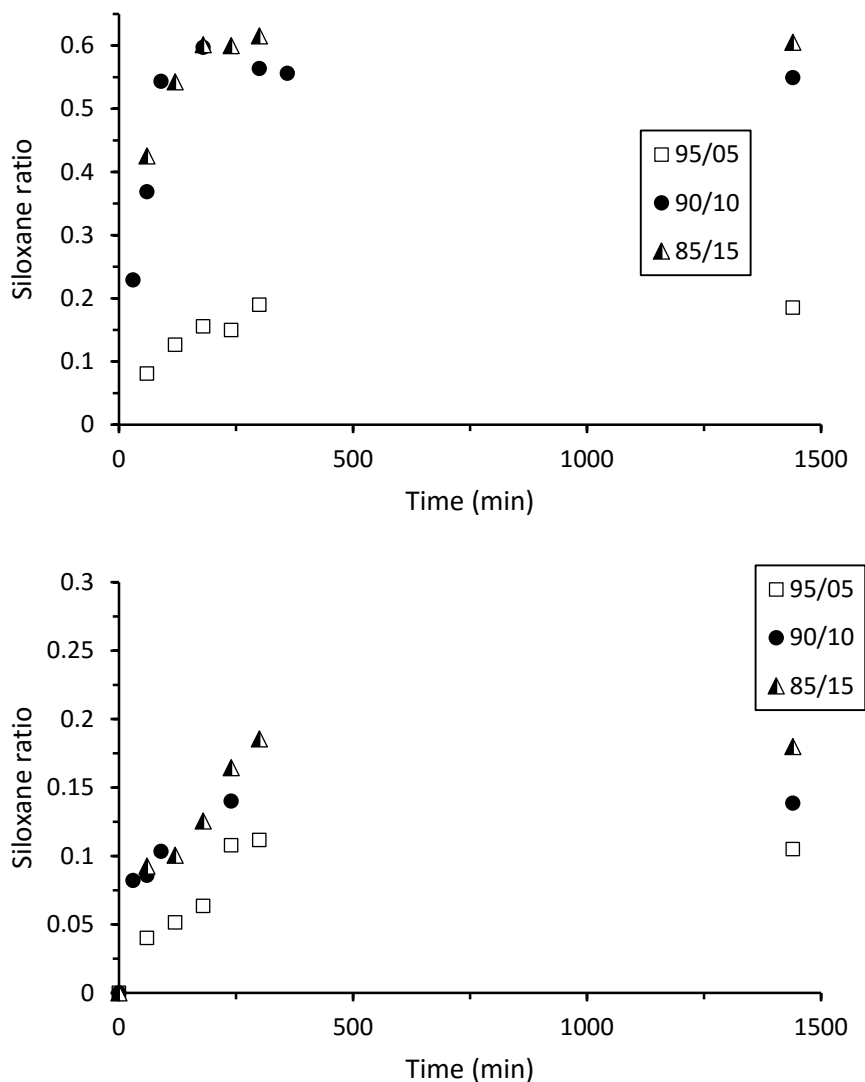


Figure 2. 18. Siloxane relative concentration determined by FTIR-ATR as a function of the reaction time for samples generated at room temperature (up) and at 50 °C (down).

The FTIR-ATR results showed that the siloxane concentration increased with the reaction time. According to this, as siloxane has a low surface tension, the contact angle should increase with the reaction time. However, as shown in Figure 2.16. at long reaction times the contact angle decreased. This fact shows that the surface composition is not the only factor that controls the surface hydrophobicity. As it is well known that the surface roughness modifies the wetting properties of the samples^{17,18}, the roughness was calculated from AFM data. A description of the measurements method is shown in Annex II.

Figure 2.19. shows the mean roughness (Ra) calculated in the films obtained at room temperature (up) and at 50 °C (down) for the 5, 10 and 15 % PDMS formulations. The average deviation for the Roughness Ra data was of ± 3 nm for the room temperature samples and ± 2.5 nm for the 50 °C samples.

As can be observed, in the room temperature generated surface (Figure 2.19. up), the maximum roughness were obtained at intermediate reaction times. This behaviour was observed for all compositions. It is important to remark that the maximum of roughness reached for each formulation is moved to higher mixing times when the percentage of siloxane increases. It is also observed that the maximum roughness is similar for 10 and 15 % of siloxane containing samples. For the films generated at 50 °C the behaviour was the same but the maximum roughness was obtained at shorter reaction times.

In literature, similar roughness values were obtained for 20 % of siloxane containing system¹⁶. It is interesting to note that the reaction time where the maximum roughness was reached was the same as the time where the maximum contact angle was obtained. According to this, the surface siloxane concentration is not the only

factor that governs the sample hydrophobicity and the surface roughness plays an important role.

This result is not in accordance with literature data⁶, where for similar systems it is said that the contact angle does not depend on the formation of any structured surface. However, our results showed that the contact angle of the structured surfaces were slightly higher, as a result of the increased roughness.

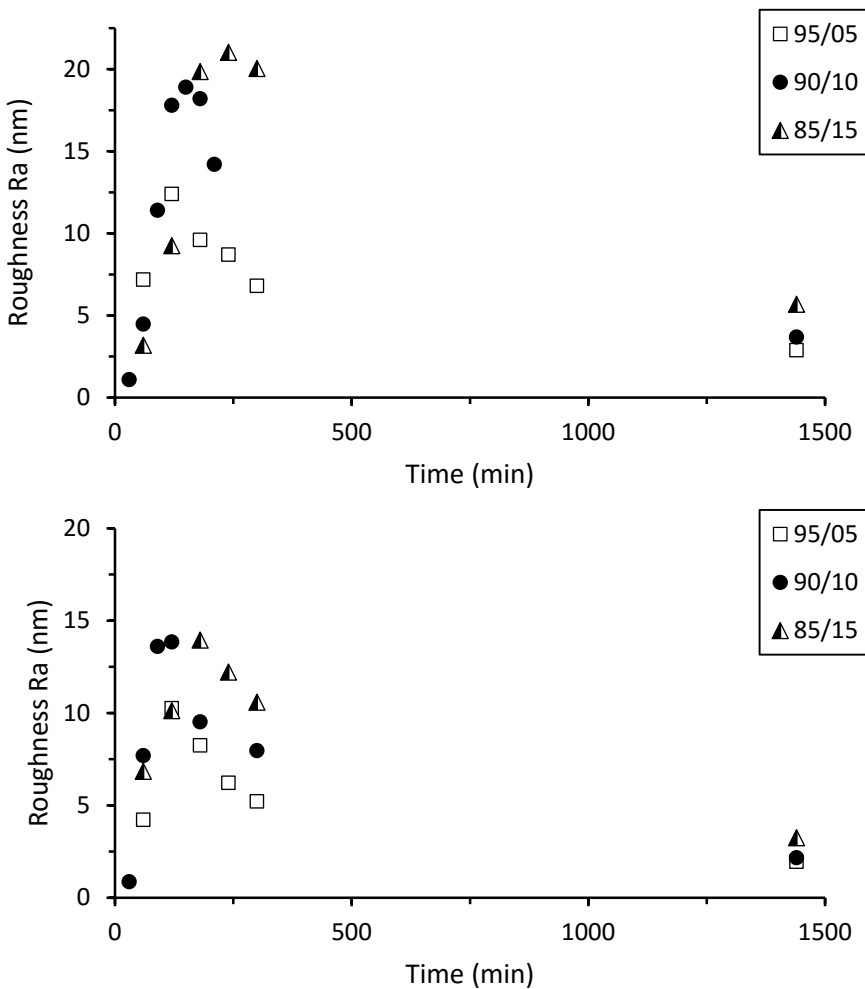


Figure 2.19. Superficial roughness obtained by AFM images of films obtained at room temperature (up) and at 50 °C (down).

It is clear that structured surfaces were generated as a consequence of the phase separation between the siloxane and PCL segments. In order to study the phase separation of the samples, DMTA measurements were carried out. Figure 2.20. shows as an example the thermogram of the sample obtained at 60 minutes of reaction and casted at room temperature.

All the samples showed a single maximum in the $\text{Tan } \delta$ that, according to previous results, can be assigned to the glass transition temperature of the PCL/IPDI segments¹³. The transition assigned to the segmental motion of the PDMS units at about $-95\text{ }^{\circ}\text{C}$ ^{1,3} could not be detected because of the low concentration of this component.

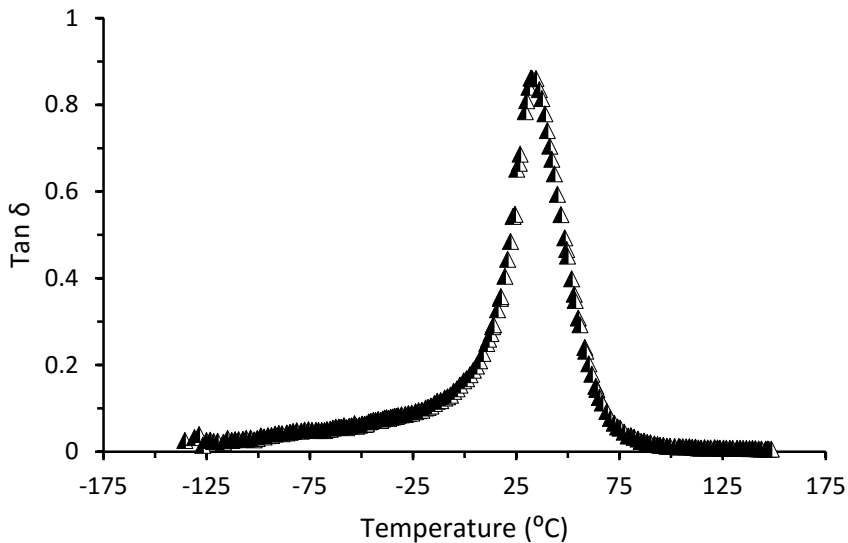


Figure 2.20. $\text{Tan } \delta$ versus temperature for the sample obtained after 60 minutes of reaction at room temperature.

It is interesting to note that the temperature of the $\text{Tan } \delta$ maximum changed slightly with the reaction time and casting temperature. Figure 2.21. shows the values of the

maximum in $\text{Tan } \delta$ as a function of the reaction time for the samples obtained by casting at room temperature (up) and at 50 °C (down).

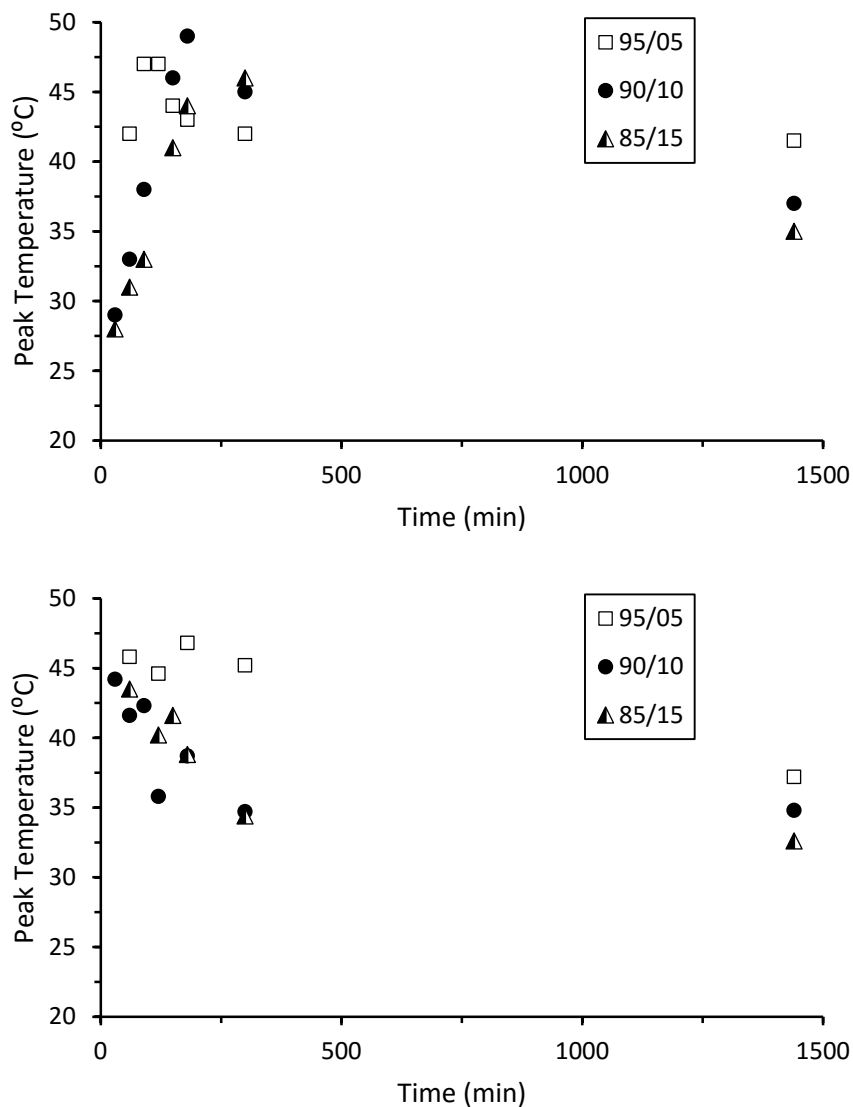


Figure 2.21. Maximum $\text{Tan } \delta$ versus reaction time in films obtained by casting at room temperature (up) and at 50 °C (down).

For the samples obtained by casting at room temperature, the transition temperature increased slightly with the reaction time and after reaching a maximum at intermediated mixing times decreased.

As the system is phase separated and the glass transition of the PDMS units is about $-95\text{ }^{\circ}\text{C}$, the lower temperature of the $\text{Tan } \delta$ can be associated to a higher phase mixing. On the contrary, higher phase separation will lead to higher $\text{Tan } \delta$ values.

According to this, DMTA results showed that for the room temperature casted films the phase separation showed a maximum between 150 and 240 minutes of mixing time. The DMTA results for the films obtained by casting at $50\text{ }^{\circ}\text{C}$ showed $\text{Tan } \delta$ values lower than those obtained for the room temperature casted samples, which mean that the phase separation was lower when the samples were casted at the higher temperature.

These results agreed with the AFM studies showed previously, where, for all formulations, higher phase separation were recorded at intermediate mixing time.

2.6.2. Anti-biofouling behaviour

Poly(dimethyl siloxane) or silicone materials have been the focus of extensive research in the development of minimally adhesive surfaces¹⁹. These materials have also led to studies of their utility as potential anti-fouling materials for marine applications, among other things, owing to their good fouling-release performance. However, PDMS has some obvious disadvantages, such as poor adhesion to substrates, low mechanical strength and high cost.

The self-stratified Poly(Urethane/Siloxane) coatings try to solve some of the PDMS disadvantages such as their poor adhesion while keeping the anti-biofouling properties. These kinds of novel non-toxic fouling-release coatings are used to combat biofouling²⁰⁻²³. In previous sections²⁴, it has been reported the synthesis and surface hydrophobicity (via water contact angle measurements) of a series of Poly(Urethane/Siloxane) copolymers. It is interesting to note that the addition of small quantities of Poly(dimethyl siloxane) increased the water contact angle substantially. In addition, higher contact angles were obtained when the systems presented a phase separated morphology.

According to some literature results, the anti-fouling ability of block copolymers is also related to the phase separated morphology^{6,25}. Bearing in mind these results, the present section is devoted to determine the anti-biofouling capacity of these phase separated copolymers through protein sorption measurements.

The sorption of the protein Bovine Serum Albumine (BSA) of three different formulations containing 5 %, 10 % and 15 % of siloxane, whose morphology was determined in the previous section, was evaluated by static sorption test using a colorimetric method²⁶, by Surface Plasmon Resonance (SPR) and by Quartz Crystal Microbalance with dissipation monitoring (QCM-D)²⁷. The sorption data were related to the sample morphology.

a) Static sorption tests

Static sorption test were performed using the Bio-Rad Protein Assay (colorimetric method), which is a dye-binding assay in which a differential colour change of a dye

occurs in response to various concentration of protein. The standard procedure advised by Bio-Rad was followed. The employed method is described in Annex II.

Typical sorption profiles of BSA for samples generated at room temperature measured using the dye-binding assay are shown in Figures 2.22., 2.23. and 2.24. In all cases, the data of reference polyurethane without siloxane are included for comparison purposes.

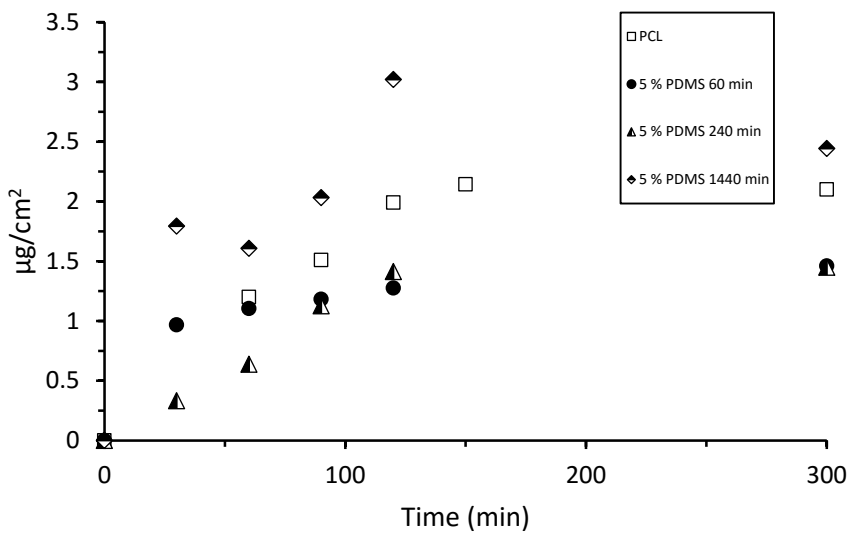


Figure 2.22. Sorption of the BSA protein over films generated at room temperature with 5 % of PDMS versus time.

The sorption of BSA is influenced by the surface affinity and diffusion rate of the protein through the solution. At 300 minutes, nearly full coverage on each of the surfaces was observed.

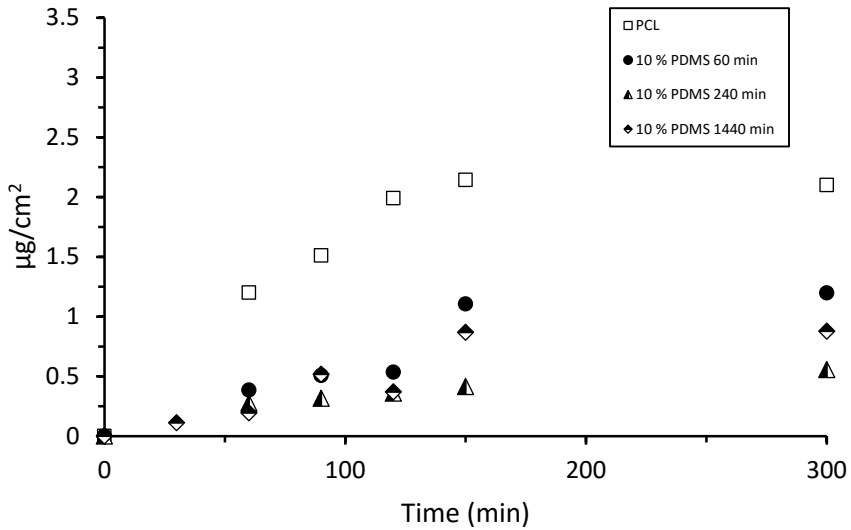


Figure 2.23. Sorption of the BSA protein over films generated at room temperature with 10 % of PDMS versus time.

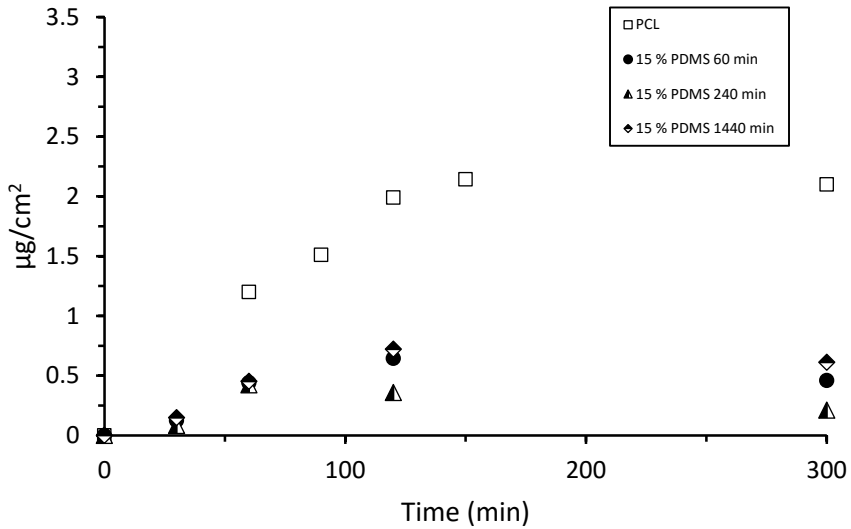


Figure 2.24. Sorption of the BSA protein over films generated at room temperature with 15 % of PDMS versus time.

For the samples containing 5 % of siloxane, regardless the mixing time, the sorption values were similar to those obtained for the reference polyurethane. However, reduced protein sorption was obtained for samples containing 10 and 15 % of siloxane. This result proved that the siloxane reduced the sorption of the protein and therefore that these coatings could be interesting alternatives as fouling release coatings. Similar conclusions have been reported using different bio assay measurements for Poly(Urethane/Siloxane)²² and for polyester/polysiloxane coatings²⁸.

The BSA sorption curves of the samples obtained by casting at 50 °C showed a very similar behaviour to the data obtained in the room temperature casted samples. Table 2.2. shows as a summary the BSA sorption values at 300 minutes for samples casted at different temperatures and times.

PDMS %	Mixing time (min)	Adsorption (25 °C) ($\mu\text{g}/\text{cm}^2$)	Adsorption (50 °C) ($\mu\text{g}/\text{cm}^2$)
0	240	2.1	2.2
5	60	1.5	1.4
	240	1.4	1.5
	1440	2.4	3.2
10	60	1.2	1.0
	240	0.6	0.2
	1440	0.9	0.5
15	60	0.6	0.8
	240	0.2	0.6
	1440	0.6	0.8

Table 2. 2. BSA Protein sorption at 300 minutes for coatings obtained at room temperature 25 °C and at 50 °C.

As can be observed, for each composition and casting temperature the sorption of BSA was lower in the samples obtained at 240 minutes, where the samples presented nanostructured morphology and higher contact angles.

Comparing the data of different composition containing samples, it is clear that 5 % of siloxane was not enough to reduce significantly the protein sorption. The data obtained for the 10 and 15 % of siloxane were not clear. Thus, for the samples casted at room temperature the best results were obtained for the 15 % of siloxane containing samples while for the samples casted at 50 °C the sample containing 10 % of siloxane showed a better behaviour.

b) Surface Plasmon Resonance (SPR) tests

The second technique used to determine the protein sorption behaviour, as a preliminary study, was the Surface Plasmon Resonance (SPR). The samples were prepared by spin-coating (2500 r.p.m. for 30 second in a SCC-200 Spin-Coater) over gold sensors. After the spin-coating, the samples were cured at 80 °C for 45 minutes. In order to determine the protein sorption behaviour a three step experiment was carried out. In the first step, a Phosphate Buffer Saline (PBS) solution was passed over the sensor to make the background. After that, the BSA protein solution (0.1 mg/mL) was introduced into the system for one hour and finally the PBS solutions were again used, in order to remove the adsorbed protein.

The experiment was carried out for reference PU without siloxane and for a film generated at room temperature for a 10 % PDMS sample of 180 minutes of mixing time (phase separated sample).

As can be observed in Figure 2.25., an important decrease in the adsorption of the protein was observed for the siloxane containing sample. Although the preliminary results were encouraging, some technical problems with the equipment avoid the possibility of further investigations.

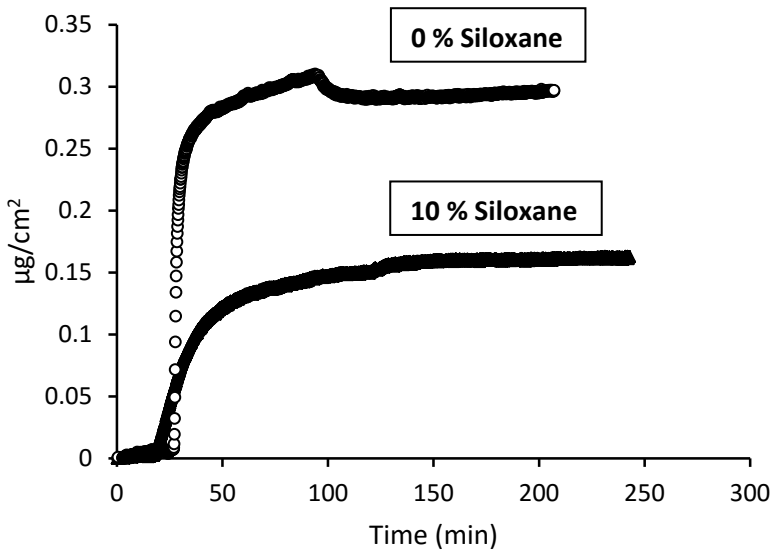


Figure 2.25. Protein mass adsorption per unit area as a function of experiment time for SPR experiments.

c) Quartz Crystal Balance with dissipation (QCM-D) measurements

The third technique used to determine the protein sorption behaviour was the Quartz Crystal Balance with dissipation monitoring (QCM-D). The samples were prepared by spin-coating (2500 r.p.m. for 30 second) over gold surfaces. After the spin-coating, the samples were cured at 80 °C for 45 minutes.

The data obtained from the static sorption test showed that the nanostructured samples gave rise to lower BSA sorption values. In order to obtain information about the reason for this behaviour, the sorption of BSA of samples containing 10 % of siloxane casted at room temperature was studied by QCM-D. Samples obtained at 60, 120 and 240 minutes of mixing time were selected in order to study the behaviour of a non-nanostructured sample (60 minutes) and two nanostructured samples containing different morphologies (120 and 240 minutes).

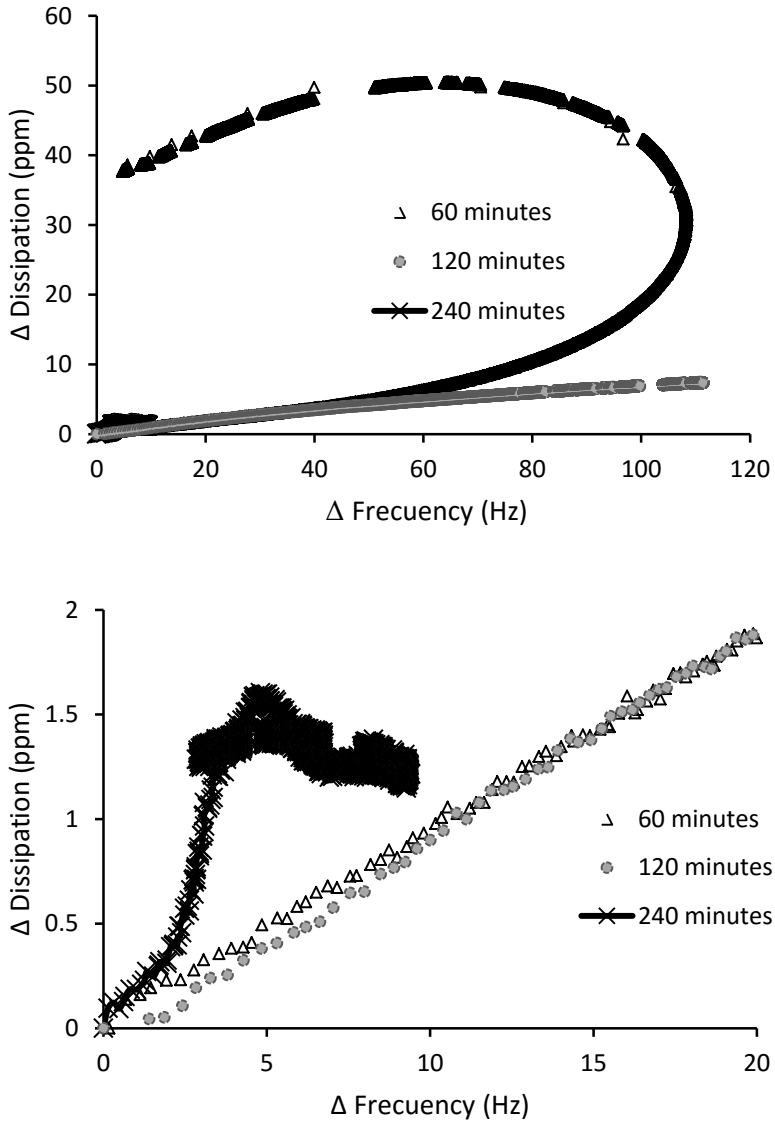


Figure 2.26. Dissipation (D) versus Frequency (F) for the samples containing 10% of siloxane obtained at 60, 120 and 240 minutes of mixing time casted at room temperature during water conditioning.

The down Figure is scale expanded graph of the up Figure.

Prior to the experiments, the sensors were stabilized overnight under a constant water flux. In order to understand if there was a general difference between the three samples as regards interaction with water, we represented the experimental data through plotting dissipation (D) as a function of frequency (F). So while time is eliminated as a parameter in this type of graph, it can implicitly be understood that time increases together with the frequency. Figure 2.26. shows the results of this calculation.

As can be seen, all the samples showed an initial water sorption in parallel with an increase in dissipation. However, the maximum frequency reached by the nanostructured sample obtained after 240 minutes mixing was clearly lower than the values that presented the other samples, indicating that the water sorption ability of this sample was lower.

Samples obtained at 60 and 120 minutes, showed a similar behavior up to about 40 Hz and afterwards a significant increment in the dissipation occurred in the non-nanostructured sample (60 minutes). In addition, when the frequency was close to 100 Hz the dissipation abruptly increased while no significant changes were observed in the frequency. At the end of the experiment, a decrease of the frequency and the dissipation related to water desorption was observed. This result evidenced that the polymer underwent swelling up to a point where it rearranged significantly and water desorption occurred. As this was the only sample that was not nanostructured it can be thought that the initial higher water swelling was related to the lower hydrophobicity of the sample. However, after water swelling the polymer was rearranged, promoting phase separation and therefore reducing the water sorption.

This data, hence, already indicated that the nanostructuring of the polymer changed the interaction with water, based on either the overall hydrophilicity of the polymer, its morphology, or both. The same conclusions were extracted from the contact angle measurements, where the nanostructured samples presented higher values than the homogeneous ones.

Subsequently, the respective sensors were put into contact with different concentrations of BSA in aqueous solution up to a maximum of 100 mg BSA/L. A successive increase of the BSA concentration was carried out without intermediate flushing with water or removal of the already adsorbed BSA. As a consequence, we could only see well pronounced adsorption kinetics for the first adsorption step, which was rather similar for all three polymers (about 2 Hz for the fifth harmonic). A subsequent stepwise increase of the BSA concentration resulted in a mere continuous decrease of the frequency without reaching any distinct plateau value (data not shown).

We represented the experimental data through plotting dissipation (D) as a function of frequency (F), rather than representing concentration dependent adsorption data (of which we have actually only one per polymer because the accumulative increase of BSA in solution did not yield well defined adsorption data).

The results are shown in Figure 2.27. The frequency represents the quantity of BSA adsorbed on the surface while the dissipation reflects the “rigidity” with which BSA adsorbs. Low frequency values naturally represent the beginning of the experiments with low BSA concentration in the water, and high frequencies represent data toward the end of the experiment where the BSA concentration was maximum.

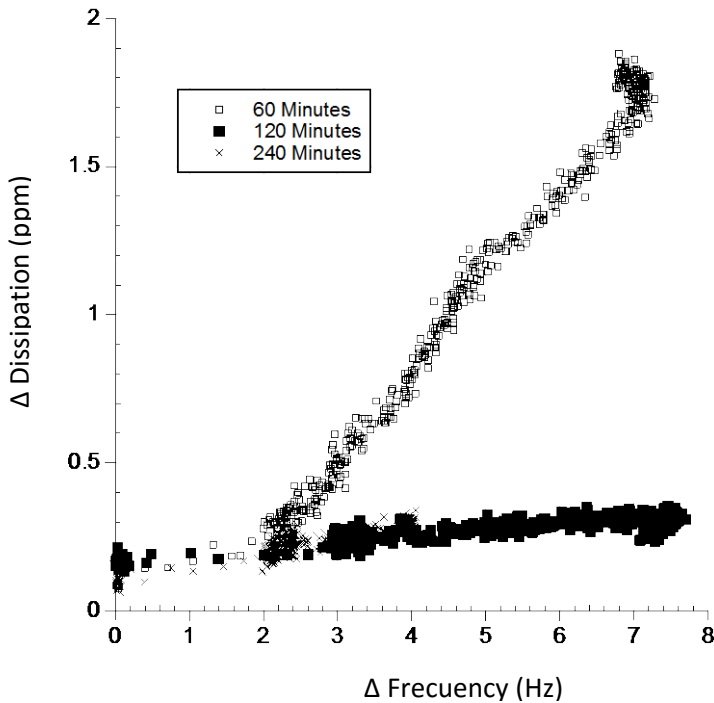


Figure 2.27. Dissipation (D) versus Frequency (F) for the samples containing 10 % of siloxane obtained at 60, 120 and 240 minutes of mixing time casted at room temperature during adsorption of BSA in water. The values represented were taken from the fifth harmonic.

As can be seen, for a frequency up to about 2 Hz, all the studied samples showed a similar dependence dissipation/frequency. This confirmed precisely the observation that during first contact with BSA, no difference was seen in the degree of adsorption. Minor differences in the absolute value of the dissipation which can be seen were not considered as significant, based on our experience and the noise of the measurement. However, with increasing BSA concentration in the water, distinct adsorption behavior was observed: the polymer obtained after 60 min mixing adsorbs as much as the one mixed for 120 minutes ($F=7-8$ Hz), but with a significantly higher dissipation. Such a high dissipation, that was only seen in the non-nanostructured sample (mixing 60 minutes) indicated a more viscoelastic “film”

of BSA and was most probably due to a higher content of water resulting in a more “loosely” adsorbed BSA.

The dissipation followed almost exactly the same trend as a function of frequency in the two nanostructured samples, obtained after 120 and 240 minutes mixing. It can be speculated that in nanostructured samples BSA was adsorbed in a different conformation that did not retain water as much. This result confirms some literature data where it is indicated that the disruption of protein adsorption requires compositional heterogeneity to create a mismatch between the nanodomains and the anchoring sites of the protein^{25,27}.

Finally it can be remarked that the sample obtained after 240 minutes mixing presented a reduced sorption of BSA (compared to the other samples the maximum frequency was half). This result was also obtained from static sorption measurements shown in the previous section (see Table 2.2.) and revealed that while BSA was adsorbed in the same manner and conformation in the two nanostructured samples, the amount of interaction sites decreased to 50 %.

2.7. Conclusions

Finally, the most relevant conclusions of this chapter are summarizing.

- ✓ Polyurethane-siloxane thermoset copolymers containing varying amounts of siloxane show a phase separated structure that depend on the conversion of the reaction and casting temperature.

- ✓ The siloxane surface concentration increases with the reaction conversion. However, the water contact angle, the surface roughness and the phase segregation show a maximum at intermediate reaction conversions.
- ✓ According to contact angle, surface roughness and phase segregation data, the phase separation give rise to a higher surface roughness that in combination with a higher siloxane surface concentration increase the water contact angle of the surfaces.
- ✓ The static BSA sorption measurements show that the adsorption of BSA is reduced when the coatings show a phase separated structure.
- ✓ The water sorption of the samples as well as the swelling of the polymer measured by QCM-D confirms the data obtained by static BSA sorption. The dissipation data can be used to emphasize differences in the polymer morphology. QCM-D technique gives significant information not only about BSA adsorption kinetics but also about how this adsorption takes place.

2.8. Bibliography

1. Hernandez, R., Weksler, J., Padsalgikar, A. & Rutn, J. Microstructural Organization of Three-Phase Polydimethylsiloxane-Based Segmented Polyurethanes. *Macromolecules*. **40**, 5441–5449 (2007).
2. Pergal, M. V., *et al.* Synthesis and characterization of novel urethane-siloxane copolymers with a high content of PCL-PDMS-PCL segments. *J. Appl. Polym. Sci.* **122**, 2715–2730 (2011).

3. Tsi, H.Y., *et al.* Characteristics of the phase transition of poly(siloxane/ether urethane) copolymers. *Polym. Test.* **30**, 50–59 (2011).
4. Schmidt, J. J., Gardella, J. A. & Salvati, L. Surface studies of polymer blends. 2. An ESCA and IR study of poly(methyl methacrylate)/poly(vinyl chloride) homopolymer blends. *Macromolecules.* **22**, 4489–4495 (1989).
5. Liu, L., Jiang, B. & Zhou, E. Study of semicrystalline-amorphous diblock copolymers: 1. Microphase separation, glass transition and crystallization of tetrahydrofuran-methyl methacrylate diblock copolymers. *Polymer.* **37**, 3937–3943 (1996).
6. Majumdar, P., Stafslie, S., Daniels, J. & Webster, D. C. High throughput combinatorial characterization of thermosetting siloxane–urethane coatings having spontaneously formed microtopographical surfaces. *J. Coat. Technol. Res.* **4**, 131–138 (2007).
7. Majumdar, P. & Webster, D. C. Preparation of Siloxane–Urethane Coatings Having Spontaneously Formed Stable Biphasic Microtopographical Surfaces. *Macromolecules.* **38**, 5857–5859 (2005).
8. Zhang, Y., Feng, Z., Feng, Q. & Cui, F. The influence of soft segment length on the properties of poly(butylene terephthalate-co-succinate)-b-poly(ethylene glycol) segmented random copolymers. *Eur. Polym. J.* **40**, 1297–1308 (2004).
9. Sheth, J. P., *et al.* Probing the Hard Segment Phase Connectivity and Percolation in Model Segmented Poly(urethane urea) Copolymers. *Macromolecules.* **38**, 5681–5685 (2005).
10. Priscariu, C., *et al.* The effect of hard segment ordering in copolyurethane elastomers obtained by using simultaneously two types of diisocyanates. *Polymer.* **44**, 5407–5421 (2003).
11. Guan, R., *et al.* Effect of casting solvent on the morphology and performance of sulfonated polyethersulfone membranes. *J. Memb. Sci.* **277**, 148–156 (2006).
12. Hernandez, R., *et al.* A Comparison of Phase Organization of Model Segmented Polyurethanes with Different Intersegment Compatibilities. *Macromolecules.* **41**, 9767–9776 (2008).

13. Majumdar, P. & Webster, D. C. Surface microtopography in siloxane–polyurethane thermosets: The influence of siloxane and extent of reaction. *Polymer*. **48**, 7499–7509 (2007).
14. Majumdar, P. & Webster, D. C. Influence of solvent composition and degree of reaction on the formation of surface microtopography in a thermoset siloxane–urethane system. *Polymer*. **47**, 4172–4181 (2006).
15. Bakirova, I. N., Zenitova, L. A. & Rozental, N. A. Effect of AcetylAcetone on the reaction of polyethylene glycol adipate with diisocyanate in the presence of phenolic Mannich bases and properties of castable polyurethanes. *Russ. J. Appl. Chem.* **79**, 811–813 (2006).
16. Pergal, M. V., *et al.* Microstructure and properties of poly(urethane-siloxane)s based on hyperbranched polyester of the fourth pseudo generation. *Prog. Org. Coat.* **76**, 743–756 (2013).
17. Assender, H., Bliznyuk, V. & Porfyrakis, K. How surface topography relates to materials properties. *Science*. **297**, 973–976 (2002).
18. Verplanck, N., Coffinier, Y., Thomy, V. & Boukherroub, R. Wettability switching techniques on superhydrophobic surfaces. *Nanoscale Res. Lett.* **2**, 577–596 (2007).
19. Yilgör, E. & Yilgör, I. Silicone containing copolymers: Synthesis, properties and applications. *Prog. Polym. Sci.* **39**, 1165–1195 (2014).
20. Ekin, A., *et al.* Synthesis, formulation, and characterization of siloxane–polyurethane coatings for underwater marine applications using combinatorial high-throughput experimentation. *J. Coat. Technol. Res.* **4**, 435–451 (2007).
21. Majumdar, P., Ekin, A. & Webster, D. C. Thermoset Siloxane-Urethane fouling release coatings. *Smart Coatings*. **957**, 5–61 (2007).
22. Sommer, S., *et al.* A preliminary study on the properties and fouling-release performance of siloxane–polyurethane coatings prepared from poly(dimethylsiloxane) (PDMS) macromers. *Biofouling*. **26**, 961–972 (2010).

23. Bodkhe, R. B., *et al.* The effect of formulation variables on fouling-release performance of stratified siloxane-polyurethane coatings. *J. Coat. Technol. Res.* **9**, 235–249 (2012).
24. Santiago, A., *et al.* Urethane/Siloxane Copolymers with Hydrophobic Properties. *Macromol. Symp.* **321-322**, 150–154 (2012).
25. Amadei, C., *et al.* Revealing Amphiphilic Nanodomains of Anti-Biofouling Polymer Coatings. *ACS Appl. Mater. Interfaces.* **6**, 4705–4712 (2014).
26. Li, F., *et al.* Surface modification of PES ultrafiltration membrane by polydopamine coating and poly(ethylene glycol) grafting: Morphology, stability, and anti-fouling. *Desalination.* **344**, 422–430 (2014).
27. Baxamusa, S. H. & Gleason, K. K. Random Copolymer Films with Molecular-Scale Compositional Heterogeneities that Interfere with Protein Adsorption. *Adv. Funct. Mater.* **19**, 3489–3496 (2009).
28. Réhel, K., Linossier, I., Azemar, F. & Fa, F. Development of hybrid antifouling paints. *Prog. Org. Coat.* **87**, 10–19 (2015).

Chapter 3

Preparation of superhydrophobic
silica surfaces by basic Sol-Gel
method with self-cleaning
applications

Chapter 3:

Preparation of superhydrophobic silica surfaces by basic Sol-Gel method with self-cleaning applications

3.1.	Introduction	95
3.2.	Materials	99
3.3.	“Grafting to” nanoparticles	101
	3.3.1. Synthesis	101
	3.3.2 Results and Discussion	104
3.4.	“Co-condensation” nanoparticles	113
	3.4.1 Synthesis	113
	3.4.2 Results and Discussion	114
3.5.	“Grafting to” and “Co-condensation” comparison	120

3.6.	Introduction of nanoparticles in the polymer matrix	120
3.6.1.	Films generated by casting	121
3.6.2.	Films generated by Spin-Coating	123
3.6.3.	Films generated by spraying	126
3.7.	Self-cleaning effectiveness	128
3.8	Conclusions	129
3.9	Bibliography	130

3.1. Introduction

The research activity of this chapter is addressed to the synthesis of superhydrophobic surfaces with self-cleaning applications using the basic Sol-Gel method. The aim of this process consisted of the introduction of the nanoparticles, previously synthesized, on the surface of a Poly(methyl methacrylate) (PMMA) matrix. It was assumed that the presence of the nanoparticles in the polymeric surface would increase its roughness and decrease the wettability of the generated system.

The synthesis and characterization of nanoparticles have attracted the attention of the research world in recent years. It is well known that particles with nanometric sizes, display many unique properties¹⁻⁶ due to the small size and the high surface area. If these nanoparticles are dispersed in a polymeric matrix, the resulting material will show interesting properties such as the previously mentioned reduced wettability.

The Sol-Gel method is a versatile chemical process which involves the transition of a system from a colloidal liquid, named sol, into a solid gel phase⁷⁻⁹. This technique offers many advantages, among which are the low process temperature, the ability to control the composition and the homogeneity of the final product¹⁰.

The Sol-Gel technology allows the preparation of materials in a wide variety of forms, from ultra-thin film¹¹ coatings to nanoparticles¹². The typical procedure requires hydrolysis (Figure 3.1.) and condensation (Figure 3.2.) steps of an alkoxy silane in the presence of a catalyst, which is the factor that controls the final product. Two kind of catalysts can be used for the Sol-Gel process, either acid¹³ or base¹⁴.

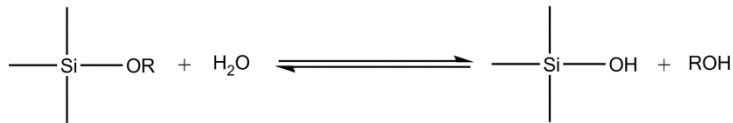


Figure 3.1. Scheme of alkoxysilane hydrolysis.

A basic catalyst produces a high pH environment which deprotonates the silanols of the system, creating a negative charge on the surface of the forming and growing nucleus. This charge generates an electrostatic repulsion between the nucleus formed which prevents the cross-linking of the silica intermediates, preventing the aggregation.

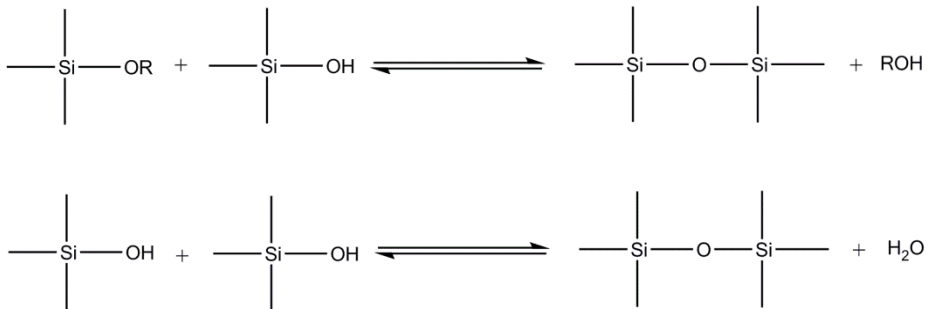


Figure 3.2. Scheme of the silanol condensation reactions.

In the late 60s, due to the necessity to synthesize uniform, non-agglomerating silica nanoparticles, Stöber et al.¹⁵ developed a new method, probably the most popular and widely employed, for silica nanoparticle preparation. This method consists of the synthesis of silica nanoparticles by means of the hydrolysis and condensation of tetraethyl orthosilicate (TEOS) using water and ammonium hydroxide (NH₄OH) as catalyst and alcohol as solvent.

By controlling the environment in which the silica nanoparticles are generated, it is possible to synthesize particles with sizes ranging from 50 nm to 2 μm . The size can be tuned by adjusting the solution temperature, the catalyst concentration (NH_4OH or H_2O) or using different alcohols as solvent. The effect of the reaction time in the synthesis of the nanoparticles does not have significant influence on the silica nanoparticle size. An increase in the catalyst concentration enhances the condensation reaction rate producing larger silica particles. The increase of the temperature of the solution, gives rise to nanoparticles with smaller diameters. Multiple factors such as surface energy, diffusion and solubility are affected by changes in the temperature.

The surface of the nanoparticles synthesized by Sol-Gel method contains silanol groups and therefore is hydrophilic. The synthesis of hydrophobic silica particles involves their functionalization. Organosilanes are one of the few chemicals that react with the inert silica nanoparticles using their surface silanols. These compounds can generate an inorganic network by hydrolysis and condensation of the silane functional groups. However, their organic functionality can impart hydrophobic properties to the surface of the nanoparticle.

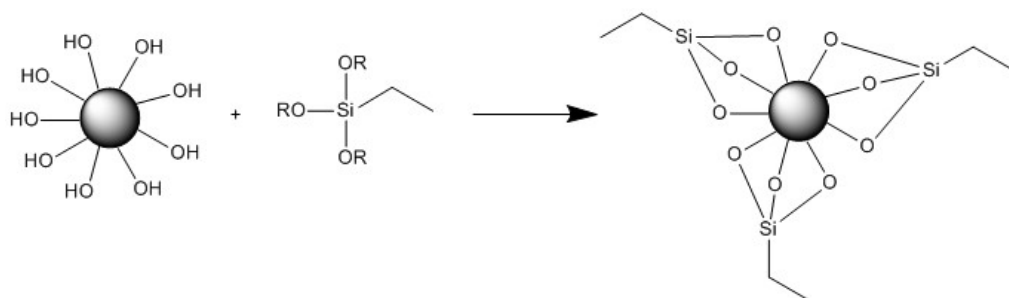


Figure 3.3. Example of “grafting to” reaction process.

There are two methodologies for attaching organosilanes to silica nanoparticles. The “grafting to” methodology involves a post-modification¹⁶ of the silica surface with another hydrolysis/condensation reaction in the presence of the organosilane reactive. This approach provides a defined spherical structure with the organic functionalities on the surface as can be observed in Figure 3.3.

The co-condensation method¹⁷ involves the condensation of the alkoxy silane (usually tetraethyl orthosilicate, TEOS) with another organosilane, which incorporates organic groups and their properties into the silica matrix not over the silica surface as can be seen in the Figure 3.4. This creates higher density of available organic functionalities but might have an undesirable effect on the size and shape of the formed particles.

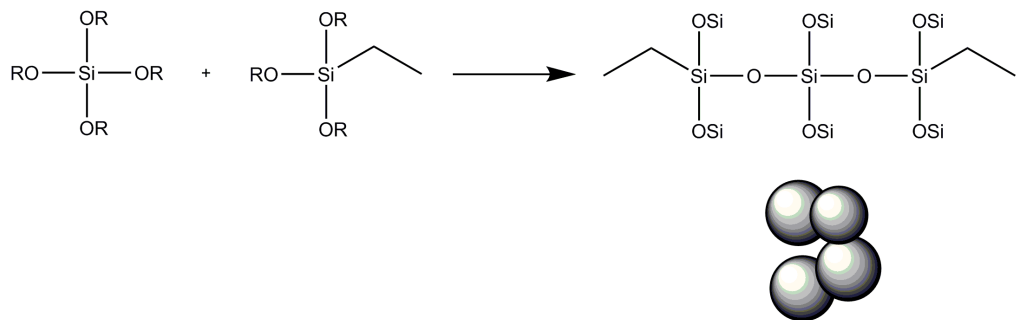


Figure 3.4. Example of “co-condensation” reaction process.

Commonly, Sol-Gel reactions are performed using traditional heat transfer equipment such as oil baths, sand baths and heating jackets. These heating techniques are, however, rather slow and a temperature gradient can be developed

within the sample. In addition, local overheating can lead to product, substrate and reagent decomposition.

In order to overcome these disadvantages, in the last few years, new heating processes have been studied of which microwave heating is one. In contrast with the conventional heating methods, in microwave heating, the radiation passes through the walls of the vessel and heats only the reactants and solvent, not the reaction vessel itself. The temperature increase is supposed to be uniform throughout the sample, which can lead to fewer by-products and/or decomposition products.

The use of the microwave radiation¹⁸ has been extensively investigated during recent years due to it being generally much faster, cleaner and more economical than conventional methods. Microwave radiation is absorbed directly into solvents having a large dielectric constant like water or alcohols, and enables rapid heating compared to conventional heating processing, where the container is heated from the outside, and is less effective. In the first microwave experiments the control and setting of reaction parameters was problematic but, in recent years, specialized systems that are adapted to chemical synthesis have extended the possibilities of microwave-assisted reaction engineering.

Compared with the conventional methods, the microwave assisted Sol-Gel process decreases the reaction time. Moreover, smaller, more monodispersed and purer particles are obtained¹⁹.

3.2. Materials

Tetraethyl orthosilicate (TEOS) GC grade which was purchased from Sigma-Aldrich, was the precursor chosen to make the particles. This alkoxy silane, as can be seen in

Figure 3.5., has four hydrolysable groups in its structure. The reactant has a molecular weight of 208.33 g/mol and its density is $\rho = 0.933$ g/mL.

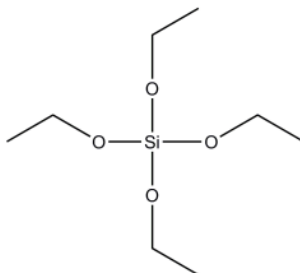


Figure 3.5. Tetraethyl orthosilicate (TEOS) structure.

Hexadecyl trimethoxy silane (HDTMS Figure 3.6.) was the organosilane selected to react with the inert silica nanoparticles using the surface silanol groups. It is supposed that the organic chain of this precursor will impart hydrophobic properties to the nanoparticles surface. In addition, this compound has a competitive price. HDTMS was purchased from Sigma-Aldrich and its properties are a molecular weight of 346.62 g/mol and $\rho = 0.89$ g/mL.

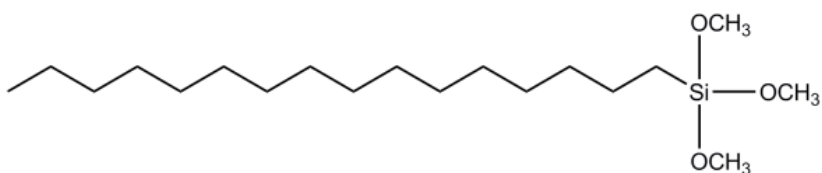


Figure 3.6. Hexadecyl trimethoxy silane (HDTMS) structure.

Ammonia sol. (28-30 % NH_3 basis, MW: 35.05 g/mol and $\rho = 0.9$ g/mL) ACS reagent which was purchased from Sigma-Aldrich, was the basic catalyst selected. The water

used was doubly distilled and deionized (Milli-Q, 18 M Ω cm). Finally, ethanol absolute PRS which was purchased from Panreac, was chosen as reaction solvent.

Poly(methyl methacrylate) was used as the matrix where the silica nanoparticles were introduced. This compound was selected as a model of a class of polymers used in the field of paints and coatings: acrylic polymers. Acrylic paints and coatings have shown good adhesion to different surfaces and are therefore one of the most commonly employed compounds in commercial paint and coating formulations. It is clear that in order to obtain hydrophobic material it would have been more appropriate to select a silicon or fluorinated matrix that presents a lower surface energy than acrylic matrixes and, therefore higher water contact angle values. However, it must be taken into account that our goal was to obtain a hydrophobic surface using slight modifications of the commercial formulations and therefore, the acrylic polymers are better candidates. Poly(methyl methacrylate) (PMMA) was purchased by Sigma-Aldrich.

3.3. “Grafting to” nanoparticles

3.3.1. Synthesis

The “grafting to” method involves the generation of the silica nanoparticles in the first step and the functionalization of these particles in the second with the hydrophobic precursor (HDTMS) as can be seen in Figure 3.7. The Sol-Gel process was carried out using the microwave assisted heating method.

As mentioned, hydrophobic nanoparticles were obtained using a two-step process. In the first step, three different diameter silica nanoparticles (S, M and L depending

on their size) were synthesized from the hydrolysis and condensation of TEOS and in the second step these nanoparticles were coated with different amounts of HDTMS.

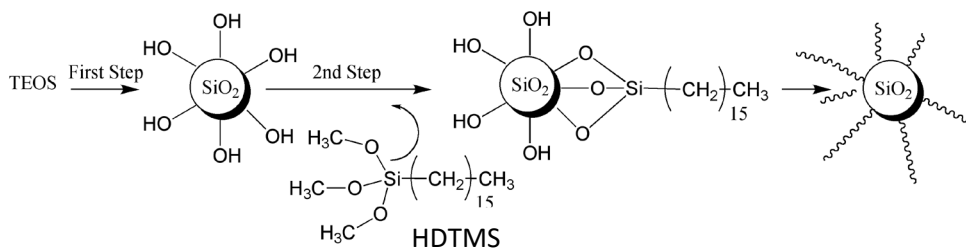


Figure 3.7. Preparation of hydrophobic silica nanoparticles using “grafting to” method in two steps.

a) First step

The nanoparticles synthesis methodology was established in a previous work of the group²⁰. In that work the effect of 4 variables (ammonia and water concentration, reaction temperature and reaction time) on the particle size and conversion obtained in the microwave assisted silica synthesis was analyzed. Taking into account these results, the proportions of ammonia and water were carefully selected to obtain different size nanoparticles. The employed methodology is summarized below.

Experiment	$\frac{mol\ water}{mol\ TEOS}$	$\frac{mol\ Ammonia}{mol\ TEOS}$
S	7.9	1.19
M	18.2	1.19
L	18.2	3.55

Table 3.1. Reagents used in the first step of the nanoparticles synthesis.

3 mL of TEOS, 50 mL of ethanol and the required amounts of water and ammonia were introduced into the reaction vessel. The amount of the reagent used is summarized in Table 3.1. The microwave heating process was carried out by using

the MARS5X (CEM corporation) microwave system where the temperature is directly measured in the microwave vessel. The maximum power of the microwave was selected to 800 W and the power was automatically varied from 0 to 100 % in order to reach 50 °C in 10 minutes. The microwave frequency was 2.45 GHz. The reactions were carried out in sealed Teflon vessels (GreenChem, CEM corporation) under magnetic stirring for three hours.

b) Second step

After the finalization of the first step the reaction was allowed to cool to 30 °C in the microwave vessel, after which, the required amounts of HDTMS were quickly added. Nine experiments were performed adding 1, 2 and 3 mL of HDTMS to each type of nanoparticles generated in the first step (S, M and L). Table 3.2. summarizes the employed formulations. The second step was carried out under microwave irradiation at 50 °C for 3 hours, using the same conditions employed in the first step.

Experiment	First step	HDTMS (mL)
S+1	S	1
S+2	S	2
S+3	S	3
M+1	M	1
M+2	M	2
M+3	M	3
L+1	L	1
L+2	L	2
L+3	L	3

Table 3. 2. Reagents used in the second step of the nanoparticles synthesis.

3.3.2. Results and Discussion

a) Conversion and diameter of the nanoparticles

The conversion of the first step was calculated by infrared spectroscopy (FTIR). The spectra of an aliquot of the reaction products were recorded immediately after the completion of the first step. The decrease in absorbance of the infrared band at 960 cm^{-1} assigned to $\delta\text{ C-CH}_3$ was used to calculate the conversion as described in literature²⁰. The conversion of the second step was determined from the carbon content, calculated by elemental analysis (Microanalyzer CHNS-932 LECO) after drying the samples for at least one week.

Dynamic Light Scattering measurements (DLS) were used to determine the diameter of the particles at room temperature. All samples were measured in ethanol three times and the final value was the average of all of them. The experimental conditions of the measurements are summarized in Annex II.

Table 3.3. shows the results of the diameter of the pure silica nanoparticles synthesized in the first step and the conversion of the reaction as a function of the reaction parameters.

Experiment	$\frac{\text{mol water}}{\text{mol TEOS}}$	$\frac{\text{mol Ammonia}}{\text{mol TEOS}}$	D (nm)	σ_{n-1} (nm)	Conversion (%)	σ_{n-1} (%)
S	7.9	1.19	24	2	57	1
M	18.2	1.19	47	12	80	1
L	18.2	3.55	146	4	98	1

Table 3.3. Particle size and conversion of the pure silica nanoparticles generated in the first step.

As can be seen, the conversion of the system increased with the increase of the amount of ammonia and water. In addition, the size of the particles obtained was different for each relation of catalyst. It is important to note that the particle size of the nanoparticles underwent a considerable increase with the ammonia concentration. Comparing the results with literature data^{21,22} obtained with conventional heating, the same trends were observed.

The conversion of the second step was measured by elemental analysis because the FTIR absorptions assigned to the methoxysilane groups coming from HDTMS were overlapped with solvent bands and therefore the calculation of the reaction conversion by FTIR was not possible. Table 3.4. shows the reaction conversion obtained in the different experiments.

Experiment	HDTMS (mL)	$\frac{mol\ water}{mol\ TEOS}$	$\frac{mol\ Ammonia}{mol\ TEOS}$	Conversion (%)	σ_{n-1} (%)
S+1	1	7.9	1.19	*	*
S+2	2			93	2
S+3	3			94	1
M+1	1	18.2	1.19	91	1
M+2	2			96	2
M+3	3			96	1
L+1	1	18.2	3.55	92	1
L+2	2			89	1
L+3	3			90	1

Table 3.4. Conversion of the second step.

The results of the S+1 nanoparticles do not appear in the Table due to the gelation that occurred during that experiment. As can be seen, in all cases very high conversions were obtained. In order to verify this result, the conversion was also calculated by thermogravimetry (TGA).

Figure 3.8. shows the thermogram of sample L+3 and its derivative. A two stage heating program was used. In the first stage, the sample was heated from 40 to 600 °C at a rate of 10 °C /min using Nitrogen as a carrier gas. In the second step, heating was performed from 600 to 800 °C at a rate of 40 °C/min, this time using Air as carrier gas.

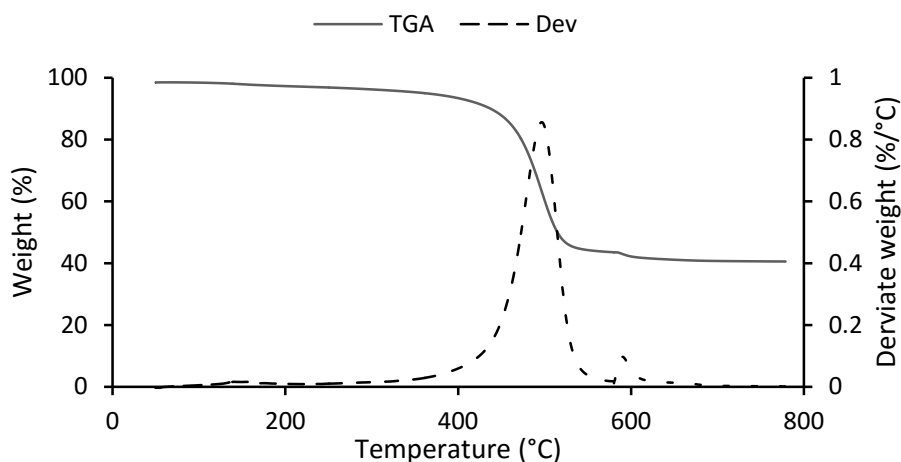


Figure 3.8. TGA curve with its derivative of the sample L+3.

As can be seen, the sample lost near 50 % of its weight in the 400-550 °C temperature range. This weight loss was related to the degradation of the alkyd chain of the organosilane HDTMS and offered the possibility of calculating the conversion of the second step of the reaction²³. The results are summarized in Table 3.5.

As observed in Table 3.5., the high conversion obtained from elemental analysis was confirmed by TGA analysis. Therefore, according to the conversion results for the second step, it could be concluded that the functionalization of the system was high.

Experiment	Conversión (%)	σ_{n-1} (%)
S+2	89	3
S+3	93	3
M+1	89	4
M+2	92	3
M+3	96	2
L+1	91	3
L+2	93	3
L+3	93	2

Table 3.5. Conversion of the second step calculated using TGA data.

The diameter of the particles generated after the second step could not be measured by DLS because the poly dispersity index was very high and therefore the morphology of the particles was observed by Transmission Electron Microscope (Figures 3.9., 3.10. and 3.11.).

The TEM images of the samples generated from the lowest diameter silica particles (experiment S, Figure 3.9.) showed the presence of large aggregates. In the images of the samples generated from silica particles of 47 nm in the first step (experiment M, Figure 3.10.), a distribution of two different size (≈ 25 and 50 nm) nanoparticles was observed. We can assume that the particles of 50 nm were generated in the first step and that the addition of HDTMS in the second step generated the small nanoparticles. Therefore, it seems that the second precursor gave rise to new particles that covered the silica ones generated in the first step. The same effect was observed in the samples generated from experiment L (Figure 3.11.). The large particles with diameters near 200 nm could be generated in the first step, meanwhile the smaller particles (80 nm) could be generated in the second step. It must be pointed out that the size of the particles generated in the second step of the experiment did not change with HDTMS concentration.

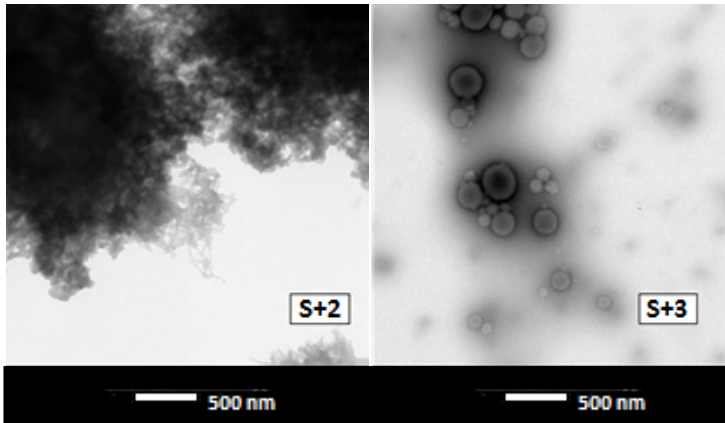


Figure 3.9. TEM images of the samples generated in experiments S+2 and S+3.

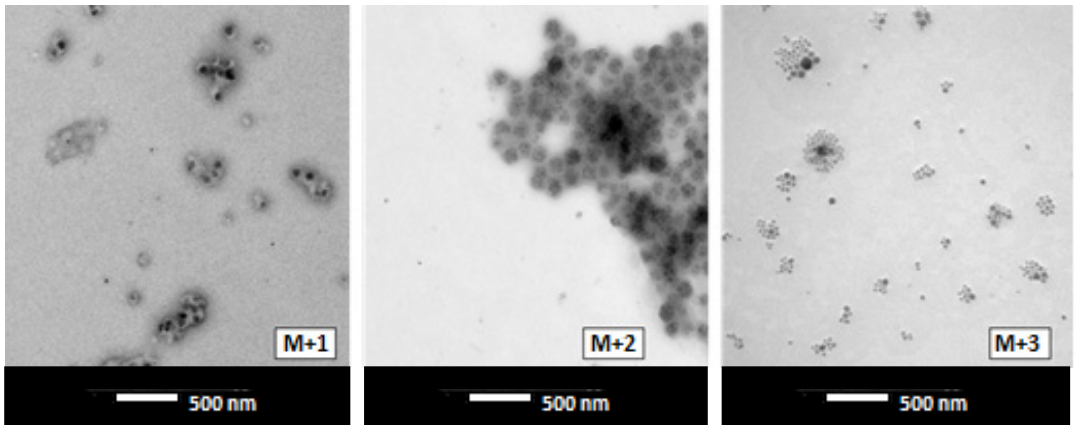


Figure 3.10. TEM images of the samples generated in experiments M+1, M+2 and M+3.

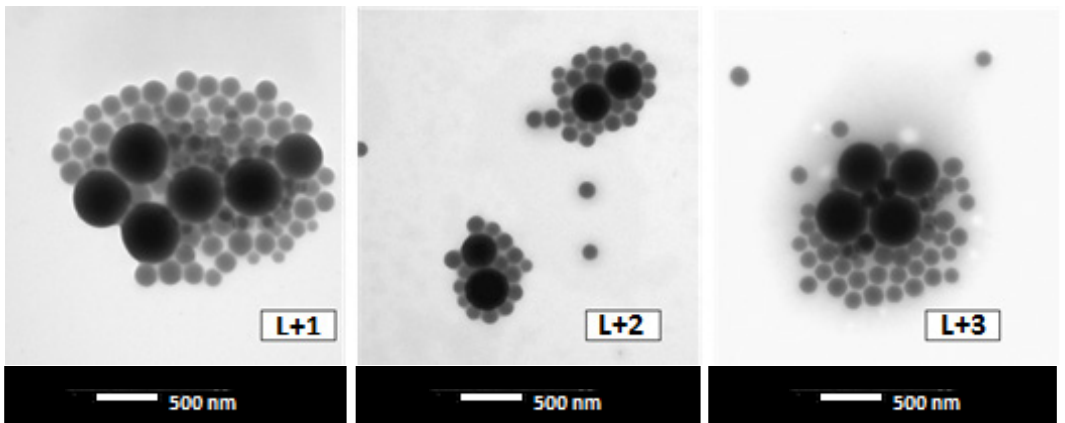


Figure 3.11. TEM images of the samples generated in experiments L+1, L+2 and L+3.

However, the size of the new particles depended on the experimental conditions of the first step. Thus, the new particles generated in the second step of experiment L were larger than those obtained in the same step of experiment M. As the water content of these two experiments was the same, it can be argued that the size of the nanoparticles increased with ammonia content, as previously reported for only TEOS containing nanoparticles.

Finally, in order to compare the effectiveness of microwave heating with conventional heating methods, one of the reactions was performed in a single neck flask equipped with a reflux condenser heated in a thermostatic oil bath for three hours in each step. The diameter of the nanoparticles obtained in this experiment and the conversion of the reaction was calculated as explained previously and the obtained results are summarized in Table 3.6.

Experiment	D 1st step (nm)	σ_{n-1} (nm)	1st step		2nd step	
			Conversion (%)	σ_{n-1} (%)	Conversion (%)	σ_{n-1} (%)
Microwave	26	6	57	7	93	2
Conventional heating	24	10	41	12	74	8

Table 3.6. Comparison between conventional heating and microwave heating.

As can be observed in Table 3.6., the conversion for conventional heating in the first step was around a 15 % lower than the obtained for microwave assisted synthesis. However, the size of the particles obtained in both cases was very similar. According to this, it can be concluded that microwave heating did not have any effect on the particle size.

Taking into account the results of the second step for conventional and microwave experiments, it can be seen that the microwave systems obtain 20 % more conversion than conventional methods. These results agreed with the literature data for microwave synthesis^{24,25}, and can be explained taking into account the rapid and homogeneous heating throughout the reaction vessel caused by microwave heating.

b) Chemical characterization

The chemical characterization of the nanoparticles was performed by Silicon Solid State Nuclear Magnetic Resonance (²⁹Si NMR).

In order to explain the NMR spectra, Lippmaa nomenclature was used²⁶. In this nomenclature the Silicon atom is called T or Q depending on the number of the Oxygen atoms linked to Silicon (T=3; Q=4). In addition, a subscript is added to give information about the number of the Oxygen atoms linked to another Silicon atom. Figure 3.12. shows the structures coexisting in the Sol-Gel process.

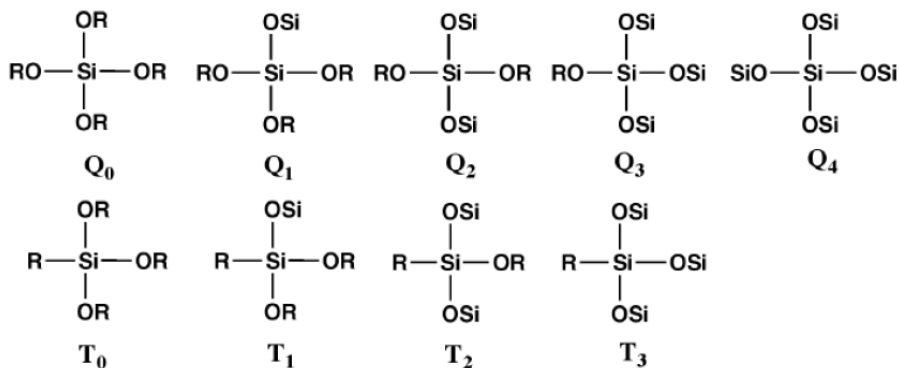


Figure 3.12. Structures coexisting in the Sol-Gel process, as called by Lippmaa.

Figure 3.13. shows the spectra of the nanoparticles obtained from experiment L after adding 1, 2 and 3 mL of HDTMS. In the spectrum of the sample containing only TEOS (L+0) two peaks were observed, which can be attributed to Silicon atoms linked to four Oxygen atoms (Q structures) with 3 or 4 condensation degree. The lower condensation degree species were not observed and therefore, it was concluded that the condensation degree of TEOS in this sample was high, in accordance with the conversion results outlined previously.

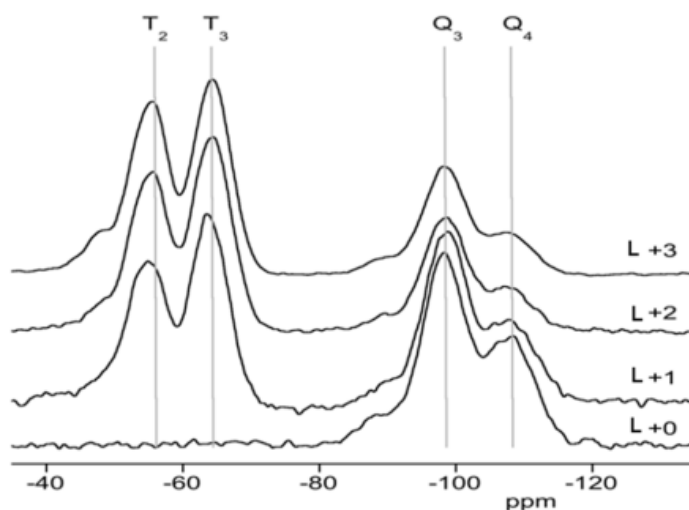


Figure 3.13. ^{29}Si solid state NMR spectra of nanoparticles of experiments L+0, L+1, L+2 and L+3.

In the spectra of samples containing HDTMS, in addition to Q peaks, two new signals, assigned to Silicon atoms linked to three Oxygen atoms (T structures) were also observed²⁷. These signals can be assigned to T_2 and T_3 species. As expected, due to the high conversion, high condensation species signals appear in the spectra. There was no significant difference in the relative intensity between T_2 and T_3 with the HDTMS concentration, suggesting that the condensation degree was not affected by the precursor concentration. The ^{29}Si -NMR experiments of the other

samples were similar and therefore it can be concluded that the condensation degree of the alkoxy silane moieties was high.

c) Wettability

The solid content of the dispersions generated in all the experiments was adjusted to 2 wt. %. Then, 5 mL of the dispersion was cast over 45 mm diameter aluminum pans and dried at room temperature for at least one week.

The water contact angles of the samples were measured and the results are summarized in Table 3.7.

Sample	Angle θ_{av} (°)	σ_{n-1} (°)	Angle θ_r (°)	σ_{n-1} (°)	Hysteresis (°)
S+2	144	1	140	1	4
S+3	150	1	146	1	4
M+1	156	2	151	3	5
M+2	142	1	140	1	2
M+3	147	1	145	1	2
L+1	150	2	145	1	5
L+2	151	1	149	1	2
L+3	152	1	150	1	2

Table 3.7. Resume of the advancing and receding contact angle data for all samples.

As can be observed, the water contact angle of all the surfaces was higher than 140 °. As mentioned in the introduction, contact angles higher than 120 ° can only be obtained if the hydrophobic surface is roughened. According to this, the high contact angle obtained in these surfaces is due to the roughness generated by the silica nanoparticles. In addition, the hysteresis values were low. This fact indicates that there was almost no contact between the liquid drop and the surface, and therefore the advancing and receding angles were similar giving rise to low

hysteresis values. Therefore, it can be concluded that the water drop was in the Cassie-Baxter state in which the water drop did not penetrate into the rough peaks.

Finally, it is interesting to remark that a dependency between the particle size and morphology and the contact angle was not observed. This can be explained considering that the particles obtained in the second step governed the surface properties of the coating.

3.4. “Co-condensation” nanoparticles

3.4.1. Synthesis

The co-condensation method involves the use of TEOS with HDTMS in one single reaction step. The hydrophobic properties, which are incorporated by HDTMS, are supposed to be inside the silica particle, and not only on the surface as in the “grafting to” method. The preparation method was as follows.

3 mL of TEOS, 50 mL of ethanol and the required amounts of water and ammonia were introduced in to the reaction vessel. Before the addition of the catalysts (ammonia and water) the required amounts of HDTMS were added. The microwave heating process was carried out under the same parameters as the used in the “grafting to” method (section 3.3.1.).

A total of nine reactions were performed (Table 3.8.). The conditions of catalyst, the amount of water and ammonia were the same as those used in the grafting to nanoparticles.

Experiment	HDTMS (mL)	$\frac{mol\ water}{mol\ TEOS}$	$\frac{mol\ Ammonia}{mol\ TEOS}$
S+1	1	7.9	1.19
S+2	2		
S+3	3		
M+1	1	18.2	1.19
M+2	2		
M+3	3		
L+1	1	18.2	3.55
L+2	2		
L+3	3		

Table 3.8. Formulation of the one step co-condensation experiments.

3.4.2. Results and Discussion

a) Conversion and diameter of the nanoparticles

The same techniques used to characterize “the grafting to” nanoparticles were employed.

The conversion of the condensation reaction of the methoxysilane groups of the HDTMS was calculated by Elemental Analysis assuming total conversion in the tetraethoxysilane condensation. The obtained results are shown in Table 3.9.

Experiment	Conversion (%)	σ_{n-1} (%)
S+1	78	4
S+2	83	5
S+3	84	4
M+1	88	3
M+2	84	4
M+3	85	3
L+1	80	5
L+2	88	6
L+3	83	3

Table 3.9. Conversion of the condensation reaction of the methoxysilane groups.

It can be seen that the conversion in all cases was high, close to 85 %. However, the obtained values were lower than those observed for the two step process (Table 3.4.).

As in the final particles obtained in the two step method, the size of the nanoparticles could not be measured by the DLS method because they presented a high polydispersity. Therefore the morphology of the particles was observed by TEM images.

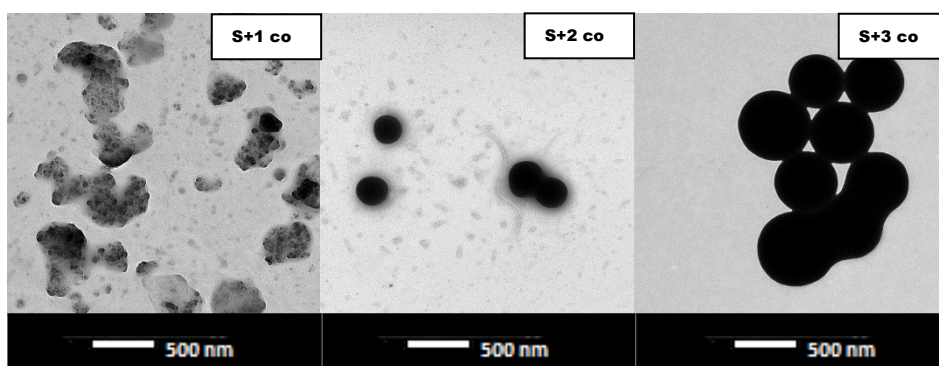


Figure 3.14. TEM images of the samples generated in experiments S+1, S+2 and S+3 co-condensation.

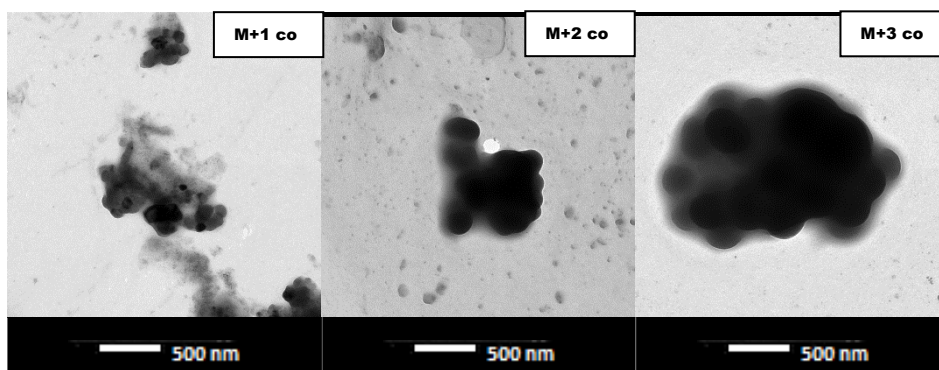


Figure 3.15. TEM images of the samples generated in experiments M+1, M+2 and M+3 co-condensation.

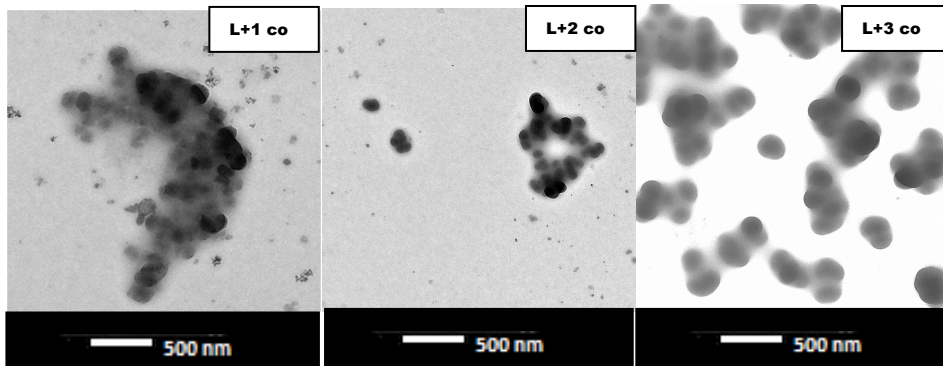


Figure 3.16. TEM images of the samples generated in experiments L+1, L+2 and L+3 co-condensation.

TEM images of all experiments are shown in the Figures 3.14., 3.15. and 3.16. As can be observed, all the samples presented agglomerates constituted of several nanoparticles.

It is important to note that in the nanoparticles obtained using the same reaction conditions but the two step process a distribution of two different size nanoparticles was observed. However, the nanoparticles obtained in the one step process presented a monomodal distribution, suggesting that secondary nucleations did not happen during the synthesis.

In the one step method, for each experiment, higher particle sizes were obtained when increasing the HDTMS amount. In addition, there was not a clear relation between the particle size and the water and ammonia relation. However, it can be assumed that at least in the experiments where 3 mL of HDTMS were added (S+3, M+3 and L+3) the particle size was lower in the sample obtained using more water and ammonia. This result is not easy to explain because as stated in literature²⁸ when obtaining pure silica particles, the particle size increases with the water and

ammonia concentration. It seems that the hydrophobic chain of HDTMS changes this pattern.

b) Chemical characterization

Figure 3.17. shows as example the ^{29}Si NMR spectra of the nanoparticles obtained from experiment L with 1, 2 and 3 mL of HDTMS via co-condensation. Two types of signals are visible, Q peaks (Silicon atoms linked to four Oxygens) and T peaks (Silicon atoms linked to three Oxygens). Focusing on the region of Q peaks (-100 ppm), three signals assigned to Q_2 (-94 ppm), Q_3 (-102 ppm) and Q_4 (-110 ppm) species appear in all the spectra. The relative intensity of all peaks was similar for all nanoparticles, suggesting that the condensation degree was not affected by the formulation.

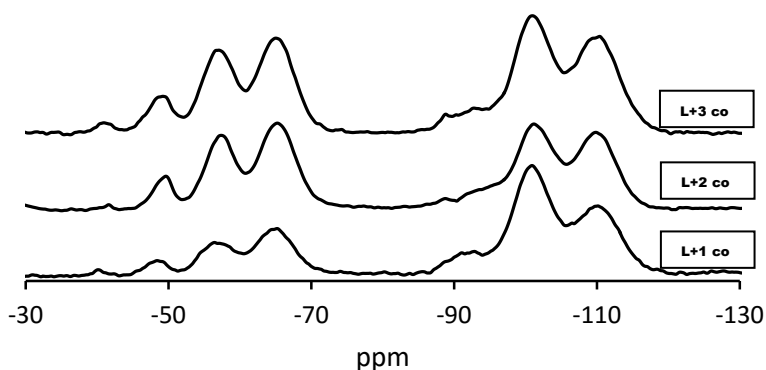


Figure 3.17. ^{29}Si solid state NMR spectra of nanoparticles of experiments L+1, L+2 and L+3 co-condensation.

In the T region, the spectra show 3 different bands that could be assigned to T_1 (-50 ppm), T_2 (-58 ppm), and T_3 (-63 ppm), species. A small shoulder at -42 ppm that could be assigned to T_0 type Silicon atoms was also detected. It is clear that both Q and T type silicon atoms presented high condensation degrees, as the more intense signals were assigned to Q3 and T3 species. In addition, there were no significant differences in the relative intensity between T_2 and T_3 signals with the HDTMS concentration, suggesting that the condensation degree was not affected by the precursor.

However, the condensation degree was lower than that of the nanoparticles obtained using the two step procedure. This result is in accordance with the conversion data calculated by Elemental Analysis and could be due to the lower reaction time employed in the one step procedure.

c) Wettability

Different surfaces were prepared using the same methodology employed in the previous section. The nanoparticles concentration for generating the surface was the same as in the “grafting to” method. The water contact angle of each sample, as its hysteresis are shown in Table 3.10.

As can be seen in Table 3.10., the contact angle of all nanoparticles was high, but not as high as in the nanoparticles obtained using the two step method. This decrease could be related to a lower surface hydrophobicity of the nanoparticles obtained in the one step methodology. It can be supposed that as a consequence of the reaction conditions, a part of the hydrocarbonated chain of the HDTMS could be inside the nanoparticles. In addition, as a consequence of the lower condensation degree of the nanoparticles described in this section, the surface can contain uncondensed

silanol groups. Both effects were able to reduce the surface hydrophobicity and therefore these nanoparticles presented lower water contact angle values.

Sample	Angle θ_{av} (°)	σ_{n-1} (°)	Angle θ_r (°)	σ_{n-1} (°)	Hysteresis (°)
(S+1) co	138	7	130	6	8
(S+2) co	139	6	127	6	12
(S+3) co	139	5	130	7	9
(M+1) co	142	5	132	5	10
(M+2) co	140	5	131	6	9
(M+3) co	138	6	127	7	11
(L+1) co	141	5	129	6	12
(L+2) co	139	5	125	6	15
(L+3) co	140	6	127	4	14

Table 3.10. Advancing and receding contact angles of the samples generated in one step process.

Moreover, the surfaces generated from the nanoparticles obtained using the co-condensation procedure presented higher values of the water contact angle hysteresis than those obtained using a two-step procedure. The lower hydrophobicity of the former could be responsible for this behavior but it should be taken into account that the morphology of the nanoparticles obtained in the two methodologies was different. Thus, the nanoparticles obtained in the two step procedure presented a distribution of two different size nanoparticles while only one size nanoparticles were obtained in the co-condensation method. The higher heterogeneity of the former gave rise to a rougher surface and therefore also explained the lower values of the water contact angle hysteresis.

3.5. “Grafting to” and “co-condensation” comparison

Using both, one and two step methodologies, hydrophobic surfaces were obtained. However, in order to prepare superhydrophobic surfaces, the nanoparticles obtained in the co-condensation method presented water contact angle hysteresis values that were too high. This is why all the polymeric surfaces were prepared using the nanoparticles generated using the two step procedure.

3.6. Introduction of nanoparticles into the polymer matrix

A simple way to produce hydrophobic surfaces is by introducing nanoparticles which impart roughness, as mentioned in the introduction. With a careful selection of the polymer and particles, the surface morphology can be controlled.

The particles generated as described in the previous section could be of great interest in order to obtain hydrophobic surfaces. These nanoparticles were mixed with Poly(methyl methacrylate) that was chosen as a representative member of the more complex acrylic polymers, usually employed as paints and coatings. In literature many kind of methods can be found in order to introduce the particles into the polymeric matrix such as casting, spin-coating, dip-coating and spraying. In this work, different methods were used, trying to select the one that provides the highest hydrophobicity to the surface.

As previously mentioned, the nanoparticles obtained using the two step methodology were selected because they presented low hysteresis values and are therefore more appropriate when obtaining hydrophobic surfaces with self-cleaning properties. All the nanoparticles synthesized in the two step methodology showed

interesting wettability behaviour. Among these nanoparticles, the ones synthesized in the L+3 experiment were selected because these experimental conditions gave rise to high conversion.

3.6.1. Films generated by casting

a) Preparation

PMMA powder was dissolved in Toluene at lab temperature (25 °C) to form a solution of a concentration of 10 wt. % (mass fraction). The L+3 silica nanoparticles used in the mixing were dried for 24 hours at room temperature, after a cleaning step in which the nanoparticles were centrifuged at 12500 r.p.m. for 10 minutes at 10 °C in a Sigma 3-30K centrifuge. The dried nanoparticles were mixed with the polymer solution at different percentages. The resultant mixtures were magnetically stirred for at least 1 hour. The dispersions were casted over aluminum at lab temperature, allowing the formation of the PMMA-SiO₂ nanocomposite film. For comparison, a pure polymer solution (without any nanoparticle) and the nanoparticle dispersion were also prepared.

b) Results and discussion

The films obtained by casting were about 250 ± 50 nm thick. The thicknesses were recorded using Duocheck ST-10 electromagnetic equipment. They were opaque and very fragile, with many cracks on the surface.

The water contact angle and hysteresis value of the nanocomposite PMMA-SiO₂ generated by casting are shown in Table 3.11.

wt.% nanoparticles	Angle θ_{av} (°)	σ_{n-1} (°)	Angle θ_r (°)	σ_{n-1} (°)	Hysteresis (°)
0	82	1	80	1	2
33	137	3	129	2	8
50	142	2	136	2	6
67	143	2	137	2	6
100	152	1	150	1	2

Table 3.11. Advancing and receding contact angles of PMMA-SiO₂ nanocomposites generated by casting.

As can be observed, a high increase of the contact angle was obtained by adding nanoparticles into the polymeric matrix. Thus PMMA showed a water contact angle of 80 ° approximately and the addition of 33 wt. % of silica nanoparticles increased the angle to near 140 °. The values of the hysteresis were not excessively high, less than 10 °, this confirms that when a water drop was on the surface it did not penetrate into the roughness, as described by the Cassie-Baxter model. Low values of hysteresis minimize the adhesion of water and therefore these surfaces are of interest because self-cleaning properties are expected.

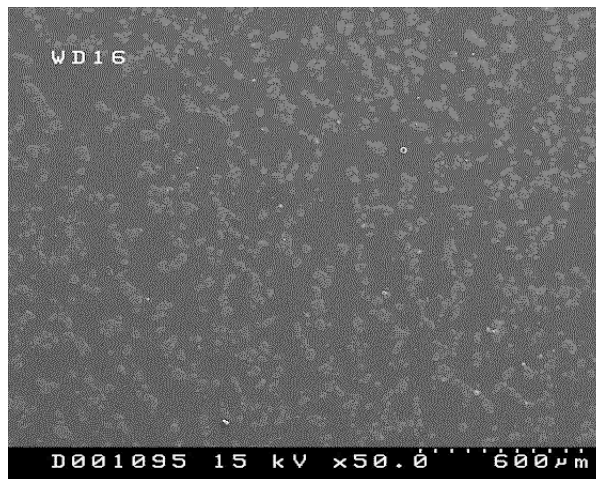


Figure 3.18. SEM of PMMA-SiO₂ surface with 50 wt. % of nanoparticles.

Scanning Electron Microscopy (SEM) was used to observe the nanoparticle distribution on the film surface. Figure 3.18. shows the SEM image of the 50 wt. % of nanoparticles containing sample.

It was seen that the nanoparticles inside the PMMA matrix were randomly distributed generating aggregates (island-like distribution), which produced the increase of the hydrophobicity.

These results agreed with the literature data⁴, where superhydrophobic properties containing surfaces were generated by casting of polymer/nanoparticle mixtures. The surfaces obtained in the present work showed satisfactory wettability results. However, as mentioned, the generated films were very fragile, limiting their use.

3.6.2. Films generated by spin-coating

a) Preparation

PMMA powder was dissolved in Toluene at lab temperature (25 °C) to form a solution of a concentration of 10 wt. % (mass fraction) as in the previous section. Dried silica nanoparticles (L+3 grafting to) were mixed with the polymer solution at different percentage of particles. The resultant mixtures were magnetically stirred for at least 1 hour to form dispersions. The dispersions were spin-coated at lab temperature and at 2500 r.p.m. for 40 seconds in a SCC-200 Spin-Coating allowing the formation of the PMMA-SiO₂ nanocomposite films over aluminum surfaces. For comparison a pure polymer solution (without any nanoparticles) and the nanoparticle film were also prepared.

b) Results and discussion

The films obtained by Spin-Coating were transparent and about 80 ± 20 nm thick over a glass substrate. The result is the difference between the glass plus the film minus the thickness of the glass substrate.

The values of the water contact angle and hysteresis on the prepared surfaces are shown in Table 3.12.

wt. % nanoparticles	Angle θ_{av} (°)	σ_{n-1} (°)	Angle θ_r (°)	σ_{n-1} (°)	Hysteresis (°)
0	84	2	80	3	4
33	110	6	94	8	16
50	121	7	100	6	14
67	130	7	113	7	17
100	137	7	119	7	18

Table 3.12. Advancing and receding contact angles of PMMA-SiO₂ nanocomposites generated by spin-coating.

As can be observed, the introduction of nanoparticles increased the water contact angle of the surface. However, comparing the values obtained by spin-coating with those obtained by casting it is clear that for the same nanoparticles content higher contact angles were obtained in the surfaces generated by casting. For example, for the samples containing 33 wt. % of nanoparticles, contact angles of 137° and 110° were obtained for samples generated by casting and spin-coating respectively.

However, as previously mentioned, in order to obtain a hydrophobic surface in addition to a high water contact angle, low values of hysteresis are mandatory. Unfortunately, the hysteresis values of the surfaces obtained by spin-coating were higher than 10° .

The morphology of all the surfaces obtained by spin-coating was analyzed by Scanning Electron Microscopy (SEM). As an example Figure 3.19. shows the SEM image of the surface obtained for the sample containing 50 wt. % of nanoparticles.

As can be observed, the sample surface did not present roughness. No silica particles were evident on the surface of the sample and therefore it was assumed that they were inside the PMMA matrix, giving rise to low values of the water contact angle.

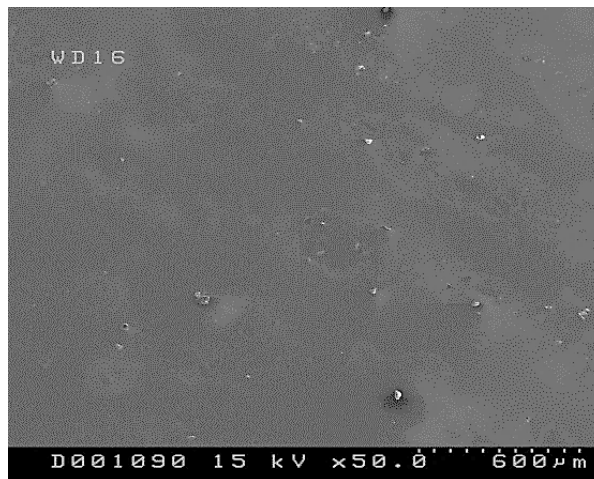


Figure 3.19. SEM of PMMA-SiO₂ nanocomposite generated by Spin-Coating surface (50 wt. % of nanoparticles).

These results do not match literature data where it is stated that the hydrophobicity of the films generated via spin-coating is high²⁹. This can be due to the poor dispersion of the nanoparticles in the film. It can be supposed that as the viscosity of the dispersion was not very high, the nanoparticles were displaced to the edge of the film due to the spinning process which provoked a non-homogeneous dispersion of the nanoparticles in the film.

3.6.3. Films generated by spraying

a) Preparation

A PMMA film was prepared by casting a 10 wt. % PMMA/Toluene solution over an aluminium surface. Simultaneously, L+3 nanoparticles, obtained using the two-step procedure, were dispersed in Ethanol at a concentration of 20 wt. %. The dispersion of the nanoparticles was sprayed over the PMMA dry film. The sprayer used to generate the superhydrophobic surface was a flask-type sprayer of 200 mL. The distance between the film and sprayer was kept constant at 40 centimetres, and the flow of N₂ was kept constant at 10 mL/min. Different samples were obtained varying the spraying time, afterwards, the samples were dried at room temperature for 24 hours before making any measurement.

b) Results and discussion

The samples obtained via this method were opaque. The lack of transparency increased with the spraying time due to the increase of the amount of nanoparticles on the surface.

Spraying time (s)	Angle θ_{av} (°)	σ_{n-1} (°)	Angle θ_r (°)	σ_{n-1} (°)	Hysteresis (°)
0	82	1	80	1	2
5	141	3	132	2	9
10	150	2	142	4	8
15	153	3	146	3	7
30	158	3	153	2	5

Table 3.13. Advancing and receding contact angles of PMMA-SiO₂ nanocomposites generated by spraying.

The water contact angle and hysteresis value of the PMMA-SiO₂ surfaces generated by spraying are shown in Table 3.13.

As can be seen, for all experiments, superhydrophobic surfaces characterized by high advancing water contact angle, and hysteresis values less than 10 ° were obtained. Thus, at low spraying times, a dramatic increase was observed in the water contact angle that increased from 82 °, corresponding to the pure PMMA, to 140 ° for sample obtained with five seconds of spraying time. These results demonstrated that the spraying method can be an effective way to obtain superhydrophobic surfaces.

Figure 3.20. shows the SEM image of the surface of the sample obtained by spraying for 10 seconds. As can be seen, the surface presented high roughness. In addition, the nanoparticles were agglomerated creating micro domains that gave the surface a dual micro-nano roughness similar to that described in literature for the surface of the Lotus Flower leaf. This particular morphology could be the responsible for the high contact angle and low hysteresis values that these surfaces presented. Similar results were observed in literature using this method of creating superhydrophobic surfaces³⁰.

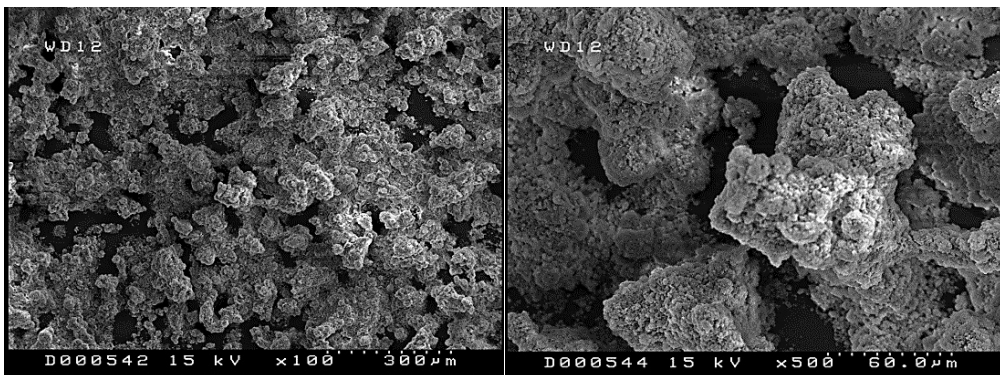


Figure 3.20. SEM images of the 10 second spraying surfaces showing the micro-nano scale topography.

3.7. Self-cleaning effectiveness

In order to determine the suitability of these PMMA-SiO₂ samples to be applied in the generation of self-cleaning surfaces, the water sliding angle was measured. For this experiment, water drops were placed on the surface of a PMMA-SiO₂ sample that was tilted until the drop rolled down the surface.

The experiment was carried out using the sample obtained by spraying silica nanoparticles for 10 seconds and, the water rolled over the surface when the angle was close to 5°.

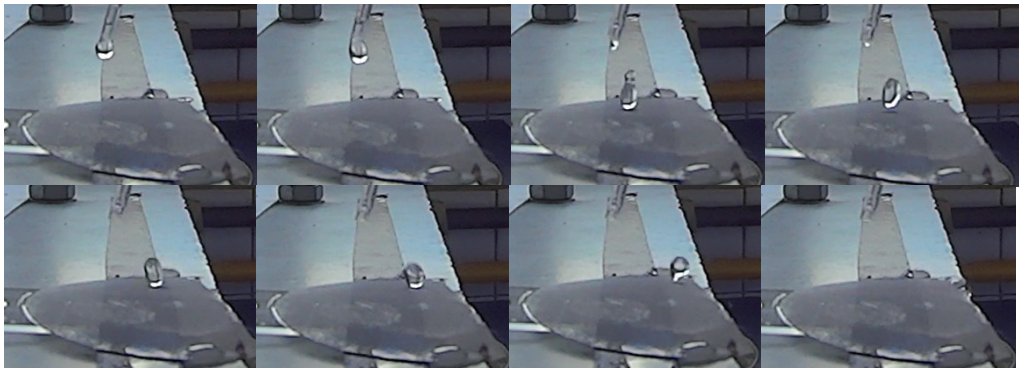


Figure 3.21. Frame sequence of the passage of a drop of water on the surface.

Figure 3.21. shows the frame sequence of the passage of a drop of water on the surface of this sample. As can be observed in the images, the water leaves the surface quickly without leaving any trace. It is interesting to note that the drop moves across the film in less than 1 second, making it useful in the field of the self-cleaning surfaces.

3.8. Conclusions

The main conclusions that can be extracted from the generation of hydrophobic surfaces by the addition of silica nanoparticles to polymeric matrixes are summarized below.

- ✓ Hydrophobic silica nanoparticles are obtained by Tetraethyl Orthosilicate (TEOS) and Hexadecyl Trimethoxy Silane (HDTMS) base catalyzed hydrolysis and condensation Sol-Gel process. Particle size and morphology are governed by the water and catalyst concentration.
- ✓ Microwave assisted synthesis increases the Sol-Gel reaction conversion.
- ✓ The addition of the HDTMS in a second step gives rise to nanoparticles with bimodal size distribution. These nanoparticles are more hydrophobic than those obtained when the two precursors are simultaneously added to the reaction vessel.
- ✓ The introduction of the silica nanoparticles in Poly(methyl methacrylate) increases the contact angle of the generated surfaces. However, the films containing nanoparticles are opaque.
- ✓ Surfaces with contact angles higher than 140° are obtained spraying hydrophobic nanoparticles over PMMA films. These coatings present low sliding angles and are therefore very good candidates for use in the field of self-cleaning surfaces.

3.9. Bibliography

1. Rüdiger, A., *et al.* Nanosize ferroelectric oxides-Tracking down the superparaelectric limit. *Appl. Phys. A Mater. Sci. Process.* **80**, 1247–1255 (2005).
2. Noguez, C. Optical properties of isolated and supported metal nanoparticles. *Opt. Mater.* **27**, 1204–1211 (2005).
3. Wang, H., *et al.* Superhydrophobic coatings fabricated with polytetrafluoroethylene and SiO₂ nanoparticles by spraying process on carbon steel surfaces. *Appl. Surf. Sci.* **349**, 724–732 (2015).
4. Efome, J. E., *et al.* Effects of superhydrophobic SiO₂ nanoparticles on the performance of PVDF flat sheet membranes for vacuum membrane distillation. *Desalination.* **373**, 47–57 (2015).
5. Tahmasebi, N. & Mohammad, S. Synthesis and optical properties of Au decorated colloidal tungsten oxide nanoparticles. *Appl. Surf. Sci.* **355**, 884–890 (2015).
6. Radoi, M. B., *et al.* Influence of TiO₂ nanoparticles on formation mechanism of PANI/TiO₂ nanocomposite coating on PET fabric and its structural and electrical properties. *Surf. Coat. Technol.* **278**, 38–47 (2015).
7. Brinker, C. J., *et al.* Sol-Gel thin film formation. *J. Non-Cryst. Solids.* **121**, 294–302 (1990).
8. Zeldin, M., Wynne, K. J. & Allcock, H. R. Inorganic and Organometallic Polymers. *ACS Symposium Series.* **360**, (1988).
9. Brinker, C. J., *et al.* Inorganic and Organometallic Polymers. *ACS Symposium Series.* **360**, 26–314 (1988).
10. Leyva-Porras, C., *et al.* Low-temperature synthesis and characterization of anatase TiO₂ nanoparticles by an acid assisted Sol-Gel method. *J. Alloys Compd.* **647**, 627–636 (2015).

11. Dubois, G., *et al.* Molecular network reinforcement of Sol-Gel glasses. *Adv. Mater.* **19**, 3989–3994 (2007).
12. Chung, Y. T., *et al.* Synthesis of minimal-size ZnO nanoparticles through sol-gel method: Taguchi design optimisation. *Mater. Des.* **87**, 780–787 (2015).
13. Faure, J., *et al.* A new sol-gel synthesis of 45S5 bioactive glass using an organic acid as catalyst. *Mater. Sci. Eng. C.* **47**, 407–412 (2015).
14. Takeda, Y., Komori, Y. & Yoshitake, H. Direct Stöber synthesis of monodisperse silica particles functionalized with mercapto, vinyl and aminopropylsilanes in alcohol-water mixed solvents. *Colloids Surf. A.* **422**, 68–74 (2013).
15. Stöber, W., Fink, A. & Bohn, E. Controlled growth of monodisperse silica spheres in the micron size range. *J. Colloid Interface Sci.* **26**, 62–69 (1968).
16. Graf, C., Vossen, D., Imhof, A. & Van Blaaderen, A. A general method to coat colloidal particles with silica. *Langmuir.* **19**, 6693–6700 (2003).
17. Van Blaaderen, A., Van Geest, J. & Vrij, A. Monodisperse colloidal silica spheres from tetraalkoxysilanes: Particle formation and growth mechanism. *J. Colloid Interface Sci.* **154**, 481–501 (1992).
18. Bondioli, F., *et al.* Synthesis of zirconia nanoparticles in a continuous-flow microwave reactor. *J. Am. Ceram. Soc.* **91**, 3746–3748 (2008).
19. Roy, R., Komareni, S. & Yang, L. J. Controlled Microwave Heating and Melting of Gels. *J. Am. Ceram. Soc.* **68**, 392–395 (1985).
20. Mily, E., *et al.* Silica nanoparticles obtained by microwave assisted Sol-Gel process: Multivariate analysis of the size and conversion dependence. *J. Sol-Gel Sci. Technol.* **53**, 667–672 (2010).
21. Vasconcelos, D. C., Campos, W. R., Vasconcelos, V. & Vasconcelos, W. L. Influence of process parameters on the morphological evolution and fractal dimension of sol-gel colloidal silica particles. *Mater. Sci. Eng. A.* **334**, 53–58 (2002).

22. Lindberg, R., *et al.* Multivariate analysis of the size dependence of monodisperse silica particles prepared according to the Sol-Gel technique. *Colloids Surf. A.* **123-124**, 549–560 (1997).
23. Sengupta, R., *et al.* Polyamide-6,6/in situ silica hybrid nanocomposites by Sol-Gel technique: Synthesis, characterization and properties. *Polymer.* **46**, 3343–3354 (2005).
24. Hwang, Y. K., Chang, J. S., Kwon, Y. V. & Park, S. E. Microwave synthesis of cubic mesoporous silica SBA-16. *Microporous Mesoporous Mater.* **68**, 21–27 (2004).
25. Bahadur, N. M., *et al.* Fast and facile synthesis of silica coated silver nanoparticles by microwave irradiation. *J. Colloid Interface Sci.* **355**, 312–320 (2011).
26. Lippmaa, E., *et al.* Structural studies of silicates by solid-state high-resolution silicon-29 NMR. *J. Am. Chem. Soc.* **102**, 4889–4893 (1980).
27. Komori, Y., Nakashima, H., Hayashi, S. & Sugahara, Y. Silicon-29 cross-polarization/magic-angle-spinning NMR study of inorganic-organic hybrids: Homogeneity of Sol-Gel derived hybrid gels. *J. Non-Cryst. Solids.* **351**, 97–103 (2005).
28. Santiago, A., *et al.* Preparation of superhydrophobic silica nanoparticles by microwave assisted sol-gel process. *J. Sol-Gel Sci. Technol.* **61**, 8–13 (2012).
29. Wang, J., *et al.* Preparation of superhydrophobic poly(methyl methacrylate)-silicon dioxide nanocomposite films. *Appl. Surf. Sci.* **257**, 1473–1477 (2010).
30. Manoudis, P. N. & Karapanagiotis, I. Modification of the wettability of polymer surfaces using nanoparticles. *Prog. Org. Coat.* **77**, 331–338 (2014).

Chapter 4

Preparation of porous silica surfaces by acid Sol-Gel method with anti-reflecting applications

Chapter 4:

Preparation of porous silica surfaces by acid Sol-Gel method with anti-reflecting applications

4.1.	Introduction	139
4.2.	Materials	142
4.3.	Synthesis	143
4.4.	Thin-film generation	145
4.5.	Thin-film characterization	146
4.6.	Results and discussion	147
	4.6.1. Porosity, density and refraction index	147
	4.6.2. Mechanical properties characterization (Young Modulus)	157
	4.6.3. Wettability behaviour	162
4.7.	Conclusions	163
4.8.	Bibliography	164

4.1. Introduction

Due to the unique characteristic of high accessible surface area and low density, porous substrates with controlled porosity, pore shape and distribution are useful in a wide range of applications such as electronics¹⁻³, energy storage⁴⁻⁷, catalysis^{8,9}, sensors¹⁰⁻¹², adsorbent materials¹³, biomedical science¹⁴⁻¹⁶ and separation science¹⁷⁻¹⁹. Porous materials are made from organic substances (such as polymers)^{20,21}, from inorganic substances (such as metals and metal oxides)^{22,23} and from organic-inorganic hybrids (such as Polysilsesquioxane and metal-organic framework, MOF)²⁴⁻²⁶.

In all of the possible fields of applications for porous materials, this work focuses on anti-reflection coatings. These kinds of coatings have recently attracted great interest for their possible applications in optical devices. An ideal homogenous anti-reflective coating can achieve nearly 0 % reflection at a specific wavelength. To obtain an anti-reflecting coating, the refractive index (RI) must be lower than that of the substrate (typically glass, RI: 1.52). Since the lowest refractive index (RI) for a dense material is 1.34, porous materials are an obvious choice for applications requiring even lower RI. The introduction of the porosity, while necessary to decrease the refractive index, has a negative impact on the mechanical properties of the insulating materials such as Young Modulus²⁷.

In general, porous materials contain voids as the majority phase, either with a random character (disordered pore systems) or with high regularity (ordered systems). A classification for the pore system is achieved by the pore diameter D_p ²⁸. Pores below 2 nm are called micropores those in the range of $2 \text{ nm} < D_p < 50 \text{ nm}$ mesopores, while pores exceeding 50 nm macropores. According to the above definition of pore diameter, we can classify the materials into a several types, which

are microporous^{29,30}, mesoporous^{31,32}, macroporous^{33,34} and hierarchically porous materials^{35,36}.

Since the first development of the Sol-Gel system accompanied by phase separation, macroporous silica films have been successfully synthesized using various additives such as Poly(ethylene oxide)³⁷, Poly(acrylic acid), Polyacrylamide, block copolymer surfactants³⁸ (for example Pluronic P-123), cationic surfactants, and anionic surfactants. Not only macroporous silica films but also macroporous Poly silsesquioxane films can be obtained using this method.

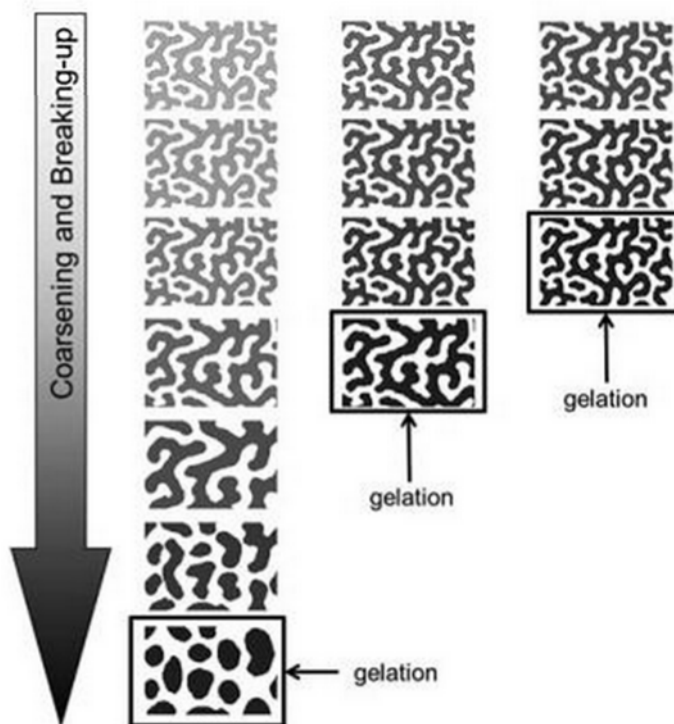


Figure 4.1. Schematic image of the Sol-Gel reaction accompanied by decomposition. The transient structure of decomposition is irreversibly frozen-in the gel morphology.

Figure 4.1. shows a scheme of the Sol-Gel process to generate a porous film. A phase separated system is built where one phase is mainly composed of silica network generated by alkoxy silane hydrolysis and condensation, and the other is composed of a porogen agent and a solvent. After the reaction of the inorganic part, the decomposition of the organic part generates the porosity.

Until now, a major setback in the realization of technological applications for these materials are their poor mechanical properties. Indeed, the incorporation of pores into brittle glasses often has a catastrophic effect on their mechanical and fracture properties. This behaviour is even more pronounced when moving from silicate to organosilicate materials due to a decrease in network connectivity, reducing the potential applications for these materials.

The strategy to prepare intrinsically tougher organosilicate glass depends on precursor monomer structure and is based on the incorporation of carbon bridging units between silicon atoms present in the organosilicate network³⁹. Compared with common silsesquioxane-based organosilicates, the absence of dangling carbon substituent bonds coupled with the presence of an organic bridge between the network silicon atoms, confers unique mechanical properties to these organic/inorganic hybrid materials, a result which dispels the common misconception that all carbon-based silsesquioxane derivatives are intrinsically weak and prone to fracture^{40,41}.

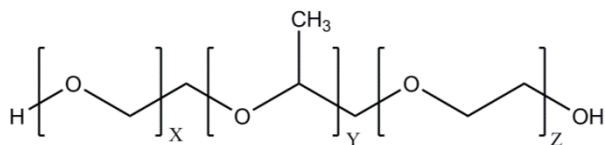


Figure 4.4. Pluronic P-123 porogen structure.

3M™ Novec™ Fluorosurfactant FC-4430 is a non-ionic polymeric fluorochemical surfactant belonging to a class of coating additives which provide low surface tensions in coating systems best served by fluorochemical surfactants. Novec fluorosurfactant FC-4430 contributes excellent wetting, spreading and leveling properties to a variety of coating systems and because of that was chosen to improve the coating properties.

2-Methoxy-1-Propanol (PMOH) was selected as solvent. It was an electronic grade solvent obtained from the Dow Chemical Company. Finally, Nitric acid (HNO₃) was selected as the acid catalyst of the Sol-Gel process and it was purchased from Sigma-Aldrich.

4.3. Synthesis

Porous film solution preparation example: to prepare a final solution containing 10 wt. % porogen, 2.0 g of BTESE were mixed with 5.09 g of 2-Methoxy-1-Propanol (PMOH) to prepare a 25 wt. % solution. Then 0.889 g of a 25 wt. % solution of porogen in the same solvent was added. Finally, 0.9 g of a 1 M solution of aqueous Nitric acid was added to the solution. In Table 4.1. the composition for all formulations used in this work is shown.

All experiments were performed in a clean room at room temperature in a 20 mL reactor.

The weight ratio of porogen to BTESE permits the control of total porosity in the thin-film. The amounts of the components were changed trying to keep the total weight similar.

Sample	BTESE (g)	Porogen (g) (25 wt. %)	FC4430 (g) (25 wt. %)	PMOH (g)	HNO₃ (g) (1M)	Total weight (g)
100/0	2.20	0.000	0.176	5.590	1.005	8.976
95/05	2.10	0.442	0.177	5.340	0.959	9.019
92.5/7.5	2.05	0.665	0.177	5.213	0.937	9.040
90/10	2.00	0.889	0.178	5.086	0.914	9.067
87.5/12.5	1.95	1.114	0.178	4.959	0.891	9.093
85/15	1.90	1.341	0.179	4.832	0.868	9.120
82.5/17.5	1.85	1.570	0.179	4.705	0.845	9.149
80/20	1.80	1.900	0.180	4.578	0.822	9.180
77.5/22.5	1.75	2.032	0.181	4.450	0.800	9.213
75/25	1.70	2.267	0.181	4.323	0.777	9.245

Table 4.1. Formulation composition for the process with different amounts of porogen.

Depending on the porogen agent (Pluronic® or Brij®), the solution was allowed to react for different times. In the case of Pluronic P-123, the films were obtained after 24 hours of reaction. On the other hand, the Brij35 formulations were allowed to react for 16 hours due to the different viscosity of the solution generated with the porogen. For each formulation, three films were obtained in order to determine the reproducibility of the system.

The general scheme for the Sol-Gel reaction is shown in Figure 4.5.

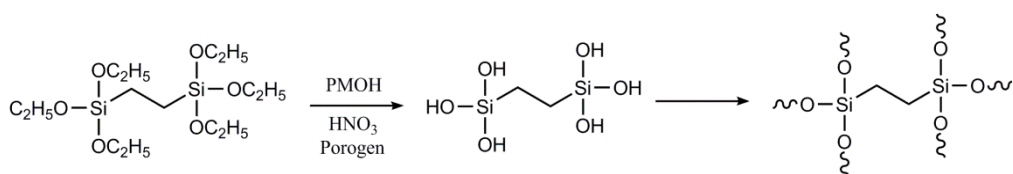


Figure 4.5. BTESE Sol-Gel schematic reaction in acid medium.

The reaction, as shown in Figure 4.5., consists of two steps, the hydrolysis of the alkoxy silane and the condensation of the silanol groups. The carbon bridge is maintained in the final structure.

4.4. Thin-film generation

Thin-films (~330 nm) were obtained by spin-coating the above solutions (500 μ L) on clean silicon wafers. The spin-coater speed used for preparing the films was 2500 r.p.m. for 30 seconds for 0-10 % formulations and 3000 r.p.m. for 30 seconds for the rest of the formulations (12.5-35 %) in a SCC-200 Spin-Coater. The films were first hot plate baked at 125 $^{\circ}$ C for 2 min, then heated under Nitrogen from 60 $^{\circ}$ C to 450 $^{\circ}$ C at 3.2 $^{\circ}$ C/min and held at 450 $^{\circ}$ C for 2 hours using a YES® bake oven.

4.5. Thin-film characterization

a) Thickness, refractive index, density and pore size

Thickness and refractive index of the porous films generated were measured using Spectral Reflectometer (SR). Specular X-Ray Reflectivity (XRR) was used to characterize the sample density and its thickness.

Pore size and its distribution were measured by Ellipsometric Porosimetry (EP) using Toluene as organic solvent adsorbent.

A description of these techniques, as well as a description of the employed equipment and the experimental conditions can be found in Annex II.

b) Mechanical properties characterization (Young Modulus)

The mechanical properties were measured by two methods; Surface Acoustic Wave Spectroscopy (SAWS) and Quasistatic Nanoindentation (NI). A description of these techniques can be found in Annex II.

c) Wettability characterization

The wettability behaviour was determined by Static water contact angle (CA) measurements. A description of the experimental conditions employed can be found in Annex II.

4.6. Results and Discussion

The choice of the porogen agent is of great importance in the thin-film making process^{42,43} as it impacts the quality of the film, the dielectric constant, the pore size and distribution. Therefore, two different commercial porogens were selected in order to create the porosity in the thin-films, Pluronic P-123 and Brij35.

4.6.1 Porosity, density and refractive index

Film thicknesses and refractive indexes of the porous films generated by Pluronic P-123, determined by Spectral Reflectometry are presented in Table 4.2.

Sample	Refractive Index	Dev.	Thickness (nm)	Dev.(nm)
100/0	1.477	0.001	330	2
92.5/7.5	1.365	0.002	399	1
90/10	1.344	0.006	412	4
85/15	1.293	0.002	469	6
80/20	1.259	0.002	466	1

Table 4.2. Thicknesses and refractive indexes determined for Pluronic films.

As expected, film thickness increased with the porogen concentration. This result can be explained due to the increase of the viscosity of the system produced by the

porogen. In addition, a decrease of the refractive index with the porogen percentage was observed. Figure 4.6. shows the relation between the refractive index and the porogen Pluronic P-123 concentration.

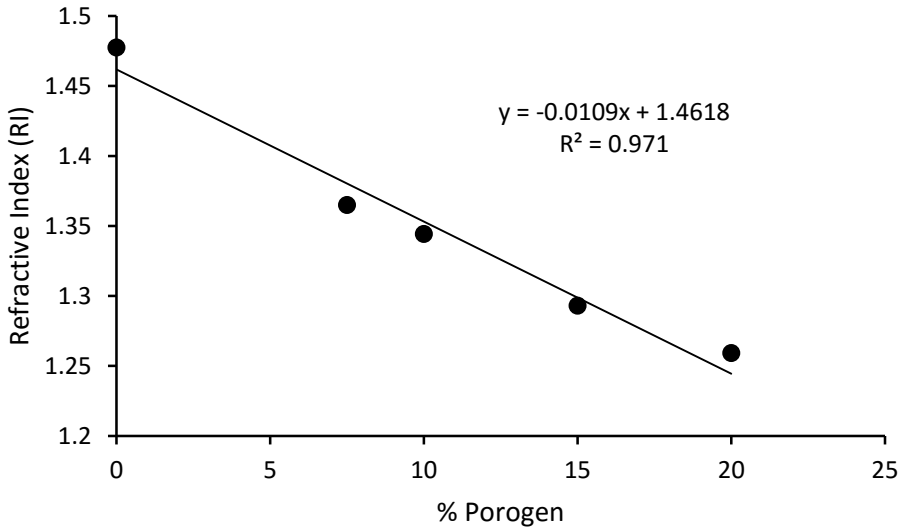


Figure 4.6. Refractive indexes of the films as a function of the percentage of porogen.

As can be seen in Figure 4.6. a linear relationship was obtained for the refractive index decay with the Pluronic P-123 concentration in the system. This result is due to porosity generated by the decomposition of the porogen agent that decreased the refractive index⁴⁰.

X-Ray studies were carried out in order to confirm these data. Figure 4.7. shows an example of an X-Ray spectrum, concretely the spectrum of the 92.5/7.5 sample and its fitting.

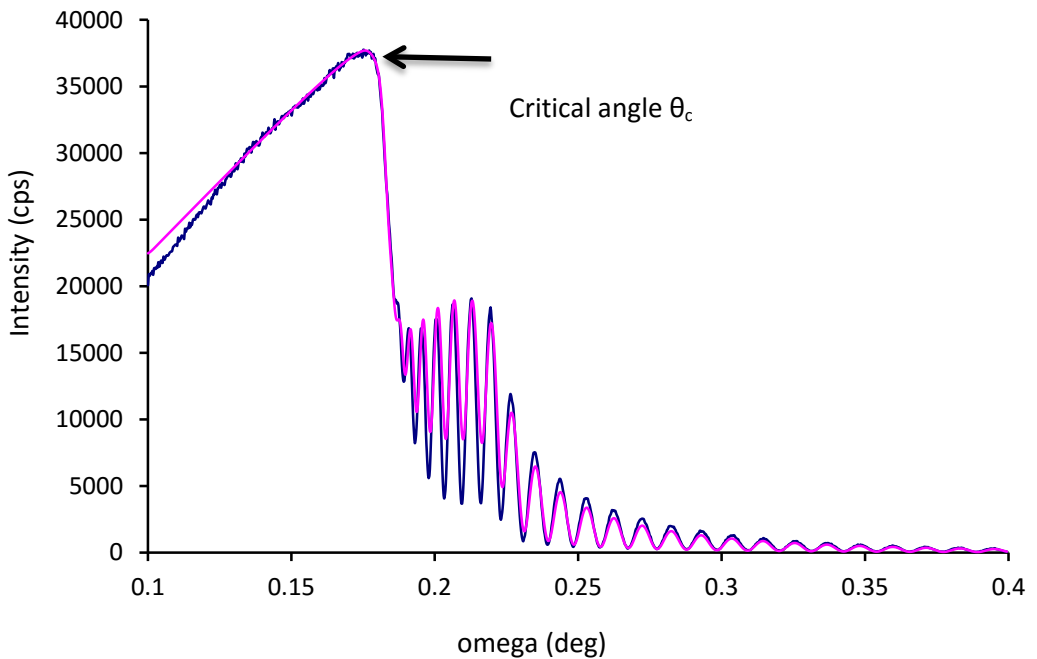


Figure 4.7. Example of the X-Ray spectrum of the 92.5/7.5 sample.

All samples were measured twice in order to determine the reproducibility of the synthesis. From the point where the intensity fell, the critical angle was calculated. This angle could be related with the film density. In addition, fitting the interference bands, the film thickness could be determined. Film thicknesses and density of the porous films, determined by X-Ray studies are presented in Table 4.3.

As expected, the film density decreased with the Pluronic P-123 concentration. The linear dependence between these two parameters can be seen in Figure 4.8. These results indicate that the density of the film can be tailored with the porogen concentration.

Sample	Density (g/cm ³)	Dev. (g/cm ³)	Thickness (nm)	Dev.(nm)
100/0	1.49	0.03	328	1
92.5/7.5	1.14	0.002	411	3
90/10	1.09	0.005	469	6
85/15	0.94	0.001	466	3
80/20	0.84	0.001	398	1

Table 4.3. Summary of the X-Ray results for the pluronic made porous films.

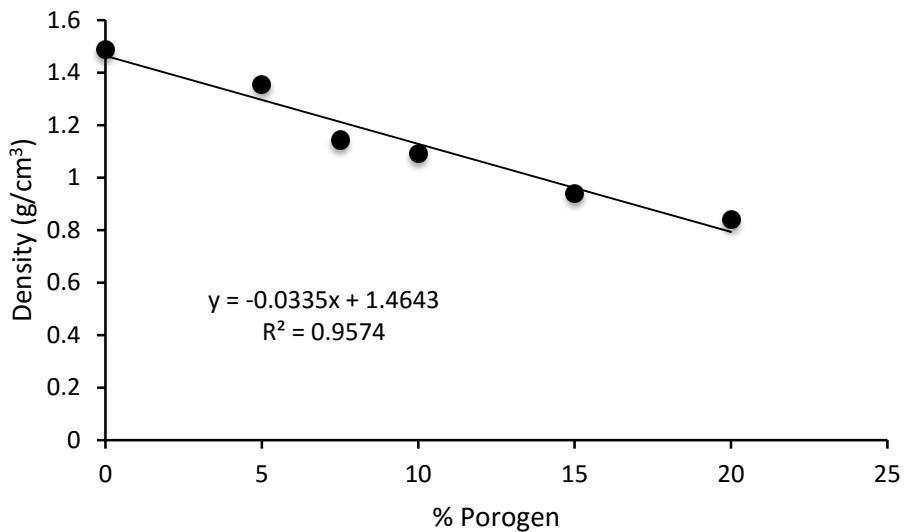


Figure 4.8. Density of the films determined by X-Ray analysis as a function of porogen (Pluronic P-123) percentage.

Porous films were also obtained using Brij35 porogen. The film characterization data obtained by Spectral Reflectometry and X-Ray studies are summarized in Table 4.4.

Sample	Refractive Index	Dev.	Thickness (nm) SR	Dev. (nm)	Density (g/cm ³)	Dev. (g/cm ³)	Thickness (nm) XRR	Dev. (nm)
100/0	1.479	0.001	338	2	1.49	0.01	338	3.7
95/5	1.434	0.001	335	1	1.36	0.008	332	0.5
92.5/7.5	1.420	0.002	331	1	1.32	0.004	329	0.9
90/10	1.405	0.001	332	0.5	1.28	0.004	331	0.4
87.5/12.5	1.383	0.001	338	2	1.22	0.001	338	1.7
85/15	1.370	0.002	333	0.5	1.18	0.006	332	1.0
82.5/17.5	1.350	0.001	340	0.5	1.12	0.003	339	0.4
80/20	1.334	0.001	315	0.5	1.07	0.001	313	0.5
77.5/22.5	1.319	0.002	319	0.5	1.02	0.003	318	0.4
75/25	1.303	0.002	321	0.5	0.96	0.01	321	0.4
70/30	1.271	0.002	336	0.5	0.87	0.003	336	0.7
65/35	1.245	0.002	349	0.5	0.79	0.001	349	0.8

Table 4.4. Summary of refractive index, thickness and density of the Brij35 films.

As expected, the density and the refractive indexes decreased with the porogen concentration. As in the case of the films generated with Pluronic P-123 porogen, linear dependence was observed for both, refractive index and density as a function of the porogen concentration, as shown in Figure 4.9.

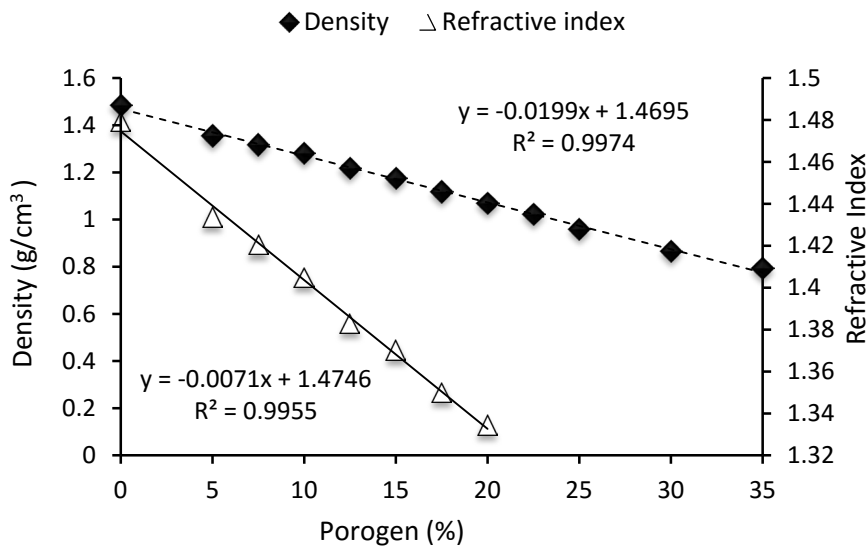


Figure 4. 9. Density and refractive indexes of the Brij35 films as a function of the porogen concentration.

Finally, the EP studies were performed to determine the porosity and the size of the pores present in the system. In order to determine that, the Toluene adsorption-desorption experiments were made. Figures 4.10. and 4.11. show an example of the information obtained by this method.

Figure 4.10. shows the adsorption-desorption of Toluene as a function of the exercised relative pressure. Using these data and applying the Kelvin model for micropores and Dubonin-Radushkevich model for mesopores, the pore size and porosity was calculated (Figure 4.11.).

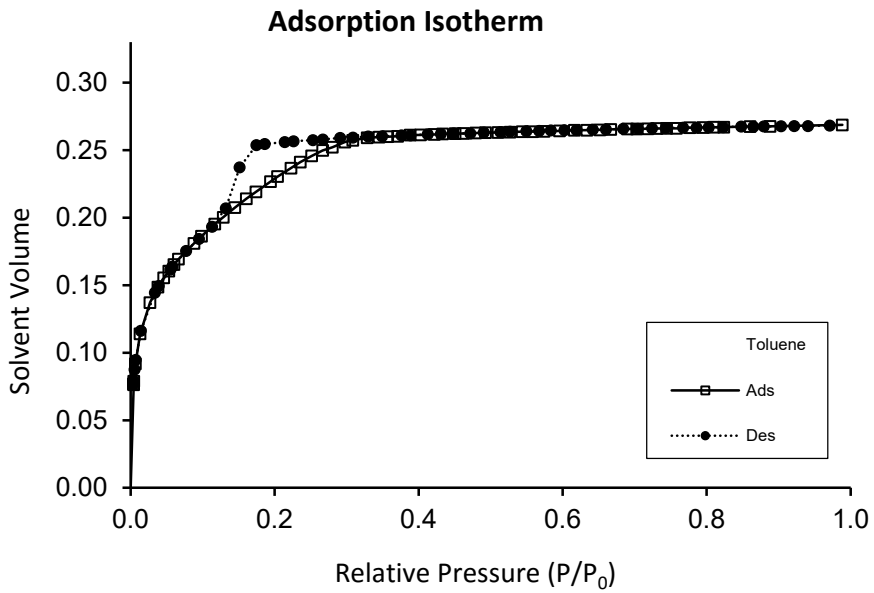


Figure 4.10. Example of the EP graph of adsorption-desorption measured with Toluene as a adsorbant.

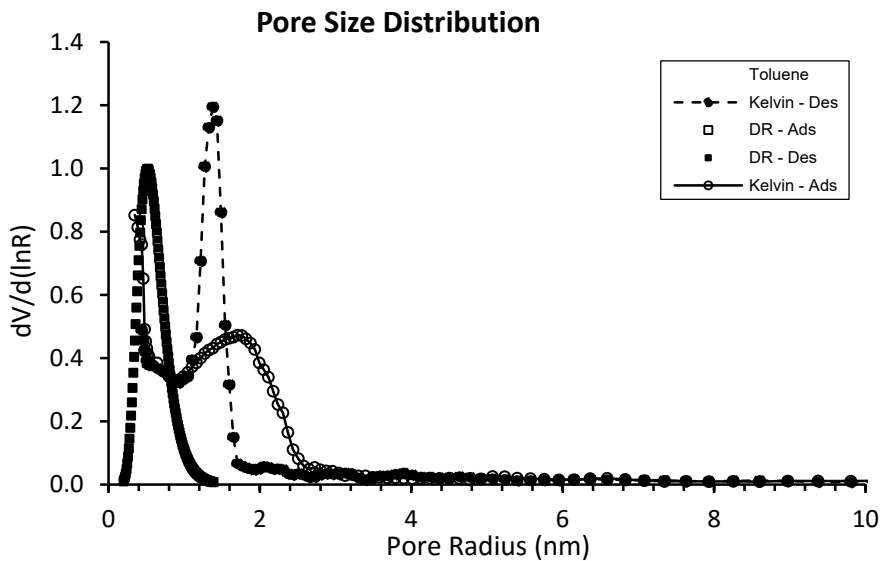


Figure 4.11. Pore size distribution determined by the EP study using Kelvin and Dubinin-Radushkevich models.

Table 4.5. and Table 4.6. show the porosity and the pore size for Pluronic P-123 and Brij35 porous film respectively.

Sample	Porosity (%)	Dev. (%)	Micropore (nm)	Dev. (nm)	Mesopore (nm)	Dev. (nm)
100/0	9.6	0.5	0.32	0.04	0.39	0.03
92.5/7.5	26.9	2	0.52	0.03	1.38	0.03
90/10	31	1	0.54	0.05	1.95	0.05
85/15	40.2	1.4	0.65	0.04	3.13	0.05
80/20	44.6	2	0.69	0.05	3.21	0.06

Table 4.5. Summary of the porosity results determined by EP analysis for the films generated with Pluronic P-123 porogen.

As can be seen in both Tables, the films generated by Sol-Gel without any porogen, had a small percentage of porosity. This percentage increased linearly with the concentration of the porogen in the system.

A comparison between the two porogens used for creating pores in the thin-film is shown in Figure 4.12.

As can be seen in Figure 4.12., in both cases the porosity increased linearly with the amount of the porogen. In addition, the increase was more pronounced in the case of Pluronic P-123 porogen. This result can be explained from the basis of the higher molecular weight of Pluronic P-123 in comparison with Brij35.

Sample	Porosity (%)	Dev. (%)	Micropore (nm)	Dev. (nm)	Mesopore (nm)	Dev. (nm)
100/0	6.4	0.3	0.17	0.03	0.39	0.03
95/5	15.0	1	0.30	0.04	0.46	0.03
92.5/7.5	17.6	0.6	0.31	0.04	0.46	0.03
90/10	19.5	0.4	0.34	0.03	0.46	0.05
87.5/12.5	23.9	0.5	0.42	0.05	0.50	0.04
85/15	25.2	0.7	0.46	0.04	0.73	0.04
82.5/17.5	29.4	0.4	0.53	0.04	0.93	0.04
80/20	31.1	0.5	0.56	0.05	0.99	0.05
77.5/22.5	34.2	0.3	0.60	0.06	1.16	0.04
75/25	37.3	0.8	0.63	0.05	1.27	0.05
70/30	43.3	1	0.72	0.04	1.43	0.04
65/35	48.4	0.9	0.75	0.05	1.49	0.04

Table 4. 6. Summary of the porosity results determined by EP analysis for the films generated with Brij35.

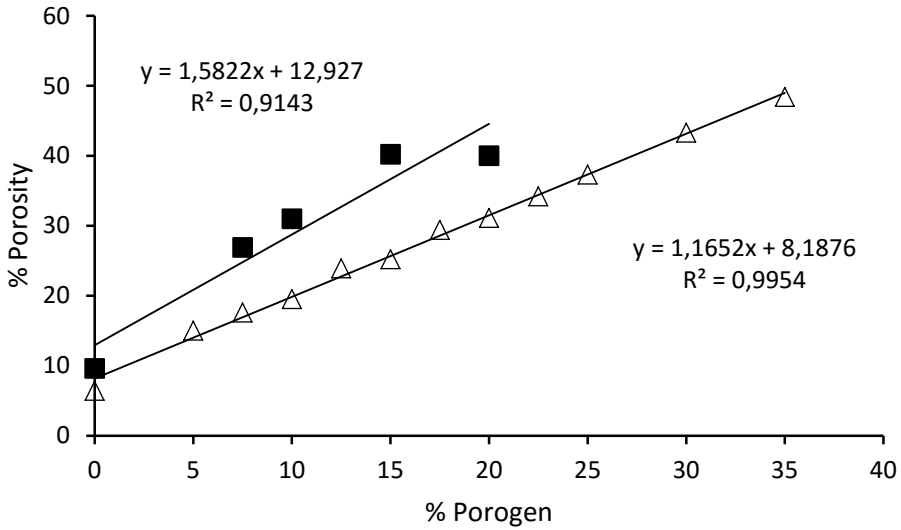


Figure 4.12. The relation of the percentage of porosity as a function of the porogen in the formulation for the both porogen agent (Pluronic P-123 in square and Brij35 in triangle).

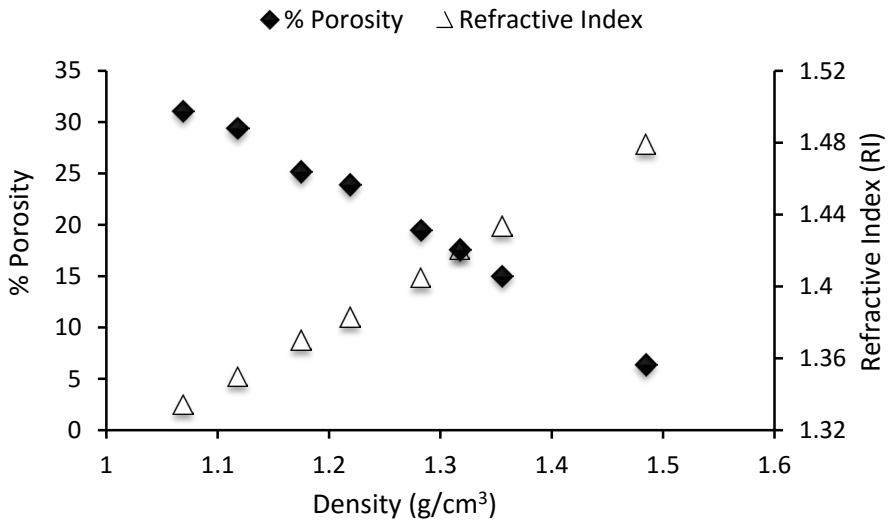


Figure 4.13. Porosity and refractive index as a function of the density for films obtained from both porogens.

The pore size increased with the amount of porogen. In addition, for the same porogen concentration, the sample generated using Pluronic P-123 showed higher pore size than the sample generated using Brij35.

For both systems a linear dependence for the porosity and the refractive index with the porogen concentration was found. Figure 4.13. shows the percentage of the porosity and the refractive index as a function of the density for both systems. As can be observed in Figure 4.13., a linear dependence was observed in both cases.

4.6.2. Mechanical properties characterization (Young Modulus)

a) Pluronic P-123

As previously discussed, two methods were chosen to determine the Young Modulus of the system, the SAWS and the Quasi-Static Nanoindentation.

Figure 4.14. shows the Young Modulus obtained by SAWS as a function of film density. As can be seen, the Young modulus increased linearly with the density of the film. The loss of the mechanical properties of the porous films can be related to the presence of the pores. It is worth mentioning that the linear dependence between the density and the Modulus has also been observed in literature⁴¹ for systems generated with carbon bridges containing alkoxy silanes, as studied in the present work. However, for alkoxy silanes without these bridges, according to literature results, a power law dependence of the Modulus with the density has been described. This result can be explained taking into consideration the decrease in the network connectivity that happens in the non-carbon bridged organosilanes.

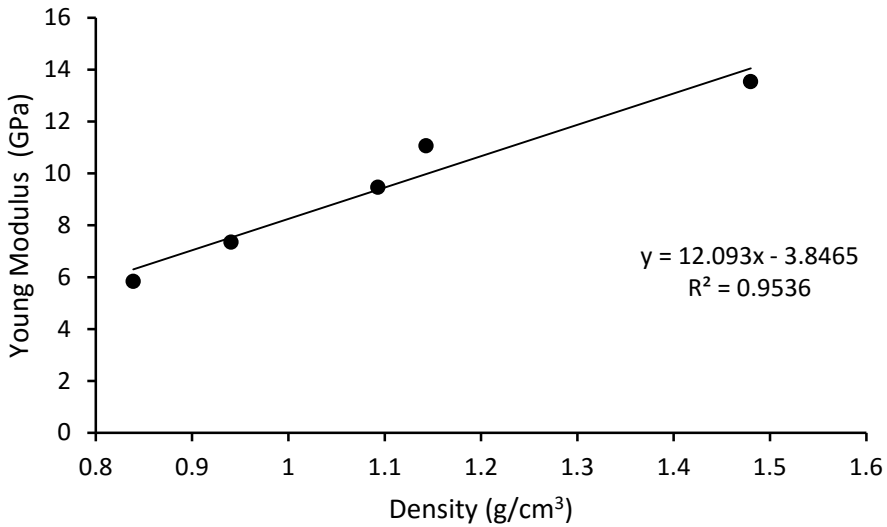


Figure 4.14. Young Modulus determined by SAWS technique as a function of the material's density.

Figure 4.15. shows the Young Modulus determined by Nanoindentation as a function of the density of the films.

As can be seen, a linear dependence was also obtained when the nanoindentation method was used to determine the Young Modulus. The data obtained by the two methods are compared in the Table 4.7.

For the samples containing low porosity, both methods gave rise to similar values of the Young Modulus. However, for the sample 80/20, which presented high porosity, the value obtained by NI was noticeably higher than the obtained by SAWS technique. This result can be explained from the basis that the porosity was collapsed during the NI measure generating a densification in the system. This result emphasizes that the nanoindentation technique is not appropriate to calculate the modulus of highly porous materials.

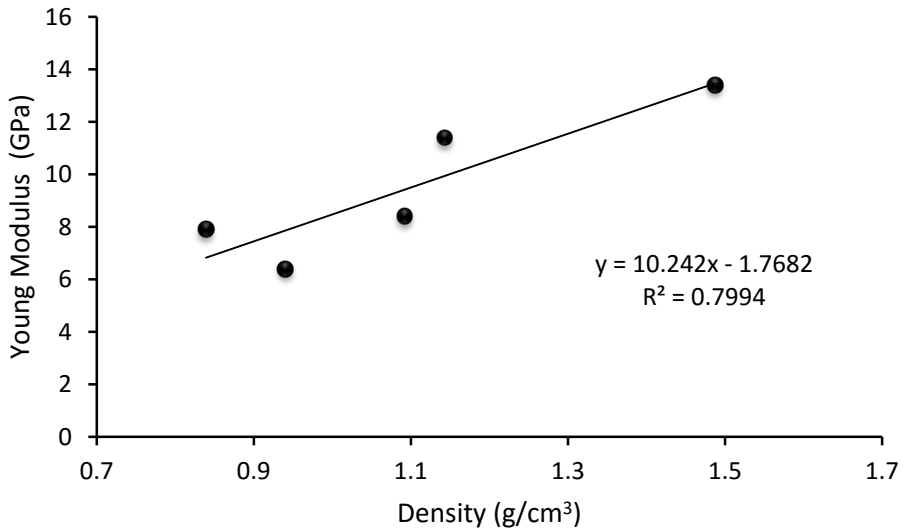


Figure 4.15. Young Modulus calculated by nanoindentation studies as a function of the density.

Sample	E' SAWS (GPa)	Dev (GPa)	E' NI (GPa)	Dev (GPa)	ΔE (%)
100/0	13.5	2	13.4	0.4	1
92.5/7.5	11.1	0.5	11.4	0.5	3
90/10	9.3	0.5	8.4	0.8	10
85/15	7.1	0.4	6.4	0.6	10
80/20	5.7	0.3	7.9	0.8	40

Table 4.7. Comparison between the Young Modulus determined by SAWS and NI techniques.

b) Brij35 porogen

Figure 4.16. shows the Young Modulus as a function of density measured by SAWS and NI techniques of all formulations synthesized with the porogen Brij35.

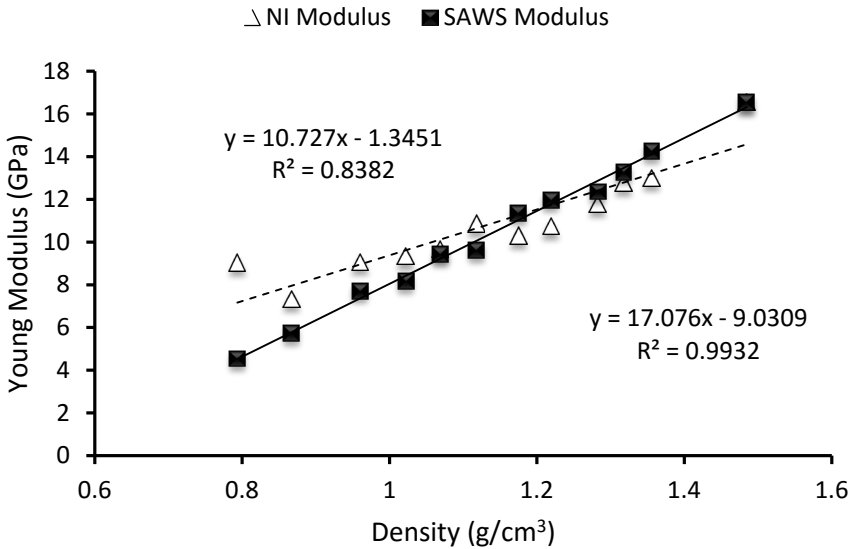


Figure 4.16. Young Modulus determined by SAWS and NI as a function of density.

As can be seen, in both cases the Young Modulus decreased with the presence of the porogen in the formulation. The decrease was very similar in both cases. However, when the percentage of porogen was high (the porosity of the system was high too) the results between both techniques are different. That could be explained due to the densification of the system when the tip of the nanoindenter penetrated into the film.

c) Comparison of both systems

Figure 4.17. shows the variation of the Young Modulus determined by SAWS as a function of density for both porogens.

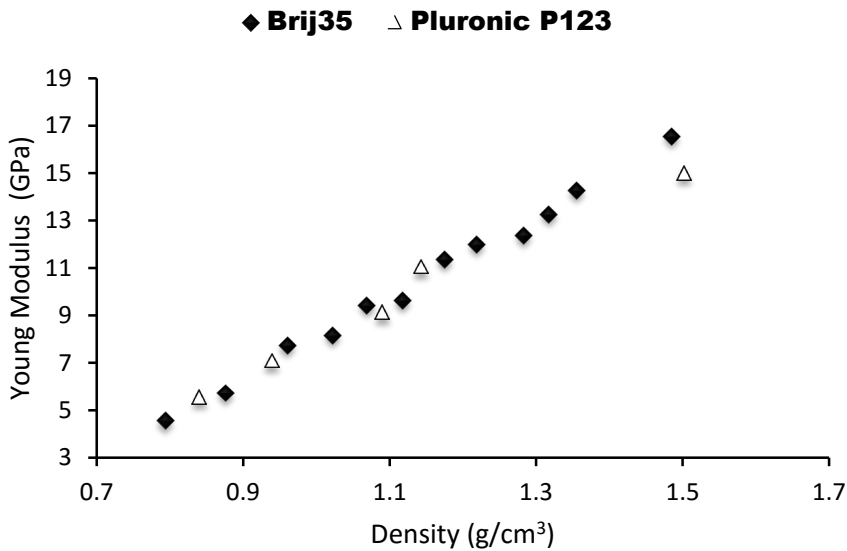


Figure 4.17. The Young Modulus as a function of the density for both porogens used in the study (Brij35 and Pluronic P-123).

As can be seen in Figure 4.17., the porogen used to generate the porosity did not have any influence in the mechanical properties. That can be explained taking into account that both porogens gave rise to pores of similar size and distribution.

4.6.3. Wettability behaviour

The wetting behaviour of the porous surfaces is also of great importance in some of their applications. Water contact angle measurements were performed in order to evaluate this property. Table 4.8. shows the results obtained for dynamic measurements for the films obtained with Pluronic P-123 porogen.

Sample	Angle θ_{av} (°)	σ_{n-1} (°)	Angle θ_r (°)	σ_{n-1} (°)	Hysteresis (°)
100/0	21	2	17	3	4
90/10	15	2	14	3	1
80/20	12	2	11	2	1

Table 4.8. Advancing and receding contact angle values for the films generated with different amounts of Pluronic P-123.

As can be observed, all the samples showed low contact angle values, characteristic of hydrophilic surfaces. As the films were generated by acid Sol-Gel process, the surface contained silanol groups and was therefore, hydrophilic.

In addition, a slight decrease in the contact angle with the porogen concentration in the formulation was observed.

Table 4.9. shows the results obtained for dynamic contact angle measurements for the films obtained using Brij35 porogen.

As in the samples obtained using Pluronic P-123 porogen, low contact angle values were obtained, which indicated that the surface of the samples was hydrophilic.

Sample	Angle θ_{av} (°)	σ_{n-1} (°)	Angle θ_r (°)	σ_{n-1} (°)	Hysteresis (°)
100/0	20	1	18	3	2
85/15	14	2	13	2	1
70/30	10	3	9	4	1

Table 4.9. Advancing and receding contact angle values for the films generated with different amounts of Brij35.

4.7. Conclusions

Finally, the most relevant conclusions for this chapter are summarized below.

- ✓ Porous silica films can be obtained by acid Sol-Gel reaction accompanied by a porogen decomposition.
- ✓ Film density and refractive indexes decrease linearly with the porogen concentration. Comparing the two porogens, for the same concentration, Pluronic P-123 is more effective than Brij35.
- ✓ Contrary to what is shown in literature, the Young Modulus increases linearly with the density of the system. This result can be explained due to

the high network connectivity that imparts the employed organosilicate, with carbon bridging units.

- ✓ At low porosities, the Nanoindentation method is appropriate to determine the Young Modulus of the porous materials. At high porosities, however, the densification of the material during the measurement gives rise to erroneous values of the Young Modulus.

4.8. Bibliography

1. Volksen, W., Miller, R. D. & Dubois, G. Low dielectric constant materials. *Chem. Rev.* **110**, 56–110 (2010).
2. Koshida, N. & Koyama, H. Visible electroluminescence from porous silicon. *Appl. Phys. Lett.* **60**, 347–349 (1992).
3. Ratchford, D., Yeom, J., Long, J. P. & Pehrsson, P. E. Influence of inhomogeneous porosity on silicon nanowire Raman enhancement and leaky mode modulated photoluminescence. *Nanoscale*. **7**, 24–27 (2015).
4. Djurfors, B., Broughton, J. N., Brett, M. J. & Ivey, D. G. Microstructural characterization of porous manganese thin films for electrochemical supercapacitor applications. *J. Mater. Sci.* **38**, 4817–4830 (2003).
5. Ma, Y., *et al.* Titanium Dioxide-Based Nanomaterials for Photocatalytic Fuel Generations. *Chem. Rev.* **114**, 9987-10043 (2014).
6. Huang, S. Y., *et al.* Charge recombination in dye-sensitized nanocrystalline TiO₂ solar cells. *J. Phys. Chem. B.* **101**, 2576–2582 (1997).
7. Shin, H. C. & Liu, M. Three-dimensional porous copper-tin alloy electrodes for rechargeable lithium batteries. *Adv. Funct. Mater.* **15**, 582–586 (2005).

8. Bertero, M., Puente, G. & Sedran, U. Products and coke from the conversion of bio-oil acids, esters, aldehydes and ketones over equilibrium FCC catalysts. *Renewable Energy*. **60**, 349–354 (2013).
9. Bhawe, Y., *et al.* Effect of cage size on the selective conversion of methanol to light olefins. *ACS Catal.* **2**, 2490–2495 (2012).
10. Jin, Z., *et al.* Application of nano-crystalline porous tin oxide thin film for CO sensing. *Sens. Actuators. B.* **52**, 188–194 (1998).
11. Pacholski, C. Photonic crystal sensors based on porous silicon. *ACS Sensors*. **13**, 4694–713 (2013).
12. Moshnikov, V. A., *et al.* Porous silicon with embedded metal oxides for gas sensing applications. *J. Non-Cryst. Solids*. **358**, 590–595 (2012).
13. Makal, T. A., Li, J. R., Lu, W. & Zhou, H. C. Methane storage in advanced porous materials. *Chem. Soc. Rev.* **41**, 7761–7779 (2012).
14. Knežević, N. Ž., Ruiz-Hernandez, E., Hennink, W. E. & Vallet-Regi, M. Magnetic mesoporous silica-based core/shell nanoparticles for biomedical applications. *RSC Adv.* **3**, 9584–9593 (2013).
15. Li, Z., *et al.* Mesoporous silica nanoparticles in biomedical applications. *Chem. Soc. Rev.* **41**, 2590–2605 (2012).
16. Luwang Laiva, A., *et al.* Novel and simple methodology to fabricate porous and buckled fibrous structures for biomedical applications. *Polymer*. **55**, 5837–5842 (2014).
17. Castricum, H. L., *et al.* Tuning the nanopore structure and separation behavior of hybrid organosilica membranes. *Microporous Mesoporous Mater.* **185**, 224–234 (2014).
18. Agirre, I., *et al.* Hybrid organosilica membranes and processes: Status and outlook. *Sep. Purif. Technol.* **121**, 2–12 (2014).
19. Bloch, E. D., *et al.* Hydrocarbon Separations in a Metal-Organic Framework with Open Iron (II) Coordination Sites. *Science*. **335**, 1606–1611 (2012).

20. Thomas, A., Goettmann, F. & Antonietti, M. Hard templates for soft materials: Creating nanostructured organic material. *Chem. Mater.* **20**, 738–755 (2008).
21. Wan, Y., Shi, Y. & Zhao, D. Supramolecular aggregates as templates: Ordered mesoporous polymers and carbons. *Chem. Mater.* **20**, 932–945 (2008).
22. Velev, O. D. & Kaler, E. W. Structured porous materials via colloidal crystal templating: from inorganic oxides to metals. *Adv. Mater.* **12**, 531–534 (2000).
23. Hoa, M., Lu, M. & Zhang, Y. Preparation of porous materials with ordered hole structure. *Adv. Colloid Interface Sci.* **121**, 9–23 (2006).
24. Yang, S. J., *et al.* MOF-Derived Hierarchically Porous Carbon with Exceptional Porosity and Hydrogen Storage Capacity. *Chem. Mater.* **24**, 464–470 (2012).
25. Wu, R., *et al.* MOF-templated formation of porous CuO hollow octahedra for lithium-ion battery anode materials. *J. Mater. Chem. A.* **1**, 11126–11129 (2013).
26. Zhou, H. C., Long, J. R. & Yaghi, O. M. Introduction to Metal–Organic Frameworks. *Chem. Rev.* **112**, 673–674 (2012).
27. Chen, Z., Wang, X., Giuliani, F. & Atkinson, A. Microstructural characteristics and elastic modulus of porous solids. *Acta Mater.* **89**, 268–277 (2015).
28. Sing, K. S., *et al.* Reporting Physisorption data for Gas/Solid Systems with Special Reference to the Determination of Surface Area and Porosity. *Pure Appl. Chem.* **57**, 603–619 (1985).
29. Krishna, R. Separating mixtures by exploiting molecular packing effects in microporous materials. *Phys. Chem. Chem. Phys.* **17**, 39–59 (2015).
30. Krishna, R. Evaluation of procedures for estimation of the isosteric heat of adsorption in microporous materials. *Chem. Eng. Sci.* **123**, 191–196 (2015).
31. Linares, N., *et al.* Mesoporous materials for clean energy technologies. *Chem. Soc. Rev.* **43**, 7681–7717 (2014).

32. Kelly, J. A., *et al.* Evaluation of form birefringence in chiral nematic mesoporous materials. *J. Mater. Chem. C* **2**, 5093-5097 (2014).
33. Fan, W. Q. *et al.* Titanium dioxide macroporous materials doped with iron: synthesis and photo-catalytic properties. *Cryst. Eng. Comm.* **16**, 116-122 (2014).
34. Yiotis, A. G., Salin, D. & Yortsos, Y. C. Pore Network Modeling of Drying Processes in Macroporous Materials: Effects of Gravity, Mass Boundary Layer and Pore Microstructure. *Transp. Porous Media.* **110**, 175-196 (2015).
35. Gaikwad, P., *et al.* Photon transport in cylindrically-shaped disordered meso-macroporous materials. *Opt. Express.* **22**, 7503–13 (2014).
36. Nogami, M. Proton conductivity in sol–gel-derived P_2O_5 – TiO_2 – SiO_2 glasses. *Solid State Ionics.* **166**, 39–43 (2004).
37. Gawel, B., Gawel, K. & Oye, G. Sol-Gel synthesis of non-silica monolithic materials. *Materials.* **3**, 2815–2833 (2010).
38. Volentiru, E., *et al.* Silica sol – gel protective coatings against corrosion of zinc substrates. *Period. Polytech. Chem. Eng.* **58**, 61–66 (2014).
39. Shea, K. J. & Loy, D. A. Bridged polysilsesquioxanes. Molecular-engineered hybrid organic-inorganic materials. *Chem. Mater.* **13**, 3306–3319 (2001).
40. Dubois, G., *et al.* Superior mechanical properties of dense and porous organic/inorganic hybrid thin films. *J. Sol-Gel Sci. Technol.* **48**, 187–193 (2008).
41. Dubois, G., *et al.* Molecular network reinforcement of Sol-Gel glasses. *Adv. Mater.* **19**, 3989–3994 (2007).
42. Hedrick, J. L., *et al.* Application of complex macromolecular architectures for advanced microelectronic materials. *Chem. Eur. J.* **8**, 3308–3319 (2002).
43. Ree, M., Yoon, J. & Heo, K. Imprinting well-controlled closed-nanopores in spin-on polymeric dielectric thin films. *J. Mater. Chem.* **16**, 685-697 (2006).

44. Saha, R. & Nix, W. D. Effects of the substrate on the determination of thin film mechanical properties by nanoindentation. *Acta Mater.* **50**, 23–38 (2002).

Chapter 5

General conclusions

5. Conclusions

The main objective of the present thesis was centred in obtaining functional materials with specific applications as anti-biofouling, self-cleaning and anti-reflective coatings. These types of materials present a great academic and commercial interest.

All the systems described in this thesis are hybrid organic/inorganic materials based on Silica that try to make a contribution to the development of economically and technically competitive coatings. The main conclusions that can be extracted for the different coatings are summarized below.

For the anti-biofouling coatings

- ✓ Polyurethane-Siloxane thermoset copolymers present a phase separated structure that depends on the reaction conversion and casting temperature. The phase separation gives rise to a higher roughness that in combination with a higher siloxane surface concentration increases the water contact angle, and consequently the hydrophobicity of the samples.

- ✓ Bovine Serum Albumin (BSA) adsorption is reduced if the sample is phase separated. Nanostructured samples containing low siloxane concentration have potential applications as anti-biofouling coatings.

- ✓ The development of coatings with good anti-biofouling properties demands a rigorous control of the phase separation process.

For the self-cleaning surfaces

- ✓ Hydrophobic silica nanoparticles obtained by Tetraethyl orthosilicate (TEOS) and Hexadecyl trimethoxy silane (HDTMS) base catalyzed hydrolysis and condensation using a two-step process can be used to impart hydrophobicity to polymeric matrixes.
- ✓ The introduction of silica nanoparticles in Poly(methyl methacrylate) increases the contact angle of the generated surfaces. Coatings obtained by spraying, present contact angles higher than 140° , low sliding angles and are, therefore, very good candidates to be used in the field of self-cleaning coatings.
- ✓ However, the films containing nanoparticles are fragile and opaque which limits their use.

For the anti-reflective coatings

- ✓ Porous silica surfaces can be obtained by acid catalyzed Sol-Gel reaction accompanied by porogen decomposition. The film density and refractive index can be controlled by the porogen concentration, which allows the tuning of these properties.
- ✓ The Young Modulus decreases linearly with the film density. This result can be explained with the high network connectivity that imparts the employed organosilicate with carbon bridging units.
- ✓ At high porosities, the nanoindentation technique is not appropriate to calculate the Young Modulus of the prepared coatings.

As a final conclusion it can be emphasized that the results of this thesis have demonstrated that the Silicon chemistry offers the possibility of prepare a wide array of functional coatings tailored to a variety of uses and environments. In the last years, the development of functional “smart” coatings is a subject of growing interest. The anti-biofouling, self-cleaning and anti-reflection coatings described in this work try to make a contribution to establish the relation between the obtained surface morphology and the properties of the coating.

Finally, it must be pointed out that in the three types of presented coatings there are obviously aspects that have not been covered in this thesis and constitute plans regarding further future research topics.

In relation to anti-biofouling surfaces, more work should be done to determine the anti-biofouling abilities of these coatings. Regarding the self-cleaning materials it is clear that the obtained surfaces present good properties but that there are still some problems to solve, such as the film appearance and the durability of the self-cleaning property. In relation to the anti-reflecting coatings, the results of this thesis constitute the initial steps of the research group in this area, which presumably will continue in future works.

Annex I

Summary
Resumen

Los recubrimientos son aplicados sobre diferentes superficies con fines fundamentalmente decorativos y de protección. Sin embargo, hoy en día el mercado de estos materiales está siendo sometido a unas especificaciones cada vez más severas. Así, los recubrimientos actuales deben, además de ser decorativos y protectores del sustrato, impartir al mismo otras propiedades adicionales como por ejemplo baja adherencia a los microorganismos, facilidad de limpieza y propiedades auto-reparables. El desarrollo de este tipo de materiales, conocidos bajo el nombre de “recubrimientos funcionales” requiere del control de las propiedades tanto físicas (fundamentalmente de la morfología) como químicas de las superficies generadas. Dentro de este campo, la presente tesis pretende realizar una aportación al desarrollo de tres tipos de recubrimientos “funcionales” que brinden a los mismos resistencia a los microorganismos (anti-biofouling), propiedades autolimpiables (self-cleaning) y propiedades anti-reflejantes (anti-reflecting).

El desarrollo de los recubrimientos funcionales ha estado muy ligado a la modificación de la mojabilidad de los materiales. Así, las superficies hidrófobas, son aquellas sobre las que el agua forma ángulos de contacto superiores a 90° . Especialmente interesantes son las superficies sobre las que el agua forma ángulos superiores a 150° , conocidas como “superhidrofóbas”. Estas superficies, cuyo ejemplo más conocido lo constituyen las hojas de la flor de Lotto, presentan importantes aplicaciones en el campo de los recubrimientos autolimpiables y anti contaminación biológica.

Los materiales que presentan una baja energía superficial como los fluoropolímeros y las siliconas dan lugar a superficies hidrófobas sobre las que el agua presenta ángulos de contacto elevados. Sin embargo, mediante la “química” no es posible obtener ángulos de contacto superiores a 120° , que sólo se logran si la superficie es además rugosa. Mediante la combinación de una apropiada química y morfología

superficial es posible obtener superficies sobre las que el agua presenta ángulos de contacto superiores a 150° . Las propiedades que pueden presentar este tipo de materiales han generado un gran interés, por lo que el desarrollo de metodologías para la obtención de los mismos ha constituido, en los últimos años, uno de los grandes retos tecnológicos del campo de los recubrimientos.

El primero de los recubrimientos hidrófobos que se exploró en este trabajo fueron los copolímeros de bloque Poliuretano/Poli(dimetil siloxano) que dan lugar a la formación espontánea de separación de fases entre sus componentes. Este tipo de recubrimientos, cuyas propiedades anti contaminación biológica ya han sido contrastadas, presentan una superficie hidrófoba debido tanto a la migración del componente siloxano a la superficie como a la rugosidad que el mismo le imparte.

Para la obtención de estos copolímeros se utilizó un Diisocianato cicloalifático (el Diisocianato de Isoforona, IPDI), y dos polioles, uno de ellos basado en Poli(dimetil siloxano) (PDMS) y el otro en Policaprolactona (PCL). Se realizaron diversas síntesis variando la relación entre los polioles. Los copolímeros estudiados generaban espontáneamente una separación de fases que aumentaba la rugosidad del sistema como se pudo comprobar mediante Microscopia de Fuerza Atómica (AFM).

Las propiedades hidrófobas de las superficies obtenidas se evaluaron mediante medidas del ángulo de contacto estático, y los valores de histéresis del mismo. Se comprobó que la hidrofobicidad del sistema dependía en mayor medida de la rugosidad que de la concentración de siloxano en la superficie (medida por espectroscopia FTIR). Así, los mayores ángulos de contacto se obtuvieron para los filmes que presentaron mayor rugosidad.

La pretendida restricción en la capacidad de adhesión de microorganismos (biofouling) de estas películas se determinó utilizando medidas de adsorción de

proteínas, empleando para ello técnicas convencionales como la Espectroscopia Ultravioleta (UV) y también técnicas más sofisticadas y menos habituales como la Microbalanza de Cristal de Cuarzo con Disipación (QCM-D) y la Resonancia Superficial de Plasmones (SPR).

Dichas técnicas demostraron la mejora de la restricción de la adhesión de los microorganismos en los filmes obtenidos que presentaban separación de fases. Se consiguió demostrar la relación entre la rugosidad del sistema producida por la separación de fases y sus propiedades superficiales como su mojabilidad y la adhesión de proteínas.

Dentro de la línea de los recubrimientos hidrófobos la presente tesis contempló la síntesis de materiales que presentaran efecto auto-limpiable. Para obtener este tipo de superficies, la estrategia a seguir consistió en introducir nanopartículas inorgánicas de naturaleza hidrófoba en el seno de matrices poliméricas acrílicas.

En dicha vía, las nanopartículas fueron previamente sintetizadas mediante el proceso Sol-Gel del Tetraetil Ortosilicato (TEOS) para posteriormente en una segunda etapa funcionalizarlas consiguiendo unas nanopartículas de carácter hidrófobo. Se sintetizaron nanopartículas de diversos tamaños variando la cantidad de amoníaco y agua presente en el sistema. Para dicha obtención, se utilizó el sistema de síntesis asistida por microondas como método de calentamiento del proceso. El uso del microondas ha sido un avance en la investigación ya que mejora la conversión y reduce los tiempos de síntesis.

Una vez sintetizadas y caracterizadas las nanopartículas generadas, el objetivo fue la introducción de dichas partículas en una matriz polimérica. Se obtuvieron películas polímero/nanopartículas con diversos porcentajes. Por ello, se utilizaron los

métodos de disolución/evaporación (Casting), el pulverizado sobre la superficie (sprayado) y el spin-coating.

Según los datos obtenidos experimentalmente, las superficies obtenidas mediante disolución/evaporación (Casting) y el pulverizado fueron las que mejores propiedades de mojabilidad demostraron. Las películas obtenidas mediante spin-coating no presentaron ángulos de contacto elevados. Sin embargo, en las películas conteniendo un 33 % de nanopartículas obtenidas mediante disolución/evaporación se lograron ángulos de contacto de 137 °. Desafortunadamente estas películas eran excesivamente frágiles, y difíciles de manejar. Los mejores resultados se obtuvieron pulverizando nanopartículas sobre películas acrílicas lo que originó superficies con ángulos de contacto superiores a 140 °.

El último tipo de los recubrimientos funcionales que se exploraron fueron aquellos destinados a dar lugar a materiales con características anti-reflejantes. Para obtener estas propiedades, las películas deben presentar un índice de refracción inferior al del sustrato lo que se puede lograr introduciendo porosidad en las mismas. La estrategia seguida para obtener estos materiales consistió en realizar el proceso Sol-Gel de un organosilano (Bis (trietoxisilil) etano, (BTSE)) en presencia de un porógeno polimérico. Tras el proceso Sol-Gel, realizado en medio ácido, el porógeno se descompuso térmicamente para dar lugar al material poroso deseado.

Se utilizaron dos agentes porógenos diferentes, uno basado en Polióxido de etileno (Brij35) y el otro en un copolímero de Óxido de etileno y Óxido de propileno (Pluronic P-123). En ambos casos, se obtuvo que la porosidad de los materiales obtenidos (medida por Porosimetría Elipsométrica) aumentaba linealmente con la cantidad de porógeno utilizada, mientras que el índice de refracción disminuía linealmente. Los resultados mostraron la mayor efectividad el P-123 para la

generación de los poros, ya que para la misma cantidad de porógeno se obtuvo mayor porosidad.

La presencia de los poros hace que las superficies anti-reflejantes no presenten propiedades mecánicas adecuadas, por lo que la determinación de las mismas es un tema de gran interés. En este trabajo, se midió el módulo de Young de las superficies obtenidas mediante Nanoindentación (NI) y mediante Espectroscopia Acústica de Onda Superficial (SAWS), utilizando un nuevo protocolo establecido en el centro de IBM de Almadén donde se realizaron las medidas. A porosidades bajas los resultados obtenidos mediante ambas técnicas estaban dentro del margen de confianza (10 % de diferencia). Sin embargo, a porcentajes de porosidad elevados, se obtuvieron valores superiores mediante NI, que fueron atribuidos a la densificación que ocurre en el material como consecuencia de la penetración de la punta en la película. Dejando al lado la comparación de ambas técnicas, se observó una dependencia de disminución lineal del módulo de Young respecto a la densidad de los sistemas.

Annex II

Experimental Techniques

Annex II:

Experimental techniques

II.1.	Chemical Characterization	189
II.1.1.	Nuclear Magnetic Resonance of ^{29}Si (NMR)	189
II.1.2.	Fourier Transform Infrared Spectroscopy (FTIR)	192
II.1.3.	Elemental Analysis (EA)	193
II.2.	Thermal Characterization	194
II.2.1.	Thermogravimetric Analysis (TGA)	194
II.2.2.	Dynamic Mechanical Thermal Analysis (DMTA)	194
II.3.	Morphological characterization	195
II.3.1.	Dynamic Light Scattering (DLS)	195
II.3.2.	Electron Microscopy (EM)	195
II.3.2. a)	Scanning Electron Microscopy (SEM)	196
II.3.2. b)	Transmission Electron Microscopy (TEM)	196
II.3.3.	Atomic Force Microscopy (AFM)	197
II.3.4.	X-Ray Reflectance (XRR)	198
II.3.5.	Ellipsometric Porosimetry (EP)	200
II.4.	Mechanical properties characterization	204
II.4.1.	Nanoindentation (NI)	204

II.4.2.	Surface Acoustic Wave Spectroscopy (SAWS)	207
II.5.	Wettability properties	208
II.5.1.	Contact angle and hysteresis by goniometer	208
II.6.	Evaluation of anti-biofouling properties	209
II.6.1	Colorimetric assay for determination of protein adsorption by UV (Static Sorption Test)	210
II.6.2	Determination of protein adsorption by Surface Plasmon Resonance (SPR)	211
II.6.3	Determination of protein adsorption by Quartz Crystal Microbalance with dissipation (QCM-D)	214
II.7.	Reflection properties	216
II.7.1.	Spectral reflectometry (SR)	216
II.8.	Bibliography	216

II.1. Chemical Characterization

II.1.1. Nuclear Magnetic Resonance of ^{29}Si (NMR)

Due to the great development that the hybrid materials are experimenting in the last years^{1,2}, the Nuclear Magnetic Resonance (NMR) of ^{29}Si has become a very useful technique to characterize these kinds of materials. This is why in the last years multiple studies have been published using this technique.

As in ^1H -NMR and ^{13}C -NMR, the ^{29}Si atom changes its chemical shift depending on the chemical environment. These changes allow the characterization of all the structures that are generated around the silicon atom during the Sol-Gel process. Thus, the hydrolysis and subsequent condensation of the alkoxy silane groups that happens in the process changes the chemical environment of the silicon atom and therefore different signals are obtained for the condensed and not condensed silicon atoms. This fact enables the chemical characterization of the silica nanoparticles obtained by the Sol-Gel process.

In order to name easily all possible structures generated in the Sol-Gel process of alkoxy silanes, Lippmaa et. al³ designed a model using the following rules. The atom is called M, D, T or Q depending on the number of the oxygen atoms linked to silicon and a subscript is added to give information about the number of the oxygen atoms linked to another silicon atom as can be seen in Figure II.1.

It is to mention that the silicon nanoparticles are not soluble in the NMR solvents and therefore, solid NMR techniques must be employed to acquire the spectra of the samples.

The most employed solid NMR techniques are the called Cross Polarization (CP/MAS) and Fourier Transform Magic Angle Spinning (FT/MAS). In order to obtain

a quantitative analysis, the FT/MAS technique is preferred due to the CP/MAS results depend strongly on the experimental conditions. However, if the conditions are chosen appropriately, both techniques are suitable. In this work, the CP/MAS technique was selected to make the NMR spectra for being the most common in the research centre because it minimizes spectral acquisition time.

In this technique, the intensity of the signal in the spectrum depends on a parameter called contact time. This is the time during which the magnetization is transferred from the protons to the silicon atoms.

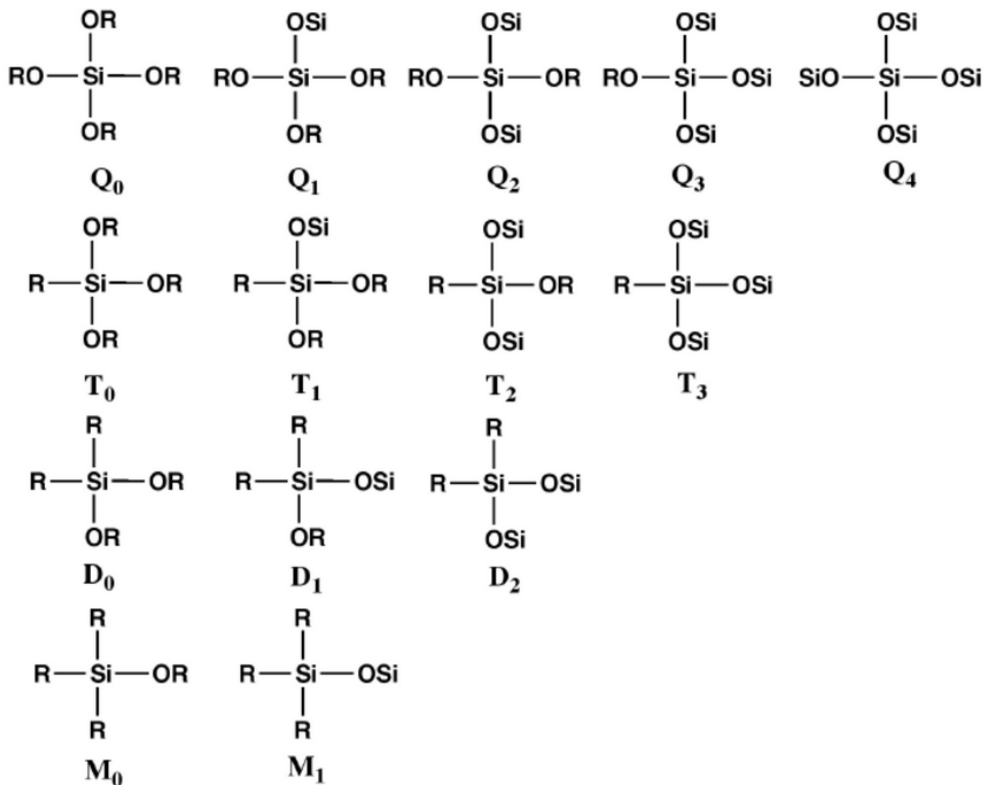


Figure II.1. Structures coexisting in the Sol-Gel process, as called by Lippmaa et al.

The dependency of the intensity of the signal as a function of the contact time is described by equation II.1:

$$M(t) = M_{cp} \left[e^{-t/T_{1\rho}^H} - e^{-t/T_{SiH}} \right] \div (1 - T_{SiH}/T_{1\rho}^H) \quad \text{Eq: II.1}$$

Where $M(t)$ is the intensity of the signal, M_{cp} is the magnetization, t is the contact time, $T_{1\rho}^H$ is the relaxation time of the spin-lattice in a rotatory system and T_{SiH} is the cross relaxation time between the ^{29}Si and ^1H spins.

This equation means that the intensity of the signal will be maximum at one contact time (t) when $T_{1\rho}^H$ and T_{SiH} have the same value for all structures. In multiple studies, these values have been measured for different structures and it has been concluded that, for the same sample, the values of the $T_{1\rho}^H$ and T_{SiH} match with the exception of the Q_4 structure.

This result could be explained due to the T_{SiH} dependence on the dipolar moment created by the ^{29}Si and ^1H spins which depends on the distance between the two atoms. As the all structures unless Q_4 have ^1H , the value of the T_{SiH} is quite similar for all of them. However, the Q_4 structures do not have any ^1H at the same distance as the other species as it can be seen in Figure II.1. Therefore, if the sample to analyse contains Q_4 kind structures, equation II.1 is not valid, and the obtained area data are not quantitative.

The results obtained in the present work are related to T and Q structures. The chemical shifts in relation with Tetramethyl Silane (TMS) of the different structures that can be generated during the Sol-Gel process are shown in Table II.1.

Structure	Chemical shift (ppm)
T ₀	-42
T ₁	-50
T ₂	-58
T ₃	-67
Q ₀	-80
Q ₁	-87
Q ₂	-94
Q ₃	-102
Q ₄	-110

Table II.1. Chemical shifts of the silicon atoms in different structures.

Following the literature and according to previous experiments of the group, Solid State NMR spectra were recorded on a Bruker 400 AVANCE III WB spectrometer 9.40T (¹H= 400 MHz).

²⁹Si CP/MAS spectra were collected by using a 4mm CP/MAS probe at a spinning of 10 KHz, using the CP pulse sequence, at 79.5 MHz, a time domain of 2K, a spectral width of 29 KHz, a contact time of 2 ms and an interpulse delay of 5 s.

II.1.2. Fourier Transform Infrared Spectroscopy (FTIR)

Fourier Transform Infrared Spectroscopy (FTIR) is a powerful technique for the analysis^{4,5}. FTIR was employed to characterize both the reagents employed, and the products obtained in this memory. This technique was also utilized to study the reaction kinetics.

All the spectra were recorded using a Nicolet 6700 spectrometer at a resolution of 2 cm^{-1} , and a total of 64 interferograms were signal averaged. The spectra were obtained from solution or dispersion casting onto KBr or KRS-5 windows.

To determine the conversion of the nanoparticles, the Infrared spectra of the dispersions were carried out using a liquid cell with KRS5 windows with a 0.1 mm path length (Spectra Tech) at a resolution of 2 cm^{-1} .

To determine the concentration of the siloxane in the surface of the copolymers, Attenuated Total Reflectance (ATR) experiments were made. These experiments were carried out using an ATR objective (Thermo Electron Corp. Infinity Replachromat) provided with a Germanium crystal mounted on a microscope (Nicolet Continuum FT-IR microscope) attached to FTIR spectrometer. A MCT detector was used. The ATR measurements were recorded at a resolution of 8 cm^{-1} and 64 scans were taken.

II.1.3. Elemental analysis (EA)

Elemental analysis is a technique that provides the total content of Carbon, Hydrogen, Nitrogen and Sulphur in a sample of organic and inorganic nature that could be solid or liquid. The element separation material is produced by high temperature combustion. In the combustion process, the sample (between 1 and 2 mg of nominal size) is encapsulated in a tin capsule. The sample is placed in the autoloader and held there until the Oxygen dose is injected. Then, the sample is dropped into the oven and the combustion occurs in an environment rich in Oxygen.

The study was performed in a LECO-932 Microanalyzer which determines the Carbon, Hydrogen, Nitrogen and Sulfur content in the silica samples.

II.2. Thermal Characterization

II.2.1. Thermogravimetric Analysis (TGA)

TGA was employed to perform the thermal characterization of the materials and to determine the wt. % of the functionalization of the silica nanoparticles. All the experiments were carried out in a TA instrument thermo balance Q 500. A two stage heating program was used. In the first stage, the sample was heated from 40 to 600 °C. at a rate of 10 °C /min using Nitrogen as a carrier gas. In the second step, heating was performed from 600 to 800 °C at a rate of 40 ° C/min, this time using Air as a carrier gas.

II.2.2. Dynamic Mechanical Thermal Analysis (DMTA)

Dynamic mechanical properties were analyzed in a Polymer Laboratories Mark III Dynamic Mechanical Analyzer DMTA in single cantilever mode. Scans of temperature from -150 to 150 °C at a frequency of 1 Hz, using a displacement of 0.050 and a heating rate of 4 °C/min were carried out in bending mode, employing samples with dimensions of 5 mm length, between 7-9 mm of width and between 1.5–1.9 mm of thickness.

In this work, DMTA was employed to study the physical properties of the different copolymers using the $\tan \delta$ (storage modulus (E')/loss modulus (E'')).

II.3. Morphological characterization

II.3.1. Dynamic Light Scattering (DLS)

Light scattering (DLS) is one of the most used techniques for the determination of particle size and particle size distribution. When a light beam impinges onto a solution or dispersion of particles, these particles scatter a fraction of light changing the wavelength of the incoming light. In this method the experiment duration is short and the sample preparation is easy. However, one of the main disadvantages is that in order to avoid multiple light scattering, the particles need to be diluted before performing the measurements.

Particle size was measured using a Coutier N4 Nanoziser. The diameter was measured 24 hours after removing the reaction vessel from the microwave. The solutions obtained were diluted 1/10 to prevent the reaction from continuing. Before measuring the particle size, the samples were introduced into an ultrasonic bath (Fisherbrand FB15053) for 20 min. The results are the overage of three measurements, each of them consisting in twelve runs.

II.3.2. Electron microscopy (EM)

A microscope is basically an optical system that transforms an object in an image, which amplifies (magnified) characteristic details of the object. In an electronic microscope, an electron beam falls on a sample. The interaction of these electrons with the atoms of the samples generates signals that are received by a detector or projected directly onto a screen.

Within the family of electron microscopes, the most common ones are the Transmission Electron Microscope (TEM) and Scanning Electron Microscope (SEM). Each microscope, allows the study of different characteristics of the samples.

II.3.2.a). Scanning Electron Microscopy (SEM)

In this manuscript a Scanning Electron Microscopy (SEM) HITACHI (S-2700 model) was used for the study of the morphology of the silica nanoparticles.

The samples were placed on a SEM disk and sputter-coated with an 8 nm Pt/Au layer (SC 500 Sputter Coater) to reduce electron charging effects.

II.3.2.b). Transmission Electron Microscopy (TEM)

Transmission Electron Microscope (TEM) images were obtained in a Philips TECNAI G2 20 TWIN (FEI) microscope, operating at an accelerating voltage of 200 kV in a bright-field image mode. This technique was employed both for the study of the morphology of the silica nanoparticles and for the films generated in the second chapter of Polyurethane /Poly(dimethyl siloxane) copolymers.

A) Nanoparticles

For the observation of nanoparticles a solution drop (diluted samples of the dispersions (0.005-0.01 wt. %) was deposited on a Formvar film Copper grid.

B) Films

The films were sectioned using an ultramicrotome device at -25 °C (Leica EMFC 6) equipped with a diamond knife. The ultrathin sections (~100 nm) were placed on 300 mesh copper grid.

II.3.3. Atomic Force Microscopy (AFM)

The Atomic Force Microscope (AFM) is a mechano-optical instrument capable of detecting forces of piconewtons. By tracking a sample, it is capable of recording continuously its topography using a probe or sharp tip with a conical or pyramidal shape. The probe is coupled to a highly flexible ribbon or microscopic lever of only about 200 microns. The Atomic Force Microscope has been essential in the development of nanotechnology because it allows the characterization and visualization of samples at nanoscale dimensions.

The Atomic Force Microscopy shows great added value compared to the electronic microscopies, due to its capacity to obtain 3D images of the surfaces. This allows quantifying the height of the surface features and therefore the possibility of obtaining a wide range of parameters associated with roughness which presents the surface. All of this simultaneously to obtain the conventional topography or phase images, without requiring additional essays.

One of the most common parameters in the roughness measures is the R_a . This parameter is the arithmetic mean of all the measures that the apparatus has acquired as can be seen in the equation shown in Figure II.2. In Figure II.2. a diagram of a surface profile of the sample to be analyzed is shown where the meaning of the equation is graphically indicated.

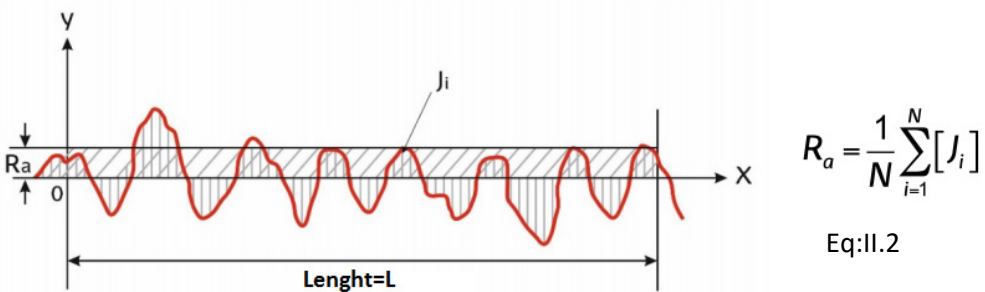


Figure II. 2. Representation of the roughness profile R_a .

Another way to express the roughness is R_q (equation II.3.) which is the square root of the irregularities in the sample of a length L . This is shown graphically in the Figure II.3.

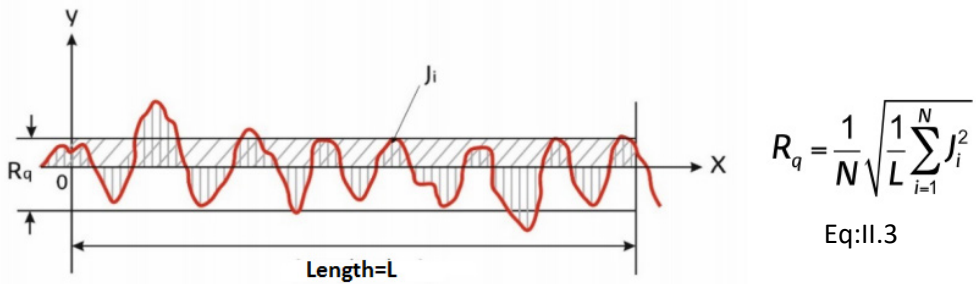


Figure II. 3. Representation of the roughness profile R_q .

The Atomic Force Microscope has several modes of operation depending on the sample. The principal operating modes of AFM include contact mode, tapping (intermittent) mode, and non-contact mode. In this manuscript, the AFM experiments were operated under tapping mode in air at ambient conditions on a Nanoscope IV of Digital Instrument using TESP tips which were obtained from Bruker.

II.3.4. X-Ray reflectance (XRR)

Determination of film thickness with high precision is important in surface science. XRR is a non-destructive and non-contact technique for thickness determination between 2-200 nm with a precision of about 1-3 °Å. In addition to thickness determination, this technique is also employed for the determination of the density and roughness of films and also of multilayers with a high precision⁶.

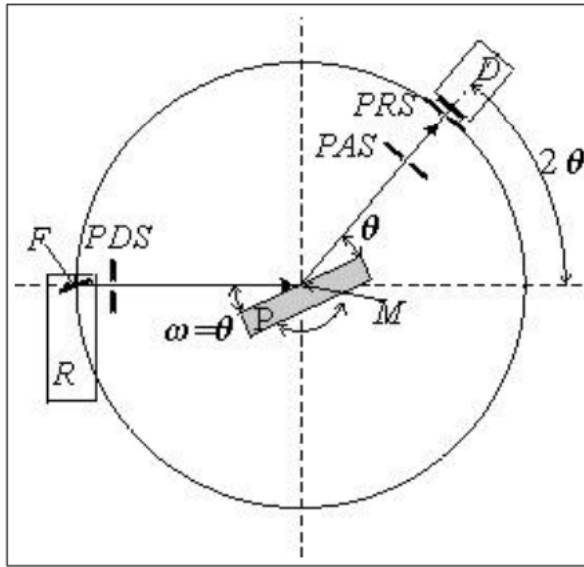


Figure II.4. Scheme of the XRR measurement.

XRR method involves monitoring the intensity of the X-Ray beam reflected by a sample at grazing angles. A monochromatic X-Ray beam of wavelength λ irradiates a sample at a grazing angle ω and the reflected intensity at an angle 2θ is recorded by a detector (see Figure II.4.). This Figure illustrates specular reflection where the condition $\omega = 2\theta/2$ is satisfied. For incident angles θ below a critical angle θ_c , total external reflection occurs. The critical angle for most materials is less than 0.3° . The density of the material is determined from the critical angle. Above θ_c the reflection from the different interfaces interferes and gives rise to interference fringes. The period of the interference fringes and the fall in the intensity are related to the thickness and the roughness of the layer (layers in case of multilayers).

Figure II.5. shows the typical plot obtained in the XRR measurement. From the point where the total reflection stops abruptly, the critical angle can be calculated. This angle is directly related to the film density. In addition, using mathematical models

that describe the specular reflectivity, the thickness and the roughness are varied until the theoretical profile matches the measurements.

The simulation values and the measurements are shown in Figure II.5.

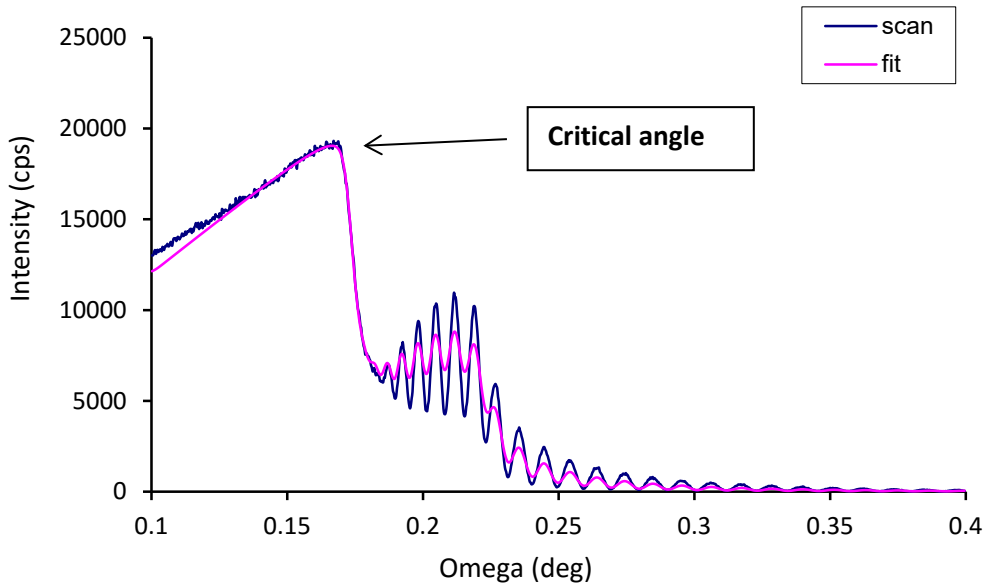


Figure II.5. XRR-measurements and simulations as an example.

The XRR measurements were performed using a diffractometer (X'Pert Pro MRD, Panalytical) with ceramic X-Ray tube (wavelength=0.154 nm) and high resolution horizontal goniometer (reproducibility $\pm 0.0001^\circ$).

II.3.5. Ellipsometric Porosimetry (EP)

Ellipsometric Porosimetry (EP) measures the changes in optical properties and thickness of porous thin-films during an adsorption cycle of an organic solvent⁷

(Figure II.6). These changes occur as the pores of the material are being filled by the adsorptive. From the measured refractive Index and thickness during the adsorption cycle, specific layer properties can be deduced: Porosity, Pore size distribution and characteristic pore size, Young's Modulus, hydrophobicity and diffusion coefficient.

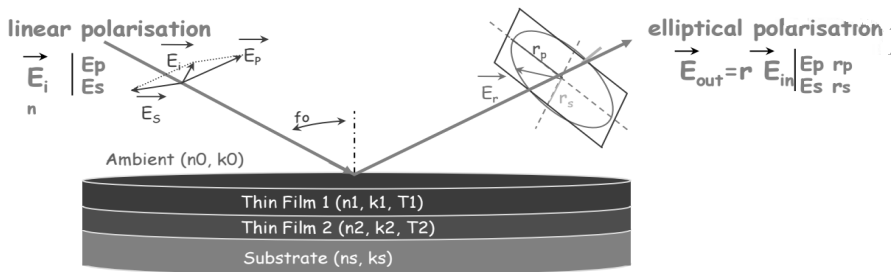


Figure II.6. Scheme of the EP measurement.

The technique can access both micro porosity (Pore diameter < 2 nm) and meso porosity (2 > Pore diameter > 50 nm) and can be used on layers from 10 nm to several μm depending on the instrument configuration. Compared to traditional Porosimeter, EP does not require sample preparation or film scratching and is well suited for very thin-film pore size and pore size distribution measurement.

The variation of the optical properties of the studied films as a function of the relative pressure was measured (Figure II.7.). This isotherm combined with the Lorentz-Lorenz equations make possible to generate an adsorption-desorption isotherms (Figure II.8.). From these isotherms it is possible to obtain the porosity and pore interconnectivity using the Kelvin model and BJH computation procedure for meso pores (See Figure II.9 and equation II.4) or the Dubinin Radushkevich model for micro pores (Figure II.10 and Equation II.5).

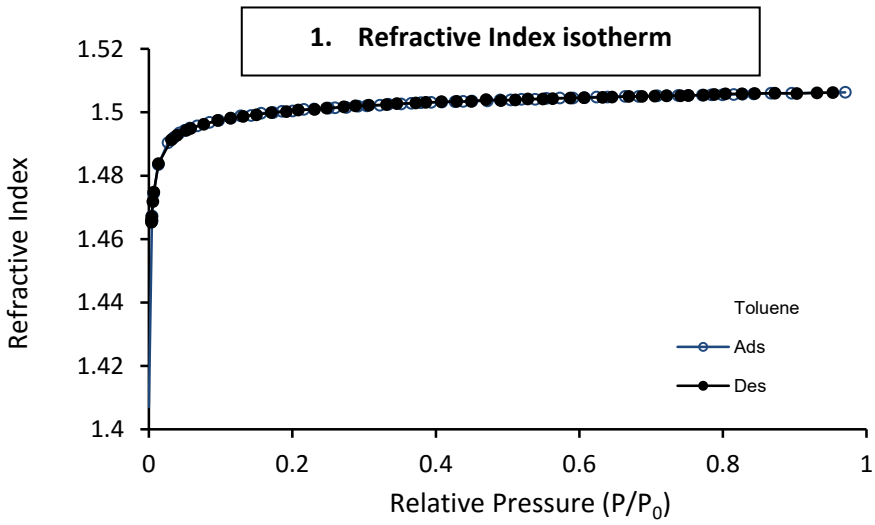


Figure II.7. Refractive index isotherm as a function of the relative pressure.

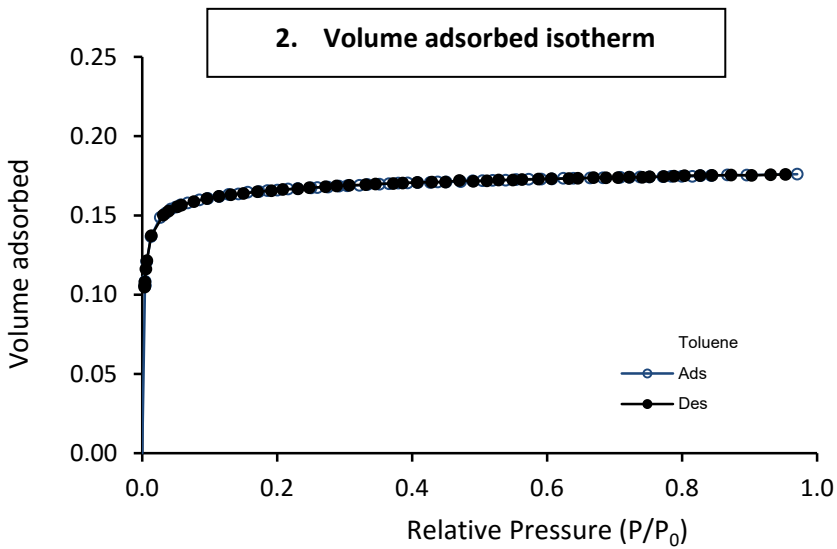


Figure II.8. Volume adsorbed isotherm generated from the refractive index isotherm with the Lorentz-Lorenz equations.

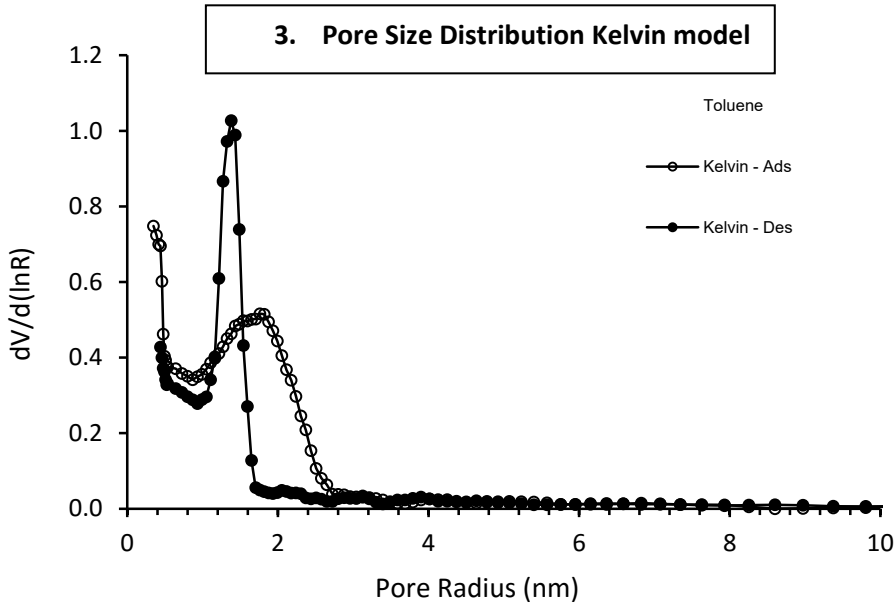


Figure II.9. Kelvin method to obtain the pore size and the distribution from EP measurements.

$$r = \frac{2\gamma V_L}{RT \ln\left(\frac{P}{P_0}\right)} \quad \text{Eq: II.4}$$

Where V_L is the molar volume adsorptive, P/P_0 relative equilibrium vapour pressures and γ the surface tension of the adsorptive.

$$\frac{W}{W_0} = e^{-\frac{[RT \ln\left(\frac{P}{P_0}\right)]^2}{(\beta E_0)^2}} \quad \text{Eq: II.5}$$

$$\text{Pore radius: } r = 6/E_0$$

Where W/W_0 is fractional filling of the micropore volume, β is scaling factor (affinity coefficient.), E_0 is characteristic energy and r is pore radius, nm.

EP study was performed using a Micrometric ASAP 2020 analyzer equipped with 1, 10 and 100 Torr transducers and Toluene as solvent.

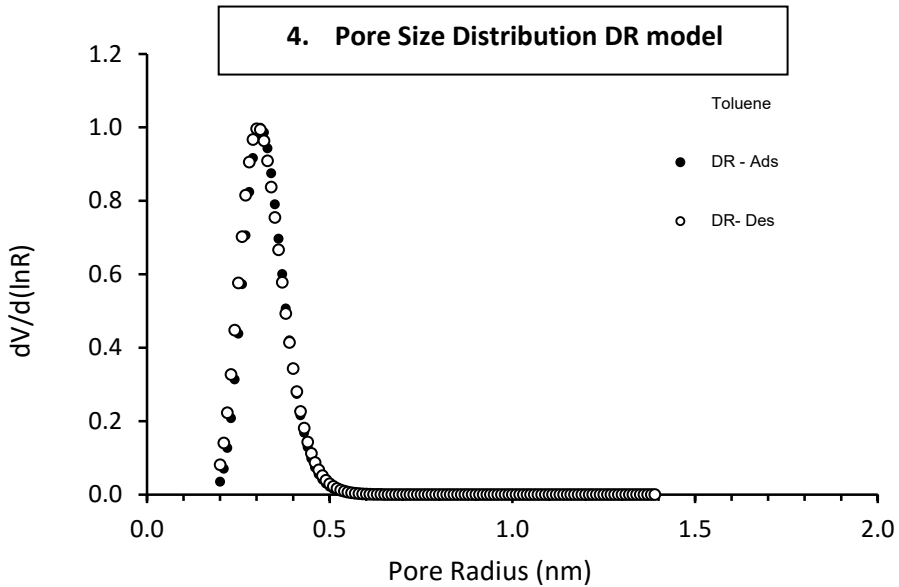


Figure II.10. Dubinin Radushkevich method to obtain the pore size and the distribution from EP measurements.

II.4. Mechanical properties characterization

II.4.1. Nanoindentation (NI)

Nanoindentation is a powerful technique used for assessing mechanical properties at nano/micro-scale^{8,9}. It is used for obtaining material parameters like elastic modulus, hardness, plastic or viscous parameters from experimental readings of indenter load and depth of penetration. The principle of nanoindentation lies in bringing a very small tip to the material surface producing an imprint.

Nanoindentation is the application of controlled load (μN - mN range), with concurrent measurement of depth (nm - μm range) through use of a hard indenter tip. A typical load-displacement curve for a ductile metal is shown in Figure II.11.

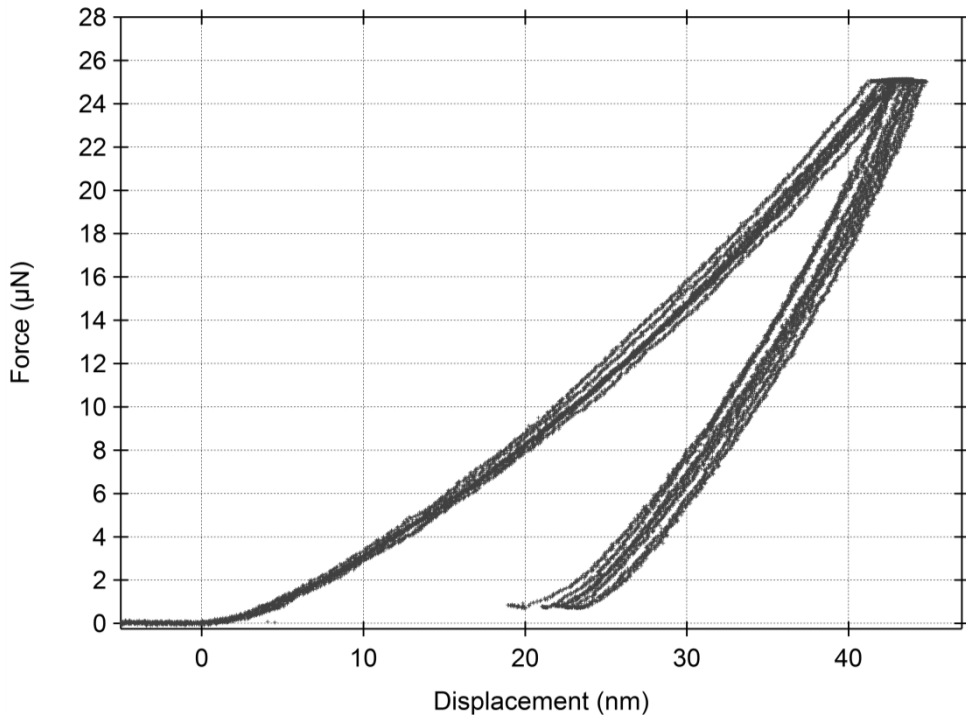


Figure II.11. Typical load-displacement curve for nanoindentation.

During the course of the instrumented indentation process, a record of the *depth* of penetration is made, and then the area of the indent is determined using the known geometry of the indentation tip. While indenting, various parameters such as load and depth of penetration can be measured. A record of these values can be plotted on a graph to create a load-displacement curve (such as the one shown in Figure

II.11). These curves can be used to calculate the mechanical properties of the material.

The slope of the curve, dP/dh , upon unloading is indicative of the stiffness (S) of the contact. This value generally includes a contribution from both the material being tested and the response of the test device itself. The stiffness of the contact can be used to calculate the reduced Young's modulus E_r .

$$E_r = \frac{1}{\beta} \frac{\sqrt{\pi}}{2} \frac{S}{\sqrt{A_p(h_c)}} \quad \text{Eq: II.6}$$

Where $A_p(h_c)$ is the projected area of the indentation at the contact depth h_c , and β is a geometrical constant on the order of unity.

The reduced modulus E_r is related to Young's modulus E_s of the test specimen through the following relationship:

$$\frac{1}{E_r} = \frac{(1-\nu_i^2)}{E_i + \frac{(1-\nu_s^2)}{E_s}} \quad \text{Eq: II.7}$$

Where the subscript i indicates a property of the indenter material and ν is Poisson's ratio.

A Quasi-static nanoindentation test was performed by applying and removing a load to a sample in a highly controlled manner with a geometrically well-defined probe. The range for the loads was from 3 μN to 30 μN . The measurements were performed in a Hysitron TI 950 TriboIndenter.

II.4.2. Surface Acoustic Wave Spectroscopy (SAWS)

Surface Acoustic Waves Spectroscopy (SAWS) is a method based on the use of the sound velocity dispersion for determination of the physical properties of materials. SAWS method allows (under definite requirements) to obtain the values of Young's modulus and density of the films simultaneously. SAWS were first explained in 1885 by Lord Rayleigh¹⁰, who described the surface acoustic mode of propagation and predicted its properties in his classic paper. Named after their discoverer, Rayleigh waves have a longitudinal and a vertical shear component that can couple with any media in contact with the surface. This coupling strongly affects the amplitude and velocity of the wave, allowing SAW sensors to directly sense mass and mechanical properties.

The studies in this thesis were carried out on LaWave type equipment (Figure II. 12). A powerful pulse of nitrogen laser falls onto the sample surface and causes local heating that leads to local thermal expansion and then to sharp increase in local mechanical stress. From the point of impact, SAW with broad spectral composition is formed. The laser beam is incident on the sample through a cylindrical lens, so the area of impact is a straight line. Nitrogen laser operating at a wavelength of 337.4 nm, a pulse power of 800 kW with a duration 0.5 ns, which corresponds to 0.4 mJ pulse energy were used. In the case of materials poorly resistant to the action of laser pulses, one can apply filters. It is clear that the laser excitation of SAWS is only possible if the film or substrate absorbs light at a wavelength of the laser. Broadband piezoelectric transducer located a few millimeters from the line of the laser beam impact is used to detect SAWS. During measurements, the distance between laser beam and piezo-sensor was precisely changed by moving the sample stage with accuracy of 1 μm . Finally, the dispersion curve is formed.

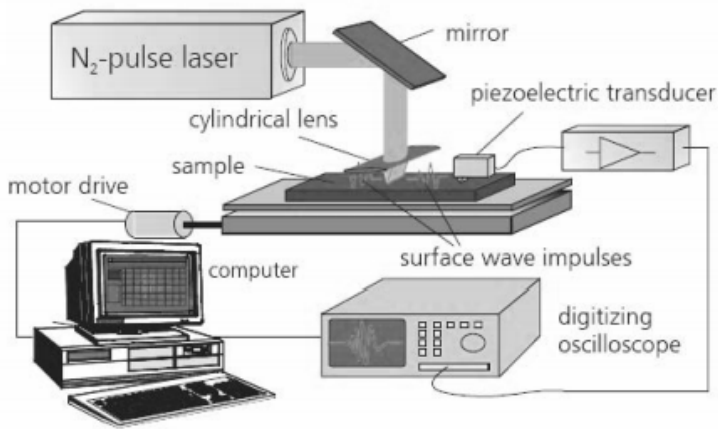


Figure II.12. Schematic representation of the Surface Acoustic Wave Spectroscopy.

II.5. Wettability properties

II.5.1. Contact angle and hysteresis by goniometer

The basic characteristic to determine in a hydrophobic/hydrophilic surface is the static contact angle that the water forms on the surface.

The static contact angle is measured by a goniometer using an optical subsystem to capture the profile of a pure liquid on a solid substrate. The angle formed between the liquid/solid interface and the liquid/vapor interface is the contact angle.

Dynamic contact angles can be measured by using two different approaches, changing the volume of the drop or by using tilting cradle. Figure II.13(a) shows the principle of the volume changing method. Briefly, a small drop is first placed on the surface. The needle is then brought close to the surface and the volume of the drop is gradually increased while recording the image at the same time. This will give the advancing contact angle. The receding angle is measured by the same way but this time, the volume of the drop is gradually decreased. In Figure II.13 (b), the principle

of the tilting cradle method is shown. The drop is placed on the substrate, which is then gradually tilted. The advancing angle is measured at the front of the drop just before the drop starts to move. The receding contact angle is measured at the back of the drop, at same time point.

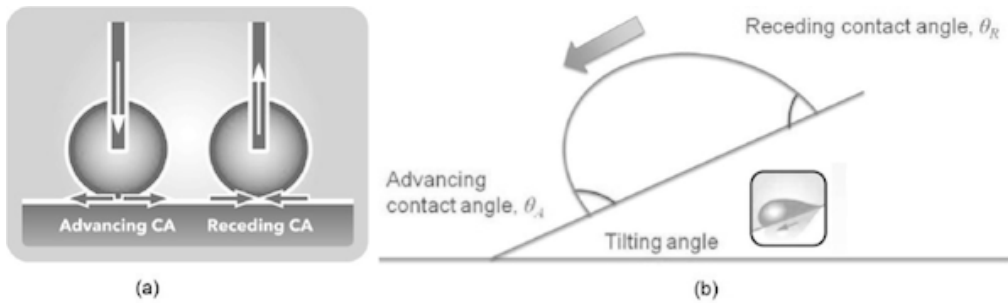


Figure II.13 . Dynamic contact angle measurements approaches. In the left (a) the volume changing method. In the right (b) the tilting cradle method.

Static and dynamic (using first approach) water contact angle (CA) measurements were carried out using the Sessile Drop method on a OCA20 contact angle goniometer at 25 °C and 55 % of relative humidity. The water drop volume used to perform the measurements was 10 μL .

II.6. Evaluation of anti-biofouling properties

The superhydrophobic surfaces that were designed and generated in this thesis intended to find its scope as materials to reduce or avoid the biofouling. In order to determine that, bioadhesion essays over these surfaces are of particular interest¹¹.

The organisms causing biofouling are diverse. Because of that, the essays to determine the anti-biofouling activities of the surfaces are diverse too. Combating

the proliferation of microorganisms over a submerged surface is very different from controlling the growth of algae or avoiding the adhesion of mussels. Therefore, there are a wide variety of laboratory test whose choice will depend on the causing organisms.

From a most basic point of view, the biofouling process originates from the formation of biofilms. These biofilm formation starts with the adsorption of organic molecules such as biopolymers and proteins. Because of that, the protein adsorption measurements in hydrophobic materials could be of great interest in order to determine the anti-biofouling effectiveness of the surfaces. Generally, a low protein adsorption is the most important prerequisite to be met by a material to be considered anti-biofouling. One of the proteins most commonly used for this kind of assay is Bovine Serum Albumin (BSA).

II.6.1. Colorimetric assay for determination of protein adsorption by UV (Static Sorption Test)

The Bio-Rad Protein Assay is a dye-binding assay where a differential colour change of a dye occurs in response to various concentrations of protein. The standard procedure advised by Bio-Rad was followed. A standard curve for the Bio-Rad Protein Assay of Bovine Serum Albumin (BSA) between 0.2 to 0.9 mg/mL was produced in order to determine the protein sorption behaviour of the films. UV-VIS transmittance spectra were obtained using a spectrophotometer Shimadzu UV-VIS-NIR 3600 using a photomultiplier tube detector. Samples with an outer surface area of 10 cm² and 200 µm of thickness were immersed in 100 mL BSA/water solution (0.45 mg/mL). At different times, 0.1 mL of the BSA/water solution were taken and after mixing with 5 mL of the dye reagent the concentration of BSA was calculated

by UV-Vis absorption at 595 nm. The amount of BSA, which was adsorbed by the sample, was calculated by a mass balance using initial and final concentration of solutions measured by UV-Vis. Triplicate experiments were carried out for all studied systems.

II.6.2. Determination of protein adsorption by Surface Plasmon Resonance (SPR)

The Surface Plasmon Resonance (SPR), also known as Surface Plasmon Spectroscopy is a technique based on the interaction between the electromagnetic radiation and the interface between a metal and a dielectric¹². Under certain conditions, and for a certain incident angle (resonance angle), an evanescent wave is produced whose energy can be absorbed by the oscillations of the metal electrons. The resonance angle is particularly sensitive to refractive index near to the interphase. Because of that, the construction of monolayers, or macromolecular interactions at the interface could be followed by changes in the resonance angle.

Figure II.14. shows a scheme of some basic components of the Surface Plasmon Resonance. In addition, Figure II.14. also illustrates the interactions between a ligand and a biomolecule.

Surface plasmons have been used to enhance the surface sensitivity of several spectroscopic measurements including fluorescence, Raman scattering, and second harmonic generation. However, in their simplest form, SPR reflectivity measurements can be used to detect molecular adsorption, such as polymers, DNA or proteins, etc. Technically, it is common that the angle of the reflection minimum (absorption maximum) is measured. This angle changes in the order of 0.1° during thin (about nm thickness) film adsorption. In other cases the changes in the absorption wavelength are followed. The mechanism of detection is based on the

change that the adsorbing molecules cause in the local index of refraction, changing the resonance conditions of the surface plasmon waves.

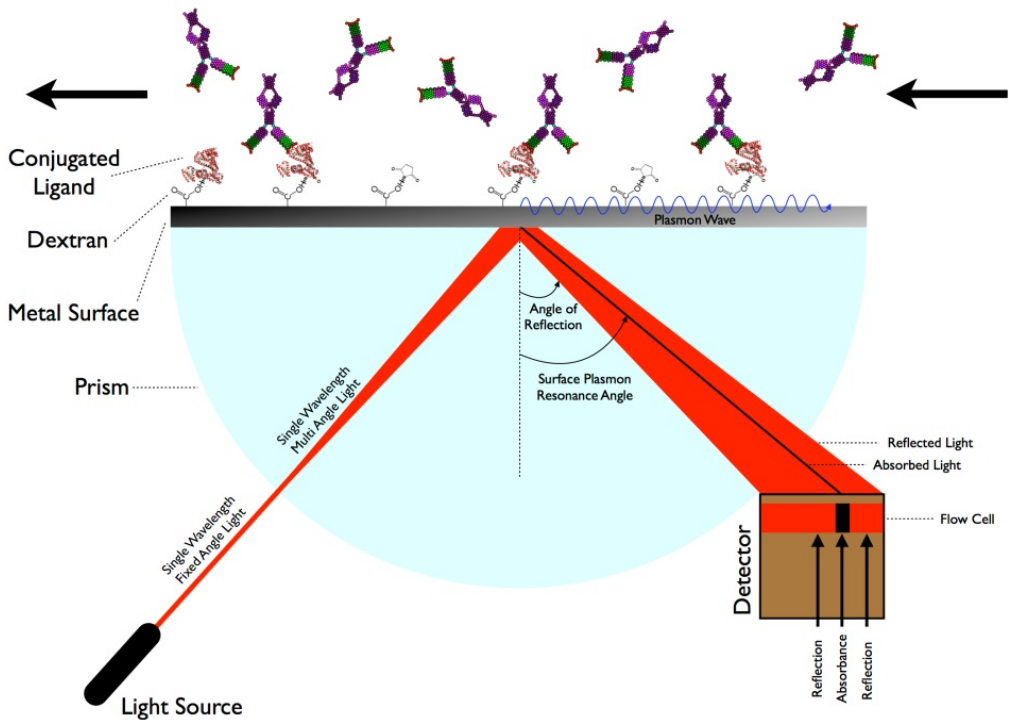


Figure II.14. Surface Plasmon Resonance (SPR) sensor scheme.

Figure II.15 (up). shows a typical spectrogram of the SPR. It can be observed that the angle changes depending on the surface or thickness. In Figure II.15 (down). the typical graph of adsorption is displayed. Three different parts can be seen in the graph, the conditioning with a buffer that does not cause any change, the protein adsorption and finally desorption of the protein induced by the rinsing with buffer.

The SPR used in this work was SPR Navi SPR 200. In order to make the experiments, a gold sensor was coated with a film obtained by spin-coating before a curing process for 45 minutes at 80 °C. Phosphate Buffer Saline (PBS) and Bovine Serum

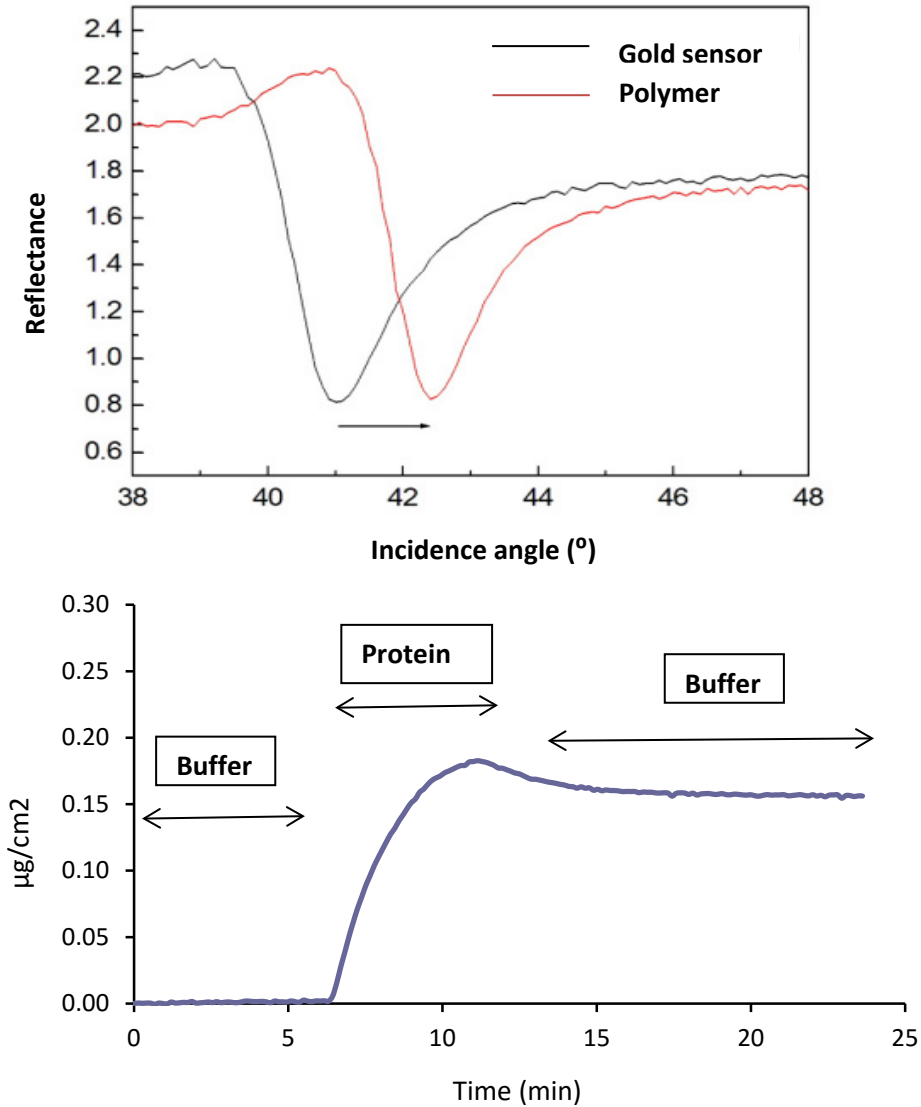


Figure II.15. Data results obtained by SPR measures. In up SPR curves for the film deposition. In down, a typical adsorption-desorption example curve.

Albumin (BSA) were used in order to analyse the anti-biofouling properties of the samples by three step measurements as shown in Figure II.15 (down). In the first step, a Phosphate Buffer Saline (PBS) solution was passed over the sensor to make

the background. After that, the protein solution (0.1 mg/mL) was introduced into the system for one hour and finally the PBS solutions were again used, in order to desorb the adsorbed protein.

II.6.3. Determination of protein adsorption by Quartz Crystal Microbalance with dissipation (QCM-D)

Another way to determine the protein adsorption kinetics is the Quartz Crystal Microbalance with dissipation (QCM-D)¹³. A QCM-D measures a mass variation per area unit by measuring the change in frequency of a quartz crystal resonator. The resonance is disturbed by the addition or removal of a small mass due to oxide growth/decay or film deposition at the surface of the acoustic resonator. The QCM-D can be used under vacuum, in gas phase and more recently in liquid environments. It is useful for monitoring the rate of deposition in thin-film systems under vacuum. In liquid, it is highly effective for determining the affinity of molecules (proteins, in particular) to surfaces functionalized with recognition sites. Larger entities such as viruses or polymers are investigated, as well. QCM-D has also been used to investigate interactions between biomolecules.

The Quartz Crystal Microbalance is essentially based on a quartz crystal or acoustic resonator. This device is very sensitive to small weight changes that occur in the surface. This allows measuring the mass deposited on the quartz glass per area unit thereof by the change in the resonance frequency experienced by the glass. Resonance is disturbed by the addition or removal of a small mass on the surface of acoustic resonator¹². The correlation between the mass accumulated on the glass and frequency is obtained by Sauerbrey equation:

$$\Delta f = \kappa_s \Delta m \quad \text{Eq:II.8}$$

where Δf is the change in frequency of the quartz glass, Δm is the deposited mass and k_s is a constant that considers the parameters of quartz crystal as are the characteristic frequency, the thickness, density and shear modulus.

The QCM-D sensor is constituted by a thin disc of quartz glass to which electrodes are fixed for stimulation and registration (Figure II.16.). Applying an external oscillating electric field to the piezoelectric material, internal mechanical stresses that induce an acoustic wave that spreads through the glass are produced.



Figure II.16. Sensor of the Quarz Crystal Microbalance with Dissipation(QCM-D).

In addition to measuring the resonant frequency, some equipments are capable to measure the dissipation (relationship between the bandwidth and frequency). This is a parameter that quantifies the damping in the system, and is related to the viscoelastic properties of the sample deposited on the sensor.

QCM-D measurements were performed on a Q-SENSE E1 system operating at 23 °C. Prior to the experiments, the sensors were stabilized overnight under a constant water flux of 100 $\mu\text{L}/\text{min}$. Subsequently, the respective sensors were put in contact

with different concentrations of BSA in aqueous solution up to a maximum of 100 mg BSA/L.

II.7. Reflection properties

II.7.1. Spectral Reflectometry (SR)

Spectral reflectometry (SR) is a method for characterizing the optical properties of a sample by measuring the reflection of an electromagnetic radiation, or more specifically, light, from an object. In this method, light is shined over the sample, and due to an interaction with the sample, some light is scattered back or reflected (hence the name "reflectometry"). By placing detectors at the path of the reflected light, the amount of light reflected back can be measured. Using the physics describing how matter interacts with light, the thickness and the refractive index of the material can be calculated.

Thicknesses and refractive indexes of the porous films generated for the spectral reflectometry (SR) experiments were measured using a Filmetrics F20 spectral reflectometer.

II.8. Bibliography

1. Almeida, J. C., *et al.* PDMS-SiO₂ hybrid materials-a new insight into the role of Ti and Zr as additives. *Polymer*. **72**, 40–51 (2015).
2. Criado, M., Sobrados, I. & Sanz, J. Polymerization of hybrid organic-inorganic materials from several silicon compounds followed by TGA/DTA, FTIR and NMR techniques. *Prog. Org. Coat.* **77**, 880–891 (2014).
3. Lippmaa, E., *et al.* Structural studies of silicates by solid-state high-resolution silicon-29 NMR. *J. Am. Chem. Soc.* **102**, 4889–4893 (1980).

4. Kann, Y., Shurgalin, M. & Krishnaswamy, R. K. Analysis method FTIR spectroscopy for analysis of crystallinity of and its utilization in evaluation of aging, orientation and composition. *Polym. Test.* **40**, 218–224 (2014).
5. Grasel, F. S., Ferrao, M. C. & Wolf, C. R. Development of methodology for identification the nature of the polyphenolic extracts by FTIR associated with multivariate analysis. *Spectrochim. Acta, Part. A.* **153**, 94–101 (2016).
6. Briscoe, W. H., *et al.* Applying grazing incidence X-Ray reflectometry (XRR) to characterising nanofilms on mica. *J. Colloid Interface Sci.* **306**, 459–63 (2007).
7. Dultsev, F. N. & Baklanov, M. R. Nondestructive Determination of Pore Size Distribution in Thin Films Deposited on Solid Substrates. *Electrochem. Solid-State Lett.* **2**, 192-194 (1999).
8. Saha, R. & Nix, W. D. Effects of the substrate on the determination of thin film mechanical properties by nanoindentation. *Acta Mater.* **50**, 23–38 (2002).
9. Bellet, D., Lamagnere, P., Vincent, A. & Brechet, Y. Nanoindentation investigation of the Young's modulus of porous silicon. *J. Appl. Phys.* **80**, 3772-3776 (1996).
10. Rayleigh, L. On Waves Propagated along the Plane Surface of an Elastic Solid. *Proc. London Math. Soc.* **17**, 4–11 (1885).
11. Majumdar, P., Stafslein, S., Daniels, J. & Webster, D. C. High throughput combinatorial characterization of thermosetting siloxane–urethane coatings having spontaneously formed microtopographical surfaces. *J. Coat. Technol. Res.* **4**, 131–138 (2007).
12. Nedelkov, D. & Nelson, R. W. Surface plasmon resonance mass spectrometry: Recent progress and outlooks. *Trends Biotechnol.* **21**, 301–305 (2003).
13. O'Sullivan, C. K. & Guilbault, G. G. Commercial quartz crystal microbalances–theory and applications. *Biosens. Bioelectron.* **14**, 663–670 (1999).

Annex III

Publications

Annex III:

Publications

III.1. “Preparation of superhydrophobic silica nanoparticles by microwave assisted sol–gel process”.

A. Santiago, A. González, J.J. Iruin, M.J. Fernández-Berridi, and L. Irusta.

Journal of Sol-Gel Science and Technology, **61**, 8-13 (2011)

III.2. “Urethane/Siloxane copolymers with hydrophobic properties”.

A. Santiago, A. González, J.J. Iruin, M.J. Fernández-Berridi, M.E. Muñoz and L. Irusta.

Macromolecular symposia, **150**, 321-322 (2012)

III.3. “Microphase separation and hydrophobicity of Urethane/Siloxane copolymers with low siloxane content”.

A. Santiago, L. Martin , J.J. Iruin, M.J. Fernández-Berridi, A. González and L. Irusta

Progress in Organic Coatings, **77**, 798–802 (2014)

III.4. “Resistance to protein sorption as a model of antifouling performance of Poly(siloxane-urethane) coatings exhibiting phase separated morphologies”.

A. Santiago, L. Irusta, T. Schäfer, A. Corres, L. Martin, and A. González

Submitted to Progress in Organic Coatings. Under Review.

Participation in Congresses

* **2012:** VI congress of young researchers in polymers (Islantilla), April 2012.

Oral communication

“Urethane/Siloxane copolymers with hydrophobic properties”

A. Santiago, A. González, L. Irusta, M.J. Fernández-Berridi and J.J. Iruin.

* **2012:** 11th European Symposium on Polymer Blends (San Sebastian), March 2012.

Poster

“Urethane/Siloxane copolymers with hydrophobic properties”

A. Santiago, A. González, L. Irusta, M.J. Fernández-Berridi, and J.J. Iruin.

* **2010:** Silicon Containing Polymers and Composites, (San Diego), December 2010.

Poster

“Superhydrophobic surfaces from silica nanoparticles obtained by microwave assisted sol-gel process”

A. Santiago, A. González, L. Irusta, M.J. Fernández-Berridi and J.J. Iruin.

Preparation of superhydrophobic silica nanoparticles by microwave assisted sol–gel process

A. Santiago · A. González · J. J. Iruin ·
M. J. Fernández-Berridi · L. Irusta

Received: 24 June 2011 / Accepted: 5 September 2011 / Published online: 15 September 2011
© Springer Science+Business Media, LLC 2011

Abstract Hydrophobic silica nanoparticles were obtained by microwave assisted sol–gel method using a two-step procedure. In the first step different size silica particles were generated from tetraethyl orthosilicate and in the second one the silica particles were hydrophobized using hexadecyl trimethoxysilane (HDTMOS). Under microwave irradiation, high conversion degrees were obtained at relatively short reaction times. The HDTMOS added in the second step instead of coating the silica nanoparticles generated new ones and therefore the final product showed a bimodal size distribution. All the synthesized nanoparticles gave rise to high water contact angles ($\approx 150^\circ$) and low hysteresis values.

Keywords Superhydrophobic silica · Microwave · Nanoparticles

1 Introduction

Superhydrophobic surfaces have aroused much interest because properties such as antisticking, anti-contamination and self-cleaning are expected [1, 2]. These surfaces present very high water static contact angles (larger than 150°) and hysteresis values (the difference between the advancing and receding angles) lower than 10° [3–5].

In nature many plants have self-cleaning leaves but the most famous ones are those of the lotus flower, which have

a contact angle of about 160° [6]. The hydrophobic nature of the Lotus leaf can be attributed not only to a low surface energy but also to a surface roughness on at least two different length scales (micro and nanometer) [7, 8]. Inspired by the extraordinary hydrophobic behavior of the Lotus leaf, many researchers have studied different methods for producing artificial superhydrophobic surfaces [3, 9, 10]. In practice, superhydrophobic surfaces can be prepared using different methods such as etching [11] and lithography [12], sol–gel processing [13–15], and electrospinning [16].

The sol–gel process is a versatile method of preparing oxide-based films on a variety of substrates in an economical way [17]. Following this methodology, the synthesis of hydrophobic silica nanoparticles [15, 18, 19] and surfaces [20–22] has been described by several authors. Monodispersed spherical silica nanoparticles can be obtained by the method originally developed by Stöber et al. [23]. In this method, aqueous alcoholic solutions of silicon alkoxide at high pH are used. The most important parameters in preparing different size silica particles seem to be water and ammonia concentrations. Thus, the silica particle size increases as the concentrations of water and ammonia increase. Silica nanoparticles can also be obtained under acidic conditions [24]. The rate of hydrolysis and condensation of the alkoxy silane is not the same under acidic or alkaline conditions and therefore the formation mechanism of these two species of silica materials is different.

The synthesis of hydrophobic silica involves the functionalization with organic silica precursors such as aliphatic hydrocarbon or fluorine containing compounds. However, the reactivity of the organic precursors is low and therefore in order to obtain high conversions, high temperatures and long reaction times are required [25]. In a

A. Santiago · A. González · J. J. Iruin ·
M. J. Fernández-Berridi · L. Irusta (✉)
Department of Polymer Science and Technology and Institute
for Polymer Materials (POLYMAT), University of the Basque
Country, P.O. Box 1072, 20080 San Sebastián, Spain
e-mail: lourdes.irusta@ehu.es

previous work, we showed that the reaction time can be reduced if the microwave heating is used when obtaining hydrophilic silica nanoparticles from tetraethyl orthosilicate [26]. Similar results were reported on literature for acid catalyzed grafting of alkylalkoxysilanes onto silica in toluene [27].

The use of microwaves as an energy source for chemical reactions and processes has been extensively investigated during recent years [28]. Microwave-assisted synthesis is generally much faster, cleaner and more economical than the conventional methods. The exact nature of microwave interaction with reactants during the synthesis of materials is somewhat unclear and speculative. However, energy transfer from the microwaves to the material is believed to occur either through resonance or relaxation, which results in rapid heating.

The motivation of this work was to develop a simple and inexpensive procedure for preparing hydrophobic silica nanoparticles at high yield, using microwave-assisted heating. Different nanoparticles were synthesized under basic catalysis using tetraethyl orthosilicate (TEOS) and Hexadecyltrimethoxysilane (HDTMOS) as silica precursors in a two-step procedure. The study had two objectives: to obtain hydrophobic silica nanoparticles with high water contact angles and low hysteresis values and to explore the effectiveness of the microwave irradiation as a way of increasing the sol–gel reaction rate.

2 Experimental

2.1 Materials

Tetraethyl orthosilicate (TEOS) GC grade, Hexadecyltrimethoxysilane (HDTMOS) and Ammonia sol. (28–30% NH₃ basis) ACS reagent were purchased from Sigma-

Aldrich. Ethanol absolute was purchased from Panreac. All products were used as received. Water was doubly distilled and deionized (Milli-Q, 18 MΩ cm).

2.2 Synthesis of superhydrophobic nanoparticles

3 mL of TEOS, 50 mL of ethanol and the required amounts of water and ammonia (Table 1) were introduced in the reaction vessel. The microwave heating process was carried out in the MARS5X (CEM corporation) microwave system. In this type of oven, the temperature is directly measured in the microwave vessel and is used as the feedback control signal to regulate the microwave power output. The maximum power of the microwave was selected to 800 W and the power was automatically varied from 0 to 100% in order to reach 50 °C in 10 min. The microwave frequency was 2.45 GHz. The reactions were carried out for 3 h in sealed Teflon vessels (GreenChem, CEM corporation) under magnetic stirring, and allowed to cool to 30 °C in the microwave.

Then, the required amounts of HDTMOS were quickly added to the same reaction vessel. The second step was carried out under microwave irradiation at 50 °C for 3 h. Figure 1 summarizes the reaction process.

In order to compare this with conventional heating methods, one of the reactions was performed in a single neck flask equipped with a reflux condenser heated in a thermostatic oil bath.

2.3 Characterization of the nanoparticles

2.3.1 Conversion

The conversion of the first step was calculated by infrared spectroscopy. The spectra of an aliquot of the reaction products were recorded immediately after the completion

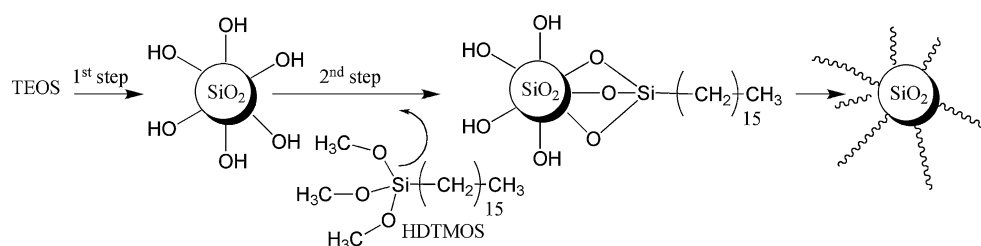
Table 1 Particle size and conversion of the experiments described

Experiment	T (°C)	Time (min)	$\frac{\text{mo/water}}{\text{mo/TEOS}}$	$\frac{\text{mo/Ammonia}}{\text{mo/TEOS}}$	D (nm)	σ_{n-1}	p	σ_{n-1}
4	50	18	7.9	1.19	26	11	0.10	0.11
8	50	18	18.2	1.19	79	28	0.40	0.02
16	50	18	18.2	3.55	138	21	0.68	0.02
4a	50	30	7.9	1.19	26	8	0.14	0.01
4b	50	60	7.9	1.19	26	8	0.29	0.01
4c	50	90	7.9	1.19	26	2	0.36	0.01
4d	50	180	7.9	1.19	24	2	0.57	0.01
8d	50	180	18.2	1.19	47	12	0.80	0.01
16d	50	180	18.2	3.55	146	4	0.98	0.01

Previously reported data are italicized

D = diameter of the nanoparticles, p = conversion, σ_{n-1} = standard deviation

Fig. 1 Preparation of hydrophobic silica nanoparticles



of the first step. Infrared spectra of the dispersions were carried out (Nicolet 6700 FTIR) using a 0.1 mm path length KRS5 windows liquid cell (Spectra Tech) at a resolution of 2 cm^{-1} . A minimum of 32 scans were signal averaged. The absorbance of the infrared band at 960 cm^{-1} was used to calculate the conversion as described in a previous paper [26].

The conversion of the second step was determined from the carbon content, calculated by elemental analysis (microanalyzer CHNS-932 LECO) after drying the samples for at least 1 week.

2.3.2 Chemical characterization

²⁹Si CP-MAS solid NMR spectra were performed in a Fourier transform Bruker 300 MHz (model Avance 300 DSX) to study the final structure of the obtained nanoparticles. The spectra were recorded using a 4 mm diameter rotor in a CP/MAS probe. The cross polarization contact time was fixed to 1.6 ms. The spectra were recorded at 59.6 MHz with a superconductor of 7 T.

2.3.3 Particle size and morphology

Dynamic Light Scattering measurements (DLS) were used to determine the diameter of the particles using a Coutier N4 Nanosizer at room temperature. The diameter was measured 24 h after removing the reaction vessel from the microwave. The solutions obtained were diluted 1/10 to prevent the reaction from continuing. Before measuring the particle size, the samples were introduced into an ultrasonic bath for 20 min. All samples were measured in ethanol 3 times and the final value was the average of all of them.

Sample morphology was determined by Transmission Electron Microscopy (TEM) using a Philips Tecnai 20 microscope working at accelerating voltage of 200 kV. Diluted samples of the dispersions (0.005–0.01 wt%) were prepared.

2.4 Dynamic water contact angle measurements

Dynamic water contact angle (CA) measurements were carried out using the sessile drop method in a contact angle goniometer (OCA20) at 25 °C and 55% of relative

humidity. The hysteresis values were calculated as the difference between the advancing and receding contact angles.

3 Results and discussion

As mentioned, hydrophobic nanoparticles were obtained using a two-step process. In the first step, three different diameter silica nanoparticles were synthesized from the hydrolysis and condensation of TEOS and in the second one the nanoparticles were coated with different amounts of HDTMOS.

3.1 First step

In order to obtain nanoparticles with diameters of about 25, 50 and 150 nm at high conversions, experiments 4, 8 and 16 from a previous work were repeated (Table 1). From those results, it is clear that the conversion was very low, especially for experiment 4. Therefore, new experiments devoted to increase the conversion were performed using higher reaction times (experiments 4 a–d, 8d and 16d in Table 1).

As can be observed, under the conditions of experiment 4, the conversion increased with the reaction time, reaching an appropriate value at 180 min. Although the conversion of experiments 8 and 16 at 18 min was clearly higher than that of experiment 4, longer reaction times also gave rise to higher conversions. According to these results and in order to obtain high conversions, the reaction time of the first step was increased to 180 min. The polydispersity index (PI) of all the particles was lower than 0.15, which implies that they are of fairly uniform size.

3.2 Second step

The final particles were obtained after adding HDTMOS in the second step. A description of the samples together with the conversion of this step, calculated by elemental analysis, is shown in Table 2.

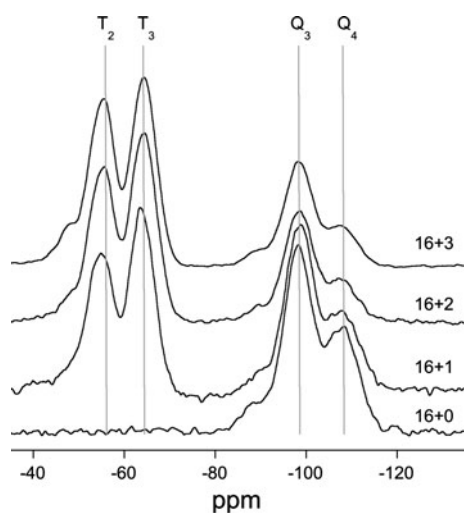
As can be observed, the conversion of all the experiments was high and no significant differences were observed among the different experiments.

²⁹Si-NMR experiments were also carried out to determine the chemical structure of the nanoparticles. Figure 2

Table 2 Conversion of the second step (calculated by elemental analysis) of the experiments described

Experiment	First step	HDTMOS (mL)	p	σ_{n-1}
4 + 1	4d	1	*	*
4 + 2	4d	2	0.93	0.02
4 + 3	4d	3	0.94	0.01
8 + 1	8d	1	0.91	0.01
8 + 2	8d	2	0.96	0.02
8 + 3	8d	3	0.96	0.01
16 + 1	16d	1	0.92	0.01
16 + 2	16d	2	0.89	0.01
16 + 3	16d	3	0.90	0.01

* Gelation occurred during this experiment. p = conversion. σ_{n-1} = standard deviation

**Fig. 2** ^{29}Si solid state NMR spectra of nanoparticles of experiments 16 + 0, 16 + 1, 16 + 2 and 16 + 3

shows the spectra of the nanoparticles obtained from experiment 16 after adding 1, 2 and 3 mL of HDTMOS.

In the spectrum of the sample containing only TEOS (16 + 0), two peaks at approximately -98 and -108 ppm were observed, which can be attributed to silicon atoms linked to four oxygen atoms (Q) containing three (Q_3) and four (Q_4) siloxane linkages respectively. Only small shoulders assignable to lower condensation degree species (Q_1 and Q_2) are observed and therefore, we can conclude that the condensation degree of TEOS in this sample was high, according to the conversion results calculated from FTIR spectra (Table 1).

In the spectra of samples containing HDTMOS, in addition to the previously mentioned peaks two new signals at -55 and -62 ppm, assigned to silicon atoms linked to three oxygen atoms (T) containing two (T_2) and three (T_3) siloxane linkages, respectively, were also observed [29]. As expected, the intensity of the bands assigned to T species

increased with HDTMOS concentration, although there was not significant difference in the relative intensity between T_2 and T_3 with HDTMOS concentration, suggesting that the condensation degree was not affected by the precursor concentration. However, the intensity of Q species was clearly lower than the expected, taking into account the mol percent of the two added precursors. This result can be explained on the basis that the cross polarization transfer to the Q_4 structures, due to the large proton silicon Q_4 distance, is difficult and consequently, a part of the Q_4 sites could not be detected in the CP-MAS experiments [30].

The ^{29}Si -NMR experiments of the other samples were similar and therefore it can be concluded that the condensation degree of the alkoxy silane moieties was high. However, the diameter of the particles could not be measured by DLS due to the very high polydispersity index and so the morphology of the particles was studied by TEM. Figures 3, 4 and 5 show the TEM images of the particles generated in the different experiments.

The TEM images of the samples generated from the lowest diameter silica particles (experiment 4 + 2, Fig. 3) showed the presence of large aggregates. However, the TEM images of the particles generated in the experiment 4 + 3 (Fig. 3) showed the presence of particles with a diameter clearly higher than the diameter of the particles generated in the first step. The samples generated from silica particles of 47 nm in the first step (experiment 8, Fig. 4), showed a distribution of two different size (≈ 25 and 50 nm) nanoparticles. We suggest that the particles of 50 nm were formed in the first step and that the addition of HDTMOS in the second step generated the small nanoparticles. Therefore, it seems that the organosilica precursor gave rise to new particles that covered the silica particles generated in the first step. The same effect was observed for the samples generated from experiment 16 (Fig. 5). The large particles (diameters close to 200 nm) could be generated in the first step, while the smaller ones (80 nm) in the second. It must be pointed out that the size of the particles generated in the second step of the experiment did not change with HDTMOS concentration. However, the size of the new particles depended on the experimental conditions of the first step. Thus, the new particles formed in the second step of experiment 16 were larger than those obtained in the same step of experiment 8. As the water content of these two experiments was the same, it can be argued that the size of the nanoparticles increased with ammonia content, as previously reported [26] for only TEOS containing nanoparticles.

3.3 Comparison with conventional heating

In order to establish the effectiveness of the microwave heating, the reaction 4 + 3 was performed using

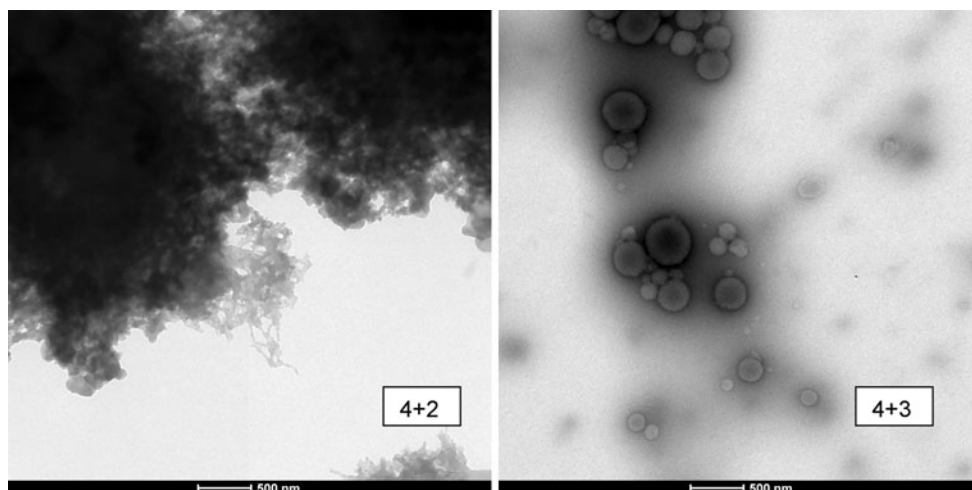


Fig. 3 TEM images of the samples generated in experiments 4 + 2 and 4 + 3

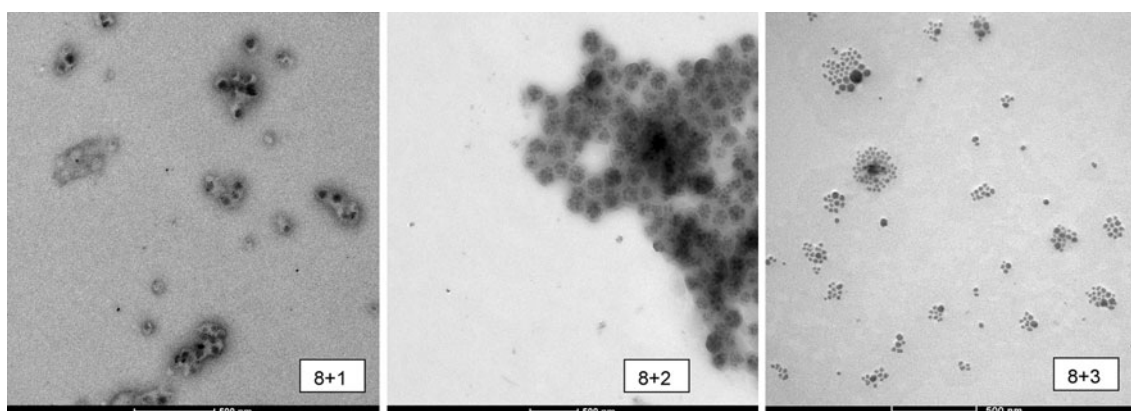


Fig. 4 TEM images of the samples generated in experiments 8 + 1, 8 + 2 and 8 + 3

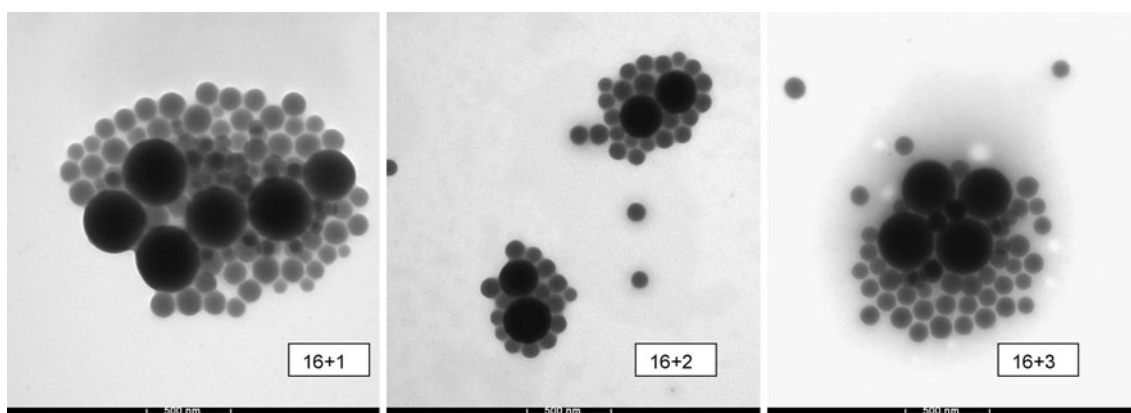


Fig. 5 TEM images of the samples generated in experiments 16 + 1, 16 + 2 and 16 + 3

conventional heating. The calculated conversions of the first and second steps were 0.41 and 0.74 respectively. These values are clearly lower than those obtained under microwave heating (0.57 and 0.94) and therefore, it can be

concluded that using microwave radiation shortens the reaction time. The size of the nanoparticles obtained in the first step without microwave heating was 24 ± 2 nm (very similar to the diameter obtained under microwave heating).

Table 3 Dynamic contact angle results

Sample	θ Average (°)	Hysteresis (°)
4 + 1	/	/
4 + 2	142	4
4 + 3	148	4
8 + 1	154	5
8 + 2	141	12
8 + 3	146	2
16 + 1	148	5
16 + 2	150	12
16 + 3	151	12

According to this, it can be concluded that the microwave heating did not have any effect on the particle size. The size of the nanoparticles obtained in the second step without microwave heating was not measured because of the high polydispersity value.

3.4 Dynamic contact angle measurements

The solid content of the dispersions generated in all the experiments was adjusted to 2 wt%. Then, 5 mL of the dispersion were cast over 45 mm diameter aluminum pans and dried at room temperature for at least 1 week. The water contact angles of the samples were measured and the results are summarized in Table 3.

As can be observed, the water contact angle of all the surfaces was high and the hysteresis values low. Therefore, these nanoparticles could be of great interest in order to obtain self-cleaning properties. However, no clear dependence between the measured contact angle and sample morphology was observed, which means that the surface behavior was governed by the particles generated in the second step.

4 Conclusions

In the microwave assisted synthesis of hydrophobic silica nanoparticles high yields were obtained at relatively short reaction times. The hydrocarbonated precursor added in the second step generated new particles, instead of coating the previously formed silica nanoparticles and, consequently, the final product showed a bimodal size distribution. Although all the synthesized nanoparticles gave rise to high water contact angles, a direct relation between contact angle and morphology of the samples could not be established.

Acknowledgments The authors would like to thank the financial support of the Basque Government (Etorrek, iNanogune II project, and Ayudas a grupos de investigación del sistema universitario vasco ITT444-10) for the development of this work.

References

- Ma M, Hill RM (2006) *Curr Opin Colloid Interface Sci* 11:193
- Feng L, Li S, Li Y, Li H, Zhang L, Zhai J, Song Y, Liu B, Jiang L, Zhu D (2002) *Adv Mater* 14:1857
- Li X-M, Reinhoudt D, Crego-Calama M (2007) *Chem Soc Rev* 36:1350
- Nakajima A, Hashimoto K, Watanabe T (2001) *Monatsh Chem* 132:31
- Gao L, McCarthy TJ (2006) *Langmuir* 22:6234
- Cheng Y-T, Rodak DE (2005) *Appl Phys Lett* 86:144101
- Gao L, McCarthy TJ (2006) *Langmuir* 22:2966
- Miwa M, Nakajima A, Fujishima A, Hashimoto K, Watanabe T (2000) *Langmuir* 16:5754
- Sun T, Feng L, Gao X, Jiang L (2005) *Acc Chem Res* 38:644
- Liu K, Yao X, Jiang L (2010) *Chem Soc Rev* 39:3240
- Zhou YH, Bin Y, Yang WF, Liu W, Wang P, Zhang W, Bello I, Lee ST (2011) *J Nanosci Nanotechnol* 11:2292
- Hwang JH, Sung-Hoon H, Lee H (2009) *J Nanosci Nanotechnol* 9:3644
- Pagliaro M, Ciriminna R, Palmisano G (2009) *J Mater Chem* 19:3116
- Burunkaya E, Kiraz N, Kesmez Ö, Asilturk M, Erdem Çamurlu H, Arpaç E (2010) *J Sol-Gel Sci Technol* 56:99
- Smitha S, Shajesh P, Mukundan P, Warriar K (2008) *J Sol-Gel Sci Technol* 48:356
- Buruaga L, González A, Irusta L, Iruin JJ (2011) *J Appl Polym Sci* 120:1520
- Zarzycki J (1997) *J Sol-Gel Sci Technol* 8:17
- Bhagat SD, Kim Y-H, Suh K-H, Ahn Y-S, Yeo J-G, Han J-H (2008) *Microporous Mesoporous Mater* 112:504
- Gellermann C, Storch W, Wolter H (1997) *J Sol-Gel Sci Technol* 8:173
- Rios PF, Dodiuk H, Kenig S, McCarthy S, Dotan A (2007) *J Adhes Sci Technol* 21:399
- Rios PF, Dodiuk H, Kenig S, McCarthy S, Dotan A (2008) *Polym Adv Technol* 19:1684
- Hou H, Chen Y (2007) *J Sol-Gel Sci Technol* 43:53
- Stöber W, Fink A, Bohn E (1968) *J Colloid Interface Sci* 26:62
- Zhao M, Zheng L, Bai X, Li N, Yu L (2009) *Colloids Surf A* 346:229
- García N, Benito E, Guzmán J, Tiemblo P (2007) *J Am Chem Soc* 129:5052
- Mily E, González A, Iruin J, Irusta L, Fernández-Berridi MJ (2010) *J Sol-Gel Sci Technol* 53:667
- García N, Benito E, Guzmán J, de Francisco R, Tiemblo P (2010) *Langmuir* 26:5499
- Wiesbrock F, Hoogenboom R, Schubert US (2004) *Macromol Rapid Commun* 25:1739
- Komori Y, Nakashima H, Hayashi S, Sugahara Y (2005) *J Non Cryst Solids* 351:97
- Peeters MPJ, Wakelkamp WJJ, Kentgens APM (1995) *J Non Cryst Solids* 189:77

Urethane/Siloxane Copolymers with Hydrophobic Properties

A. Santiago, A. González, J. J. Iruin, M. J. Fernández-Berridi, M. E. Muñoz, L. Irusta*

Summary: Different composition polyurethane-siloxane thermoset copolymers obtained from isophorone diisocyanate trimer, poly (caprolactone) triol and hydroxy terminated poly(dimethyl siloxane) were casted over aluminium surfaces. Dynamic mechanical thermal analysis (DMTA) measurements showed that the copolymers presented a phase separated morphology. The water contact angle increased with the siloxane percentage. In addition, for a fixed siloxane percentage, the water contact angle obtained in the air contact generated surface was higher than the one registered in the aluminium contact generated surface, suggesting that the low surface energy siloxane component migrated to the air contact generated surface.

Keywords: block copolymers; phase separation; polysiloxanes; polyurethane

Introduction

The generation of surfaces which present water static contact angles higher than 90° , called hydrophobic, has aroused great interest because properties such as self-cleaning and anti-biofouling are expected.^[1,2] Low surface energy materials such as fluorinated polymers and polysiloxanes^[3] are hydrophobic and therefore have high water contact angles. However, according to literature the contact angle cannot be increased beyond 120° by a purely chemical process and higher contact angles can only be obtained if the hydrophobic surface is roughened.^[4]

In practice, hydrophobic surfaces can be prepared using different methods such as etching and lithography,^[5,6] sol-gel processing,^[7,8] electrospinning^[9,10] and by nanostructuring of block copolymers.^[11]

The present paper is devoted to the generation of hydrophobic surfaces by nanostructuring of urethane siloxane

block copolymers. The particular surface properties of poly(urethane siloxane) copolymers are obtained through the segregation of incompatible and less polar soft siloxane domains towards the surface to minimize the interfacial tension with air.^[12,13,14] In addition, the siloxane domains in the surface generate a roughness that can make the water contact angle increase. These types of surfaces are of special interest as anti-biofouling^[15] coatings because they couple the toughness and good adhesion of polyurethanes with the hydrophobic surface properties of polysiloxanes.

Experimental Part

Materials

Aliphatic polyisocyanate Vestanat T 1890 E (IPDI trimer, 70 wt % in butyl acetate) was obtained from Evonik Industries. Polyethylene glycol terminated polydimethylsiloxane (PDMS, $M_n = 1000 \text{ g mol}^{-1}$, 20 wt % non siloxane component) was obtained from Gelest Inc. Trifunctional polyol (polycaprolactone, PCL, $M_n = 900 \text{ g mol}^{-1}$), dibutyltin dilaurate (DBTDL) and butyl acetate (BA) were supplied by Sigma-Aldrich.

Department of Polymer Science and Technology and Institute for Polymer Materials (POLYMAT), University of the Basque Country. P.O.Box 1072, 20080 San Sebastián, Spain
E-mail: lourdes.irusta@ehu.es

Coating Preparation

Several synthesis were made changing the relation of the polyols (PCL/PDMS) from 0 to 100 wt % of PCL and keeping constant the NCO:OH ratio 1.1:1.0.

PCL and PDMS solutions in butyl acetate (33 wt % of solids) were introduced in a 100 mL Erlenmeyer at room temperature and mixed for 1 minute under magnetic stirring. Then, the required amount of IPDI trimer and DBTDL (0.1% total solids) were added. Before gelification, the solutions were casted over aluminium pans of 43 mm diameter and kept under environmental conditions for 24 h followed by oven curing at 80 °C for 45 minutes.

Instrumentation

Samples for FTIR studies were prepared on KBr pellets using spin coating (speed 1900 r.p.m for 15 seconds). The spectra were registered on a Nicolet 6700 (Thermo Scientific) FTIR spectrometer. Scanning resolution was 4 cm⁻¹ and 10 scans were taken.

The contact angle measurements were performed in an OCA20 Instrument at static mode, in a room with controlled temperature and humidity (25 °C and 55% of relative humidity). The measurements were made from both sides of the films. The average error of the results (10 measurements were made for each sample) of the

upper face (air contact) was 3 ° and 5 ° for the face in contact with the aluminium pan.

Dynamic mechanical properties were analyzed in a Polymer Laboratories Mark III Dynamic Mechanical Analyzer DMTA in single cantilever mode. Scans of temperature from -150 to 150 °C at a frequency of 1 Hz, using a displacement of 0.050 mm and a heating rate of 4 °C.min⁻¹ were carried out in bending mode, employing samples with dimensions of 5 mm length, between 7-9 mm of width and between 1.5-1.9 mm of thickness. Atomic Force Microscopy (AFM) studies were performed on a Nanoscope IV of Digital Instrument. Experiments were operated under tapping mode in air at ambient conditions.

Results and Discussion

The polymerization reaction of the different samples was monitored by infrared spectroscopy, collecting several spectra before reaching the gel point of the reaction mixture.

Figure 1 (left) shows the scale expanded infrared spectra of sample 70/30 PCL/PDMS. As can be observed, the absorbance of the band at 2200 cm⁻¹, assigned to the isocyanate stretching vibration decreases with the reaction time, which is indicative of

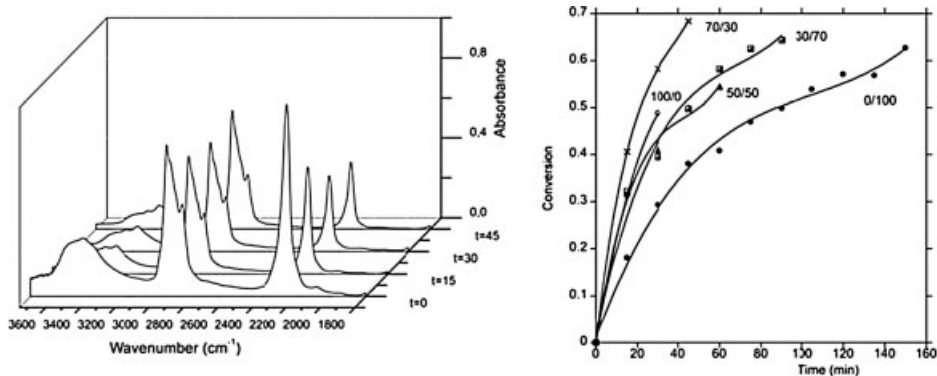


Figure 1.

Scale expanded infrared spectra of sample 70/30 PCL/PDMS vs. reaction time (left) and conversion vs. time (right) for different samples.

the polymerization process. The conversion of the reaction, shown in Figure 1 (right) can be calculated according to equation 1.

$$\text{Conversión} = 1 - \frac{(A_{2400}/A_{3000})_t}{(A_{2400}/A_{3000})_{t_0}} \quad (1)$$

where A_{2240} and A_{3000} are the areas of the absorptions at 2240 and 3000 cm^{-1} at initial time (t_0) and time (t) respectively.

As can be observed, as the content of the trifunctional polyol (PCL) in the samples increased less experimental points could be obtained because the gel point was reached at lower conversions. However, comparing the conversion obtained at the same reaction time for different systems, except for the sample containing only PCL (100/0) it seems that the conversion was lower as the PDMS content increased. This result can be explained upon the basis of a lower reactivity of PDMS polyol.

In order to study the microstructure of the samples DMTA measurements were carried out (Figure 2). For PCL/PDMS (0/100) sample, two peaks were observed (named I and III in Figure 2). The lower temperature mechanical loss process (I), located at -95°C was assigned to the segmental motion of PDMS units.^[16] In addition, the strength of this relaxation reduced with the PDMS content, supporting this assignment. The higher tempera-

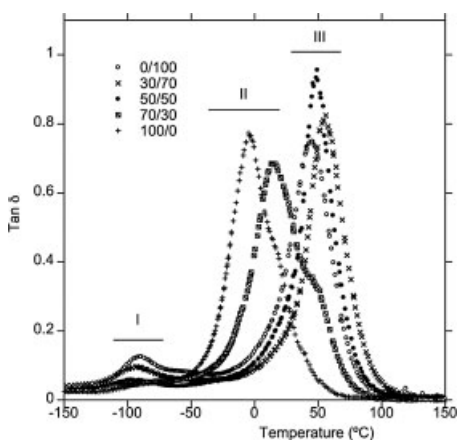


Figure 2. Tan δ vs. temperature for different samples (PCL/PDMS/IPDI).

ture segmental loss process at 48°C (III) was associated to the mixing of the PDMS final Poly(ethylene glycol) end groups with the IPDI trimer. These segments are not compatible with the PDMS units and therefore in (0/100) PCL/PDMS sample two transitions were observed.

For PCL/PDMS (100/0) sample, one main transition (II) was observed at -1°C , indicating the total compatibility between the PCL and IPDI segments. For the sample containing 30% of PDMS (70/30), the transition assigned to the PCL/IPDI segments (II) shifted towards higher temperatures and for the samples containing higher PDMS contents the transition was not detected, probably because it was overlapped with III. The shift of the II peak can be explained taking into account that there is a partial mixing between the PCL segments and the final Polyethylene glycol groups of PDMS units.

However, the position of the segmental motion of PDMS units (I) did not change with the introduction of PCL in the structure, indicating no discernible mixing between the siloxane units and PCL, and the formation of pure PDMS unit microphases.^[17]

Figure 3 shows the water contact angle of the surfaces in contact with aluminium

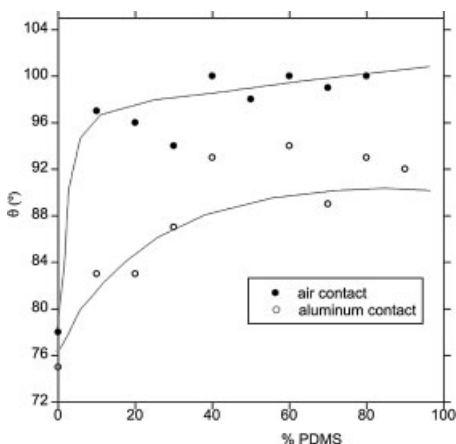


Figure 3. Water contact angles vs. siloxane content for both faces of the different films.

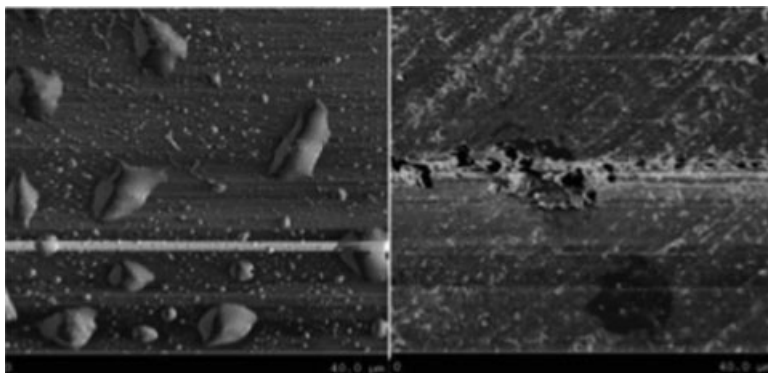


Figure 4.

AFM images ($40 \times 40 \mu\text{m}$) of the 70/30 sample (PCL/PDMS). Air contact (left) aluminium contact (right).

and air for the different composition samples. As can be seen, no PDMS containing sample showed a contact angle near 77° , characteristic of a hydrophilic surface. However, the incorporation of a 10% of PDMS to the polyol mixture caused an important increase of the water contact angle, especially on the face in contact with air, where the value increased to 96° , making the surface hydrophobic. Additional increments of the PDMS content did not significantly affect the air contact surface hydrophobicity. Moreover, comparing the data of the contact angles obtained in both surfaces, it is clear that higher angles were obtained in the air contact generated surface what means that there was a higher concentration of less polar siloxane domains in this surface.

In order to compare the morphology of the air and aluminum contact surfaces AFM images were registered (Figure 4).

The AFM image showed a two-phase morphology on the surface obtained in contact with air while a homogeneous surface was observed on the aluminum generated surface. From these results it could be deduced that probably the dispersed phase observed on the surface in contact with air is mainly composed of siloxane domains. This morphology is probably the reason of the higher water contact angle shown by this surface.

Conclusion

The DMTA results of the synthesized urethane/siloxane copolymers showed that the systems were phase separated. The sample containing only the polycaprolactone polyol was hydrophilic but the addition of small quantities of siloxane polyol increased substantially the water contact angle, changing the surface to hydrophobic. The water contact angles obtained on the surfaces generated in contact with air were higher than the obtained on the aluminum contact surface, suggesting that the siloxane content was higher in the air generated surface and evidencing the self stratification of the coating. AFM images supported this hypothesis.

Acknowledgements: The authors thank the Basque Government (PhD scholarship), The University of the Basque Country (UFI 11/56) and the Ministerio de Ciencia e Innovación (MAT2010-16171) for the funding received to develop this work.

- [1] M. Ma, R. M. Hill, *Curr. Opin. Colloid Interface Sci.* **2006**, *11*, 193.
- [2] L. Feng, S. Li, Y. Li, H. Li, L. Zhang, J. Zhai, Y. Song, B. Liu, L. Jiang, D. Zhu, *Adv Mater* **2002**, *14*, 1857.
- [3] T. Nishino, M. Meguro, K. Nakamae, M. Matsushita, Y. Ueda, *Langmuir* **1999**, *15*, 4321.

- [4] N. Verplanck, Y. Coffinier, V. Thomy, R. Boukherroub, *Nanoscale Res. Lett.* **2007**, 2, 577.
- [5] Y. H. Zhou, Y. Bin, W. F. Yang, W. Liu, P. Wang, W. Zhang, I. Bello, S. T. Lee, *J. Nanosci. Nanotechnol.* **2011**, 11, 2292.
- [6] J. H. Hwang, H. Sung-Hoon, H. Lee, *J. Nanosci. Nanotechnol.* **2009**, 9, 3644.
- [7] A. Santiago, A. González, J. J. Iruin, M. J. Fernández-Berridi, L. Irusta, *J. Sol-Gel Sci. Technol.* **2012**, 61, 8.
- [8] C. T. Hsieh, F. L. Wu, W. Y. Chen, *Surf. Coat. Technol.* **2009**, 203, 3377.
- [9] M. Minglin, M. Gupta, Z. Li, K. Zhau, K. K. Gleason, R. E. Cohen, M. F. Rubner, G. C. Rutledge, *Adv. Mater.* **2007**, 19, 255.
- [10] L. Buruaga, A. González, L. Irusta, J. J. Iruin, *J. Appl. Polym. Sci.* **2011**, 120, 1520.
- [11] F. Fenouillot, F. Méchin, F. Boisson, P. Alcouffe, T. Pokropski, T. Kallel, M. Mnif, *Eur. Polym. J.* **2012**, 48, 284.
- [12] P. Mujundar, D. C. Webster, *Polymer* **2007**, 48, 7499.
- [13] P. Mujundar, D. C. Webster, *Polymer* **2006**, 47, 4172.
- [14] Y. Tezuka, H. Kazama, K. Imai, *J. Chem. Soc., Faraday Trans.*, **1991**, 87, 147.
- [15] S. Sommer, A. Ekin, D. C. Webster, S. J. Stafslie, J. Daniels, L. J. VanderWal, S. E. M. Thompson, M. E. Callow, J. A. Callow, *Biofouling* **2010**, 26, 961.
- [16] R. Hernandez, J. Weksler, A. Padsalgikar, J. Runt, *Macromolecules* **2007**, 40, 5441.
- [17] R. Hernandez, J. Weksler, A. Padsalgikar, T. Choi, E. Angelo, J. S. Lin, L. C. Xu, C. A. Siedlecki, J. Runt, *Macromolecules* **2008**, 41, 9767.



Microphase separation and hydrophobicity of urethane/siloxane copolymers with low siloxane content



A. Santiago^a, L. Martín^b, J.J. Iruiñ^a, M.J. Fernández-Berridi^a, A. González^a, L. Irusta^{a,*}

^a POLYMAT, Department of Polymer Science and Technology, University of the Basque Country UPV-EHU, PO Box 1072, 20080 Donostia/San Sebastián, Spain

^b Group "Materials+Technologies", Department of Chemical and Environmental Engineering, Polytechnic School, University of the Basque Country UPV-EHU, Plaza Europa 1, 20018 Donostia/San Sebastián, Spain

ARTICLE INFO

Article history:

Received 19 April 2013

Received in revised form

21 November 2013

Accepted 7 January 2014

Available online 31 January 2014

Keywords:

Polyurethane–siloxane thermoset copolymers

Phase separation

Contact angle

Hydrophobicity

ABSTRACT

Polyurethane–siloxane thermoset copolymers were obtained from Isophorone diisocyanate trimer, Polycaprolactone triol and 10% of hydroxy terminated Polydimethyl siloxane. The copolymers showed a phase separated structure that depended on the conversion of the reaction and casting temperature. The different samples obtained had water contact angles higher than 90°. Moreover the contact angle values presented a maximum at intermediate reaction conversion. Although FTIR measurements showed that siloxane concentration at the surface increased with reaction time, the maximum contact angle value was related to the higher roughness calculated from AFM images. DMTA results confirmed that the phase separation was higher at intermediate conversions.

© 2014 Elsevier B.V. All rights reserved.

1. Introduction

Segmented polyurethanes present unusual properties directly related to their two-phase microstructure. This microstructure is a consequence of the thermodynamic incompatibility between the hard and soft segments [1,2].

The introduction of nonpolar macrodiols such as Polydimethylsiloxane [3–5] in the polyurethane backbone gives rise to nanostructured surfaces that can be used to generate hydrophobic materials [6–8]. Surface composition analysis of block and graft copolymers containing Polydimethylsiloxane (PDMS) segments has shown that PDMS predominates on the surface due to its immiscibility with other polyurethane components and its low surface energy [9–12]. This type of surfaces is of special interest because they have shown to be effective in reducing the interactions associated with biofouling [13,14]. PDMS elastomers with well-defined microtopographical features inhibit the settlement of fouling organisms [15–17] and this is important since copper and tributyltin (TBT) boat paints, used to prevent fouling, cause particular environmental damage.

In a previous work [18], we reported the synthesis and surface hydrophobicity (via water contact angle measurements) of

a series of copolymers obtained from Isophorone diisocyanate (IPDI), Polycaprolactone triol (PCL) and different amounts of hydroxy terminated Polydimethylsiloxane. It is interesting to note that the addition of small quantities of Polydimethylsiloxane increased substantially the water contact angle without considerable modification of the polyurethane chemical structure. Additional increments of the PDMS content did not affect the surface hydrophobicity.

Bearing in mind these results, the present work is devoted to enhance the surface hydrophobicity of a copolymer containing 10% of siloxane units. Following Webster [10,11,19] methodology, Acetylacetone was added to the formulation in order to control the phase separation of the copolymer, while trying to elucidate the role of the surface microstructure on the hydrophobicity.

2. Experimental part

2.1. Materials

Aliphatic Polyisocyanate Vestanat T 1890 E (IPDI trimer, 70 wt% in Butyl acetate) was obtained from Evonik Industries. Polydimethylsiloxane terminated in Polyethylene glycol (PDMS, Mn 1000 g mol⁻¹, 20 wt% non siloxane component) was supplied by Gelest Inc. Trifunctional polyol (Polycaprolactone, PCL, Mn 900 g mol⁻¹), Dibutyltin dilaurate (DBTDL), Butyl acetate (BA) and Acetylacetone (AA) were supplied by Sigma-Aldrich.

* Corresponding author. Tel.: +34 943015351; fax: +34 943015270.
E-mail address: lourdes.irusta@ehu.es (L. Irusta).

2.2. Coating preparation

In order to prepare coating formulation PCL (81 g, 9 mmol) and PDMS (1 g, 1 mmol) solutions in Butyl acetate (33 wt% of solids) were introduced in a 100 mL Erlenmeyer at room temperature and mixed for 1 min under magnetic stirring. The equivalent ratio between both polyols was 90:10 PCL:PDMS. Then, 10.13 g (10.6 mmol) of IPDI trimmer, NCO:OH equivalent ratio 11:10 and different amounts of AA were added. Finally DBTDL (19 mg, 0.03 mmol) was added to start the reaction.

At a variety of reaction times, between 15 min and 24 h, the solutions (4 mL) were casted over aluminium pans of 43 mm diameter following two methods. In the first one the coating was kept under room conditions for 24 h. In the second one, the coating was kept at 50 °C for 24 h on a hot plate in a fume hood. In both cases, this was followed by oven curing at 80 °C for 45 min.

2.3. Instrumentation

Samples for FTIR studies were prepared on KBr pellets using Spin Coating (speed 1900 rpm for 15 s [Spin Coater SCC-200]). The spectra were registered on a Nicolet 6700 (Thermo Scientific) FTIR spectrometer. Scanning resolution was 4 cm⁻¹ and 10 scans were taken. Attenuated Total Reflectance (ATR) experiments were carried out using an ATR objective (Thermo Electron Corp. Infinity ReFlachromat) provided with a Germanium crystal mounted on a microscope (Nicolet Continuum FT-IR microscope) attached to FTIR spectrometer. A MCT detector was used. The ATR measurements were recorded at a resolution of 8 cm⁻¹ and 64 scans were taken.

The contact angle measurements were performed in an OCA20 Instrument at Static Mode, in a room with controlled temperature and humidity (25 °C and 55% of respectively). The measurements were made by pouring a drop of 10 μL of distilled water over the surface and replicating five times for each point.

Dynamic mechanical properties were analyzed in a Polymer Laboratories Mark III Dynamic Mechanical Analyzer DMTA in single cantilever mode. Scans of temperature from -150 to 150 °C at a frequency of 1 Hz, using a displacement of 0.050 mm and a heating rate of 4 °C min⁻¹ were carried out in bending mode, employing samples with dimensions of 5 mm length, between 7 and 9 mm of width and between 15 and 19 mm of thickness.

Atomic Force Microscopy (AFM) studies were performed in a Multimode Nanoscope IV of Digital Instruments. Experiments were operated under Tapping mode in air at ambient conditions. Samples for AFM studies were prepared by casting over glass surface. Topographical and Phase images of 20 μm × 20 μm were obtained.

3. Results and discussion

The polymerization reaction resulting from a variation in AA percentage was monitored by infrared spectroscopy, and several spectra collected before the gel point of the reaction mixture was reached.

Fig. 1 shows the infrared spectrum of the sample obtained after 240 min of reaction. The absorbance of the infrared band at 2240 cm⁻¹ assigned to the isocyanate stretching vibration, whose relative concentration decreased during the polymerization process, was used to calculate the conversion as described in a previous paper [18].

In order to calculate the conversion, the absorption of the isocyanate band was normalized with a band that did not change during the polymerization process. The C–H stretching band was

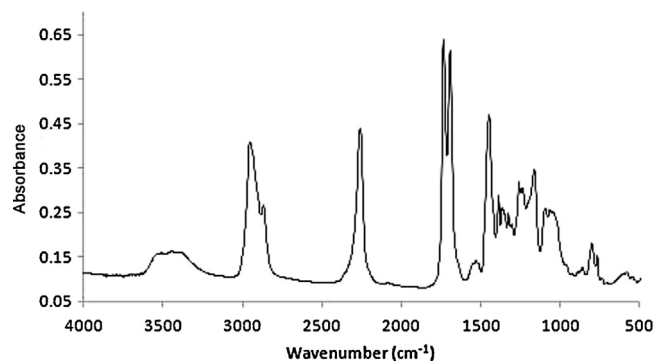


Fig. 1. Infrared spectrum of the sample obtained after 240 min of reaction.

selected for this purpose. The conversion of the reaction can be calculated according to Eq. (1)

$$\text{conversion} = 1 - \frac{(A_{2240}/A_{3000})_t}{(A_{2240}/A_{3000})_{t_0}}$$

where A_{2240} and A_{3000} are the areas of the absorptions at 2240 and 3000 cm⁻¹ at initial time (t_0) and time (t), respectively.

The conversion for samples containing different Acetylacetone (AA) concentration is shown in Fig. 2. As can be observed, the conversion increased with the reaction time. However, regardless of Acetylacetone concentration, the maximum value was always lower than 0.6. Nevertheless, only in the case of the system containing 10% of Acetylacetone (AA) was it possible to monitor the reaction for longer before the product gelled. This result proves that the Acetylacetone reduces the reaction rate and therefore the gel point is reached at longer reaction times. This fact can be explained upon the basis of the complexation of Acetylacetone with the Stannous catalyst, which decreases the catalytic effect of DBTDL [20]. Similar conversions were obtained in literature [19].

As we are interested in preparing films at different reaction conversions, the subsequent experiments were performed using 10% of Acetylacetone because this percentage delays the reaction for one day offering the possibility of controlling the conversion of the reaction.

Thus, a series of films containing 10% of AA were prepared from samples taken at different reaction times and water contact angle measurements were performed. Fig. 3 shows the values of the contact angle for films obtained at room temperature and at 50 °C as function of the reaction time.

As can be observed, in both temperatures all films showed contact angles higher than 90°, which means that this surface was hydrophobic. No significant differences were observed between

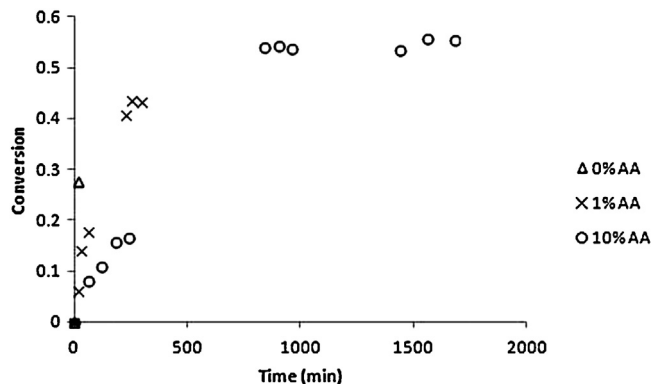


Fig. 2. Conversion vs. time for samples containing different Acetylacetone (AA) concentration.

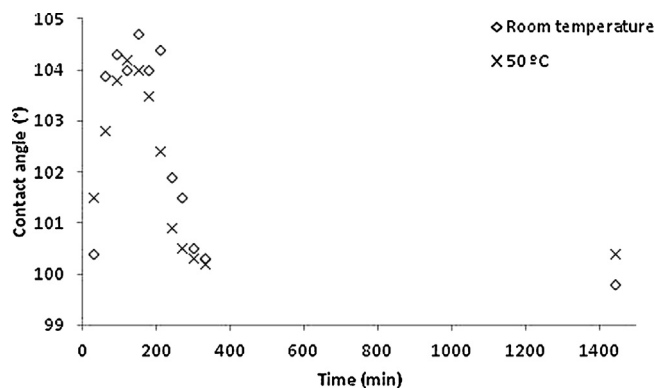


Fig. 3. Contact angle vs. time for the films obtained by casting at room temperature and at 50 °C.

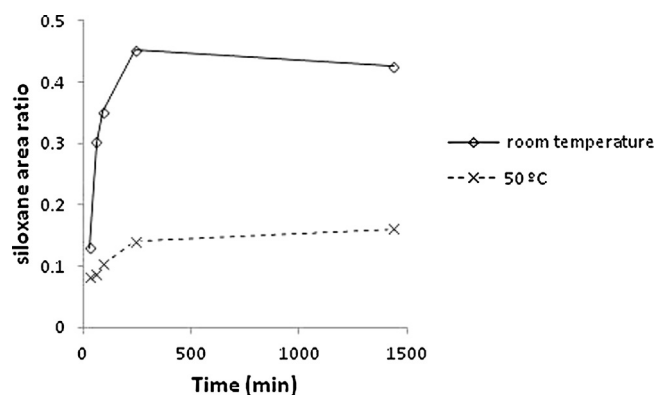


Fig. 4. Siloxane relative concentration determined by ATR as a function of the reaction time for samples generated at room temperature and at 50 °C.

50 °C and room temperature films although the surfaces obtained at 50 °C presented lower values at the maximum point.

According to literature, the hydrophobicity of the film surfaces could be due to the segregation towards the surface of the more incompatible and less polar siloxane domains so as to minimize the interfacial tension with air [10–12,19]. In order to calculate the concentration of siloxane at the surface, ATR-FTIR spectroscopy measurements were performed. The ratio of the bands at 800 cm^{-1} ,

assigned to the deformation of the siloxane methyl groups, and the band at 3000 cm^{-1} , assigned to the C–H stretching of all components was used as a relative measure of the siloxane concentration. The results obtained for the samples prepared at room temperature and at 50 °C are shown in Fig. 4.

As observed in Fig. 4 the amount of siloxane increased with the reaction progress reaching a plateau at about 300 min of reaction. In addition, the concentration of siloxane at the surface was higher in the films generated at room temperature than those at 50 °C.

As the concentration of siloxane increased with the reaction time and as siloxane has a low surface tension, the contact angle should increase with the reaction time. However, as shown in Fig. 3 at long reaction times the contact angle decreased. This fact shows that the surface composition is not the only factor that controls the surface hydrophobicity. As it is well known that the surface roughness modifies the wetting properties of the samples [6,21], AFM images of the surfaces were recorded.

Fig. 5 shows the AFM images of the films obtained by casting at different reaction times at room temperature. As can be observed, some of the images showed a phase separated structure with microtopographical surfaces. According to literature [22], the dispersed phase is composed of siloxane domains.

The images of the samples obtained after 30 and 60 min of reaction time showed a homogeneous surface. After 90 min of reaction, microdomains with uniform spherical shapes were observed. The size of these microdomains grew with the reaction time reaching a maximum at 150 min. Then, the size decreased and at 24 h no microdomains were formed.

According to these results, the reaction time and therefore, the extent of the reaction prior to film formation, had a significant influence in the microdomain formation. This behaviour has also been observed by Webster et al. [10]. According to these authors, the final mixing observed at high reaction times is related to the higher compatibility of the PDMS-IPDI/PCL-IPDI system at high conversion.

To explore the effect of film formation temperature on the generation of microtopographical surfaces, a series of coatings was prepared by casting at 50 °C. The time of reaction before casting varied from 30 min to 24 h.

Topographical and Phase images of the cured films were obtained by AFM. The Phase images are shown in Fig. 6.

As can be observed in Fig. 6, phase separated surfaces were generated at about 60 min of reaction and homogeneous surfaces were obtained after 180. In this case, the growing of the siloxane domains

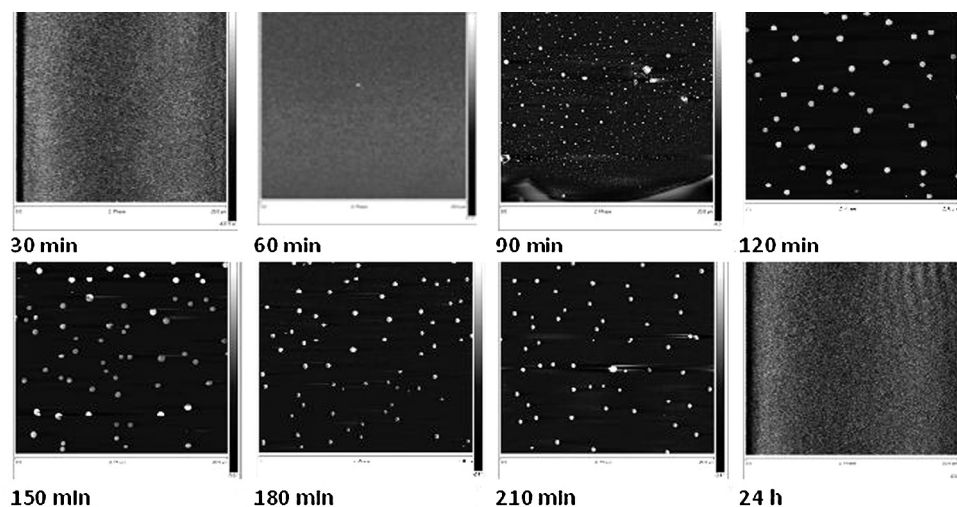


Fig. 5. AFM phase images ($20\text{ }\mu\text{m} \times 20\text{ }\mu\text{m}$) for films obtained at different reaction times at room temperature.

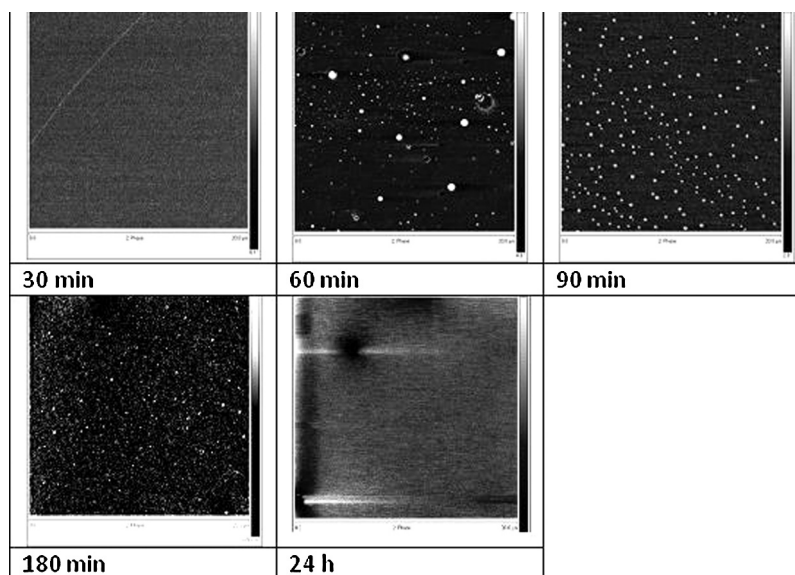


Fig. 6. AFM phase images ($20\ \mu\text{m} \times 20\ \mu\text{m}$) for films obtained by casting at $50\ ^\circ\text{C}$ at different reaction times.

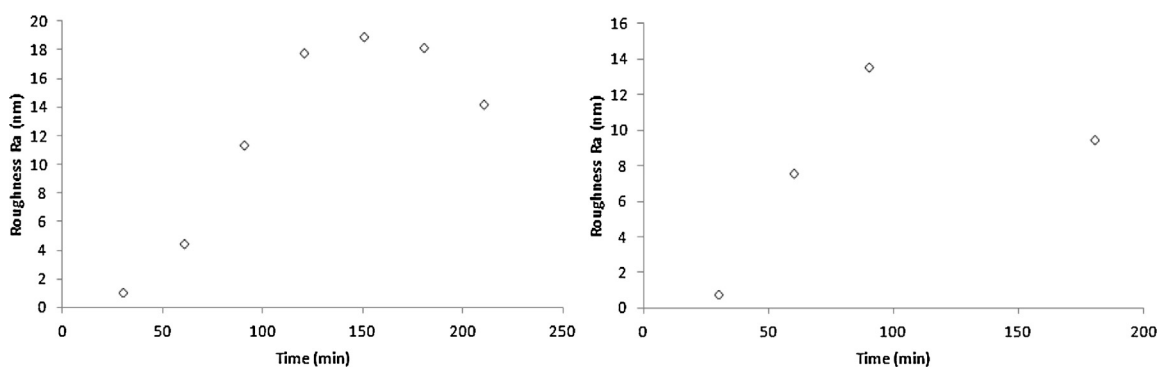


Fig. 7. Superficial roughness obtained by AFM images of films obtained at room temperature (left) and at $50\ ^\circ\text{C}$ (right).

could not be observed, probably because the microdomain formation/no formation process took place in a shorter time interval.

This result can be explained upon the basis of a faster evaporation of Acetylacetone at $50\ ^\circ\text{C}$. As described in previous paragraphs, Acetylacetone slows down the reaction rate [20] and therefore the evaporation of this compound accelerates the phase formation/no formation process.

In order to relate the contact angle measurements to the surface topography of the sample, the roughness was calculated from AFM data, using the entire image for the quantification.

Fig. 7 shows the mean roughness (R_a) calculated directly from AFM signal of the films obtained at room temperature and at $50\ ^\circ\text{C}$. As can be observed, in the room temperature generated surface, the roughness increased with the reaction time and after 150 min of reaction the roughness decreased. For the films generated at $50\ ^\circ\text{C}$ the behaviour was the same but the maximum roughness was obtained at shorter reaction times. In literature, similar roughness values were obtained for 20% of siloxane containing systems [12]. It is interesting to note that the reaction time where the maximum roughness was reached was the same as the time where the maximum contact angle was obtained. According to this, the surface siloxane concentration is not the only factor that governs the sample hydrophobicity and the surface roughness plays an important role.

This result is not in accordance with literature data [11], where for similar systems it is said that the contact angle does not depend

on the formation of any structured surface. However, our results showed that the contact angle of the structured surfaces were slightly higher as a result of the increased roughness.

It is clear that the structured surfaces are generated as a consequence of the phase separation between the siloxane and PCL segments. In order to study the phase separation of the samples, DMTA measurements were carried out. Fig. 8 shows as an example

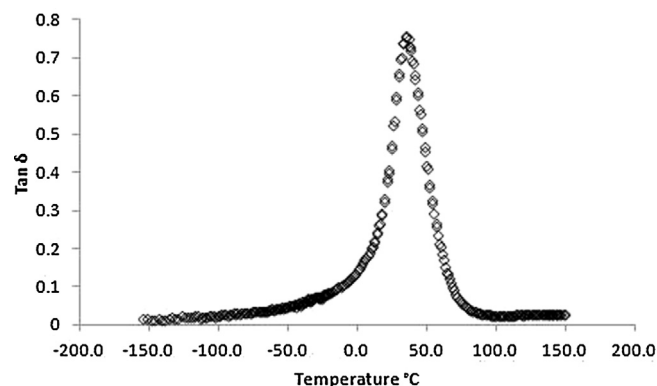


Fig. 8. $\text{Tan}\delta$ vs. temperature for the sample obtained after 60 min of reaction at room temperature.

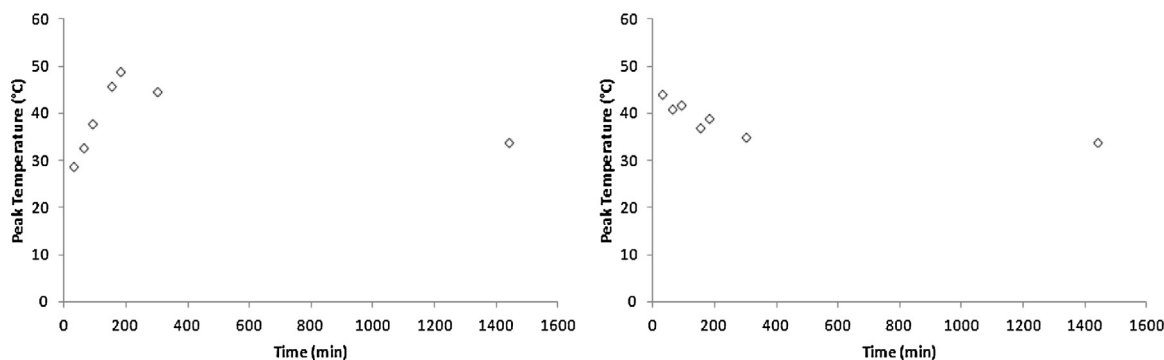


Fig. 9. Maximum $\text{Tan}\delta$ vs. reaction time in films obtained by casting at room temperature (left) and at 50 °C (right).

the thermogram of the sample obtained at 60 min of reaction and casted at room temperature.

All the samples showed a single maximum in the $\text{Tan}\delta$ that, according to previous results, can be assigned to the glass transition temperature of the PCL/IPDI segments [10]. The transition assigned to the segmental motion of the PDMS units at about -95 °C [3,5] could not be detected because of the low concentration of this component.

It is interesting to note that the temperature of the δ maximum changed slightly with the reaction time and casting temperature. Fig. 9 shows the values of the maximum in δ as a function of the reaction time for the samples obtained by casting at room temperature (left) and at 50 °C (right).

For the samples obtained by casting at room temperature, the transition temperature increased slightly with the reaction time and after reaching a maximum at 180 min decreased.

As the system is phase separated and the glass transition of the PDMS units is about -95 °C, the lower temperature of the δ can be associated to a higher mixing of the PDMS segments with the PCL/IPDI matrix. On the contrary, higher phase separation will lead to higher $\text{Tan}\delta$ values [23,24].

According to this, DMTA results show that for the room temperature casted films the phase separation showed a maximum at about 180 min of reaction time. The DMTA results for the films obtained by casting at 50 °C showed δ values lower than those obtained for the room temperature casted samples, which means that the phase separation was lower when the samples were casted at the higher temperature.

4. Conclusions

Polyurethane–siloxane thermoset copolymers containing 10% of siloxane showed a phase separated structure that depended on the conversion of the reaction and casting temperature. Samples obtained at different reaction times had water contact angles higher than 90° but maximum angles were obtained at intermediate reaction times. FTIR measurements showed that siloxane concentration at the surface increased with reaction time and therefore the maximum contact angle value was related to the higher roughness calculated from AFM images.

Acknowledgements

The authors thank the Basque Government (PhD scholarship), The University of the Basque Country (UFI 11/56) and the Ministerio de Ciencia e Innovación (MAT2010-16171) for the funding received to develop this work. Technical and human support provided by Macrobehaviour-Mesostructure-Nanotechnology SGIker service (UPV/EHU, MICINN, GV/EJ, ERDF and ESF) is also gratefully acknowledged.

References

- [1] R. Hernandez, J. Weksler, A. Padsalgikar, T. Choi, E. Angelo, J.S. Lin, L.-C. Xu, C.A. Siedlecki, J. Runt, *Macromolecules* 41 (2008) 9766–9767.
- [2] L. Irusta, M.J. Fernandez-Berridi, *Polymer* 41 (2000) 3297–3302.
- [3] R. Hernandez, J. Weksler, A. Padsalgikar, J. Runt, *Macromolecules* 40 (2007) 5441–5449.
- [4] M.V. Pergal, V.V. Antić, M.N. Govedarica, D. Goševac, S. Ostojić, J. Djonlajić, *J. Appl. Polym. Sci.* 122 (2011) 2715–2730.
- [5] H.Y. Tsi, C.C. Chen, W.C. Tsen, Y.C. Shu, F.S. Chuang, *Polym. Test.* 30 (2011) 50–59.
- [6] H. Assender, V. Bliznyuk, K. Porfyrakis, *Science* 297 (2002) 973–976.
- [7] I.P. Parkin, R.G. Palgrave, *J. Mater. Chem.* 15 (2005) 1689–1695.
- [8] M. Ma, R.M. Hill, *Curr. Opin. Colloid Interface Sci.* 11 (2006) 193–202.
- [9] S. Sommer, A. Ekin, D.C. Webster, S.J. Stafslin, J. Daniels, L.J. VanderWal, S.E.M. Thompson, M.E. Callow, J.A. Callow, *Biofouling* 26 (2010) 961–972.
- [10] P. Majumdar, D.C. Webster, *Polymer* 48 (2007) 7499–7509.
- [11] P. Majumdar, S. Stafslin, J. Daniels, D. Webster, *J. Coat. Technol. Res.* 4 (2007) 131–138.
- [12] M.V. Pergal, J.V. Džunuzović, R. Poreba, S. Ostojić, A. Radulović, M. Špirková, *Prog. Org. Coat.* 76 (2013) 743–756.
- [13] S. Krishnan, R. Ayothi, A. Hexemer, J.A. Finlay, K.E. Sohn, R. Perry, C.K. Ober, E.J. Kramer, M.E. Callow, J.A. Callow, D.A. Fischer, *Langmuir* 22 (2006) 5075–5086.
- [14] C.S. Gudipati, C.M. Creenlief, J.A. Johnson, P. Prayonpcan, K.L. Wooley, *J. Polym. Sci., Part A: Polym. Chem.* 42 (2004) 6193–6208.
- [15] M.E. Callow, A.R. Jennings, A.B. Brennan, C.E. Seegert, A. Gibson, L. Wilson, A. Feinberg, R. Baney, J.A. Callow, *Biofouling* 18 (2002) 237–245.
- [16] J.F. Schumacher, M.L. Carman, T.G. Estes, A.W. Feinberg, L.H. Wilson, M.E. Callow, J.A. Callow, J.A. Finlay, A.B. Brennan, *Biofouling* 23 (2007) 55–62.
- [17] M.L. Carman, T.G. Estes, A.W. Feinberg, J.F. Schumacher, W. Wilkerson, L.H. Wilson, M.E. Callow, J.A. Callow, A.B. Brennan, *Biofouling* 22 (2006) 11–21.
- [18] A. Santiago, A. González, J.J. Iruin, M.J. Fernández-Berridi, M.E. Muñoz, L. Irusta, *Macromol. Symp.* 321–322 (2012) 150–154.
- [19] P. Majumdar, D.C. Webster, *Polymer* 47 (2006) 4172–4181.
- [20] I.N. Bakirova, L.A. Zenitova, N.A. Rozental', *Russ. J. Appl. Chem.* 79 (2006) 811–813.
- [21] N. Verplanck, Y. Coffinier, V. Thomy, R. Boukherroub, *Nanoscale Res. Lett.* 2 (2007) 577–596.
- [22] P. Majumdar, D.C. Webster, *Macromolecules* 38 (2005) 5857–5859.
- [23] T. Choi, J. Weksler, A. Padsalgikar, J. Runt, *Polymer* 51 (2010) 4375–4382.
- [24] T. Choi, J. Weksler, A. Padsalgikar, J. Runt, *Polymer* 50 (2009) 2320–2327.

Resistance to protein sorption as a model of antifouling performance of Poly(siloxane-urethane) coatings exhibiting phase separated morphologies

A. Santiago ^(a), L. Irusta ^(a), T. Schäfer ^{(a),(c)}, A. Corres ^(a), L. Martin ^(b), and A. González ^(a)

(a) POLYMAT, Department of Polymer Science and Technology, University of the Basque Country UPV-EHU, PO Box 1072, 20080 Donostia/San Sebastián, Spain.

(b) Macrobehaviour-Mesostructure-Nanotechnology SGIker Service, Polytechnic School, University of the Basque Country UPV-EHU, Plaza Europa 1, 20018 Donostia/San Sebastián, Spain.

(c) Ikerbasque, Basque Foundation for Science, Bilbao, Spain

Abstract

In this study, bovine serum albumin (BSA) adsorption measurements were used as a model test to investigate the anti-biofouling performance of hybrid poly(siloxane-urethane) coatings. Different coatings were obtained from isophorone diisocyanate trimer, polycaprolactone triol and hydroxy-terminated poly(dimethylsiloxane). The copolymers showed a phase separated structure that depended on the mixing time and casting temperature. Two types of adsorption measurements were performed: (a) static adsorption measurements, immersing the film in a BSA solution and determining the BSA concentration of the remaining solution by UV; (b) measuring the adsorption using a quartz crystal microbalance with dissipation monitoring (QCM-D). According to static adsorption measurements, the BSA adsorption was reduced when the coatings showed a phase separated structure. In addition, QCM-D measurements, and particularly the dissipation data, showed that in nanostructured coatings the protein adsorption occurred in a conformation that prevented water retention. The latter could be the origin of the fouling resistance ability of these copolymers.

Keywords

Poly(siloxane-urethane) thermoset copolymers, phase separation, protein adsorption, QCM-D.

Highlights

Poly(siloxane-urethane) thermoset copolymers; Fouling resistance coatings; protein adsorption UV and QCM-D; phase separation reduces protein adsorption;

1. Introduction

Biofouling is generally defined as the accumulation of living organisms including microorganisms, algae and animals on a wetted surface. This undesirable colonization has a serious impact that can be environmental, economic and/or ecological. Although toxic antibiofouling coatings containing tin, copper and other biocides have provided an effective control of many fouling species, they have a detrimental impact on the environment [1,2]. In order to lessen this impact there is a growing interest in the development of non-toxic antibiofouling coatings [3,4].

Traditionally, the fouling process has been divided into different stages: the initial stage is mainly due to the adsorption of molecules, such as polysaccharides, proteins and proteoglycans, and gives rise to the so-called conditioning film [1]. This initial stage is considered problematic as it subsequently triggers severe fouling. As a result, the adsorption of proteins is considered in some studies as a simplified way of evaluating the antifouling activity of a surface [5-7]. According to this assumption, surfaces with low protein adsorption are supposed to have greater anti-fouling efficiency.

Poly(dimethylsiloxane) PDMS or silicone materials have been the focus of extensive research in the development of minimally adhesive surfaces [8]. These materials have also led to studies of their utility as potential antifouling materials for marine applications, among other things, owing to their good fouling-resistance performance. However, PDMS has some obvious disadvantages, such as poor adhesion to substrates, low mechanical strength and high cost.

Self-stratified poly(siloxane-urethane) coatings try to overcome some of these disadvantages, such as poor adhesion, while keeping the fouling-release properties. These kinds of novel non-toxic fouling-release coatings are used to combat biofouling [9-12]. Due to the thermodynamic incompatibility between the siloxane and urethane components of the coating, the low surface energy siloxane component migrates to the surface, imparting hydrophobicity.

According to literature [5], it is clear that the surfaces presenting water contact angles between 60-80° give rise to high protein adsorption. However, surfaces with contact angles lower than 20° and approaching 120° exhibit a reduction in protein adsorption. Therefore, in order to obtain an antifouling coating the surfaces with contact angles between 60-80° must be avoided. Poly(siloxane-urethane) coatings present water contact angles between 100-110° and are therefore good candidates to be applied as fouling release materials, as has been addressed in literature [11].

In previous works [13,14], we reported the synthesis and surface hydrophobicity of a series of poly(siloxane-urethane) copolymers with potential anti-fouling applications. It is interesting to note that the addition of small quantities of poly(dimethylsiloxane) increased the water contact angle and, hence, contact angle substantially. In addition, higher contact angles were obtained when the systems presented a phase separated morphology. According to some literature results, the anti-fouling ability of block copolymers is also related to the phase separated

morphology [15,16]. Bearing this in mind, the present work aims at determining the fouling-release capacity of these phase separated copolymers through protein adsorption measurements. Following the methodology used in previous work [13], acetyl acetone was added to the formulation in order to control the phase separation of the copolymer. Three different formulations containing 5 %, 10 % and 15 % of siloxane were synthesized using different mixing times to control sample morphology. The adsorption of the protein bovine serum albumine (BSA) was evaluated by using a colorimetric method [17] and by quartz crystal microbalance with dissipation monitoring (QCM-D) [18]. The adsorption data were correlated with the sample morphology.

2. Experimental Part

2.1. Materials

Aliphatic polyisocyanate Vestanat T 1890 E (IPDI trimer, 70 wt-% in butyl acetate) was obtained from Evonik Industries. Poly(dimethylsiloxane) terminated in polyethylene glycol (PDMS, Mn 1000 g mol⁻¹, 20 wt-% non siloxane component) was supplied by Gelest Inc. Trifunctional polyol (polycaprolactone, PCL, Mn 900 g mol⁻¹), dibutyltin dilaurate (DBTDL), butyl acetate (BA) and acetylacetone (AA) were supplied by Sigma-Aldrich. Bovine serum albumin protein (BSA) was supplied by Sigma-Aldrich. Dye reagent concentrate to perform the protein assay was obtained from Bio-Rad.

2.2 Coating Preparation

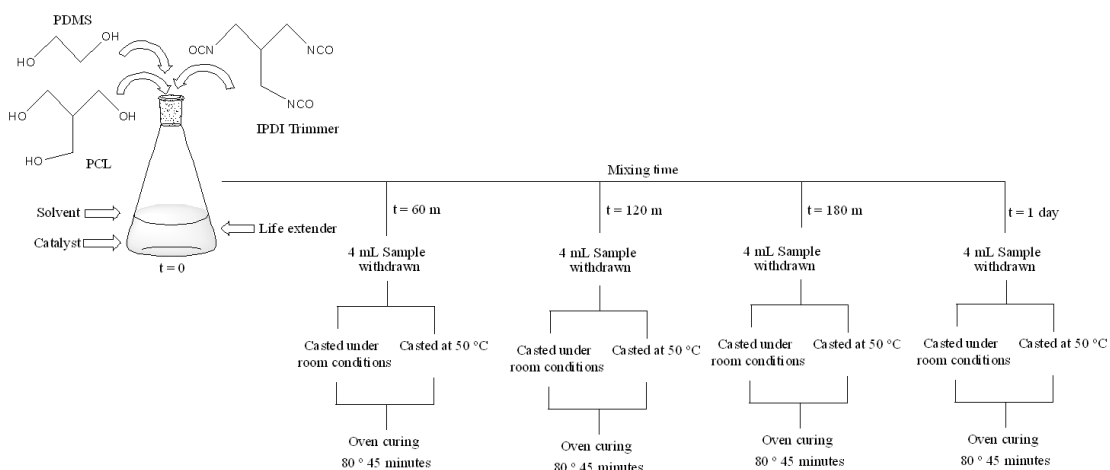


Fig.1. Scheme of the coating preparation process.

In order to prepare the coating formulation, PCL and PDMS solutions in butyl acetate (33 wt-% of solids) were introduced in a 100 mL erlenmeyer at room temperature and mixed for 1 min under magnetic stirring. The equivalent ratio between both polyols changed between 95:05 to 85:15 PCL:PDMS. Then, the required amount of IPDI trimer, NCO:OH equivalent ratio 1.1:1.0,

and 10% of AA were added to the reaction mixture. Finally, DBTDL (19 mg, 0.03 mmol) was added to start the reaction. At a variety of mixing times, between 60 min and 24 h, the solutions (4 mL) were cast over aluminium pans of 43 mm diameter following two methods. In the first, the coating was kept under room temperature for 24 h. In the second, the coating was kept at 50 °C for 24 h on a hot plate in a fume hood. In both cases, this was followed by oven curing at 80 °C for 45 minutes. The overall process is summarized in Fig.1.

2.3 Contact angle measurements

The contact angle measurements were performed in an OCA20 Instrument at static mode at controlled temperature and humidity (25 °C and 55 %, respectively). The volume of the deionized water droplets was 5 µL. For each composition, three films were analyzed and the contact angle measurements were made with five replicates for each film.

2.4 Atomic Force Microscopy studies

Atomic Force Microscopy (AFM) studies were performed in a Multimode Nanoscope IV of Digital Instruments. Experiments were operated under tapping mode in air at ambient conditions. Samples for AFM studies were prepared by casting over a glass surface. Topographical and phase images of 20 µm X 20 µm were obtained.

2.5 Protein sorption studies

The protein adsorption onto the polymer surface was analyzed using two different techniques. The first one was the Bio-Rad Protein Assay, which is a dye-binding assay where a differential colour change of a dye occurs in response to various concentrations of protein [19]. The standard procedure advised by Bio-Rad was followed. A standard curve for the Bio-Rad Protein Assay of bovine serum albumin (BSA) between 0.2 to 0.9 mg/mL was generated in order to determine the protein sorption behaviour of the films. UV-VIS transmittance spectra were obtained using a spectrophotometer Shimadzu UV-VIS-NIR 3600 using a photomultiplier tube detector. Samples with an outer surface area of 10 cm² and 200 µm of thickness were immersed in 100 mL BSA/water solution (0.45 mg/mL). At different times, 0.1 mL of the BSA/water solution were taken and after mixing with 5 mL of the dye reagent the concentration of BSA was calculated by UV-Vis absorption at 595 nm. The amount of BSA adsorbed by the sample was calculated by a mass balance using initial and final concentration of solutions measured by UV-Vis. Triplicate experiments were carried out for all systems studied.

The second technique used to determine the protein sorption behaviour was a quartz crystal microbalance with dissipation monitoring (QCM-D). Polymer-coated sensors were obtained by spin-coating the solutions onto a gold sensor (diameter = 14 mm, Q-SENSE, Sweden) at a rate of 2500 rpm for 30 seconds using a Lot Oriel SCC 200 spin-coater. After the spin coating, the samples were cured at 80 °C for 45 minutes.

QCM measurements were performed on a Q-SENSE E1 system operating at 23 °C. Prior to the experiments, the sensors were stabilized overnight under a constant water flux of 100 µL/min. Subsequently, the respective sensors were put in contact with different concentrations of BSA in aqueous solution up to a maximum of 100 mg BSA/L.

3. Results and discussion

3.1. Morphology and hydrophobicity of the coatings

The phase separation degree of the Poly(siloxane-urethane) copolymers depends on the reaction conversion as described by Webster et al [20]. In a previous paper [13] we presented similar results to those obtained by Webster using a copolymer containing 10% of siloxane. In that paper, the conversion was controlled by varying the mixing time, and the highest phase separated morphology was obtained at intermediate mixing times. Following the same methodology, in the present paper a series of films were prepared varying the siloxane content.

Topographical and phase images of the cured films were obtained by AFM. The phase images of samples generated at room temperature are shown in Fig. 2.

As can be seen, some of the images showed a phase separated structure with microtopographical surfaces, the dispersed phase being composed of siloxane domains. For each composition, no phase separated images were obtained at low and high mixing times and domain formation was observed at intermediate times. According to these results, the formation of microtopographical surfaces only occurred when the films were cast at intermediate conversion. When the conversion was higher, total miscibility between the urethane and siloxane components was obtained. The behaviour of the samples containing 10 and 15 % of PDMS was similar. However, in the sample containing 5 % of PDMS, the phase separated structures and the final mixing were obtained at lower mixing times.

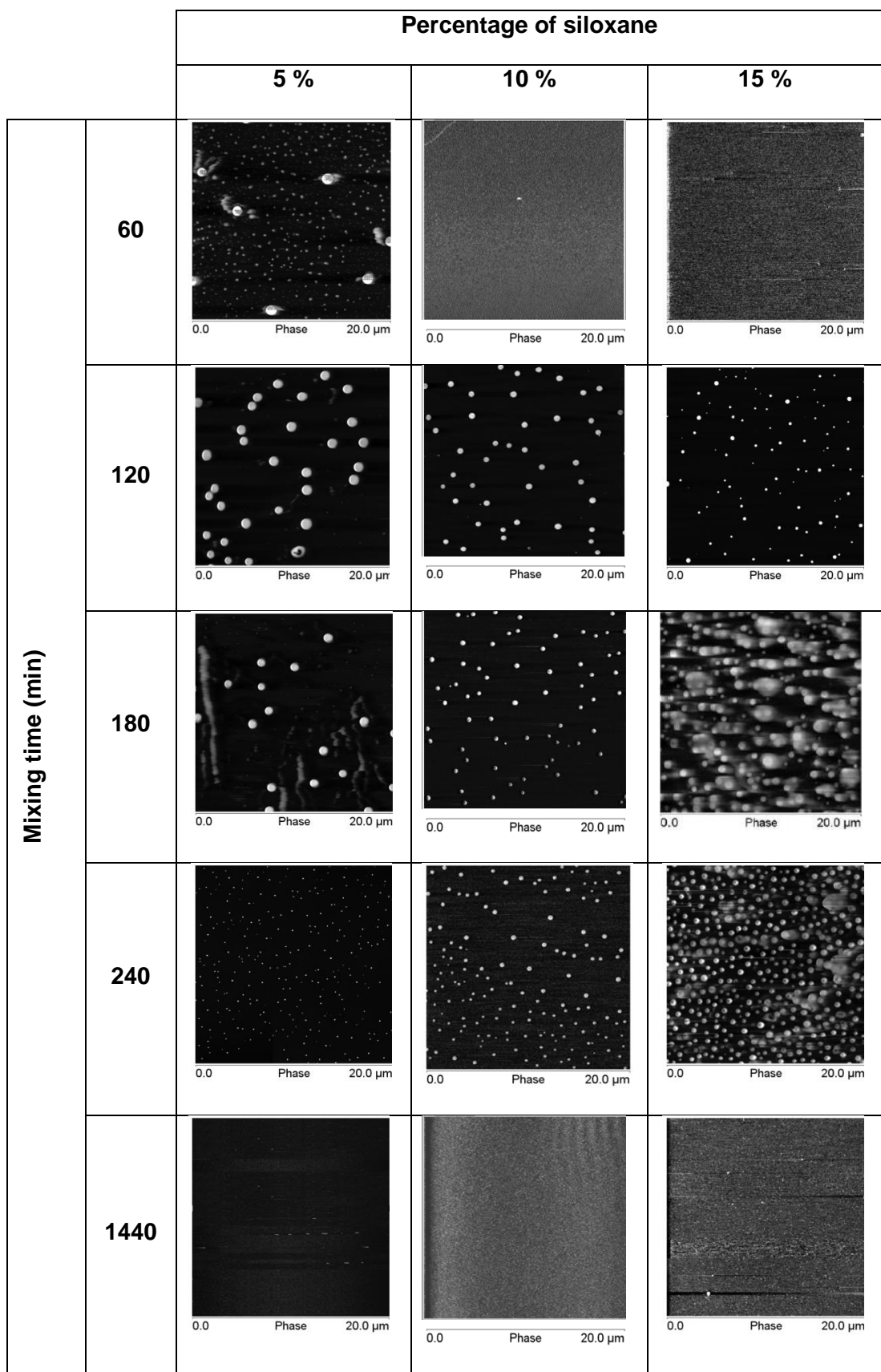


Fig. 2 AFM phase images (20 μm X 20 μm) for films obtained at room temperature with different amounts of PDMS at different mixing times.

The morphology of the coatings obtained at 50 °C is shown in Fig. 3.

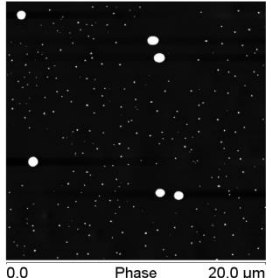
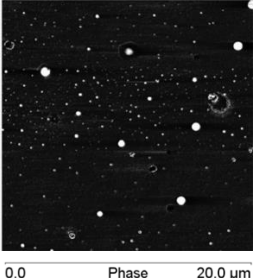
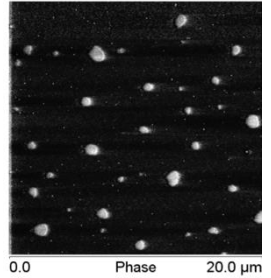
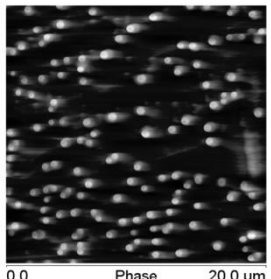
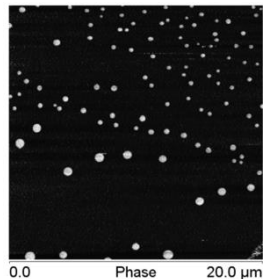
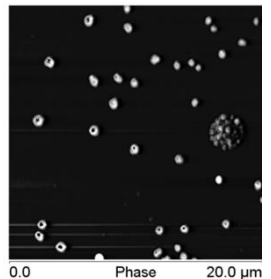
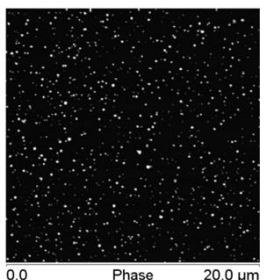
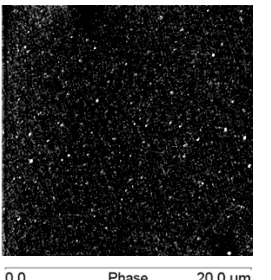
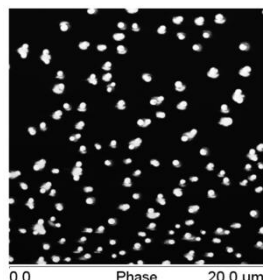
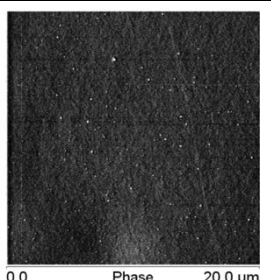
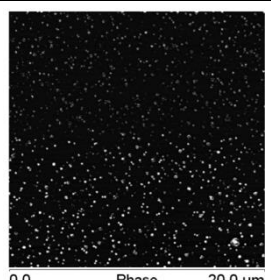
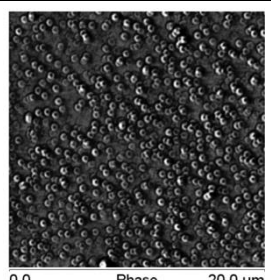
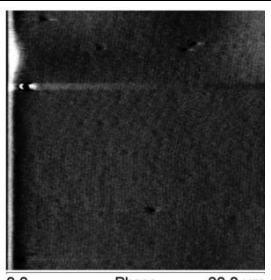
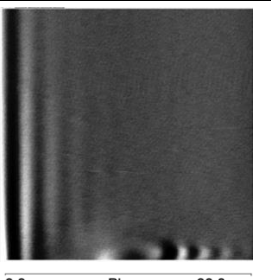
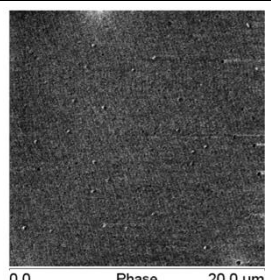
		Percentage of siloxane		
		5 %	10 %	15 %
Mixing time (min)	60			
	120			
	180			
	240			
	1440			

Fig 3. AFM phase images (20 μm X 20 μm) for films obtained at 50 $^{\circ}\text{C}$ with different amounts of PDMS at different mixing times.

In the case of the images obtained for films generated at 50 $^{\circ}\text{C}$ (Fig. 3), the behaviour was the same as that obtained for the room temperature cast samples. However, the microdomain formation process took place within a shorter time interval. This result could be explained on the basis of a faster evaporation of acetyl acetone at 50 $^{\circ}\text{C}$. As described in a previous paper [13] acetyl acetone slowed down the reaction rate and therefore the evaporation of this compound accelerated the phase formation process.

The hydrophobicity of the samples obtained at different mixing times was calculated by means of water contact angle measurements. The results are summarized in Fig 4.

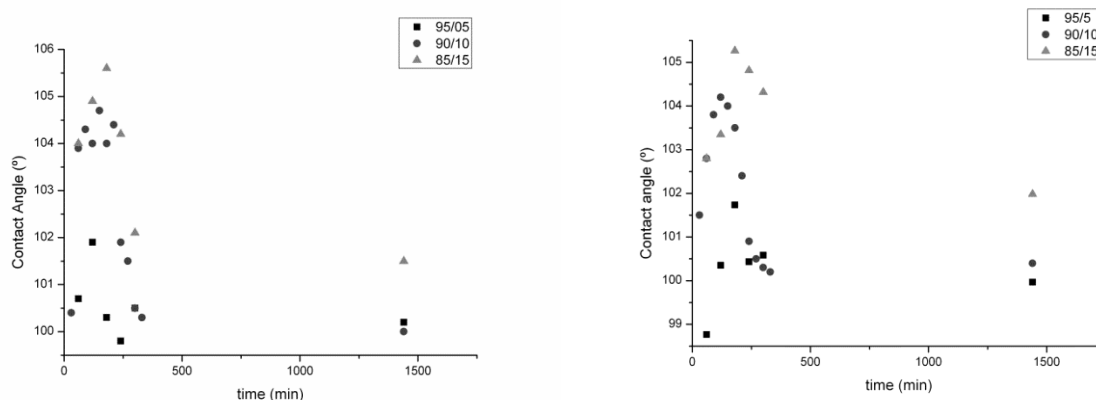


Fig 4. Contact angle values for the coatings generated at room temperature (left) and at 50 $^{\circ}\text{C}$ (right).

As can be observed, all the coatings showed contact angles higher than 90 $^{\circ}$ indicating that all surfaces were hydrophobic. In addition, regardless of sample composition and casting temperature, the maximum contact angles were obtained at intermediate mixing times. In relation to the sample composition, and for both temperatures, the maximum contact angles of samples containing 10 and 15% of siloxane were of the same order, although slightly higher values were obtained for the sample containing 15 % of siloxane. Lower contact angle values were obtained for samples with 5% of siloxane. Finally, it must be pointed out that for samples cast at 50 $^{\circ}\text{C}$, the maximum of the contact angles was obtained at mixing times lower than in the samples cast at room temperature.

All these results clearly showed that higher contact angles were obtained for samples generated at intermediate mixing times, and where the samples presented nanostructured morphologies. According to this, the surface morphology plays an important role in the surface wetting behaviour.

3.2. Evaluation of the antifouling performance

Protein adsorption measurements were performed as a simple way to evaluate the antifouling performance.

a) Static adsorption tests

Typical adsorption profiles of BSA for samples generated at room temperature and measured using the dye-binding assay are shown in Fig 5. In all cases, the data of a reference polyurethane without siloxane are included for comparison purposes.

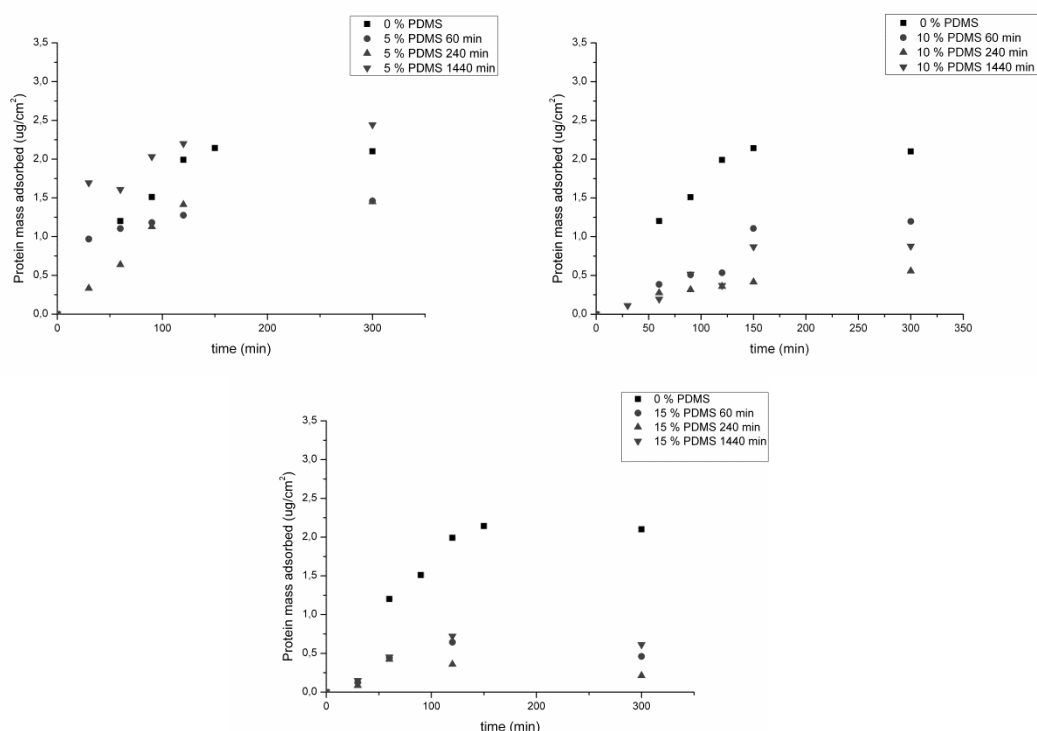


Fig 5. Sorption of the BSA protein over different films generated at room temperature versus time. A) Adsorption for films with 5% of PDMS (left). B) Adsorption for films with 10% of PDMS (right). C) Adsorption for films with 15% of PDMS (below).

The adsorption rate of BSA is influenced by the surface affinity and diffusion rate of the protein through the solution. At 300 minutes, nearly full coverage of each of the surfaces was observed.

For the samples containing 5% of siloxane, regardless the mixing time, the adsorption values were similar to those obtained for the reference polyurethane. However, reduced protein adsorption was obtained for samples containing 10 and 15 % of siloxane. This result proved that the siloxane reduced the adsorption of the protein. Therefore, these coatings could be interesting candidates as fouling release coatings. Similar conclusions have been reported using different Bio Assay measurements for poly(siloxane-urethanes) [21] and for polyester/polysiloxane coatings [22].

The BSA adsorption curves of the samples obtained by casting at 50 °C showed very similar behaviour to the data obtained from samples cast at room temperature. Table 1 summarizes the BSA adsorption values at 300 minutes for samples cast at different temperatures and times.

Table 1

BSA Protein adsorption at 300 minutes for coatings obtained at room temperature and at 50 °C.

PDMS %	Mixing time (min)	Adsorption (25°C) ($\mu\text{g}/\text{cm}^2$)	Adsorption (50°C) ($\mu\text{g}/\text{cm}^2$)
0	240	2.1	2.2
5	60	1.5	1.4
	240	1.4	1.5
	1440	2.4	3.2
10	60	1.2	1.0
	240	0.6	0.2
	1440	0.9	0.5
15	60	0.6	0.8
	240	0.2	0.6
	1440	0.6	0.8

As can be observed, for each composition and casting temperature the adsorption of BSA was lower in the samples obtained at 240 minutes where the samples presented nanostructured morphology and higher contact angles.

Comparing the data of different composition containing samples, it became clear that 5% of siloxane was not enough to significantly reduce the protein adsorption. The data obtained for 10 and 15 % of siloxane were not conclusive. Thus, for the samples cast at room temperature, the best results were obtained for samples containing 15% of siloxane. For those cast at 50 °C, the sample containing 10% of siloxane showed less protein adsorption.

b) Quartz Crystal Microbalance (QCM-D) Measurements

The data obtained from the static adsorption test showed that the nanostructured samples gave rise to lower BSA adsorption values. In order to obtain information about the reason for this behaviour, the adsorption of BSA of samples containing 10% of siloxane cast at room temperature was studied by QCM-D. Samples obtained at 60, 120 and 240 minutes of mixing time were selected in order to study the behaviour of a non-nanostructured sample (60 minutes) and two nanostructured samples containing different morphologies (120 and 240 minutes) (See Fig. 2).

Prior to the experiments, the sensors were conditioned overnight under a constant water flux. In order to understand if there was a general difference between the three samples as regards interaction with water, we represented the experimental data from conditioning through plotting dissipation (D) as a function of frequency. Whilst time is eliminated as an explicit parameter in this type of representation, it can implicitly be understood for these studies that time increases along with frequency as adsorption proceeds.

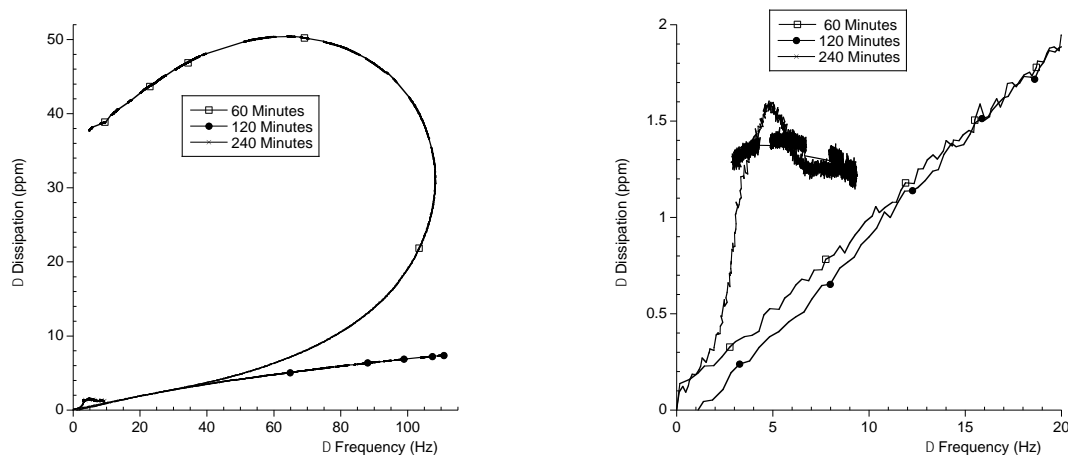


Fig 6. Dissipation (D) versus frequency (F) for the samples containing 10% of siloxane obtained at 60, 120 and 240 minutes of mixing time cast at room during water conditioning (left), and detail of the graph (right).

As can be seen from Fig. 6, for all samples an initial water sorption went along with an increase in dissipation. However, the interaction with water of the nanostructured sample obtained after 240 minutes mixing was clearly less than that of the other two samples, indicating that the water sorption ability of this sample was lower (Fig. 6, detail).

Samples obtained at 60 and 120 minutes showed a similar behavior up to about 40 Hz. At higher frequencies (water uptake), the sample of less mixing time showed a non-linear and very pronounced increase in dissipation, followed by a decrease in frequency (water loss) but maintaining high dissipation values. This result evidenced that the polymer underwent a strong swelling up to a point where it rearranged significantly and water desorption occurred. As this was the only sample that was not nanostructured, it may be concluded that the initial higher swelling owing to the water uptake was related to the lower hydrophobicity of the sample. After swelling, however, the polymer rearranged, promoting phase separation and therefore in turn reducing water sorption.

These data, hence, already indicated that the nanostructuring of the polymer modulated the interaction with water, based on either the overall hydrophilicity of the polymer, its morphology, or both. This is in line with results from respective contact angle measurements, where the nanostructured samples presented higher values than the homogeneous ones.

Subsequently, the respective sensors were put into contact with different concentrations of BSA in aqueous solution up to a maximum of 100 mg BSA/L. Samples were exposed to a successive increase in BSA concentration without intermediate flushing with water or removal of the already adsorbed BSA. The data obtained were then again represented independent of time in a dissipation-frequency plot, with the results shown in Fig 7. The frequency represents the quantity of BSA adsorbed on the surface while the dissipation reflects the “rigidity” with which BSA adsorbs. Low frequency values naturally represent the beginning of the experiments with

low BSA concentration in the water, and high frequencies represent data toward the end of the experiment where the BSA concentration was maximum.

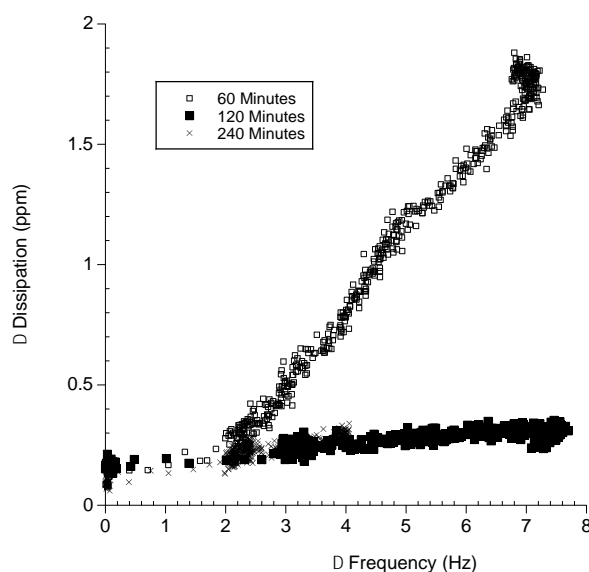


Fig 7. Dissipation (D) versus frequency (F) for the samples containing 10% of siloxane obtained at 60, 120 and 240 minutes of mixing time casted at room temperature during adsorption of BSA in water. The values represented were taken from the fifth harmonic.

As can be seen, for a frequency up to about 2 Hz, all samples showed a similar dependence of dissipation on frequency. Hence, during a first contact with BSA, no difference was seen in the degree of adsorption. Minor variations amongst the dissipation values were statistically not significant. With increasing BSA concentration, however, a distinct adsorption behavior was observed for the sample of less mixing time as it adsorbed as much as the one mixed for 120 minutes ($F=7-8\text{Hz}$), but with a significantly higher dissipation. This higher dissipation of the non nanostructured sample (mixing 60 minutes) indicated a more viscoelastic adsorption “film” of BSA and was most probably due to a higher water content resulting in a more “loosely” adsorbed BSA.

The dissipation of the two nanostructured samples (120 and 240 minutes of mixing, respectively) followed an almost identical trend as a function of frequency. It may be speculated that on nanostructured samples BSA was adsorbed in a different conformation that did not retain water as much as it did in the non-nanostructured one. This result would be in line with literature data which indicate that the disruption of protein adsorption requires compositional heterogeneity to create a mismatch between the nanodomains and the anchoring sites of the protein [15,18].

Finally, it should be noted that the sample obtained after 240 minutes mixing presented a reduced adsorption of BSA: compared to the other two samples the maximum frequency reached was only half. This result was also obtained from static sorption measurements shown in the previous section (see table 1) and revealed that while BSA adsorbed in the same manner

and conformation on the two nanostructured samples, the amount of interaction sites decreased by 50% for the one with longer mixing times.

Conclusions

In conclusion, static measurements showed that the adsorption of BSA was reduced when the coatings showed a phase separated structure. From the QCM-D measurements, we could clearly see differences in the water sorption between the samples as well as the swelling of the polymer, which is in agreement with the BSA adsorption data. Data from QCM-D furthermore allowed obtaining a qualitative evidence on how BSA adsorbed under presumably different conformations onto the sample films studied. The latter is particularly interesting as it might provide insights into how easily the adsorbed protein can be removed from the surface, if required.

Acknowledgements

The authors acknowledge the University of the Basque Country UPV/EHU (UFI 11/56) and, the Basque Government (Ayuda a grupos de investigación del sistema universitario vasco IT618-13 and PhD scholarship) and the Ministerio de Economía y competitividad (CTQ2013-4113-R) for the funding received to develop this work. Technical and human support provided by Macrobehaviour-Mesostructure-Nanotechnology SGIker Service of UPV/EHU is also gratefully acknowledged.

References

- [1] D. M. Yebra, S. Kiil, K. Dam-Johansen, *Progress in Organic Coatings* 50 (2004) 75–104.
- [2] T. Vladkova, *Surface Modification Approach to Control Biofouling*. Springer Series on Biofilms, doi: 10.1007/7142_2008_22 135 135 Springer-Verlag Berlin Heidelberg 2008.
- [3] A. M. Brzozowska, F.J. Parra-Velandia, R. Quintana, Z. Xiaoying, S. S. C. Lee, L. Chin-Sing, D. Jańczewski, S.L.M. Teo, J. G. Vancso*, *Langmuir* 30 (2014) 9165–9175.
- [4] D. L. Schmidt, R. F. Brady, K. Lam, D. C. Schmidt, M. K. Chaudhury, *Langmuir* 20 (2004) 2830-2836.
- [5] C. P. Stallard, K. A. McDonnell, O. D. Onayemi, J. P. O’Gara, D. P. Dowling, *Biointerphases* 7 (2012) 31-43.
- [6] S. M. G. Demneh, B. Nasernejad, H. Modarres. *Colloids and Surfaces B: Biointerfaces* 88 (2011) 108–114.
- [7] P.A. George, B. C. Donose, J. J. Cooper-White. *Biomaterials* 30 (2009) 2449–2456.
- [8] E. Yilgör, I. Yilgör, *Progress in Polymer Science* 39 (2014) 1165–1195.
- [9] P. Majumdar, A. Ekin, D..C. Webster DC, *Smart coatings* 957 (2007) 5-61.

- [10] A. Ekin , D.C. Webster, J.W. Daniels, S.J. Stafslie, F. Cassé, J. Callow, J. Coatings Technol. Res. 4 (2007) 435–451.
- [11] S. Sommer, A. Ekin, D.C. Webster, S.J. Stafslie, J. Daniels, L.J. VanderWal LJ, Biofouling 26 (2010) 961-972.
- [12] R.B. Bodkhe, S.E.M. Thompson, C. Yehle, N. Cilz, J. Daniels, S.J. Stafslie SJ, J. Coatings. Technol. Res 9 (2011) 235-249.
- [13] A. Santiago, L. Martin, J.J. Iruin, M.J. Fernández-Berridi , A. González, L. Irusta, Progress in Organic Coatings 77 (2014) 798–802.
- [14] A. Santiago, A. González, J. J. Iruin, M. J. Fernández-Berridi, M. E. Muñoz, L. Irusta, Macromol. Symp. 321-322 (2012), 150–154.
- [15] C. A. Amadei, R. Yang, M. Chiesa, K. K. Gleason, S. Santos, ACS Appl. Mater. Interfaces 6 (2014) 4705–4712.
- [16] P. Majumdar, S. Stafslie, J. Daniels, D. C. Webster, J. Coat. Technol. Res., 4 (2007) 131–138.
- [17] F. Li, J. Meng, J. Ye, B. Yanga, Q. Tiana, C. Deng, Desalination 344 (2014) 422–430.
- [18] S. H. Baxamusa, K.K. Gleason, Adv. Funct. Mater. 19 (2009) 3489–3496.
- [19] M.A. Bradford, Anal Biochem 72 (1976) 248–254.
- [20] P. Majumdar, D. C. Webster, Macromolecules 38 (2005) 5857-5859.
- [21] S. Sommer, A. Ekin, D.C. Webster, S.J. Stafslie, J. Daniels, L.J. Vander Wal, S.E.M. Thompson, M.E. Collow, J.A. Collow, Biofouling 26 (2010) 961-972.
- [22] F. Azemar, F. Fäy, K. Réhel, I. Linossier, Progress in Organic Coatings 87 (2015) 10–19.